UTS UNIVERSITY OF TECHNOLOGY SYDNEY

# Investigating Cardiovascular Mechanotransduction: Insights from Cardiac Models Under Simulated Microgravity and Radiation

**by Carin Alsani Basirun**

Thesis submitted in fulfilment of the requirements for
the degree of

**Doctor of Philosophy**

under the supervision of Prof. Joanne Tipper, Dr. Carmine Gentile and Dr. Giulia Silvani.

University of Technology Sydney
Faculty of Engineering and IT

June 2024

# CERTIFICATE OF ORIGINAL AUTHORSHIP

I, **Carin Alsani Basirun**, declare that this thesis is submitted in fulfilment of the requirements for the award of Doctor of Philosophy in the **School of Biomedical Engineering, Faculty of Engineering and IT**, at the University of Technology Sydney.

This thesis is wholly my own work unless otherwise referenced or acknowledged. In addition, I certify that all information sources and literature used are indicated in the thesis.

This document has not been submitted for qualifications at any other academic institution.

This research is supported by the Australian Government Research Training Program.

Signature:

Production Note:
Signature removed prior to publication.

Carin Alsani Basirun

Date: 28/05/2024

# ACKNOWLEDGEMENTS

I would like to dedicate this thesis to my family, who have been my constant support and provided a safe space for me throughout this endeavour. This is for my parents, Mama and Papa, San San and Lee, who sacrificed their comfortable life and moved to a foreign country with no English, leaving family, friends, and status behind for a better life for my sister and I. Thank you to my sister, Celin, for stepping up. Additionally, thank you to Nori for being a source of joy.

First and foremost, I would like to thank Professor Joanne Tipper for her patience and support, sitting through all my tears and helping me complete this PhD. I couldn't have done it without you. Although not my primary supervisor from the start, Joanne has been a constant source of reassurance. I am especially thankful that Joanne took on the role of my primary supervisor, despite it being so late in my PhD journey. Joanne, thank you for being a wonderful PI, supervisor, teacher, mentor, and friend.

I would also like to express my appreciation for Dr. Giulia Silvani, who is my role model and inspiration. Her love for science and knowledge is inspiring and contagious. Without her by my side, I would not have persevered. Giulia, thank you for being my supervisor from the start, the only constant and safe space. Your guidance, patience, and friendship have been invaluable.

I would also like to thank my co-supervisor, Dr. Carmine Gentile, for his insights, knowledge, and consistent support. To my supervisors and collaborators at ANSTO, I am immensely grateful for the support and safe space provided for my research. Special thanks to Mel, Nick, Jun, and Ryan, for always making time for me and helping me reach the finish line. This research was also supported by an AINSE Ltd. Residential Student Scholarship (RSS).

A special thank you to everyone I have worked with in the lab, for being great sounding boards and sources of support and joy throughout the long hours and unsuccessful experiments. I would like to acknowledge my previous supervisor, for starting me on this journey. The experience taught me the importance of perseverance and solidified my own beliefs and integrity.

Last but not least, to my best friends who have been patient and understanding with me these last few years, dealing with the stress, busyness, and poor communication. Thank you, Chelsea, Jessie, Nik, Emilie, and Kareena.

## FORMAT OF THESIS

This thesis is submitted as a conventional thesis, consisting of seven chapters. The focus of the thesis is centred around the investigation of the impact of simulated microgravity and radiation on the cardiac cells and models from a 2D monolayer model, a 3D collagen hydrogel model, and subsequently, a hybrid 3D bio-printed heart-on-chip model.

1. Introduction: Introduces the research, including background, motivation, aims, objectives, and scope. Highlights the significance of studying cardiovascular mechanotransduction under simulated microgravity and radiation.

2. Literature Review: Reviews existing literature on cardiac mechanotransduction, focusing on how heart cells respond to mechanical stimuli like microgravity and radiation. Identifies gaps and opportunities for further research.

3. General Materials and Methods: Details the materials and methods used, including experimental setups, cell culture techniques, and analytical methods to study the effects of simulated microgravity and radiation on cardiomyocytes.

4. 2D Cardiomyocyte Responses: Summarizes the process of culturing cardiomyocytes in two-dimensional environments, assessing their responses to microgravity and radiation.

5. 3D Collagen Hydrogel Model Responses: Investigates the mechanical properties and responses of three-dimensional collagen hydrogel heart models exposed to simulated microgravity and radiation.

6. Hybrid Heart-on-a-Chip: Presents the development of a three-dimensional heart-on-a-chip system for the study of the biological responses of cardiomyocytes in this platform.

7. Conclusions and Future Directions: Summarize the main research findings, contributions and proposes future research directions based on the advances made.

# LIST OF PUBLICATIONS

Silvani, G., Bradbury, P., **Basirun, C.**, et al. (2022). Testing 3D printed biological platform for advancing simulated microgravity and space mechanobiology research. *npj Microgravity, 8*(19).

Silvani, G., **Basirun, C**., Wu, H., Mehner, C., Poole, K., Bradbury, P., & Chou, J. (2021). A 3D-Bioprinted Vascularized Glioblastoma-on-a-Chip for Studying the Impact of Simulated Microgravity as a Novel Pre-Clinical Approach in Brain Tumor Therapy. *Advanced Therapeutics, 4*(11), 2170033.

**Basirun, C**., Ferlazzo, M. L., Howell, N. R., Liu, G.-J., Middleton, R. J., Martinac, B., Narayanan, S. A., Poole, K., Gentile, C., & Chou, J. (2021). Microgravity × Radiation: A Space Mechanobiology Approach Toward Cardiovascular Function and Disease. *Frontiers in Cell and Developmental Biology, 9*, 750775.

Xiang, Y., **Basirun, C**., Chou, J., Warkiani, M. E., Török, P., Wang, Y., Gao, S., & Kabakova, I. V. (2020). Background-free fibre optic Brillouin probe for remote mapping of micromechanics. *Biomedical Optics Express, 11*(6687-6698).

# ABSTRACT

This thesis investigates the effects of simulated microgravity (s-μG) and ionizing radiation (IR) on cardiomyocytes using both two-dimensional (2D) and three-dimensional (3D) culture models to understand the impact of spaceflight conditions on cardiovascular health. The primary aim is to elucidate how these stressors influence cellular behaviour, mechanotransduction pathways, and DNA damage responses.

The first aim characterised the initial responses of AC-16 cardiomyocytes to s-μG, IR, and their combined effects in a 2D environment. Methods included cell viability assays, gene expression analysis, and DNA damage assessment through γ-H2AX foci formation. Results showed decreased cell proliferation and viability under s-μG, with IR causing notable DNA damage. Combined exposure exacerbated DNA damage without additive effects on YAP1 nuclear localization.

The second aim developed a 3D collagen-based hydrogel for studying cardiomyocyte responses. Methods included fabrication of 3D hydrogels, cell embedding, and viability assays under s-μG and IR conditions. Preliminary results indicated the 3D environment buffered gene expression changes and enhanced cell viability compared to 2D cultures. However, combined s-μG and IR exposure significantly increased DNA damage.

The third aim optimized 3D bioprinting techniques to create a hybrid heart-on-a-chip model for simulating the cardiac microenvironment. Techniques included using bioinks and incorporating human cardiac fibroblasts. Assessments revealed significant findings related to cell viability, proliferation, and functionality under s-μG and IR conditions, demonstrating the model's potential for studying spaceflight-induced cardiovascular risks.

In conclusion, this thesis advanced our understanding of cardiomyocyte behaviour under spaceflight-like conditions and developed innovative models for future investigations. The insights gained will inform strategies to protect cardiovascular health in space, ensuring astronaut safety on extended missions. Through comprehensive evaluation of s-μG and IR effects in both 2D and 3D environments, this research lays a foundation for future studies aimed at mitigating space travel health risks.

# LIST OF ABBREVIATIONS

| | |
|---|---|
| 2D | Two-Dimensional |
| 2-deltaCt | Two-Delta Ct |
| 3D | Three-Dimensional |
| ANOVA | Analysis of Variance |
| ANSTO | Australian Nuclear Science and Technology Organisation |
| BSA | Bovine Serum Albumin |
| BTHS | Barth Syndrome |
| CAD | Computer-Aided Design |
| cDNA | Complementary DNA |
| CGR | Cosmic Galactic Rays |
| CPCs | Cardiac Progenitor Cells |
| Ct | Cycle Threshold |
| CVS | Cardiovascular System |
| CVD | Cardiovascular Diseases |
| DAPI | 4',6-Diamidino-2-Phenylindole |
| DDR | DNA Damage Response |
| DMEM | Dulbecco's Modified Eagle Medium |
| DNA | Deoxyribonucleic Acid |
| ECM | Extracellular Matrix |
| EthD-1 | Ethidium Homodimer |
| EVA | Extra Vehicular Activities |
| FBS | Fetal Bovine Serum |
| FIJI | FIJI is a Module of ImageJ |
| FOV | Field of View |
| GOI | Genes of Interest |
| Gy | Gray |
| HA | Hyaluronic Acid |
| HCAEC | Human Coronary Artery Endothelial Cells |
| HKG | Housekeeping Gene |
| hiPSC-CMs | Human Induced Pluripotent Stem Cell-derived Cardiomyocytes |
| ICC | Immunocytochemistry |
| ISS | International Space Station |
| KSC | Kennedy Space Centre |
| M | Sample Mean / Arithmetic Mean |
| Mdn | Median |
| MI | Myocardial Ischemia |

| | |
|---|---|
| MIP | Maximum Intensity Projection |
| MS | Mean Square |
| MSE | Mean Square Error |
| MSSF | Microgravity Simulation Support Facility |
| n | Technical replicates within a biological replicate |
| N | Independent biological replicates |
| NRCM | Primary Rat Neonatal Cardiomyocytes |
| pATM | Phosphorylated ATM |
| PBS | Phosphate Buffered Saline |
| PCR | Polymerase Chain Reaction |
| PDMS | Polydimethylsiloxane |
| PFA | Paraformaldehyde |
| PGA | Polyglycolic Acid |
| PEG | Polyethylene Glycol |
| PCL | Poly(caprolactone) |
| PLA | Polylactic Acid |
| RNA | Ribonucleic Acid |
| RPM | Random Positioning Machine |
| RT-qPCR | Reverse Transcription Quantitative Polymerase Chain Reaction |
| RWV | Rotating Wall Vessel |
| s-μG | Simulated Microgravity |
| SD | Standard Deviations |
| SE | Standard Error |
| SEM | Standard Error of the Mean |
| SPE | Solar Particle Events |
| UTS | University of Technology, Sydney |
| UV | Ultraviolet |
| v/v | Volume per Volume |
| w/v | Weight per Volume |
| YAP | Yes-associated Protein |

# TABLE OF CONTENTS

# LIST OF FIGURES

# LIST OF TABLES

# Chapter 1 -

## Introduction

## 1.1 BACKGROUND

This introductory chapter sets the stage for an in-depth discussion on the significance of cell mechanobiology in advancing our understanding and treatment of cardiovascular diseases (CVD), which stand as a major health challenge globally and the leading cause of mortality in Australia. CVD accounts for one in four deaths in Australia, with over 43,500 fatalities annually, and imposes a significant economic burden, with costs approximating AUD 14.3 billion each year due to healthcare expenses (Australian Institute of Health and Welfare., 2024). The intricate relationship between cellular mechanics and cardiovascular health is underscored by the critical function of cardiomyocytes—cardiac muscle cells that constitute about 75% of the adult human heart's volume (Mathur et al., 2016). The scale of cardiomyocyte depletion can range dramatically from acute loss due to necrosis triggered by insufficient blood supply to gradual attrition over many years due to chronic conditions like hypertension and valvular disease. This variability highlights the complexity of CVD and the pressing need for advanced research and modelling techniques to better understand and combat these conditions. (Laflamme & Murry, 2011).

Given the high fatality rates and economic costs associated with cardiovascular diseases, researchers have been motivated to increase their understanding of cardiac physiology through mechanobiology. Mechanobiology is a field that examines how physical forces and changes in cell or tissue structure influence cellular behaviour, playing a pivotal role in understanding disease mechanisms and identifying potential therapeutic strategies. Mechanical forces such as blood flow, pressure, and tissue stiffness are crucial regulators of cell function within the cardiovascular system, directly impacting disease onset and progression. The increasing interest in space exploration and space biology has introduced a new dimension to mechanobiology in CVD research.

Spaceflight presents a unique environment that subjects biological systems to extreme conditions, notably microgravity and heightened cosmic radiation. These factors significantly disrupt normal cellular and tissue function, offering an unparalleled opportunity to study cardiovascular responses under conditions of mechanical unloading and environmental stress. Microgravity, by reducing the mechanical forces that normally act on the cardiovascular system, leads to diminished mechanical stimuli that are essential for maintaining cardiac muscle mass, vascular integrity, and overall heart health. Studies have shown that astronauts experience up to a 20% reduction in cardiac output and a 10-15% decrease in heart mass during missions longer than six months, alongside a marked increase in arterial stiffness—an effect comparable to 20 years of aging on Earth (Hughson et al., 2016). The impact of space radiation further complicates these effects, exposing astronauts to radiation levels 50-100 times higher than those on Earth. This heightened exposure accelerates oxidative stress, damages DNA, and triggers inflammatory responses, significantly increasing the risk of cardiovascular complications. Evidence suggests a 30-40% higher risk of coronary heart disease

among populations exposed to high-dose radiation, underscoring the compounded dangers of prolonged space missions (Boerma et al., 2016).

These unique space conditions present an opportunity to study cardiovascular responses, enabling researchers to explore the cellular and molecular mechanisms that drive CVD in extreme environments. Specifically, microgravity disrupts mechanotransduction pathways in cardiomyocytes, leading to cytoskeletal reorganisation, altered gene expression, and impaired cellular function. Meanwhile, radiation exacerbates these disruptions by inducing DNA damage and compromising the cell's ability to repair, which not only amplifies the detrimental effects of microgravity but also mirrors the pathological changes seen in aging and CVD on Earth (Moreno-Villanueva et al., 2017). By leveraging these extreme conditions, researchers can gain critical insights into the pathophysiology of CVD, identifying novel biomarkers and potential therapeutic targets. This approach extends beyond astronaut health, offering broader implications for the general population. Understanding how cells and tissues adapt—or fail to adapt—to these harsh conditions can inform the development of innovative interventions to mitigate the effects of CVD, ultimately advancing our capacity to treat cardiovascular diseases and improve long-term health outcomes.

To address the challenges of conducting experiments in space, researchers have developed microgravity simulators, such as the random positioning machine (RPM), to closely mimic the microgravity environment experienced in space at the cellular level. These simulators create a near-weightless state by continuously altering the orientation of biological samples, effectively randomising the direction of gravity and preventing cells from sensing a stable gravitational force. This disruption closely replicates the microgravity conditions that cells experience during spaceflight, leading to similar alterations in cellular behaviour, morphology, and function. Microgravity simulators like RPMs provide a practical and accessible approach for studying the biological effects of microgravity, laying the groundwork for deeper insights into how these conditions impact cellular mechanotransduction and overall cardiovascular health. More on the mechanisms and specific impacts of these simulations will be discussed in Section 1.2.2.

Parallel to the advancements in simulating space conditions, the limitations inherent in traditional cardiac research models, such as *in vitro* slices of adult human hearts and animal testing, have been recognised. These methods face practical challenges, including a shortage of organ donors, the limited viability of heart tissue cultures, and methodological limitations in their ability to accurately mimic the human heart's intricate physiology (Cameli et al., 2022). As a result, recent efforts have shifted towards creating three-dimensional (3D) models that better replicate the heart's native environment, incorporating the extracellular matrix (ECM), multiple cell interactions, and mechanical stimuli. These advancements offer a more relevant platform for organ and disease modelling, potentially accelerating the development of therapeutic interventions (Ribas et al., 2016).

While these two approaches— simulation of the space environment and the creation of 3D cardiac models—are distinct in their methodologies, they are united in their overarching goal: to enhance our understanding of cardiac mechanobiology. This introduction lays the groundwork for the following extensive literature review, emphasising the critical importance of integrating cell mechanobiology into cardiovascular research. The following literature review will provide a comprehensive overview of the current landscape of cardiovascular research, highlighting the role of mechanobiology in understanding cardiac function, the limitations of existing models, and the potential of advanced 3D models and space condition simulators. These innovative approaches are set to enhance the understanding of cardiovascular health, both in the context of space and on Earth.

## 1.2 EFFECTS OF SPACE CONDITIONS ON THE CARDIOVASCULAR SYSTEM

New approaches and concepts are needed to understand the complexity of cardiac function and disease onset. Interestingly, the effects of spaceflight on the human body have been shown to mimic an accelerated aging process, resulting in cardiovascular changes that closely resemble those seen in CVD (Hughson et al., 2016). One notable effect is the increased stiffness in the carotid artery, a hallmark of aging, which can also be induced by microgravity exposure during spaceflight (Gepner et al., 2014; Hughson et al., 2016; Lakatta & Levy, 2003). As such, a deeper understanding of the cardiogenic effects of microgravity and radiation may have implications for human spaceflight and treat millions of heart disease patients on Earth.

### 1.2.1 Cardiovascular System in Space: Insights from Astronaut Studies

Exposure to microgravity, which differs from the normal state of gravity, puts the human body under critical physiological changes, some of which are important to survival. Gravity is essential to fluid distribution and vital to the cardiovascular system. Under normal gravity, where the human body is upright, there is higher arterial pressure (200 mmHg) in the feet and lower pressure (70 mmHg) in the head. Meanwhile, the heart relative to arterial pressure is 100 mmHg. In a microgravity environment, this fluid distribution is altered, losing the gradient, and the fluid distribution becomes more uniform throughout the body (Demontis et al., 2017; Hargens & Richardson, 2009) This, in turn, reduces the demand for arterial blood pressure and decreases the amount of work the heart has to do, leading to cardiovascular deconditioning and increased risk of CVD.

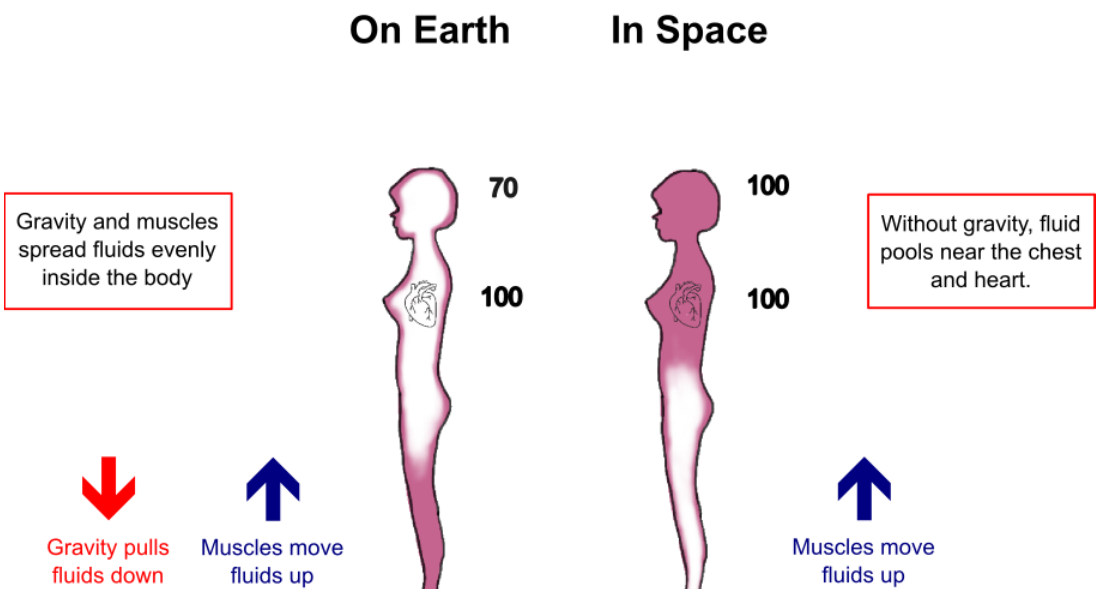


*Figure 1.1 Fluid distribution on Earth and in Space. On Earth, the feet have higher arterial pressure (200 mmHg) and lower pressure (70 mmHg) in the head. Meanwhile, the heart relative to arterial pressure is 100 mmHg. In a microgravity environment, this fluid distribution is altered, losing the gradient and becoming more uniform throughout the body.*

Head-down tilt is one ground-based analogue model for studying s-μG and, therefore, cardiovascular deconditioning effects, where previous reports utilising this model have shown a significant elevation of microvascular pressures in the head and increased capillary fluid filtration (Christ et al., 2001; Parazynski et al., 1991). These microvascular adaptations are related to the fluid redistribution phenomenon highlighted previously and, in turn, suggest vascular adaptations.

Observations from astronauts who have returned from a 6-month spaceflight have shown increased stiffness in the carotid artery, comparable to 20 years of aging (Hughson et al., 2016).This reduced cardiac function leads to a reduction in tissue mass of the heart, also known as cardiac atrophy, which ultimately causes debilitating changes in heart function. Animal models further confirmed that the space environment contributes to higher aortic stiffness, with rats exposed to high-energy radiation simulating the space environment showing significantly higher aortic stiffness over six months (Soucy et al., 2011). Arterial stiffness is believed to be a precursor to atherosclerosis and a marker for increased cardiovascular disease risk (Safar et al., 2003; Zieman et al., 2005).

Spaceflight-induced cardiovascular changes extend beyond the heart and large arteries to include microvascular and cellular alterations. Recent *in vivo* vascular studies from long-duration ISS missions have shown structural and functional changes in the carotid and brachial arteries, accompanied by elevated biomarkers of oxidative stress and inflammation, such as oxidised LDL and TNF-α (Lee et al., 2020). The heart itself often shows signs of atrophy, with changes in contractile protein gene expression and increased lipid accumulation in cardiac cells observed post-flight. While some cardiovascular adaptations may be temporary, others pose long-term consequences, as cardiovascular deconditioning during spaceflight is often not fully reversible, particularly after extended missions (Gallo et al., 2020; Vernice et al., 2020). The accelerated aging of cardiovascular function in microgravity has been noted, with some studies indicating that the functional capacity of the cardiovascular system declines at a rate significantly faster than aging on Earth (J. Rowe, 2012). This raises concerns about the potential for irreversible damage, especially in the context of future long-duration missions to destinations such as Mars, where immediate physical demands upon re-entry could pose serious risks to astronaut health. Notably, Apollo astronauts who travelled to the Moon had a higher risk of cardiovascular disease, highlighting the compounded impact of spaceflight and radiation exposure (Delp et al., 2016).

The observed changes in fluid distribution, vascular stiffness, and cardiovascular biomarkers in microgravity environments highlight critical physiological adaptations that increase cardiovascular disease risk. These insights highlight the importance of examining how these physiological changes translate to cellular and molecular alterations within the cardiovascular system. By focusing on cellular studies, particularly those using microgravity simulators, researchers can uncover critical insights into how altered mechanical forces and radiation exposure influence cellular signalling,

mechanotransduction, and tissue remodelling. This cellular-level understanding is crucial for developing targeted countermeasures to protect cardiovascular health during prolonged space missions and for potential therapeutic applications on Earth.

### 1.2.2 Microgravity and Radiation: Implications for Cardiac Physiology

From the insights gained from astronaut studies, it can be concluded that spaceflight exposure also leads to various cellular and organ adaptations. However, the *in vivo* study of cardiovascular adaptations is limited, whether through actual or ground-simulated studies. Several studies have examined microgravity's impact on cell proliferation and differentiation. These studies have demonstrated that stem cells grown in a microgravity environment grew differently from those produced under normal gravity, showing changes in division, contraction, and migration (C. Zhang et al., 2015).

Recent studies involving cardiovascular system cells looked at cardiac progenitor cells (CPCs) cultured on the ISS. Alterations to transcriptional control were measured, and found that among neonatal and adult CPCs, the significantly dysregulated microRNAs affect cytoskeletal remodelling and mechanotransduction pathways. Genes related to mechanotransduction were downregulated, while the expression of cytoskeletal genes and calcium signalling molecules was elevated considerably only in neonatal CPCs. Cytoskeletal organisation and migration were both affected by spaceflight in neonatal and adult CPCs; however, only neonatal CPCs experienced increased expression of early developmental markers and a higher potential to proliferate (Baio et al., 2018; Camberos et al., 2019, 2021).

Wnorowski et al (2019) reported that monolayers of beating cardiomyocytes derived from human induced pluripotent stem cells (hiPSC-CMs) sent to the ISS for 5.5 weeks had no significant effect on the morphology. However, some functional differences were observed, where the space-flown hiPSC-CMs had a decreased calcium recycling rate and an observed beating irregularity when the samples were assessed following their return to Earth. These results suggested that their calcium-handling-related parameters remained altered following the sample's return to normal gravity (Wnorowski et al., 2019). This study also examined the genetic responses of hiPSC-CMs to spaceflight conditions and found that DNA damage and repair genes were significantly decreased in the flight samples when compared to the post-flight and ground samples, and additionally revealed that the genes involved in the mitochondrial metabolic pathway had the most significant change. A factor to consider is that in this study, the flight samples went through the impact of launch into space and re-entry into the atmosphere, whereas the ground samples did not have to go through such transit conditions. Another consideration is the level of radiation that will be considerably higher aboard the ISS than on Earth (Wnorowski et al., 2019). Although Baio et al (2018) and Wnorowski et al (2019)

had similar microgravity conditions with the samples flown to the ISS, there were discrepancies in results including the contradiction in the expression of DNA repair genes and this may be attributed by several experimental conditions, one of them being that the type of cells used by Baio et al (2018) being progenitor cells and Wnorowski et al (2019) used differentiated cardiomyocytes. Other experimental conditions can be considered between these and other experiments in the field, including the duration of exposure to microgravity and the way the cells were processed for the assays.

Space radiation can also compromise the cardiovascular system and produce adverse effects (Hughson et al., 2016, 2018). The harmful effects of ionising radiation have been extensively studied. In higher doses of radiation (> 100 mGy), radiation has been clinically shown to lead to cardiac dysfunction over time, where cases have been reported following radiotherapy. Short and long-term effects of radiation-induced cardiovascular diseases were observed following radiotherapy treatment of cancers adjacent to the heart, including lungs, breasts, and oesophagus. The hearts of patients received 1.6 to 3.9 Gy radiation during radiotherapy treatment of peptic ulcer disease, increasing the risk of coronary heart disease (Carr et al., 2005). In breast cancer radiotherapy, women's hearts received doses of 2.7 - 6.3 Gy, which significantly increased the risk of developing ischemic heart disease (McGale et al., 2011). This mainly involves increased oxidative stress as well as inflammation, playing a role in radiation-induced cardiovascular damage (Coleman et al., 2015; Seawright et al., 2017; Soucy et al., 2011).

In a rat model, Soucy et al (2011) demonstrated the detrimental effects of ionising radiation. The rats exposed to 1 Gy high-energy iron-ion radiation at approximately 0.5 Gy/min exhibit higher aortic stiffness and more significant endothelial dysfunction four months post-radiation. Radiation-induced apoptotic signalling has also been observed by Sedelnikova et al (2007), who looked at the effect of radiation on 3D human tissue models and found that not only does the incidence of DNA double-strand breaks increase, but there was also an increase in apoptosis in bystander cells (Sedelnikova et al., 2007). Meanwhile, Sarosiek et al. performed a study using *in vivo* models. They found that the mitochondria of many adult tissues are highly resistant to pro-apoptotic signalling, leading to cell radiation resistance. These studies suggest that intrinsic apoptosis might be triggered in both *in vitro* and *in vivo* after radiation exposure. The relationship between dosage and response for some biological effects is not linear or proportional to dose (Puukila et al., 2017). However, it is unknown what impact primarily low-dose-rate radiation will have on the cardiovascular system during space exploration, particularly in compounding factors, including microgravity (Boerma et al., 2016).

When looking at the effects of both microgravity and space radiation, most studies have focused on utilising stem cells and looking into their development (Table 1.1). Currently, limited studies have explored the effects of both microgravity and space radiation as a mechanism for CVD-causing

processes. Microgravity and space radiation have been shown to exhibit significant changes at both subcellular and tissue levels. The unwavering question of whether microgravity, radiation or the dual effects have on cardiac function remains open for discovery. Ultimately, both conditions are a new type of extreme environment where researchers can uncover knowledge from the cellular to organ level. The stress and effect of microgravity from human space travel on cardiac function share traits and properties similar to that of CVD and provide a unique opportunity for researchers to expand and advance in this critical area of multidisciplinary research.

*Table 1.1 Effect of Microgravity and Radiation on Cardiovascular System Cells in vitro.*

| Cell Origin | Space μG or Simulated μG | Space Radiation/ Radiation Source | Findings | Reference |
|---|---|---|---|---|
| Human induced pluripotent stem cells - derived cardiomyocytes (hiPSC-CMs) | Space μG (ISS) | Space radiation | ▪ Decreased calcium recycling rate as well as an observed beating irregularity.<br>▪ Significant upregulation of sarcomere genes<br>▪ Significant decrease in DNA damage and repair genes<br>▪ 2,635 genes were differentially expressed among flight, post-flight, and ground control samples | Wnorowski et al., 2019 |
| Adult cardiac progenitor cells (CPCs) | Space μG (ISS)/ Simulated μG (2D clinostat) | Space radiation (ISS) | ▪ Upregulation of YAP1 expression<br>▪ Short term YAP1 activation | Camberos et al., 2019 |
| Neonatal and adult human cardiac progenitor cells (CPCs) | Space μG (ISS) | Space radiation | ▪ Mechanotransduction genes are downregulated in neonatal CPCs and upregulated in adult CPCs.<br>▪ Increased expression of early developmental markers and enhanced proliferative potential in neonatal CPCs.<br>▪ Increased expression of DNA repair genes in both adult and neonatal CPCs | Baio et al., 2018 |
| Adult and neonatal cardiac progenitor cells (CPCs) | Space μG (ISS) | Space Radiation | ▪ Transcript associated with stemness is significantly elevated.<br>▪ Key transcripts involved in cell cycle progression, cell differentiation, heart development, oxidative stress and focal adhesion were induced | Camberos et al., 2021 |

### 1.2.3 Earth-based Simulations of Space Conditions

The unique zero-gravity environment of space provides an invaluable opportunity to explore mechanosensing processes that are challenging to study on Earth. However, conducting experiments in space is demanding, costly, and limited, necessitating the development of Earth-based alternatives that simulate microgravity and radiation effects without travelling to space and without needing it to be performed in space laboratories. This is where earth-based simulations come into play.

#### *1.2.3.1 Simulated Microgravity*

Ground-based facilities (GBFs), such as the Microgravity Simulation Support Facility (MSSF) at NASA's John F. Kennedy Space Centre (KSC), have been established to enable experiments under conditions where gravity levels can be averaged to almost zero, facilitating a closer approximation of the microgravity environment of space (NASA, 2019). Among the most common techniques are Random Positioning Machines (RPM), Rotating Wall Vessels (RWV), clinostats (both 2D and 3D), and magnetic levitation. Each of these methods simulates microgravity in distinct ways, leading to varied cellular responses (Y. Zhang et al., 2022).

RPM simulates microgravity by continuously rotating samples around multiple axes, effectively averaging the gravitational force to near-zero over time. Several studies have the effectiveness of RPM's in simulating microgravity, for instance, Krause et al. (2018) showed the effectiveness of RPM in simulating microgravity by studying statoliths in Chara rhizoids, which are root-like structures in green algae that anchor the organism to a substrate. These rhizoids are highly sensitive to gravity due to the presence of statoliths—dense particles within the cells that move in response to gravitational changes. By using an RPM to disrupt normal gravitational forces, Krause et al. were able to assess the response of these statoliths, highlighting the RPMs ability to simulate microgravity conditions effectively. Brungs et al. (2019) further confirmed the RPMs usability for cellular assays, highlighting its reliability compared to traditional clinostats. RPM has been widely utilized to study various cellular responses, including cytoskeletal rearrangement, mechanosensitive ion channel activity, and gene expression alterations in the absence of gravitational effects (Calvaruso et al., 2021; Cazzaniga et al., 2020; Wuest et al., 2015). The RPM has been used to study the effects of s-μG on various cell types, including human keratinocytes, cancer cells, and immune cells. For instance, RPM has promoted cardiomyocyte differentiation and enhanced endothelial tube formation in stem cells (Grimm et al., 2009; Infanger et al., 2006; Wuest et al., 2015) Additionally, RPM have shown the potential to induce epithelial-mesenchymal transition in keratinocytes through epigenetic modifications (Ranieri et al., 2017; Sokolovskaya et al., 2020).

In contrast, RWV provide a different approach by creating a low-shear environment that mimics microgravity, promoting the growth of three-dimensional cell cultures, which are essential for studying tissue engineering applications (Moes et al., 2010; Aleshcheva et al., 2016). The unique hydrodynamic conditions generated in RWV allow for enhanced nutrient and oxygen distribution, which can influence cell proliferation and differentiation (D'Agostino et al., 2022). Studies have demonstrated that RWV can lead to changes in cellular signalling pathways and gene expression profiles, similar to those observed in real microgravity environments (Berardini, 2023). For example, Feger et al. (2016) observed decreased protein turnover and changes in mitochondrial and ribosomal protein translation in rat neonatal cardiomyocytes cultured in RWV (Feger et al., 2016).

Clinostats, available in 2D and 3D forms, simulate microgravity by rotating samples to average out the gravitational vector. However, these devices can introduce artifacts due to the rotating reference frame, which may not accurately replicate microgravity (Dijkstra et al., 2010; M. Liu et al., 2011). Research indicates that clinostats may not be as effective as RPM or RWV in certain biological contexts, particularly in terms of gene expression and cellular morphology (Manzano et al., 2012). Specific studies have shown that clinostats lead to absent tight junctions and extensive apoptosis in endothelial cells, increased cytosolic calcium in cardiomyocytes, and elevated stemness-associated genes in neonatal cardiac progenitor cells (Fuentes et al., 2015; Kang et al., 2011; C. Liu et al., 2020).

Magnetic levitation offers an alternative method of simulating microgravity by using magnetic fields to suspend cells without physical support. This technique has been particularly useful in biofabrication and tissue engineering approaches as it enables the creation of scaffold-free three-dimensional cell constructs (Anıl-İnevi et al., 2018; Sa et al., 2023). Research has demonstrated that magnetic levitation can influence growth and differentiation, though the exact mechanisms are still being investigated (Du et al., 2022). The impact of magnetic levitation varies with the strength of the magnetic field and the cellular context, underscoring the need for careful experimental design (Kamal et al., 2015).

In summary, while all these methods aim to simulate microgravity, they do so through different mechanisms, leading to distinct cellular responses. RPM and RWV are particularly effective for studying cellular behaviour in a microgravity-like environment, while clinostats and magnetic levitation offer alternative approaches with their own advantages and limitations. Understanding these differences is essential for designing experiments that accurately reflect the complexities of microgravity on biological systems. Studies, including different cell types in the cardiovascular response to s-μG, are summarised in Table 1.2.

*Table 1.2 Microgravity-Induced Cardiovascular Response*

| Cell Origin | µG Simulation Method | Findings | Reference |
|---|---|---|---|
| Human pluripotent stem cells (hPSCs) | Random Positioning Machine (RPM) | ▪ Production of highly viable and enriched cardiomyocytes<br>▪ Promote the induction of cardiac progenitors, CM differentiation, proliferation and increase cell survival of cardiac progenitors | Jha et al., 2016 |
| Endothelial cells (EA. hy926) | Random Positioning Machine (RPM) | ▪ Increase in ECM proteins and altered cytoskeletal components and intermediate filaments.<br>▪ Induced apoptosis in endothelial cells<br>▪ Formation of 3D cell aggregates; assembly to tube-like structures | Infanger et al., 2006 |
| Human pulmonary microvascular endothelial cells (HPMECs) | 3D clinostat | ▪ Tight junctions between cells were absent.<br>▪ Apoptosis-positive cells are extensively shown.<br>▪ Disorganized and depolymerised, extenuated actin filaments | Kang et al., 2011 |
| Heart cells from 2–4-day-old rats & 15-day-old chick embryos | Rotating bioreactor | ▪ Rat heart cells-based construct observed spontaneous and synchronous contraction.<br>▪ Highest fraction of total regenerated tissue mass | Freed and Vunjak-Novakovic, 1997 |
| HL-1 cardiomyocytes | 2D clinostat | ▪ Increased concentrations of cytosolic calcium and spontaneous calcium oscillations<br>▪ Induced cardiomyocyte atrophy<br>▪ Decreased cell size | Liu et al., 2020 |
| Primary rat neonatal cardiomyocytes (NRCM) | Rotating Wall Vessel (RWV) | ▪ Decreased protein turnover.<br>▪ Unaffected apoptosis, cell viability and protein degradation<br>▪ Upregulation of protein content and processes in mitochondrial protein translation<br>▪ Downregulation in proteins and protein translation in the rough endoplasmic reticulum and ribosomes | Feger et al., 2016 |
| Adult and neonatal cardiac progenitor cells (Isl-1+ CPCs) | 2D clinostat | ▪ Age-dependent responses tube formation<br>▪ Increase in growth factor expression.<br>▪ Elevated expression of stemness-associated genes in neonatal CPCs.<br>▪ Elevated transcription of DNA repair genes in neonatal CPCs | Fuentes et al., 2015 |
| Endothelial cells (EA. hy926) | Random Positioning Machine (RPM) | ▪ Formation of tube-like structure with walls of single-layered ECs | Grimm et al., 2009 |

Each simulation technique has shown advantages and disadvantages, and when chosen correctly for a given experiment, results similar to those obtained from space flight studies can be seen (Herranz et al., 2013). RPM is the most applicable method to simulate microgravity for studies that require cell culture.

#### *1.2.3.2 Simulated Radiation*

Simulating space radiation is equally essential for understanding its biological impacts, particularly concerning DNA damage, cellular repair mechanisms, and the potential for increased cancer risk among astronauts. The unique spectrum and intensity of cosmic and solar radiation, which differ significantly from terrestrial radiation, necessitate specialised simulation techniques, including particle accelerators, X-ray and gamma-ray sources, and neutron sources.

Particle accelerators, such as cyclotrons and synchrotrons, are used to simulate cosmic radiation by accelerating charged particles—protons and heavy ions—to high energies, replicating the effects of cosmic rays (Yan et al., 2020; X. Zhang et al., 2016). As these systems allow for precise control over the type and energy of particles, they provide an invaluable tool for studying the high-energy ionising component of space radiation (Sridharan et al., 2015).

X-ray and Gamma-ray Sources simulate the lower-energy components of space radiation, including solar radiation and the gamma-ray fraction of cosmic rays. X-ray and gamma-ray exposure, while less intense than high-energy cosmic rays, can induce various forms of DNA damage, including double-strand breaks(DSBs), which are particularly harmful to cellular integrity and function (L.-J. Li et al., 2010; Ochola et al., 2018). Moreover, studies indicate that the combination of X-ray exposure with microgravity exacerbates cellular damage and impairs DNA repair efficiency, underscoring the importance of simulating multiple space conditions simultaneously (Moreno-Villanueva et al., 2017; Yamanouchi et al., 2020).

Neutron Sources address the neutron component of space radiation, particularly from solar particle events. Neutrons penetrate biological tissues and cause substantial DNA damage, making their simulation critical for understanding the full spectrum of space radiation effects (Pang et al., 2014).

These Earth-based simulation techniques provide a robust foundation for investigating the complex biological effects of space radiation.

#### *1.2.3.3 Insights, Challenges, and Implications*

Studies combining radiation exposure with microgravity simulators, such as RPMs, demonstrate the synergistic effects of these stressors. A notable study by Mao et al (2016) demonstrated a significant increase in brain lipid peroxidation in mice subjected to s-μG and low-dose radiation. The radiation levels in this study were carefully controlled using calibrated radiation sources designed to mimic the doses encountered during spaceflight, such as those measured by dosimeters on the ISS. This study highlighted the synergistic effect of combined microgravity and radiation stressors, producing biological impacts more significant than their individual contributions (Mao et al., 2016). Similarly, research by Tan et al. (2020) on human bronchial epithelial Beas-2B cells exposed to s-μG and X-ray radiation utilised radiation doses calibrated to match the cumulative exposure profiles typical of long-duration space missions. By referencing data from spaceflight dosimetry, the study ensured that radiation levels were comparable to those faced by astronauts. Their findings revealed that while each stressor independently affected cell survival, their combination resulted in an additive effect on reducing cell survival and inhibiting cell proliferation. This effect was further evidenced by a significant increase in γH2AX foci formation, an early cellular response to DSBs, suggesting an enhanced response to DNA damage under combined conditions (Tan et al., 2020).

Simulated environments offer several advantages over actual space experiments, including greater control over experimental variables, reproducibility for validation, enhanced safety for researchers, and significant cost savings. However, it is essential to acknowledge that these simulations cannot fully capture the complexity of the integrated space environment, particularly the combined effects of microgravity and radiation. This observation aligns with conflicting findings from spaceflight and ground-based studies on the DNA Damage Response (DDR). For instance, studies on the ISS observed that DNA damage and repair genes were significantly decreased in flight samples compared to post-flight and ground samples (Wnorowski et al., 2019). This differed from the study by Baio et al (2018), where both neonatal and adult Cardiac Progenitor Cells (CPCs) showed increased expression of DNA repair genes. Fuentes et al (2015), who utilised s-μG, reported increased expression of DNA repair genes only in neonatal CPCs. The difference in radiation levels and type may have impacted cellular responses from spaceflight and ground-based studies (Moreno-Villanueva et al., 2017).

Despite these challenges, Earth-based simulations remain critical tools for advancing our understanding of cellular responses to spaceflight conditions. Continued research is needed to refine these models, individually and in combination, to better replicate space conditions and explore their implications for human health. This research serves as a precursor to more specialised studies, such as cardiac mechanobiology, where understanding the interplay between microgravity and radiation is essential.

## 1.3 ESTABLISHING THE CONTEXT FOR CARDIOVASCULAR MECHANOBIOLOGY THROUGH SPACE

### 1.3.1 Foundations of Cell Mechanobiology

Cell mechanobiology is a field of study that investigates the interactions between cells and their physical environment; this includes forces, stresses, and mechanical cues. This field focuses on understanding how cells sense and respond to these forces, pressures, and mechanical cues. There are three fundamental concepts of cell mechanobiology: mechanosensing, mechanotransduction, and mechanoresponses. Mechanosensing, as the name suggests, refers to the cell's ability to sense mechanical forces and properties as stimuli. This happens at the interface of cells and is also influenced by the surrounding microenvironment. Cells then can convert these mechanical stimuli into biochemical and mechanical signals, allowing them to interpret and respond to these mechanical stimuli; this is defined as mechanotransduction. Mechanoresponses refer to the specific cellular behaviours that occur in response to mechanical stimulation.

### 1.3.2 Mechanotransduction in Biological Systems

Mechanotransduction involves a complex network of signalling pathways and mechanosensitive molecules that play crucial roles in maintaining tissue homeostasis, influenced by factors such as tensile tethering, cell-cell interactions, fluid shear flow, and the mechanical behaviour of tissues (Ingber, 2003, 2006). This process involves both the intracellular and extracellular components of cells and at the subcellular levels, mechanotransduction can be further classified into their structural interactions and involved components.

Cell-ECM adhesion interactions are the most common and recognised mechanotransduction process. These interactions involve the cell's intracellular cytoskeleton, extracellular matrix, and integrins and the associated mechanical stimulus and biochemical signals brought about by various intracellular signalling pathways. The intracellular cytoskeleton is a network of interlinking filamentous proteins, filamentous actin (F-actin), intermediate filament, and microtubules. This network is located in the cytoplasm and is a critical structure for mechanical support for cell shapes and resistance to plasma membrane deformation. Additionally, it plays a vital role in connecting the nuclear matrix and the extracellular matrix for mechanotransduction. F-actin has been identified as the primary regulator and transmitter of external mechanical stimulation to cells, driving changes in cell morphogenesis. The ECM refers to the mixture of macromolecules and minerals surrounding the cells that provide structural and biochemical support. The major components of ECM are collagen, non-collagen, and proteoglycans. Additionally, ECMs provide multiple cues to the cells by their properties; these include the ECM's pore size, stiffness, and dimensionality (W. Zhang et al., 2021). Connecting the intracellular cytoskeleton and ECM at focal adhesion sites are clusters of

integrin receptors, ultimately facilitating mechanotransduction (Burridge & Chrzanowska-Wodnicka, 1996; Geiger et al., 2009).

Similarly, cell-cell adhesion interactions constitute another vital mechanotransduction process at the subcellular level. These interactions involve the connections between neighbouring cells, facilitated by adherens, gap, and tight junctions. Together, they facilitate mechanical force transmission and cell-cell communication. Adherens junctions connect the actin cytoskeleton of adjacent cells, with cadherin proteins serving as the primary regulators and components, mediating the calcium-dependent adhesion between adjacent cells. Gap junctions are intercellular channels that directly connect adjacent cells' cytoplasm, allowing for the passage and rapid exchange of ions, small molecules and signalling molecules. This direct communication allows for synchronising activities and co-ordinated responses to stimuli. Tight junctions are regions of adjacent cells that form barriers, regulating permeability and sealing intercellular spaces to restrict the passage of ions, molecules, and cells.

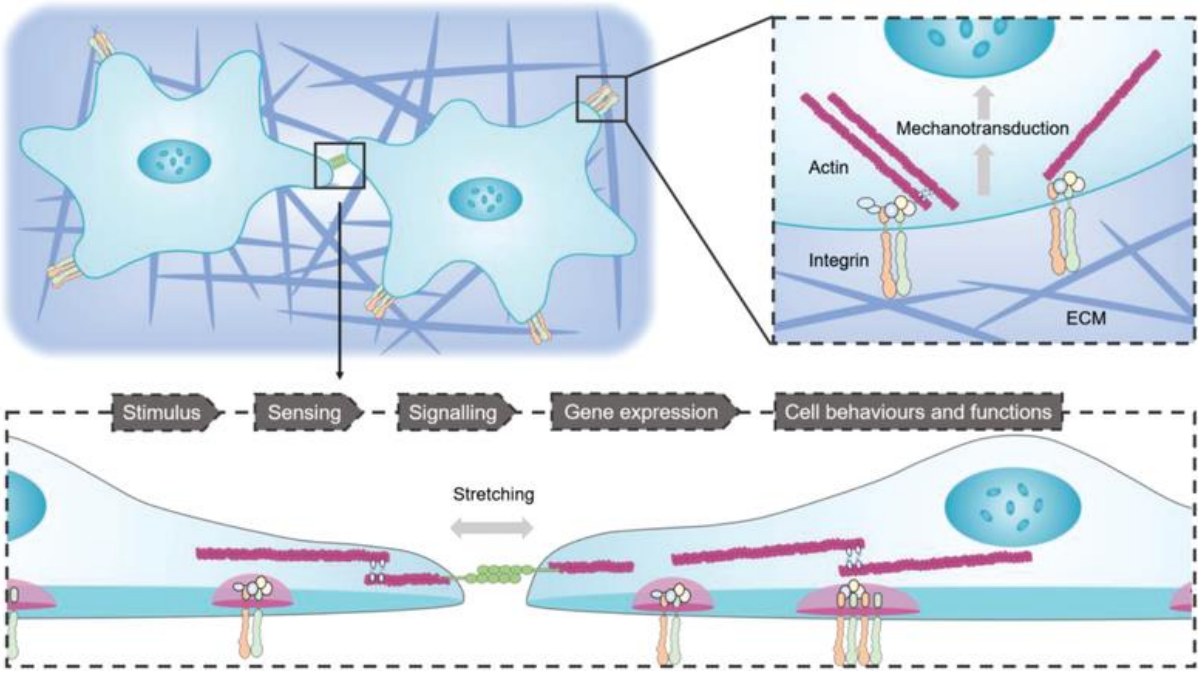


*Figure 1.2 Cellular Mechanotransduction at the Subcellular Level. This illustration highlights cell-ECM (right) and cell-cell (bottom) interactions. The expanded view on the right shows cell-ECM interactions and associated intracellular structures, while the expanded view on the bottom depicts cell-cell interactions, illustrating the mechanotransduction process from stimulus to response in terms of cell behaviours and functions. (Adapted from Sun et al., 2021).*

While ECM-cell interactions are a well-recognised aspect of mechanotransduction, other critical contributors also play significant roles in this complex process. Mechanosensitive ion channels are directly activated by mechanical forces such as stretch or pressure, leading to the rapid transduction of mechanical signals into electrical and biochemical responses. Ion channels play crucial roles in

regulating cellular activities, including ion flux, cell volume, and membrane potential. For instance, PIEZO1 channels are known to mediate mechanotransduction in various tissues, including the cardiovascular system, where they help detect changes in blood flow and pressure, thereby influencing vascular tone and heart function (Ingber, 2006; Schröder et al., 2023; Stewart & Turner, 2021; Y. Wang et al., 2021). G-Protein Coupled Receptors (GPCRs) are another class of mechanosensors that respond to mechanical forces by activating intracellular signalling cascades. These receptors modulate numerous physiological processes, including cell proliferation, migration, and apoptosis. GPCRs are also linked to the activation of downstream effectors such as RhoA and ERK, which are critical for cytoskeletal remodelling and cellular responses to mechanical stress (Martino et al., 2018; Stiber et al., 2009). Tyrosine kinase receptors, including integrins and growth factor receptors, facilitate mechanotransduction through their role in mediating cell adhesion and signal transduction. Tyrosine kinase receptors are activated by both mechanical stimuli and biochemical ligands, leading to the phosphorylation of key proteins involved in cellular growth, differentiation, and survival. Their function is critical in cardiovascular mechanobiology, as they modulate responses to shear stress and cyclic stretch, influencing vascular remodelling and cardiac function (Freedman et al., 2015; Geiger et al., 2009; Sun et al., 2008).

The integration of these mechanosensitive components with the ECM and cytoskeletal structures allows cells to effectively interpret and respond to mechanical signals. This interplay is essential for cellular adaptation to the mechanical environment, influencing various physiological processes and contributing to the pathophysiology of diseases when dysregulated (J. H. Kim et al., 2015; Martino et al., 2018). Understanding these diverse contributors to mechanotransduction enhances our knowledge of cellular responses to mechanical stimuli and their implications in health and disease.

While this overview provides a glimpse into cellular mechanotransduction, a more thorough exploration of the topic is available in the existing literature, which delves into various interactions and mechanisms in greater detail. (Cao et al., 2023; Di et al., 2023; Ingber, 2006; Martino et al., 2018) Furthermore, a more thorough exploration of specific pathways, particularly those relevant to cardiac tissue, is included in Section 1.4.2, "Mechanotransduction in Cardiomyocytes." This section delves into the cardiomyocyte-specific interactions, including the roles of YAP/TAZ and the Hippo signalling pathway, which are critical for cardiac adaptation and function.

The subsequent section extends the exploration of mechanobiology into the novel environment of space that challenges our understanding of cellular function. Space offers a unique environment that enables a deeper investigation into how organisms adapt at the cellular level to microgravity and cosmic radiation challenges, thus broadening the scope of mechanobiology into new and unexplored territories.

### 1.3.3 The Role of Gravity in Mechanical Stimuli

Gravity is a critical mechanical stimulus that continuously influences cellular and tissue behaviour on Earth, affecting processes such as fluid distribution, cellular tension, and mechanotransduction, which are particularly relevant to cardiovascular function (Demontis et al., 2017). In microgravity, the near absence of this force leads to a significant mechanical unloading, altering normal mechanosensing and mechanotransduction processes. This unique environment provides an opportunity to study how cells adapt to mechanical changes, especially regarding cardiovascular health.

Microgravity induces structural and functional changes at the cellular level, including cytoskeletal reorganisation, altered gene expression, and disrupted signalling pathways. These adaptations can negatively impact cardiovascular function, contributing to conditions such as orthostatic intolerance, cardiac atrophy, and arterial remodelling. Such changes pose potential long-term health risks, highlighting the importance of further understanding these mechanisms (Jiang et al., 2020; Sawin, 2022)

Research into the effects of microgravity on cardiovascular health aims to uncover key insights into cellular responses to altered mechanical stimuli. This knowledge is crucial for developing countermeasures to mitigate adverse cardiovascular effects in astronauts during extended space missions. By examining the interplay between gravity and mechanotransduction, researchers can explore novel strategies to protect cardiovascular health, providing broader implications for understanding mechanobiology in extreme environments.

### 1.3.4 Space as a Novel Environment for Mechanobiology Studies

Recent studies in mechanobiology have revealed the importance of cellular and extracellular mechanical properties in regulating cellular function in normal and disease states. The study of the adaptations of organisms to their environment has provided important information for understanding our basic physiological processes. Studies into the biological responses to space environments have been increasing over recent years to keep up with the technological advances that allow space travel, exploration, and habitation.

Microgravity is a condition of near weightlessness experienced in space that presents a unique and invaluable environment for advancing research in mechanobiology. Insights from space missions have shown that microgravity significantly impacts astronauts' health and the behaviour of physical systems. In orbit, such as aboard the International Space Station (ISS), astronauts live in a microgravity environment, affecting everything from bodily fluid distribution to bone density. The

human body undergoes significant adaptations in microgravity due to the reduced need to support its weight. These adaptations include a fluid shift towards the head, muscle atrophy, and bone density loss, with studies indicating that astronauts can experience a bone mass reduction of 1-2% per month while in space - a critical concern for the health of astronauts on long-duration missions (LeBlanc et al., 2000; Smith et al., 2012). Under microgravity conditions, the usual gravitational forces acting on cells and tissues are significantly reduced, altering their mechanical environment. This shift can impact cell shape, function, and differentiation, providing a novel perspective on how mechanical forces regulate biological processes (Becker & Souza, 2013; Long et al., 2015; Martino et al., 2018; Afshinnekoo et al., 2020). Notably, microgravity influences the cytoskeleton of cells, which is crucial for cell structure and function, leading to changes in cell growth and behaviour (Hughes-Fulford, 2011). This unique state of weightlessness has also been leveraged in the formation of scaffold-free tissue, enabling the observation of cellular organisation and tissue development in three dimensions—insights invaluable to tissue engineering and regenerative medicine (Aleshcheva et al., 2016).

Exploring microgravity's impact on mechanobiology offers a window into how the human body is affected and adapts under conditions vastly different from Earth's gravity. However, this endeavour has its challenges. The space environment, while providing unique opportunities for scientific discovery, also exposes astronauts to the harsh realities of space radiation. Space radiation, primarily consisting of solar particle events (SPE) and cosmic galactic rays (CGR), poses significant risks to astronauts. These phenomena comprise low and high-energy protons, alpha particles, and a minority of heavily charged particles and nuclei. SPEs are temporary increases in proton flux that can affect astronauts during their missions. Although astronauts are mainly exposed to these solar and cosmic components during Extra Vehicular Activities (EVA), the interior of spacecraft and the International Space Station (ISS) is not entirely shielded from these events. Furthermore, astronauts inside these vessels are exposed to a constant low dose of gamma radiation, approximately twice the highest natural radiation background found on Earth, as Restier-Verlet et al (2021) noted. In discussing radiation, two key measures are used: "activity," which quantifies the radiation emitted by a source, and "exposure," which assesses the radiation's effect on absorbed materials. Radiation exposure is measured in greys (Gy), a unit that allows for comparing different types of radiation based on their impact on materials. However, since radiation affects biological tissues differently, the sievert (Sv) unit measures the absorbed dose in human tissue, correlating to the biological damage caused by radiation. This distinction is crucial for understanding the risks to astronauts, as outlined by the Australian Radiation Protection and Nuclear Safety Agency (ARPANSA). The radiation doses astronauts receive vary significantly depending on the duration and distance of their missions from Earth. Estimates indicate that astronauts can be exposed to 150 mSv/year during flights on the ISS, 300–400 mSv for trips to the Moon, and significantly higher doses of 300–400 mSv/year to 1600–2300 mSv for two-year missions to Mars, as reported by Shavers et al (2004), Chancellor et al (2018),

and Restier-Verlet et al (2021). Radiation can also induce changes in cell morphology, disrupt cytoskeletal dynamics, and alter the mechanical properties of cells and tissues. For instance, exposure to high-energy particles in CGR can lead to DNA damage, oxidative stress, and changes in gene expression that affect cell function and behaviour. This is particularly relevant for mechanobiological processes such as wound healing, tissue regeneration, and stem cell differentiation, which rely on precise cellular responses to mechanical cues.

For mechanobiology research, navigating microgravity and radiation in the space environment is a special and challenging task that highlights the complex interactions between these elements in cellular and tissue-level processes. In microgravity, the lack of gravity affects cells' and tissues' structural and mechanical properties, altering their behaviour, growth, and function. Simultaneously, exposure to space radiation contributes to genetic alterations, cellular damage, and changes in the expression of critical genes that govern cell structure, repair processes, and signalling mechanisms. This simultaneous exposure can have a synergistic effect on the pathways of mechanotransduction. In conclusion, the space environment provides a distinctive platform for studying the fundamental principles of mechanobiology and offering insights into how mechanical forces and environmental stressors jointly influence biological systems. This knowledge not only advances our understanding of the effects of space travel on the human body but also has potential applications in improving tissue engineering, regenerative medicine, and cancer treatment strategies on Earth.

## 1.4 CARDIAC MECHANOBIOLOGY

The cardiovascular system (CVS) plays a critical role in maintaining proper body functions, blood flow to all body parts, and ultimately transporting vital nutrients, gases, and hormones around. The heart muscle contraction ultimately controls this blood movement through the heart and the blood vessels. Mechanical stimuli and stresses are becoming increasingly recognised as critical regulators of cell behaviour, which is, therefore, immediately relevant to the physiology of the heart as the cardiovascular system is constantly subjected to a wide range of these mechanical stresses. It has been demonstrated that cardiac tissue is mechanosensitive, and mechanobiology can govern cardiac cells' development, function, and responses to varying pathological conditions (Martino et al., 2018; Parker & Ingber, 2007). Within this context, cardiac mechanobiology emerges as a field dedicated to unravelling how cardiac cells perceive and adapt to biomechanical stimuli.

### 1.4.1 Cardiomyocytes: Structure and Function

The heart wall comprises three layers: the inner layer, the endocardium, the middle layer of the myocardium and the outer layer, the epicardium. The endocardium lines the cardiac chambers and covers the cardiac valves. The epicardium, on the other hand, serves as a surrounding that protects and lubricates the heart. Between these two layers is the myocardium, the heart muscle tissue that forms the bulk component of the heart. The myocardium comprises cardiac muscle cells, better known as cardiomyocytes, and these cells provide the cardiac muscle with its ability to contract, connected by intercalated discs. Gap junctions are a part of the intercalated discs, allowing for the transfer of stimulation from one cardiac cell to another. By doing this, the muscles can contract in a coordinated manner when there is stimulation to contract.

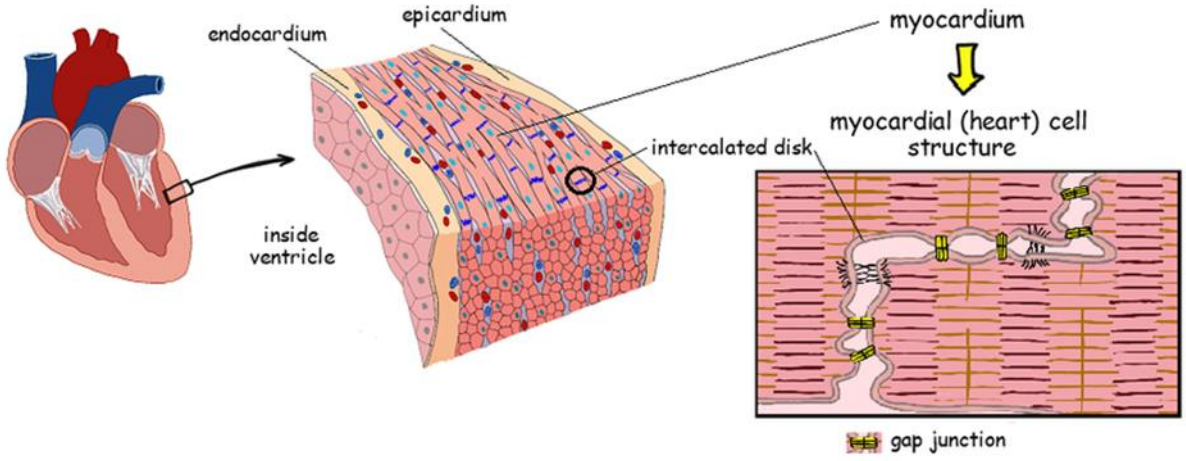


*Figure 1.3 Layers of the Heart. The inner endocardium, middle myocardium, and outer epicardium. Cardiomyocytes make up the myocardium and are responsible for its ability to contract. Intercalated discs and gap junctions connect cardiomyocytes. (Image from Ibbiologyhelp.com)*

### 1.4.2 Mechanotransduction in Cardiomyocytes

To fully understand the function and underlying mechanisms of cardiac function, it is essential to understand how cardiac cells transduce these mechanical stimuli and stresses – this is known as cardiac mechanotransduction. In the heart, mechanotransduction is a critical process that allows cardiomyocytes to sense and respond to mechanical forces such as pressure and stretch, which are constantly present due to the rhythmic contractions of the heart. Specifically, the mechanical stimuli experienced by the heart include shear flow, compression, stretch/strain, and pulsatile flow of blood. Shear flow refers to the frictional force of blood that flows along the endothelial surface. Compression involves the application of pressure to the cardiovascular tissues. Stretch and strain are mechanical stimuli that involve the deformation of cardiovascular tissues. Rhythmic changes in blood pressure and flow characterise pulsatile blood flows. (Kaarj & Yoon, 2019; McCain & Parker, 2011)

#### *1.4.2.1 Role of the Cytoskeleton in Cardiac Mechanotransduction*

Cytoskeleton plays a pivotal role in sensing mechanical stress, mediating structural remodelling and facilitating functional and mechanotransduction processes within the myocyte. In response to extracellular boundaries and mechanical loads, the cytoskeleton remodels its architecture and propagates mechanical inputs to mediate other functions within the myocytes (McCain & Parker, 2011). Auman et al (2007) demonstrated that reduction of circulation limits the extent of cardiomyocyte elongation, while disruption of sarcomere formation releases limitations on cardiomyocyte dimensions, highlighting the functional modulation of cardiac form through regionally confined cell shape changes (Auman et al., 2007). Mechanical stretch was utilised by Mihic et al. to enhance cellular maturation when cardiomyocytes derived from human embryonic stem cells were seeded into a gelatin sponge. Comparing the stretched and unstretched samples, the tested sample showed increased cell size, number, and elongation. The cyclic stretching caused by changes in the internal pressure of the cardiomyocytes also influences heart development or cardiogenesis. Ott et al (2008) employed pulsatile perfusion to examine the role of cyclic stretching, which resulted in the cyclic stretching being applied to a decellularised heart matrix containing reseeded cardiac cells. This experiment obtained viable cardiac muscles that were thick when pulsatile perfusion was used. In contrast, in an environment without perfusion, thin, weak muscles were obtained (Ott et al., 2008).

#### *1.4.2.2 Role of the Extracellular Matrix in Cardiac Mechanotransduction*

The ECM is vital in carrying and providing mechanical cues to cells (Martino et al., 2018). For cardiomyocytes, the ECM in which they grow also influence their behaviour; in particular, the stiffness of the matrix affects the contraction forces of the heart, the structure of the cytoskeleton and the intracellular calcium levels (Takahashi et al., 2013). A study conducted in 2006 by Engler and

his colleagues published a report highlighting the ability of mesenchymal stem cells (MSCs) to differentiate into multiple distinct cellular lineages when exposed to various levels of matrix stiffness (Engler et al., 2006). Similarly, Herron et al (2016) demonstrated that the stiffness of the substrate also plays a significant role in the maturation process of cardiomyocytes derived from induced pluripotent stem cells (iPSC). The researchers were able to successfully achieve maturation of iPSC within a short span of one week by culturing the cardiomyocytes on polydimethylsiloxane (PDMS) coverslips, as opposed to using conventional substrates like glass coverslips and plastic culture dishes (Herron et al., 2016). Moreover, a study conducted by Young and Engler in 2011 revealed that the presence of hyaluronic acid (HA), a substrate that can stiffen over time, led to increased levels of troponin-T (a late cardiac marker) and a time-dependent decrease in NKX2.5 (an early cardiac marker) when embryonic chicken cardiomyocytes were cultured on it. These findings suggest that the stiffness and composition of the substrate that the cells are associated with play a crucial role in the maturation of cardiac muscle. Furthermore, substrate stiffness also influenced the phenotype of cardiomyocytes where the shape of cardiomyocytes was more muscle-like, sarcomeres exhibited clearer striations, and the cells could maintain constant spontaneous beating with substrate stiffness that reflects the natural cardiac environment (Engler et al., 2008).

#### *1.4.2.3 The Hippo Signalling Pathway: YAP/TAZ in Cardiac Mechanotransduction*

Several proteins are sensitive and responsive to changes in the mechanical environment, and looking at these critical proteins could shed some light on the relationship between cell function and their responses to these mechanical cues, using their protein expressions as a measure of mechanotransduction (Chin et al., 2019; Dupont et al., 2011). Among these, the Hippo signalling pathway, particularly the Yes-associated protein (YAP) and transcriptional co-activator TAZ, plays a crucial role in cardiac mechanotransduction. This pathway is essential for development and homeostasis in mammals.

In cardiomyocytes, YAP and TAZ act as mechanosensitive transcriptional regulators that respond to mechanical cues such as ECM stiffness, cell shape, and cellular tension. When the Hippo pathway is active, it inhibits YAP and TAZ, keeping them inactive in the cytoplasm. Conversely, suppression of the Hippo pathway allows YAP and TAZ to translocate into the nucleus, where they regulate the expression of genes involved in cell proliferation, survival, and hypertrophy (Codelia et al., 2014).

YAP activation has been shown to improve cardiac regeneration. For instance, overexpression of activated YAP in cardiomyocytes increases their proliferation, leading to cardiac overgrowth in neonatal mice (Xin et al., 2011). In supporting this, it has been found that nuclear YAP protein can be detected in neonatal hearts; however, with age, the expression decreases, while the phosphorylation of YAP and consequent cytoplasmic retention, increases with age (von Gise et al.,

2012). Increased YAP phosphorylation leads to its cytoplasmic retention, inhibiting nuclear translocation and the activation of genes linked to cell proliferation and growth. Interestingly, nuclear YAP expression, typically absent in adult cardiomyocytes, was observed at the border of infarcted cardiac tissue. This observation could be attributed to the increased stiffness in the ECM within the infarcted area (Mosqueira et al., 2014). The increased stiffness is a response to heart damage, where the body initiates the deposition of fibrotic scar tissue to stabilise the damaged area. However, these scar tissues are more disorganised and less contractile than the normal myocardium, increasing the ECM's stiffness overall.

Traction force, the mechanical force exerted by cells on their ECM, is another key regulator of YAP activity. Increased traction force enhances YAP's localisation in the nucleus, facilitating its transcriptional activity and promoting cell proliferation and growth. However, when mechanotransduction is inhibited, YAP remains in the cytoplasm, preventing the activation of target genes (Dupont et al., 2011). YAP/TAZ activity is particularly significant in the context of cardiac hypertrophy and heart failure. In response to mechanical stress, YAP promotes the expression of pro-hypertrophic genes, contributing to the enlargement of cardiomyocytes as an adaptive mechanism to maintain cardiac output under increased load conditions. However, chronic activation of YAP can lead to maladaptive cardiac remodelling, contributing to heart failure. This mechanotransduction pathway underscores the delicate balance between adaptive and pathological responses in cardiomyocytes.

Additionally, YAP has been implicated in the regulation of cardiomyocyte survival under stress conditions. Activation of YAP in response to mechanical stress enhances the expression of anti-apoptotic genes, promoting cell survival during conditions such as myocardial infarction. This protective role of YAP highlights its potential as a therapeutic target in cardiac diseases characterised by excessive mechanical stress and maladaptive remodelling (Xin et al., 2013).

A summary of how different mechanical stimuli, including matrix, geometry and physical conditions, influence YAP and TAZ localisation and activity are shown in Figure 1.4.

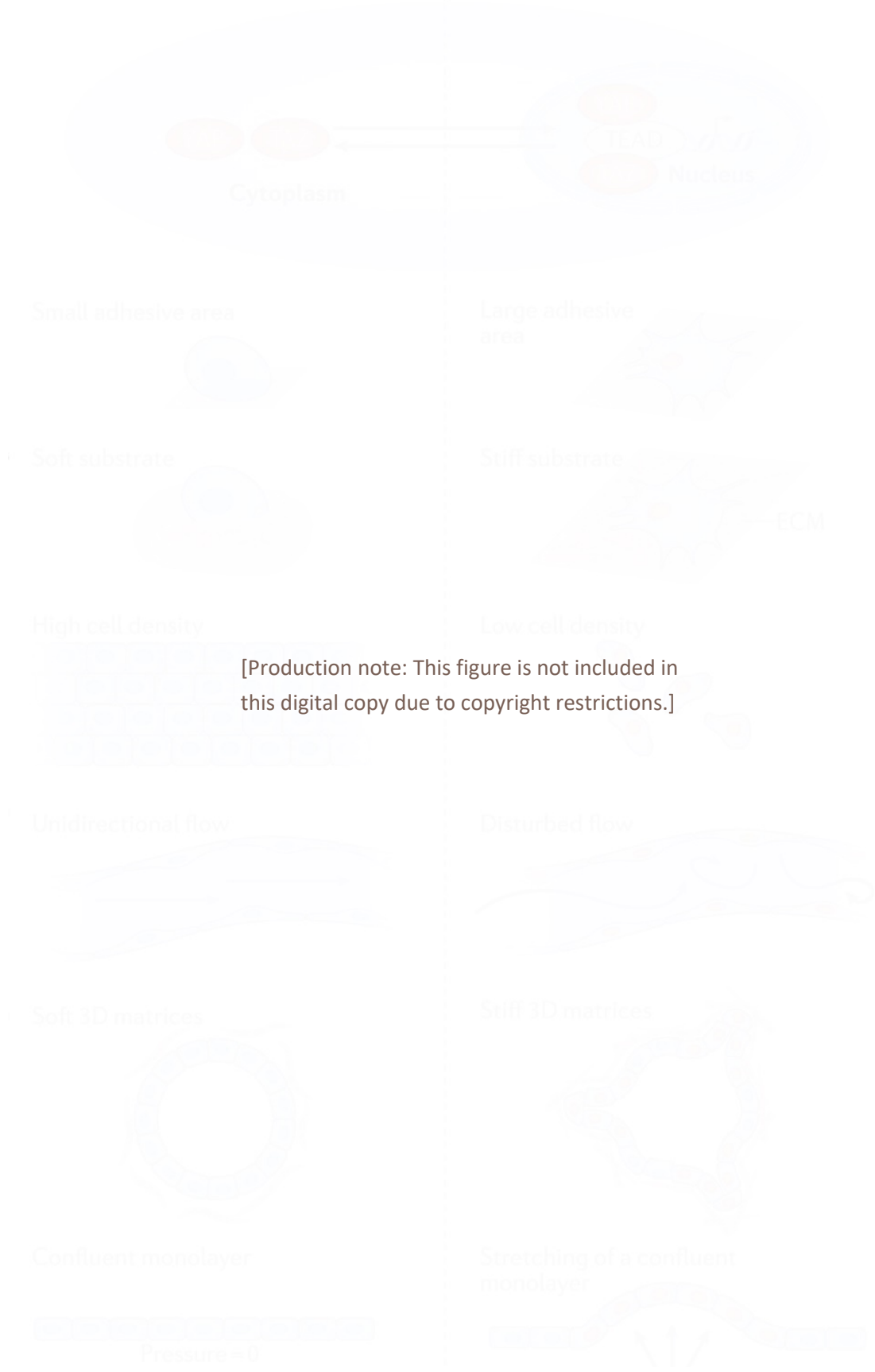


[Production note: This figure is not included in this digital copy due to copyright restrictions.]

*Figure 1.4 Influence of Mechanical Stimuli on YAP and TAZ Localization and Activity. Different mechanical stimuli affect YAP and TAZ localization and activity. YAP and TAZ inhibition with cytoplasmic localisation is shown on the left, while YAP and TAZ activation with nuclear localisation is shown on the right. (Adapted from Panciera et al., 2017).*

In conclusion, the intricate interplay between mechanical stimuli, cellular responses, and ECM dynamics underscores the critical role of mechanotransduction in cardiac physiology. Cardiac tissues exhibit remarkable sensitivity to various mechanical stimuli. These stimuli profoundly influence cellular behaviour, cytoskeletal remodelling, and structural organisation, ultimately impacting cardiac function and adaptation to pathological conditions. The literature discussed demonstrates the interplay of cell-ECM mechanotransduction processes facilitated by the mechanical stimuli experienced by the heart. Essential proteins such as YAP and TAZ act as effectors of mechanotransduction, mediating cellular responses to mechanical cues and measuring their expression, which could indicate the occurrence of mechanotransduction in cardiomyocytes. (Dupont et al., 2011; Panciera et al., 2017). The interplay between mechanical stimuli and cellular responses is equally relevant in extraterrestrial environments, where altered gravitational forces impose unique mechanical challenges on cardiac tissues.

The relevance of these mechanisms extends to extraterrestrial environments, where altered gravitational forces impose unique mechanical challenges on cardiac tissues, further emphasising the importance of studying mechanotransduction in diverse conditions.

### 1.4.3 Impact of Space Conditions on Cardiac Mechanotransduction

The effects of microgravity and radiation on the cardiovascular system, from physiological to cellular levels, include changes in cardiac and endothelial function, increased arterial stiffness, oxidative stress, inflammation, altered fluid distribution, and decreased calcium recycling rate. This highlights the space environment's unique opportunity for a more in-depth study of mechanotransduction responses in the cardiovascular system – cardiac mechanotransduction. Cardiac mechanotransduction is crucial in understanding the cardiovascular system and cardiac tissue's maturation and functional response.

Studies have documented that prolonged exposure to microgravity induces morphological alterations in the heart, such as increased sphericity and changes in ventricular dimensions, potentially affecting cardiac function. (Watenpaugh, 2016). At the cellular level, microgravity has been shown to disrupt the organisation and function of the cytoskeleton within cardiac cells, leading to alterations in cell shape, size, and cytoskeletal integrity, which are critical for maintaining cellular function and facilitating mechanotransduction (Hughson et al., 2018). For instance, disruption in the actin filaments' organisation results in altered contractility and cell morphology, with a reduction in stress fibre formation contributing to a more rounded cell shape (Ingber, 2003; Lewis et al., 1998; Vorselen et al., 2014).

Proteins sensitive to changes in the mechanical environment, such as YAP (Yes-associated protein) and TAZ (transcriptional coactivator with PDZ-binding motif), also influence cardiac tissue function and dysfunction. YAP/TAZ are key mediators of mechanotransduction, influencing cardiomyocyte proliferation and cardiac regeneration. It has been found that activation of YAP improves cardiac regeneration particularly in neonatal hearts, where its overexpression leads to increased cardiomyocyte proliferation and subsequent cardiac overgrowth (Xin et al., 2011, 2013). However, this regenerative capacity diminishes in adult hearts, where YAP expression declines and phosphorylation levels increase with age, indicating a shift in the pathways that govern cardiac repair (Del Re et al., 2013). In supporting this, it has been found that YAP protein can be detected in neonatal hearts; however, with age, the expression decreases, while the phosphorylation of YAP increases with age (von Gise et al., 2012).

Interestingly, nuclear YAP expression, typically absent in adult cardiomyocytes, appears in infarcted cardiac tissue at the border of the damaged region, likely due to the increased stiffness of the ECM in the infarcted area which can trigger YAP signalling pathways that promote cellular responses necessary for tissue repair. The mechanical properties of the ECM are crucial in determining the behaviour of cardiac cells, and alterations in these properties can lead to significant changes in gene expression profiles, including those related to YAP/TAZ signalling (Baio et al., 2018; Del Re et al., 2013; Mosqueira et al., 2014).

Notably, both spaceflight and s-μG have been shown to upregulate YAP1 gene expression in adult cardiac progenitor cells (CPCs) and downregulation in neonatal CPCs (Baio et al., 2018; Camberos et al., 2019). This suggests that microgravity can trigger various functions and responses in the heart to address damage. Furthermore, spaceflight has been associated with changes in the expression of numerous stress response genes, including those involved in the cell cycle and apoptosis, indicating that the mechanical environment can significantly impact cardiac gene regulation (Kumar et al., 2021). Similarly, a separate analysis using microarray techniques on cultured endothelial cells 24 hours following s-μG exposure revealed significant changes in 177 genes, highlighting increases in genes related to the cell's response to external stimuli and the regulation of cell motility and proliferation (Rudimov et al., 2017).

The complexity of cardiac tissue necessitates the use of advanced models to study the effects of mechanical changes on cardiac function. Such studies are critical for understanding the intricate relationships between mechanical stimuli, YAP/TAZ signalling, and cardiac health, particularly in the context of injury and repair.

## 1.5 ADVANCEMENTS IN CARDIAC MODELLING TECHNIQUES

### 1.5.1 Cell Sources

Cardiomyocytes, being muscle cells, are primarily involved in the heart's contraction and account for 75% of the heart volume in an adult human heart. Therefore, it is crucial to determine an optimal source to recreate a heart tissue model (Mathur et al., 2016). One source for this is primary cells, which have been directly harvested from the tissue. Due to being directly harvested, they would not have been transformed genetically or virally, therefore being able to retain similar qualities to their *in vivo* phenotype. Even though thin slices of adult human hearts have been reported as an *in vitro* model for pharmacologic testing (Camelliti et al., 2011), they have weaknesses, including the shortage of organ donors and low viability of heart tissues *in vitro*, which limit their applications. Furthermore, adult human cardiomyocytes are also limited due to their short *in vitro* life span and poor proliferation capability (van Amerongen & Engel, 2008). Due to their limited ability to proliferate, they cannot be expanded and studied extensively. Another consideration is that the cells may come from different donors, meaning they can behave differently due to characteristics such as age, sex, and donor genetics, which may give inconclusive results.

Most *in vitro* models developed in studies use cell lines as they are more readily available and can be expanded and, therefore, be used much more. Cell lines are more established; therefore, they are more commonly used as a cell source to model cardiac tissue regeneration and in engineering vasculature (Savoji et al., 2019). AC-16 and HL-1 are primary cardiomyocytes cell lines that can proliferate. The AC-16 cells exhibit cardiac-specific markers, and the HL-1 can maintain contractile function and keep a gene expression comparable to that of adult cardiomyocytes. However, when using cell lines, it is essential to consider that cellular behavioural changes may happen due to the culture condition. The cells may also behave specifically due to the genetic manipulation required to generate the cell line.

With the identified limitations of other cell sources, researchers have moved towards using stem cells as a cell source. Stem cells are undifferentiated cells that undergo differentiation into different specialised cells, including the ability to differentiate into cardiomyocytes (Polak, 2006). Recently, human induced pluripotent stem cells (iPSC) have been differentiated into cardiac cells to be utilised as an alternative cell source to model the human heart (van Amerongen & Engel, 2008). To fully take advantage of iPSCs as an alternative cell source to recreate heart tissue models, it is essential to address the issue surrounding the maturity of the CMs. During the heart's development, the cardiac cells undergo multiple changes to their structure, resulting in their adult phenotype (Laflamme & Murry, 2011). However, in comparison, the iPSC-derived cardiomyocytes maintain their relatively immature phenotype. They are smaller, having decreased electrical excitability, impaired excitation-contraction coupling, and incomplete adrenergic sensitivity, all features of immature cardiomyocytes (Robertson

et al., 2013). Various factors play a part in CM's maturation *in vivo*, including electrical, biochemical, mechanical, topographical, and cellular interaction cues.

Although cardiomyocytes have been the primary cellular component in generating a heart model, to reliably mimic the *in vivo* environment of the heart, it is also essential to consider and include all critical cells in the heart. The major cell types in the human heart are cardiomyocytes, smooth muscle cells, endothelial cells (ECs) and fibroblasts (Pinto et al., 2016). By co-culturing the critical cells, cells will experience cell-to-cell contact similar to the one experienced *in vivo* and provide a more relevant heart model. Previous studies have shown that ECs and fibroblasts have been utilised to generate a functional heart tissue construct that can form vascular networks among CMs (Caspi et al., 2007; Lesman et al., 2010; Radisic et al., 2008; Vuorenpää et al., 2014). Furthermore, the proliferation ability, viability and functionality of cardiomyocytes are improved when they are combined with a vascular like network. By combining cardiomyocytes with HUVECs and fibroblasts, the construct developed closely resembled the *in vivo* cardiomyocyte alignment and mimicked the native heart more closely.

### 1.5.2 Evolving Cardiac Models: From 2D to 3D

Many animal models have been utilised to model cardiovascular systems and diseases. Although they have offered insights into diseases and become valuable tools for disease modelling and drug discovery, they still need to be expanded by the differences between human and animal physiology and pathophysiology. As there are issues surrounding the physiological relevance of animal models and the ethical considerations with using animals, research has been moving towards *in vitro* models. An ideal *in vitro* cardiac model must precisely replicate the human heart's physiological or pathological requirements, including the anisotropic three-dimensional (3D) tissue structure, ECM network orientation, and vascularisation.

2D cardiac *in vitro* models have been used for decades to evaluate practical properties and test cardiotoxicity in pre-clinical phases. Although they are informative, they still cannot accurately mimic the complex 3D environment and, therefore, cannot accurately simulate the dynamic conditions of the biological and mechanical properties of the environment of the human body. An increasing number of studies have shown that 3D culture systems that mimic *in vivo* architecture and biological roles of the ECM will permit a physiologically relevant model with a level of complexity that cannot be attainable through a 2D culture (Antoni et al., 2015; Chapla et al., 2022; Gibler et al., 2021; Hodge et al., 2023; C. Liu et al., 2022; J. Shi et al., 2024; Um Min Allah et al., 2017). 3D *in vitro* models can build up more complex 3D microenvironments. Their establishment of adhesion complexes can characterise them, the variations in the cytoskeletal structure and the volume of cells significantly dissimilar from those cultured in 2D environments as monolayers (Mathur et al., 2016). When grown in 2D, cardiac cells exhibit a flattened and well-spread shape. The cardiac cells grown in 3D spheroids

were more minor and did not spread as well. They also exhibited more cell-cell contact with numerous cellular junctions, expressing more significant critical components that indicate cardiac maturation (Jang, 2017).

To model an *in vitro* environment, the utilised biomaterials and microsystems usually provide a scaffold for tissue formation, providing a highly regulated microenvironment that could incorporate specific features that aid in accurately modelling the cardiovascular system and cardiovascular diseases (Mathur et al., 2016). Various materials have been utilised for scaffold fabrication, each offering unique properties and advantages. Biodegradable polymers like polylactic acid (PLA) and polyglycolic acid (PGA) are favoured for their biocompatibility and tuneable degradation rates. Natural polymers such as collagen, fibrin, gelatin, and hyaluronic acid closely resemble ECM composition, offering excellent biocompatibility and bioactivity. Synthetic polymers like polyethylene glycol (PEG) and polyacrylamide (PAA) provide precise control over mechanical and chemical properties, facilitating scaffold customisation. Another option for scaffolds is decellularised tissues that retain ECM structure and biochemical cues, making them ideal scaffolds for tissue regeneration. Hydrogels composed of alginate, agarose, or chitosan provide a hydrated environment suitable for 3D cell culture. The selection of scaffold material depends on the desired tissue type, mechanical properties, degradation kinetics, and compatibility with cell types and culture conditions, ensuring an optimal tissue development and regeneration microenvironment. Specifically looking at the heart, it is supported by extensive networks of 3D ECM, which consist of fibrous proteins, adhesive glycoproteins, and proteoglycans, which have structural and non-structural roles in aiding and directing cell behaviour (Parker & Ingber, 2007).

### 1.5.3 Cutting-edge Technologies to Further Advance Cardiac Modelling.

Research has looked into various promising fabrication methods to advance cardiac modelling and create a physiologically relevant model. 3D bioprinting of multi-cellular, highly complex soft tissue structures has gained significant traction in the last few years owing to the increasing availability of bioprinters and innovative bioinks. The 3D bioprinting methods can place hydrogel bioinks encapsulated with cells layer by layer, ultimately replicating the 3D architecture of tissues and organs. This layer-by-layer approach has significantly impacted several fields since its inception, including engineering, manufacturing, and medical fields, to name a few. Combinations of different based inks have also been shown to be advantageous. 3D bioprinted constructs printed using composite hydrogels and anchored to a poly(caprolactone) (PCL) frame developed into compact and universally supported cardiac muscles with synchronous contraction (Z. Wang et al., 2018). These cardiac tissues can synchronously contract, confirmed by the connection and alignment of cardiomyocytes, with an inflow of calcium spreading across the entire tissue. Having anchor points to attach cellularized

constructs permits the natural force to induce compactness within a tissue structure, facilitating its development.

The greatest challenge of 3D bioprinting functional tissue is the creation of vascular networks. For the survival of tissues, cells need to transfer nutrients, oxygen, growth factors, biochemical signalling factors, carbon dioxide and metabolic waste between each other and their surroundings. To create a successful model to enhance tissue regeneration, the model would need to facilitate this process via the simultaneous growth of vasculature (Sarker et al., 2018). The challenge presented within bioprinting vasculature lies in the limitation of print speed and resolution of current printers. Furthermore, achieving vascularity is a lengthy process, which may impact cell viability through this vascularisation process. To conquer this obstacle sacrificial material that can be flushed away after depositing other materials over it has been utilised, leaving a vascular network behind and allowing for perfusion of the microchannels (Xie et al., 2020). Another possible method to produce perfusable microchannels is by producing tube-like structures promptly after the fabrication process using multi-axial nozzles, as shown by a study by Zhang et al. in 2013 and Gao et al. in 2017. Alternatively, the process of self-assembly, which involves printing vascular cells precisely into the engineered tissues, can also be utilised. The creation of macro vasculature is anticipated to produce the surrounding capillaries through natural vascular remodelling.

To understand the pathophysiology of cardiovascular diseases and to provide more control over the environments for system and disease modelling, researchers have also been retreating from models that are scaffold-based to micro physiological systems that are highly miniaturised, which are now more commonly known as "heart-on-a-chip" technology. This technology allows extra control of the 3D microenvironments, with numerous functionalities and reproducibility. Chen et al. showed that valvular tissue and disease could be mirrored using a combination of hydrogel and microfluidics. The study used multiple compartments to construct a valvular and vascular compartment within a 3D microenvironment (Chen et al., 2013). Since a thin, porous membrane separated the cells, this technique allowed valvular endothelial cells (VECs) and valvular interstitial cells (VICs) to communicate through paracrine signalling. The study used GelMA hydrogels to encapsulate the fibroblast-like VICs, whilst the VECs were then seeded on PDMS-based microchannels coated with fibronectin. Flow-induced shear stress could stimulate VECs physiologically with this microfluidic device. When inactive VICs were activated into myofibroblasts that expressed alpha-smooth muscle actin (α-SMA), this indicated valvular pathological remodelling, as this increased their ECM synthesis and contractile features. From the results, it can be concluded that this microfluidic-based system can be applied to examine the biological and pathological interaction of valvular endothelial and valvular interstitial cells (Chen et al., 2013).

Another example of using the microfluidics heart-on-chip technology was a study of hypoxia-induced myocardial injury conducted by Ren et al (2013). In this study, heart-on-a-chip was fabricated using a PDMS-based microfluidic device. This device had four functional units, which resulted in the simulated interface of myocardial tissue and micro capillaries. This device has a central culture chamber as well as two channels parallel from each other that were separated by micropillar arrays. This, in turn, represented the interface between the blood vessels and cardiac tissue. As part of this study, a specific oxygen consumption-blocking reagent was introduced into one of the lateral channels to mimic the hypoxia-induced conditions. After this induction of hypoxia, the morphology of the cardiomyocytes changed, where the intracellular actin bundles shrank and disassembled. This device demonstrated an increase in CM apoptosis, a feature of myocardial ischemia (MI), indicating this device's accurate recapitulation of the disease (Ren et al., 2013).

In recent years, iPSC-derived CMs have been used alongside microdevice technologies to create *in vitro* models of cardiac disease; for example, Wang et al (2018) were able to successfully develop the cardiomyopathy of Barth syndrome (BTHS) using microfluidic technologies, muscular thin films and iPSCs. By generating the iPSCs from patients with BTHS, differentiating them into patient-specific iPSC-derived cardiomyocytes, and subsequently seeding them onto muscular thin films, the pathophysiology of BTHS such as mitochondrial dysfunction, impaired calcium handling, oxidative stress, and abnormal cardiac remodelling could be demonstrated (G. Wang et al., 2014).

Overall, these studies indicate that using a combination of technologies to create a microdevice has the potential to recapitulate the cardiovascular system and functions as well as having the potential to model diseases associated with the heart in a human-relevant model, which could, therefore, be used to test potential therapies.

## 1.6 RESEARCH GAP AND NEED FOR THE STUDY

The literature review highlights critical gaps in current research methodologies and understanding, especially in cardiac mechanobiology under space conditions. These gaps span a wide array of aspects, from the simulation of microgravity and radiation to the development and application of cardiac modelling techniques, indicating a profound need for enhanced research in these areas.

One significant limitation identified is the challenge of accurately replicating the complex interplay between microgravity, radiation, and cardiac function through Earth-based simulations. While substantial research has been conducted on the effects of microgravity and radiation independently, limited studies have combined these two external stressors when examining their impact on cardiovascular cells. Furthermore, discrepancies in findings between spaceflight and Earth-based studies indicate the inherent challenge in replicating the complex interplay of microgravity and radiation found in space environments through Earth-based simulations. This limitation underlines the importance of further research combining these stressors in a more integrated manner to fully understand their impact on cardiac function.

Moreover, the unique conditions of space offer a valuable opportunity to study the nuanced effects of these conditions on the cardiovascular system. This environment provides a novel lens through which the mechanotransduction mechanisms related to cardiac function and the potential onset of diseases can be explored. Given the similarities between the impacts of the space environment and the processes of aging and cardiovascular deconditioning, space provides a unique vantage point for investigating CVD-related mechanisms.

To ensure the reliability and applicability of research findings, it is crucial that the cardiovascular systems used in studies closely mirror the actual organ model. Given the dynamic and complex nature of the cardiovascular system, more complex models, such as 2D models or animal models, may need to be revised to replicate the proper functionality or responses observed *in vivo*. This point emphasises the critical need for advanced modelling and simulation techniques that can accurately reflect the implications of the space environment on cardiac health.

# Chapter 2 -

## Hypothesis and Study Aim

## 2.1 JUSTIFICATION FOR THE PROPOSED RESEARCH APPROACH

The approach suggested here aims to decipher the fundamental mechanisms governing cardiac function by applying cardiac models that accurately simulate the cardiac responses to complex space conditions. This is crucial for deepening our understanding of the principles that govern cardiac functionality and devising interventions to mitigate the adverse effects of space travel on cardiovascular health and potentially cardiovascular diseases on Earth. Pivotal to this research is the investigation into the impacts of microgravity and IR effects on cardiac health. Studying these extreme conditions offers a rare window into a broader understanding of cardiac behaviour, from individual cells to the entire organ system. The adoption of cardiac models and simulation of space conditions also serves as a means to explore cardiac mechanobiology, offering secondary insights into the adaptation and functionality of cardiac systems beyond the primary scope of CVD impact analysis, providing a novel pathway to investigate the cardiac function and disease uniquely. Through this research, the thesis endeavours to significantly contribute to the field, setting the stage for future discoveries and interventions in cardiovascular health.

In addressing the complex dynamics of cardiac function and the impact of space conditions, this research strategically begins with analysing cardiomyocytes in a 2D environment, establishing a foundational reference point for subsequent investigations. This approach allows for the initial exploration of cellular responses under controlled conditions before progressing to more physiologically relevant models. The transition to examining these cells within a 3D *in vitro* model is pivotal, aiming to encapsulate a more physiological representation of cardiac behaviour under simulated space conditions. This methodological progression is designed to underscore the critical importance of employing advanced, physiologically relevant *in vitro* models in cardiac research. This approach enhances the accuracy of the research findings. It paves the way for a deeper discussion on the implications of transitioning from traditional 2D cultures to more sophisticated 3D models in cardiac mechanobiology.

In addressing the experimental design challenges posed by studies on the effects of s-μG and IR on cardiomyocytes, our methodology necessitates a cell model that combines robustness with physiological relevance. The AC-16 cardiomyocyte cell line choice over primary cardiomyocytes was based on several critical considerations that align with the research's objectives. Primary cardiomyocytes have limited proliferative capacity, high variability between isolations, ethical and availability constraints, and a relatively short lifespan in culture. In contrast, the AC-16 cardiomyocyte line, derived from adult human ventricular cardiomyocytes fused with a cancer cell line, allows for indefinite proliferation, ensuring a consistent and scalable cell source. This attribute is particularly advantageous for studies requiring extensive experimental setups or prolonged durations, which is characteristic of IR exposure investigations. Furthermore, the practicality of AC-16 cells facilitates

the execution of large-scale and high-throughput experiments, allowing for the efficient screening of potential cardioprotective agents against microgravity and IR-induced cellular damage.

## 2.2 HYPOTHESIS

This study is driven by the need to understand how heart cells, specifically cardiomyocytes, respond to extraordinary environmental factors, especially focusing on mechanotransduction – the process by which cells convert mechanical stimuli into biochemical signals.

The unique challenges posed by microgravity and IR in space, raise critical questions about cardiomyocyte behaviour and the implications for cardiac function and disease. Mechanotransduction is crucial in cardiac functionality and is significantly impacted under these conditions. A hypothesis has been developed to provide a framework for this investigation and guide the experimental approach.

**"Exposure of cardiomyocytes to simulated microgravity and radiation in advanced cardiac models will alter mechanotransduction pathways, providing insights into the potential effects of space conditions on cardiac function and the development of related diseases."**

## 2.3 STUDY AIM AND OBJECTIVES

The primary aim of this PhD project is to assess the impact of s-μG and IR on human cardiomyocytes. A critical component in achieving this objective is creating a model that faithfully replicates the cardiac environment. This overarching aim is further delineated into three specific aims outlined below.

**Aim 1:**

To Sequentially and Comprehensively Evaluate Cardiomyocyte Responses Under Simulated Microgravity, Radiation, and Their Combined Impact Exposure in a 2D Environment.

**What**: This aim focuses on characterising cardiomyocyte responses under individual and combined stressors of s-μG and IR in a controlled 2D environment.
**Why**: Understanding how cardiomyocytes respond to these stressors in 2D provides foundational insights into cellular adaptations that occur during space travel and radiotherapy exposure.
**How**: Cardiomyocytes will be cultured in 2D using standardised cell culture platforms with exposure to s-μG simulated via RPM and IR exposure achieved using X-RAD 320 radiation. Specific methodologies include:

- **Objective 1**: To characterise the impact of s-μG on cardiomyocyte proliferation, viability, and gene expression changes, using assays like ELISA and confocal imaging to provide detailed insights into cellular adaptation mechanisms under microgravity conditions.
- **Objective 2**: To define cardiomyocyte responses to IR through dose-dependent assessments of DNA damage and repair, using γH2AX as a key biomarker for quantifying DNA repair processes.
- **Objective 3**: To investigate the combined effects of s-μG and IR on cellular proliferation, viability, gene expression, and DNA damage, integrating data from the preceding objectives to understand compounded stress responses.
- **Objective 4**: To examine mechanotransduction pathways and morphological changes with a focus on YAP translocation between the nucleus and cytoplasm, utilising advanced imaging techniques to observe cellular adaptations.

**Aim 2:**

To Develop a 3D Collagen Model and Comprehensively Evaluate the Impact of Simulated Microgravity, Radiation and Their Combination on Cardiomyocytes in a 3D Environment.

**What**: This aim focuses on developing and validating a 3D collagen-based hydrogel model to simulate a more physiologically relevant cardiac environment and evaluate cellular responses under s-μG, IR, and their combination.

**Why**: A 3D model offers a closer approximation to *in vivo* conditions, allowing for a more accurate assessment of cardiomyocyte behaviour and the influence of environmental dimensionality on stress response.

**How**: A 3D collagen hydrogel scaffold will be developed to facilitate cell embedding and functionality, allowing for a dynamic evaluation of cellular responses. Key methodologies include:

- **Objective 1**: To develop and validate the 3D collagen scaffold, optimising hydrogel composition and cross-linking techniques to enhance scaffold stability and cell viability.
- **Objective 2**: To evaluate the impact of s-μG, IR, and their combination on cardiomyocyte mechanotransduction pathways (e.g., YAP1) and DNA damage using 3D-specific imaging and analysis techniques.
- **Objective 3**: To compare cardiomyocyte reactions between 2D and 3D environments to identify critical differences in cellular behaviour and stress response attributable to environmental dimensionality.

**Aim 3:**

To Design, Develop, and Fabricate a 3D Hybrid Heart-on-a-Chip Model for Simulating the Cardiac Microenvironment

**What**: The final aim is to develop a sophisticated 3D Heart-on-a-Chip device that integrates bioprinting technology to replicate the cardiac microenvironment, including extracellular matrix and vascular structures.

**Why**: This advanced model aims to provide a comprehensive platform for studying cardiomyocyte function under physiologically relevant conditions, enhancing the translational value of findings.

**How**: The Heart-on-a-Chip will be fabricated using state-of-the-art 3D bioprinting techniques, focusing on optimising biomaterials and device design. The process involves:

- **Objective 1**: To optimise 3D bioprinting methodologies and materials, including the selection of bioinks that closely mimic the structural and functional properties of native cardiac tissues.
- **Objective 2**: To perform biological assessments of the 3D bioprinted heart model, including cell viability, proliferation, and functional assays, to validate the model's capacity to replicate the cardiac microenvironment under s-μG and IR conditions.
- **Objective 3**: To design and fabricate the hybrid Heart-on-a-Chip device, incorporating bioprinted cardiac tissues to replicate the cardiac extracellular matrix and vascular features, enabling detailed investigations of cellular responses in a near-physiological setting.

## 2.4 PROJECT SIGNIFICANCE

The proposed research endeavours to contribute to the fast-growing field of cell mechanobiology, particularly focusing on the mechanotransduction processes in cardiomyocytes. The unique approach of this study lies in using microgravity and IR as tools to gain a novel perspective on cardiac mechanotransduction. By simulating these space-like conditions, the research endeavours to unravel the complexities of how cardiomyocytes function and respond at a molecular level.

Understanding the behaviour of cardiomyocytes in response to microgravity and IR has significant implications for astronaut health in space travel and cardiovascular research on Earth. The methodology employed in this research, encompassing a progression from two-dimensional cell cultures to a more sophisticated bioprinted hydrogel heart-on-a-chip system, represents a novel approach to cardiac modelling. This strategy provides a more comprehensive and physiologically relevant platform for studying the complexities of the heart. It bridges the gap between simpler *in vitro* studies and the intricate realities of cardiac function and disease mechanisms. The heart-on-a-chip model, in particular, offers an exceptional opportunity to study the responses of cardiomyocytes in a dynamic, controlled environment. Leveraging the unique microenvironment of s-μG combined with IR exposure, this research aims to identify key cellular markers and mechanosensing receptors associated with cardiac function and disease.

## 2.5 IMPACT OF EXTERNAL CHALLENGES ON THESIS PROGRESS

This thesis has been developed under extraordinary circumstances that have significantly impacted its progression and completion timeline. The period of my doctoral research coincided with a series of unforeseen challenges. The following summarises the key issues encountered during my PhD:

1. Supervisory Changes: The most substantial of these challenges was a prolonged period without effective supervision. From 2022 through much of 2023, my primary supervisor was unavailable due to an extended period of leave, which severely limited my access to essential guidance and feedback. Following this period, my primary supervisor left the university. This disruption was partially alleviated by appointing a new primary supervisor in August 2023, whose support was invaluable. However, the absence of consistent supervision for over a year significantly impeded my project's momentum, leading to delays and uncertainties in decision-making.
2. COVID-19 Pandemic: The COVID-19 pandemic introduced unprecedented restrictions, including lockdowns and limited access to research facilities, which directly hindered my experimental work and collaborative interactions. Lockdowns and laboratory access restrictions delayed my experimental work, where no laboratory work could be conducted for approximately six months. Furthermore, upon return, the capacity of the laboratory was reduced, only allowing access for a limited time (maximum of three days a week) to adhere to social distancing protocols, which persisted for nearly a year. Remote work requirements also hindered collaborative efforts and limited my access to ANSTO (partner organisation for this thesis), extending my project's timeline.
3. Technical and Physical Challenges: My research project, which relied on specific methodologies, encountered technical difficulties, equipment malfunctions, and unexpected experimental setbacks. These challenges, combined with shortages of critical reagents and equipment due to delays in the global supply chain as an additional effect of the COVID-19 pandemic, required considerable time to address and resolve, further delaying the research process. Additionally, repetitive strain injury (RSI) from extensive laboratory work and the physical demands of frequent travel between research facilities contributed to periods of reduced productivity and burnout. These physical and logistical challenges affected my well-being and necessitated work habits and project timeline adjustments.

This disclaimer acknowledges the impact of these external factors on the research and provides context for any adjustments made to the project timeline and methodology. Despite these obstacles, diligent efforts have been made to maintain the quality of the research. This thesis, therefore, represents not only my academic journey but also a journey of resilience in the face of unprecedented challenges.

# Chapter 3 -

## Materials and Methods

## 3.1 EQUIPMENT

The equipment and its respective suppliers are listed in Appendix A - Table 1.

## 3.2 CHEMICALS, REAGENTS AND CONSUMABLES

Appendix A lists chemicals, reagents, and their respective suppliers, as shown in Appendix A, Table 2.

## 3.3 CELLS

To create a cardiac model, three cell types were utilised: human cardiomyocytes (AC-16), adult human coronary artery endothelial cells (HCAEC), and adult human cardiac fibroblasts (hCFs). The cells used in this study and suppliers are listed in Table 3.1

*Table 3.1 Cells Used in This Study*

| Cell Line | Type | Species | Complete Culture Medium | Source |
|---|---|---|---|---|
| **AC-16** | Cardiomyocytes | Human | DMEM-F12, 12.5% (v/v) FBS,2 mM L-Glutamine, 1% (v/v) penicillin-streptomycin | Millipore |
| **HCF** | Fibroblasts | Human | Cardiac Fibroblast Growth Medium, 10% (v/v) FBS, 2mM L-Glutamine, 1% (v/v) penicillin-streptomycin | Gifted by Dr Carmine Gentile, University of Technology Sydney |
| **HCAEC** | Endothelial Cells | Human | MesoEndo Cell Growth Medium, 10% (v/v) FBS, 2mM L-Glutamine, 1% (v/v) penicillin-streptomycin | Gifted by Dr Carmine Gentile, University of Technology Sydney |

AC-16 cells were selected as the primary cell model due to their suitability for the experimental conditions involving s-μG and IR. These cells are not contractile cardiomyocytes; they lack striations and do not exhibit spontaneous contractility, resembling cardiac myofibroblasts, particularly after prolonged subculture and dedifferentiation. This dedifferentiated state results in the loss of contractile properties and sarcomeric organisation, making AC-16 cells more akin to myofibroblast-like cells, which are stable and predictable under non-physiological stress conditions.

The selection of AC-16 cells was driven by the need for a robust and adaptable model that could withstand the extensive optimisation required for these challenging experimental exposures. The absence of spontaneous contraction in AC-16 cells reduces variability in cellular responses, enabling a clearer assessment of the effects of microgravity and radiation. Their use facilitated the development

and refinement of experimental protocols, ensuring reliable and consistent results in a complex and controlled setting.

It was planned that once all experimental factors, including exposure conditions, were fully optimised, AC-16 cells would be substituted with a more appropriate cardiomyocyte model. This approach aimed to refine the initial experimental design using AC-16 cells and then transition to a fully contractile cardiomyocyte once the conditions were optimised, thus enhancing the physiological relevance of the findings.

## 3.4 GENERAL STOCK SOLUTIONS

### 3.4.1 Phosphate Buffered Saline (PBS)

Sterile phosphate-buffered saline (PBS) was purchased from Sigma for tissue culture. For non-sterile uses, PBS was prepared by adding one PBS tablet to 100 mL of distilled water. Stock solutions of 500mL were prepared each month (Stored in 4°C).

### 3.4.2 AC-16 CMs Complete Cell Culture Media

AC-16 cardiomyocytes were cultured in DMEM/F12 without phenol red and supplemented with 12.5% (v/v) FBS, 100U.mL L-Glutamine, and 100µg.ml-1 Penicillin-Streptomycin Solution (Stored in 4°C).

### 3.4.3 Blocking Buffer

1% (w/v) BSA in PBS: Blocking Buffer was prepared by mixing 5g of bovine serum albumin (BSA) with 50 mL of PBS to achieve a final concentration of 1% (w/v) (Stored at 4°C).

### 3.4.4 Collagen Coating Solution

50 µg. mL-1 Collagen Type I in 20 mM acetic acid: A coating concentration of 50µg/mL was achieved by diluting Collagen Type I stock solution with 20 mM acetic acid to a final volume of 5mL (Stored at 4°C).

### 3.4.5 HCAECs Complete Cell Culture Media

HCAECs were cultured in MesoEndo Cell Growth Medium supplemented with 10% (v/v) FBS, 100U.mL L-Glutamine, and 100µg.ml-1 Penicillin-Streptomycin Solution (Stored in 4°C).

### 3.4.6 HCF Complete Cell Culture Media

HFCs were cultured in a Cardiac Fibroblast Growth Medium supplemented with 10% (v/v) FBS, 100U.mL L-Glutamine, and 100µg.ml-1 Penicillin-Streptomycin Solution (Stored in 4°C).

### 3.4.7 Paraformaldehyde (PFA) Fixation Solution

4% (v/v) PFA in PBS: A stock solution of PFA Fixation Solution with a concentration of 4% (v/v) PFA was prepared by diluting 12.5 mL of 40% PFA in PBS, making a final volume of 50 (Stored at 4°C).

### 3.4.8 Permeabilization Buffer

0.5% (v/v) Triton X-100 in PBS: Permeabilization Buffer stock solution of 0.5% (v/v) was prepared by diluting 0.5 mL of Triton X-100 with PBS to a final volume of 100mL (Stored in 4°C).

## 3.5 GENERAL METHODS

### 3.5.1 Tissue Culture

The tissue culture experiments in this study were conducted to maintain cell lines under controlled laboratory conditions. The cells were sustained in culture media and incubated in a humidified environment at 37°C with 5% (v/v) $CO_2$. All cell culture procedures strictly adhered to aseptic techniques and were conducted within a class II biosafety cabinet to ensure the sterility of the process. The incubation of cells was conducted at 37°C in an atmosphere containing 5% (v/v) $CO_2$ in air.

#### *3.5.1.1 Resurrection of cells*

The vial containing approximately $1x10^6$ cells was removed from the liquid nitrogen storage facility and thawed rapidly in a 37°C water bath to resurrect cells. Thawed cells (approximately 1 mL) were transferred to a sterile 15 mL centrifuge tube, followed by the slow addition of pre-warmed cell culture media (approximately 9 mL). This gradual addition of media helped prevent osmotic shock to the cells. Subsequently, the cell suspension was gently mixed by pipetting up and down. The tube was centrifuged at 300 x g for 5 minutes to isolate cell pellets. After discarding the supernatant to eliminate residual cryopreservative (DMSO), the cells were resuspended in 10-15 mL of media and transferred to a T75 tissue culture flask. These cells were then incubated at 37°C in an atmosphere containing 5% $CO_2$ (v/v) in air, and the culture media were replaced the following day to facilitate their adaptation to the new environment.

#### *3.5.1.2 Maintenance of cells*

Regular maintenance was performed to ensure cell lines' continued viability and growth. The culture media were replaced every 3-4 days for each cell line. This routine change of media provided essential nutrients and removed waste by-products. Cells were passaged when they reached approximately 80% confluence, ensuring that they remained within the logarithmic phase of growth.

#### *3.5.1.3 Passaging of cells*

The passage of cells was performed when cell cultures reached approximately 80% of confluency. The culture medium was gently removed from the tissue culture flask, and the cells were washed with sterile PBS. Following this wash with PBS, 3-5 mL of trypleE solution was applied for 3-5 minutes at 37°C to facilitate cell detachment. Once detachment was confirmed via observation through a brightfield microscope, a complete culture medium was added to the flask to neutralise the effects of trypleE solution, followed by gentle rotation to ensure even cell suspension. The dissociated cell suspension was then transferred to a 15 mL conical tube, and the cells were centrifuged at 300 x g

for 5 minutes, separating the cells from the supernatant. After discarding the supernatant and loosening the cell pellet, a culture medium was added for thorough resuspension. Cell viability and concentration were determined using a haemocytometer and trypan blue exclusion assay as described in section 3.5.1.4. Cells were either transferred for further culture and passaging at a split ratio ranging from 1:5 to 1:10 or used for experiments at the desired cell seeding density.

#### *3.5.1.4 Cell viability and cell seeding calculation with Trypan Blue*

Overall cell viability was monitored regularly using the Trypan Blue exclusion assay. This method involved staining a sample of cells with Trypan Blue. This dye penetrates non-viable cells with compromised membranes, enabling the identification of the live and dead cells in culture. Steps to passage cells were followed (section 3.5.1.3). After centrifugation and acquiring cells in suspension, a 10 µL aliquot of resuspended cells was mixed in a 1:1 ratio with a 0.4% (w/v) Trypan Blue dye. The cells were s then manually counted using a Neubauer hemocytometer (Figure 3.1).

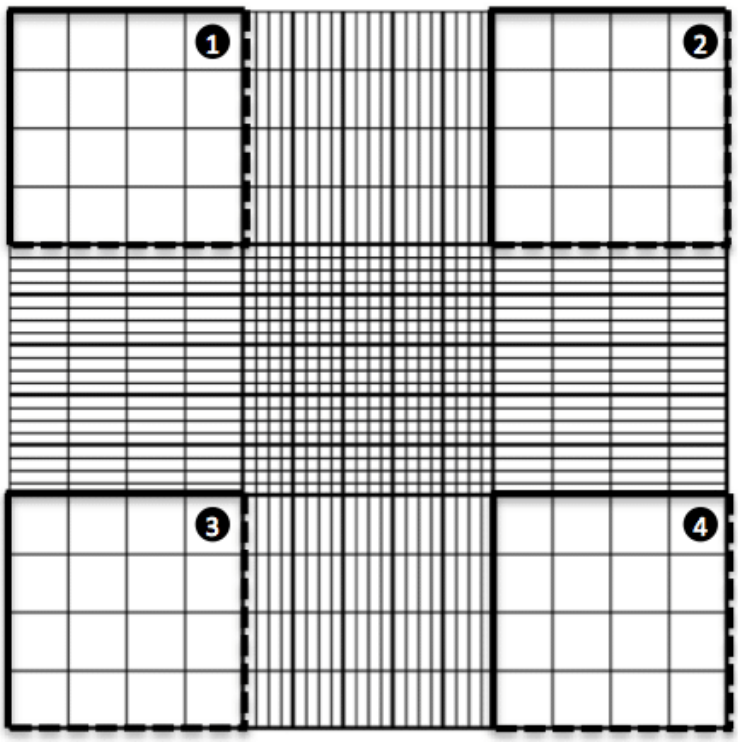


*Figure 3.1 Schematic Representation of a Hemocytometer. The hemocytometer grid is divided into four large squares (1-4) and further subdivided into smaller squares. The central squares are more finely divided to enable accurate cell counts within a given volume, facilitating the determination of cell concentration in the suspension.*

Non-viable cells were identified by their blue dye uptake, while viable cells displayed no dye uptake and remained colourless. The average count of cells in the four outer quadrants was determined, with cells positioned on the solid outer line included while those on the outer dotted lines were not. The

formula (Eq.1) calculates cells/mL with the obtained cell count. The count of viable and non-viable cells determined the percentage of live cells in the culture (Eq.2)

$$Number\ of\ Cells\ (Cells/mL) = \left(\frac{total\ cells\ counted}{\mathrm{n}}\right) \times 10^4 \times D.F. \qquad (Eq.1)$$

Where:

n = number of squares counted

DF = dilution factor

$$Cell\ Viability\ (\%) = \frac{\#\ of\ live\ cells}{(\#\ of\ live\ cells + \#\ of\ dead\ cells)} \times 100 \qquad (Eq.2)$$

#### *3.5.1.5 Cell Cryopreservation*

Cryopreservation was employed to preserve the cell lines for future experiments and to prevent genetic drift. The cells were prepared for cryopreservation following the cell trypsinisation procedure described in Section. 3.5.1.2 It is resuspended in a cell freezing medium (FBS with 10% (v/v) DMSO) and stored at a density of at least $1x10^6$ cells. $mL.^{-1}$ in a sterile cryovial. The freezing process was executed using a Nalgene slow freeze Mr Frosty container filled with isopropanol in a -80°C freezer for approximately 24 hours, enabling a controlled and gradual reduction in temperature, thus preserving the integrity of the cell lines during storage. Cryovials were stored in a liquid nitrogen tank for longer storage and stability.

### 3.5.2 *in vitro* Simulation of Microgravity and Radiation

This section describes the experimental methods utilised to investigate the physiological responses of AC-16 cardiomyocyte cells under conditions simulating extraterrestrial environments. The experiments were designed to mimic the unique stressors of spaceflight, specifically microgravity and ionising radiation. The equipment and general parameters and set-up are described below.

#### *3.5.2.1 Microgravity Simulator - Random Positioning Machine (RPM)*

To assess how cardiac cells respond to microgravity, cells were subjected to s-μG using RPM equipment available at the University of Technology Sydney (UTS) and the Australian Nuclear Science and Technology Organisation (ANSTO). The RPM is a device designed to continuously alter the orientation of its contents, thereby averaging the gravitational vector to near zero over time, effectively simulating a microgravity environment.

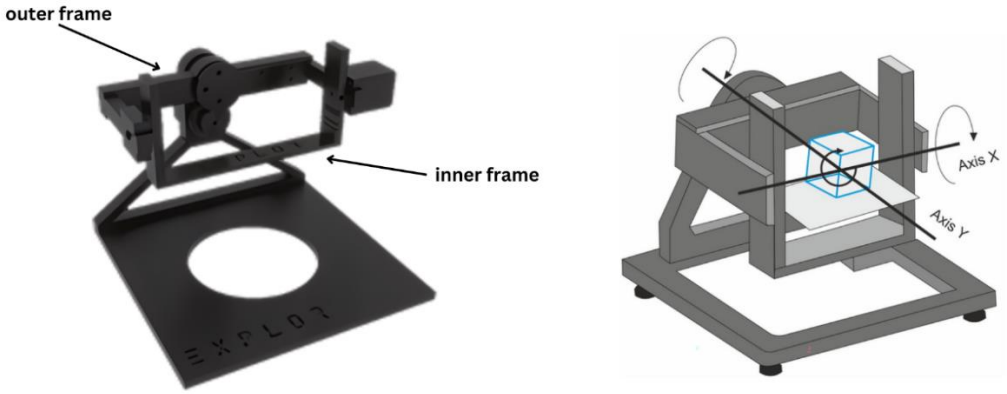


*Figure 3.2 Diagram of the RPM Used in This Study. The RPM consists of two independently rotating frames: the outer frame rotates around a horizontal axis (Axis Y), and the inner frame rotates around an axis perpendicular to the outer frame (Axis X). The left panel shows the RPM hardware, while the right panel illustrates the rotation axes.*

The RPM operates through an automatic rotation mechanism designed to randomly change the direction of the gravity vector experienced by the cells. This is accomplished by two independently rotating frames:

- The Outer Frame: Rotates around a horizontal axis.
- The Inner Frame: Rotates around an axis perpendicular to the outer frame.

The rotation of these frames is controlled by a built-in algorithm, which automatically adjusts the speed and direction of each frame to ensure a random positioning effect. This randomness is critical to prevent cells from adapting to a fixed orientation, thereby effectively simulating microgravity conditions. The default operational parameters provided by the manufacturer ensured the uniform distribution of gravitational forces over time. This technique is widely recognised for its effectiveness in microgravity simulations, as described in Sections 1.2.3.1.

Prior to loading the cells onto the RPM for microgravity simulation, all wells and flasks were carefully filled with culture media to prevent the formation of air bubbles, which could interfere with the exposure of cells to s-μG. This preparation ensured that the cells remained fully immersed in culture media throughout the rotation, thus preventing shear stress or other mechanical disturbances from air-liquid interfaces. The treatment involved varying the duration of exposure to s-μG, with a static control consisting of flasks placed in the same incubator but not mounted on the RPM.

#### *3.5.2.2 Radiation Simulator - X-RAD 320*

To assess the effects of ionising radiation on cardiac cells, the X-RAD 320 precision irradiation system from Precision X-Ray Inc., available at ANSTO, was utilised. This system is recognised for its reliability and precision in delivering controlled doses of radiation. The X-RAD 320 design allows for precise dosimetry calibration, delivering X-ray radiation through an adjustable collimator that controls the radiation field size and shape, allowing for targeted exposure of cell samples.

The X-RAD 320 is widely used for simulating space radiation on Earth, particularly for replicating the lower-energy components of space radiation, such as solar radiation and gamma rays. Although these radiation types are less intense than cosmic rays, they still pose significant biological risks, including DNA damage and impaired cellular function (Section 1.2.3.2.)

Cells were exposed to varying absorbed doses of ionising radiation, ranging from 0.5 Gy to 12 Gy, with non-irradiated samples (0 Gy) serving as the control group. The irradiation was conducted under controlled conditions, with meticulous dosimetry calibration to ensure accurate and consistent radiation exposure across all samples.

#### *3.5.2.3 Combination of Microgravity and Radiation - RPM and X-RAD 320*

For the simultaneous exposure of AC-16 cardiomyocyte cells to s-μG and IR, the RPM was enclosed within a standard $CO_2$ incubator to maintain optimal culture conditions (37°C and 5% $CO_2$), whilst the X-RAD 320 is positioned directly next to the incubator. This close proximity allowed for quick and controlled sample transfer between the RPM and X-RAD 320, minimising handling time and

reducing exposure to non-experimental conditions. The setup is illustrated in Figure 3.3, showing the relative positioning of the RPM within the incubator and the X-RAD 320 radiation source.

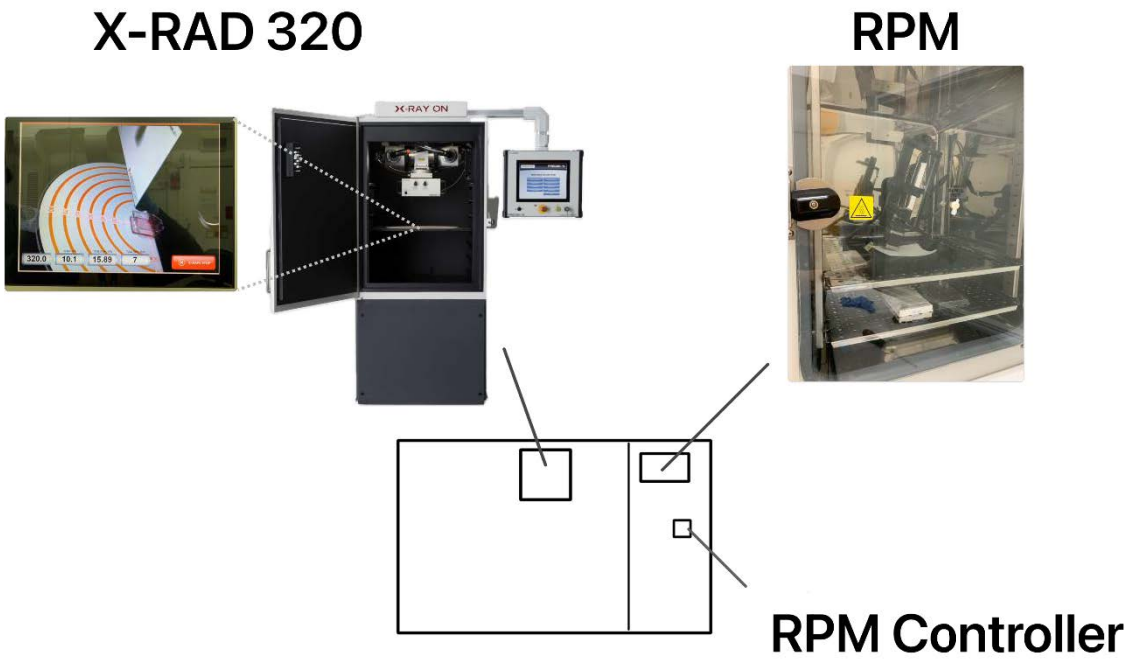


*Figure 3.3 Experimental Setup for Simultaneous Exposure of Cardiomyocytes to s-μG and IR. The RPM is positioned inside the incubator adjacent to the X-RAD 320, enabling efficient sample transfer between microgravity simulation and radiation treatment.*

A sequential approach was employed to investigate the combined effects of s-μG and IR. For the combined treatment, cells were first exposed to s-μG by mounting them on the RPM 24 hours before IR. This pre-exposure period allowed the cells to acclimate to the s-μG conditions, as the effects of the RPM are optimised over time. Concurrently, static control cells were placed in the same incubator without RPM exposure, ensuring a consistent environment across all samples. The following day, the samples were irradiated with the desired radiation dosage using the X-RAD 320. After irradiation, the samples were either returned to the RPM for continued exposure to s-μG or kept as static controls. Cellular responses were evaluated at predetermined time points to assess the individual and combined effects of s-μG and radiation. This approach enabled a systematic investigation of how cardiac cells respond to s-μG, radiation, and their combined effects, ensuring controlled and consistent conditions throughout the experiment.

#### *3.5.2.4 Approach and Adaptation to Facilitate Experimental Conditions Set Up*

Each well was meticulously prepared in the experimental setup to ensure controlled exposure conditions. This process was crucial to maintaining the samples' integrity and avoiding media leakage while subjecting them to s-μG using the RPM. Firstly, a silicone snap-on plug was employed to seal each well securely. These plugs were chosen as their design fit snugly into the well openings, creating

a reliable barrier against any potential media leakage. This step was vital to prevent contamination and cross-contamination between wells and preserve each well's environment. To further enhance the experimental setup, a gas-permeable hydrophobic porous sealing film, specifically the AeraSeal™ film from Sigma, was used to seal the wells. This specialised sealing film was chosen for its unique properties: it allowed for controlled gas exchange while maintaining a watertight seal. This was particularly important for regulating the wells' oxygen and carbon dioxide levels, simulating the experiment's required environmental conditions.

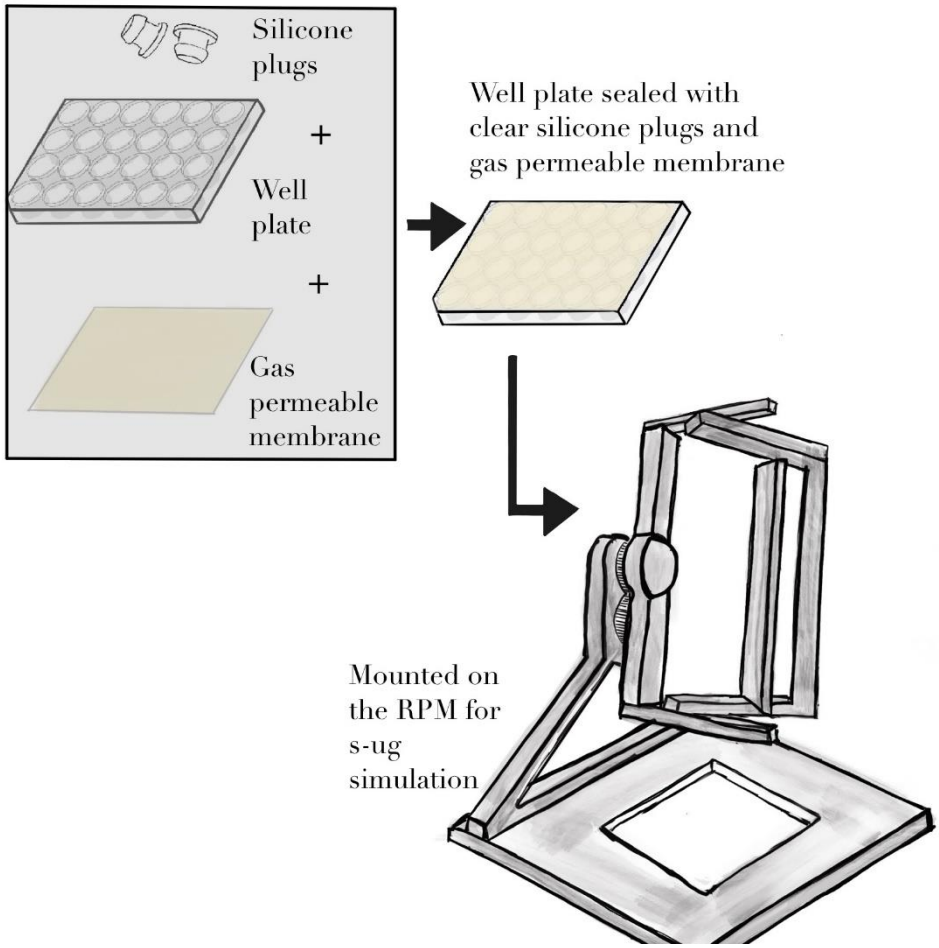


*Figure 3.4 Schematic Representation of the Experimental Setup for Simulating Microgravity (s-μG) Conditions. The well plate is sealed with silicone plugs and a gas-permeable membrane to ensure adequate gas exchange. This sealed well plate is then mounted on the RPM, which simulates microgravity conditions for cell culture experiments. The RPM enables continuous and random orientation changes, effectively mimicking the effects of microgravity on the cultured cells.*

## 3.6 BIOLOGICAL EVALUATION METHODS

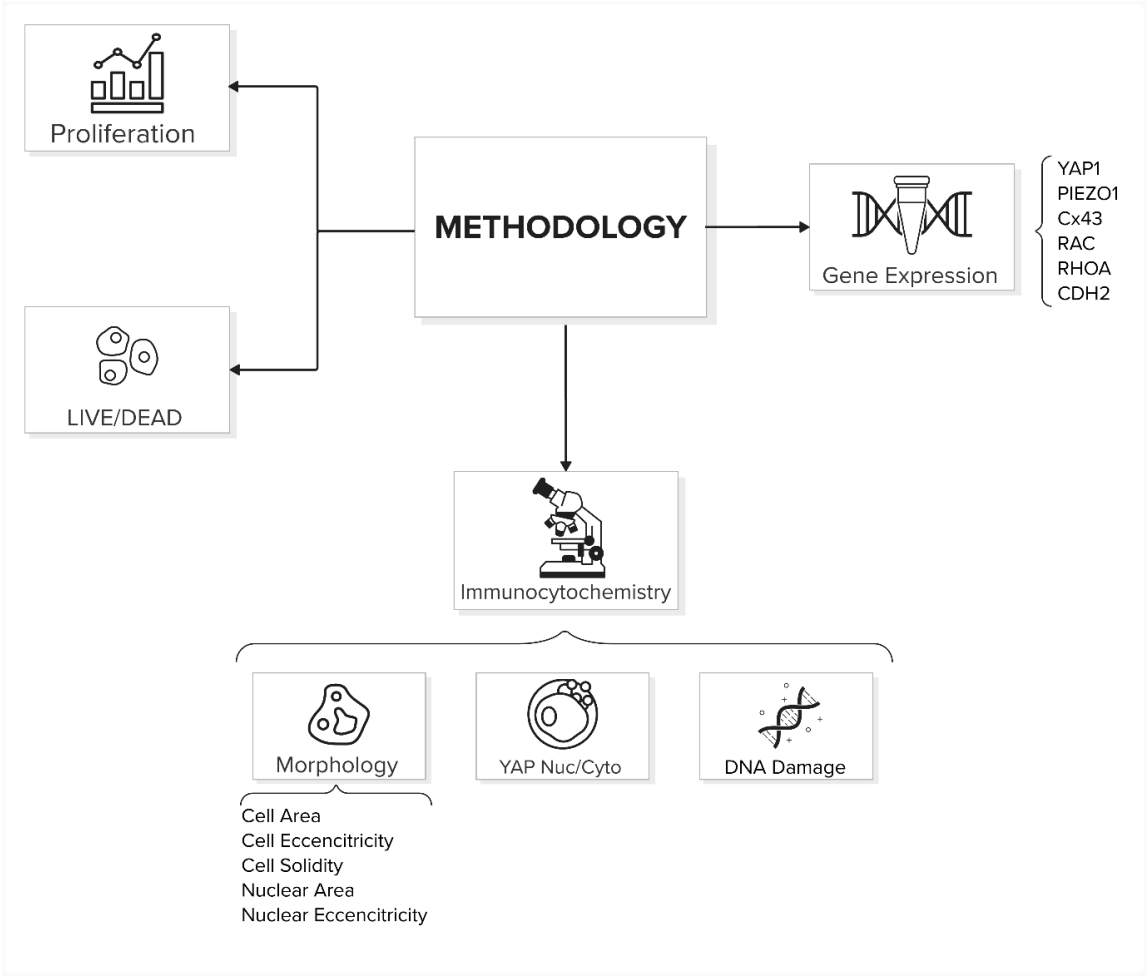


*Figure 3.5 Summary of Methods Utilised in This Study.*

### 3.6.1 Cell Proliferation by Resazurin-Based Assay

A resazurin-based assay was employed to examine the proliferative capacity of the cells and the impact of the experimental treatments. This assay reduces resazurin, a non-fluorescent blue compound, to its highly fluorescent pink derivative, resorufin, by metabolically active living cells. Therefore, a higher level of fluorescence indicates that more resazurin has been metabolically converted, suggesting increased cell viability and proliferation. Proliferation was assessed by utilising PrestoBlue™ Cell Viability Reagent for this resazurin-based assay. The procedure began with the aspiration of the cell culture medium from each well, followed by a gentle wash with PBS to minimise cell disturbance. 100µL of a 1:10 dilution of PrestoBlue™ Cell Viability Reagent in PBS was added to each well. Plates were then incubated at 37°C, shielded from light, for one hour to allow for the metabolic conversion of resazurin to its fluorescent derivative, resorufin. Post incubation, the fluorescence intensity of the converted resorufin was measured using a plate reader. The plate reader was configured to use an excitation wavelength of 560 nm and an emission wavelength of 590 nm,

with readings taken from the bottom of the wells to assess the fluorescence produced by the cells. Additionally, the absorbance of all wells was measured at 570 nm (experimental) and 600 nm (reference) wavelengths.

Fluorescence and absorbance readings were used to calculate the relative proliferation level. Data processing involved the subtraction of blanks - control samples without cells - from the raw readings; subsequently referred to as Corrected RFU. This subtraction was essential to eliminate background noise and ensure that the resulting values accurately reflected the cellular activity.

### 3.6.2 Cell Viability by LIVE/DEAD Assay

The viability of cardiomyocytes was evaluated using the Live/Dead assay, which was selected for its efficiency and lower probability of user error. This assay allowed for the automated counting of cells and provided a representative cell population analysis.

Following the conclusion of treatments for each group, the cells were initially washed with PBS and prepared to use with the Live/Dead Assay kit provided by Invitrogen. Subsequently, the cells were stained with two fluorescent dyes: 1 μM calcein-AM, which emits green fluorescence and indicates live cells, and 4 μM ethidium homodimer, emitting red fluorescence to mark dead cells. Additionally, Hoechst 33342 dye, emitting blue fluorescence, was used to label the nuclei of all cells, providing a total cell count. The staining process entailed incubating the samples in 100uL of solution containing the dyes in combination, diluted in sterile, culture-grade PBS, at 37°C for 30 minutes. After the 30-minute incubation, the samples were washed with 100uL of culture-grade PBS at least twice at room temperature to remove any excess dye and ensure the clarity of the subsequent imaging.

Cells were imaged using a fluorescent microscope with three channels (GFP, Texas Red, DAPI) at 20x magnification. At least five fields of view (FOV) were captured per time point, ensuring a substantial cell count for each time point and a robust sample size for accurate viability assessment.

Image acquisition for experiments including 3D hydrogels was done utilising z-stacks encompassing at least five wells with a minimum of three FOV, maintaining a step size of 1 μm. Following image acquisition, z-stacks were processed in FIJI to eliminate collagen autofluorescence noise and create maximum-intensity projection (MIP) images.

Subsequently, images were analysed using FIJI (ImageJ) software with a custom macro (detailed in Appendix B), enabling semi-automated analysis of cell viability, categorising cells based on their live (green) and dead (red) fluorescence. Using this macro also allowed for image batch processing, enhancing the viability assessment's efficiency and consistency.

Live and dead cells were quantified independently, with the viability percentage formula (Eq. 2) applied to calculate the proportion of viable cells. To quantitively compare the impact of s-μG on cell viability at different durations to s-μG, cell viability measures in the s-μG group were normalised against a static control group at each time point. This normalisation, benchmarking the initial 0-hour measurement as 100%, allowed for comparisons on a relative scale, thereby minimising the experimental setup inherent variability and enhancing the accuracy of interpreting s-μG effects.

### 3.6.3 Reverse transcription-quantitative polymerase chain reaction (RT-qPCR)

To investigate the mechanisms involved in cardiac mechanotransduction, changes in gene expression within cardiomyocytes under the influence of microgravity, radiation, or a combination of both were examined. The analysis used Reverse Transcription Quantitative Polymerase Chain Reaction (RT-qPCR). The selected genes for this study were chosen based on their critical involvement in fundamental cellular functions within cardiomyocytes, reflecting their significance in regulating cellular growth, mechanical responses, mitochondrial function, cytoskeletal dynamics, intercellular communication, and structural integrity (Table 3.6.1). Their corresponding primer sequences are detailed in Table 3.2.

*Table 3.2 Overview of Genes Analysed in the Study.*

| Gene | Protein | Description |
|---|---|---|
| **Genes of Interest (GOI)** | | |
| **YAP1** | Yes-Associated Protein 1 | A key regulator of the Hippo signalling pathway and is important in cell growth and tissue regeneration. |
| **RAC2** | Ras-Related C3 Botulinum Toxin Substrate 2 | Involved in cytoskeletal organisation and cell motility, impacting mechanotransduction pathways. |
| **CX43** | Connexin 43 | Codes for a protein in gap junction formation are essential for cardiac intercellular communication. |
| **CDH2** | Cadherin 2 | Encodes N-cadherin, crucial for cardiomyocyte adhesion and tissue integrity. |
| **RHOA** | Ras Homolog Family Member A | Regulates actin cytoskeleton and cell contractility, mediating cellular responses to mechanical forces. |
| **Housekeeping Genes (HKG)** | | |
| **GAPDH** | Glyceraldehyde-3-Phosphate Dehydrogenase | |
| **GUSB** | Beta-Glucuronidase | |
| **TBP** | TATA-Box Binding Protein | |

In molecular biology, gene annotations are critical for understanding the roles and functions of various genes within the cell. Specifically, they were grouped into categories reflective of their biological process. The focus was on two predominant biological processes: cell structure and motility regulation and signal transduction and intercellular communication mechanisms.

*Table 3.3 Selected Genes of Interest Categorised by Biological Processes.*

| Biological Process | Description | Genes |
|---|---|---|
| **Signal Transduction and Communication** | Signal reception and transmission within and between cells, including roles in organ size regulation, mechanotransduction, mitochondrial function, apoptosis, cell proliferation, and cell-cell communication. | YAP1<br>CX43 |
| **Cell Structure and Motility** | It involves the regulation of the cytoskeleton, affecting cell shape, motility, and adhesion. Essential for cell morphology and movement. | RHOA<br>RAC2<br>CDH2 |

### *3.6.3.1 Primer Design and Efficiency Determination*

Gene-specific primers were meticulously designed using the NCBI Primer-BLAST tool to ensure high specificity and efficiency for the target genes to facilitate gene expression study. Specific details regarding the primer sequences can be found in Table 3.4.

*Table 3.4 Gene-Specific Primers and Corresponding Sequences for RT-qPCR Analysis*

| Gene | Direction | Primer Sequence |
|---|---|---|
| **YAP1** | Forward | TAGCCCTGCGTAGCCAGTTA |
| | Reverse | TCATGCTTAGTCCACTGTCTGT |
| **RAC2** | Forward | CAACGCCTTTCCCGGAGAG |
| | Reverse | TCCGTCTGTGGATAGGAGAGC |
| **CX43** | Forward | GGTGACTGGAGCGCCTTAG |
| | Reverse | GCGCACATGAGAGATTGGGA |
| **CDH2** | Forward | TCAGGCGTCTGTAGAGGCTT |
| | Reverse | ATGCACATCCTTCGATAAGACTG |
| **RHOA** | Forward | AGCCTGTGGAAAGACATGCTT |
| | Reverse | TCAAACACTGTGGGCACATAC |
| **GAPDH** | Forward | GGAGCGAGATCCCTCCAAAAT |
| | Reverse | GGCTGTTGTCATACTTCTCATGG |
| **GUSB** | Forward | CTCATTTGGAATTTTGCCGAT |
| | Reverse | CCGAGTGAAGATCCCCTTTTTA |
| **TBP** | Forward | CACGAACCACGGCACTGATT |
| | Reverse | TTTTCTTGCTGCCAGTCTGGAC |

A primer efficiency determination step was incorporated into the workflow to validate the effectiveness of the primers. This involved creating a standard curve using known concentrations of cDNA samples. The primer efficiency was calculated based on the slope of the standard curve, ensuring that the primers exhibited high efficiency (Appendix C for efficiency curve)

### *3.6.3.2 Sample Preparation and CT Value Derivation*

Cell Lysis

Lysis Buffer from the RNeasy Mini Kit containing 1% (v/v) 2-mercaptoethanol disrupted cell membranes while preserving RNA integrity. After cell lysis, the resulting lysates were stored at -80°C to prevent RNA degradation until further processing.

RNA Isolation, Quantification and Purity Evaluation

RNA extraction was conducted using the RNeasy Mini Kit following the manufacturer's protocol. This kit employs silica-based columns to selectively bind and elute RNA from the cell lysates, ensuring high-quality RNA. The quality and quantity of the isolated RNA samples were assessed using a NanoDrop spectrophotometer. Absorbance measurements at 260 nm were used to determine RNA concentration. Additionally, the A260/A280 and A260/A230 ratios were calculated to evaluate RNA purity, with values around 2.0 and 2.2, respectively, indicating high-quality RNA.

cDNA Synthesis

Complementary DNA (cDNA) synthesis was performed using the iScript™ cDNA Synthesis Kit. The isolated RNA samples were reverse transcribed into cDNA, following the manufacturer's instructions to generate 25 ng/uL of stock cDNA.

RT-qPCR

RT-qPCR was conducted with prepared cDNA and gene-specific primers using SYBR Green PCR Master Mix. Reaction volumes were 10 µL for 96-well plates and 5 µL for 384-well plates, with concentration as indicated in Table 3.5. Samples were pipetted into the respective plates in triplicate for data reproducibility.

*Table 3.5 Reaction Components, Volumes and Final Concentration of a PCR Reaction*

| **Component** | **Volume/10uL Reaction (uL)** | **Volume/5 uL Reaction (uL)** | **Final Concentration 1X** |
|---|---|---|---|
| iTaq Universal SYBR Green Supermix (2x) | 5 | 2.5 | 1X |
| Forward and reverse primers | 1 | 0.5 | 500nM |
| DNA template (add at Step 4) | 2 | 2 | 1ng |
| Nuclease-free H2O | 2 | 0 | - |
| Total reaction mix volume | 10 | 5 | |

The RT-qPCR run protocol was conducted using the appropriate equipment for the well format, as detailed in Appendix A – Table 1. The protocol is as follows:

• Initial Hold:

95°C for 30 seconds (denaturation step) with a ramp rate of 1.6°C/second.

• PCR:

Step 1: 95°C for 5 seconds (denaturation step) with a ramp rate of 1.6°C/second.

Step 2: 60°C for 20 seconds (annealing/extension step) with a ramp rate of 1.6°C/second.

This PCR step is repeated for 40 cycles.

• Melt Curve (used to verify the specificity of PCR by melting PCR products):

Step 1: 95°C for 15 seconds with a ramp rate of 1.6°C/second.

Step 2: 60°C for 1 minute with a ramp rate of 0.05°C/second.

Step 3 (Dissociation): 95°C for 15 seconds.

A screenshot of the protocol settings, specifically from the QuantStudio 12K Flex Real-Time PCR System (Applied Biosystems), is provided in Figure 3.6 for reference. This figure illustrates the temperature profile and timing for each stage of the RT-qPCR cycle, including the initial hold, two-step PCR cycling, and melt curve analysis.


*Figure 3.6 Run Protocol for RT-qPCR Analysis on the QuantStudio 12K Flex Real-Time PCR System. The figure illustrates the temperature profile and timing for each stage of the RT-qPCR cycle. The protocol begins with an initial hold at 95°C for 30 seconds, followed by 40 cycles of two-step PCR: denaturation at 95°C for 5 seconds and annealing/extension at 60°C for 20 seconds. The cycle concludes with a melt curve analysis consisting of a 95°C step for 15 seconds, a 60°C step for 1 minute, and a final dissociation step at 95°C for 15 seconds. Each temperature step is annotated with ramp rates, with data collection points and pauses indicated in the diagram.*

Melt Curve Analysis

Melt curve analysis was performed immediately after the amplification phase of RT-qPCR to assess the specificity of the primers and the purity of the amplified products. The analysis involved gradually

increasing the temperature and monitoring the fluorescence to detect the dissociation of the DNA duplexes.

The results showed single, sharp peaks for each primer set, indicating that a single, specific product was amplified without significant primer-dimer formation or non-specific product formation. This confirms the specificity and reliability of the primers used in the gene expression analysis. In instances where multiple peaks are observed during melt curve analysis, this suggests the presence of non-specific amplification or primer-dimer artifacts. Data obtained from qPCR runs exhibiting multiple peaks in the melt curve analysis were considered unreliable due to potential non-specific amplification. Such data were excluded from the final analysis. The experiments were repeated after troubleshooting to ensure that only data reflecting specific amplification are included.

Gene Expression Quantification

The Comparative Ct (ΔΔCt) Method was used in gene expression quantification. This method involved calculating the ΔCt value for each sample by subtracting the Ct value, derived from RT-qPCR, of the GOI from the Ct value of a series mean of stable HKG (GAPDH, GUSB, TBP) within the same reaction plate. This calculation normalises for variations in RNA quantity and quality across samples. A higher amount of target RNA corresponds to a lower ΔCt value due to the inverse relationship between Ct number and RNA abundance. The ΔΔCt value was then computed by comparing the ΔCt of each treatment condition to the ΔCt of a control condition.

For subsequent expression representation and plotting, fold change was used instead of ΔCt or ΔΔCt values to provide a more intuitive and direct visualisation of gene expression changes. Fold changes were calculated using the formula $2^{(-\Delta\Delta Ct)}$. Subsequently, log2 transformed into a linear scale, where fold changes above 0 indicate upregulation, below 0 indicate downregulation and a value of 0 signifies no change in expression compared to the control. For a more detailed explanation of the calculation and interpretation of ΔCt, ΔΔCt and Fold Change, refer to Appendix D.

Statistical Analysis

For statistical analysis, ΔCt or ΔΔCt values were utilised due to their normalised nature, which accounts for variations in sample loading and PCR efficiency. Statistical evaluation of gene expression changes over time, comparing different treatment conditions, was carried out using two-way ANOVA with Šídák's multiple comparisons tests or Tukey's multiple comparisons. GraphPad Prism was used for the statistical analysis using ΔΔCt values to mitigate biases associated with log-transformed data.

## 3.7 IMMUNOCYTOCHEMISTRY

Immunocytochemistry (ICC) represents an intricate technique that visualises specific proteins and peptides within cells that play critical roles in cellular responses to mechanical stimuli. This section outlines a general ICC protocol, which is versatile for both 2D and 3D cell culture systems, with further specific details provided in subsequent chapters.

For cells in 2D, the initial phase of the experiments focused on assessing the effects of s-μG over time. This involved examining the mechanotransduction response in cells before and 72 hours following exposure to either s-μG or static control conditions. A subsequent experiment with a combination of s-μG and IR exposure was conducted to explore the combined impact of s-μG and IR exposure on cellular behaviour. For the combined exposure experiments, cells had to adapt to s-μG conditions as outlined in Section 3.5.2.4, which resulted in 72 hours of s-μG exposure and 48 hours post-IR period. For cells in 3D, only the combined exposure experiments were conducted, and therefore, the AC-16 cardiomyocytes in collagen hydrogels were analysed after 72 hours of s-μG exposure and 48 hours post-IR period.

The following general steps were common to all culture systems. The culture medium was removed at each analysis time, and cells were washed at least twice with PBS at room temperature. The cells were then fixed with 4% (v/v) PFA (Section 3.4.6) at room temperature, ensuring the preservation of cellular structure and morphology. The coverslips or 3D hydrogels were washed twice with PBS and stored at 4°C until antibody labelling was performed. A permeabilisation step was performed using Triton X-100 permeabilisation buffer (Section 3.4.7), which was then washed with PBS twice at room temperature to facilitate effective antibody penetration. This was followed by a blocking step with a BSA blocking buffer (Section 3.4.2) to minimise non-specific antibody binding. The cells were then incubated with primary antibodies that target specific proteins; a process conducted under controlled conditions. Following the incubation with primary antibodies, the cells were washed thoroughly with PBS twice more and then incubated with species-specific secondary antibodies that were fluorescently labelled. In addition to antibody staining, cells were stained for F-actin using Phalloidin 594, thus enabling the visualisation of the cytoskeleton structure within the cells. The final step of the procedure involved staining the nuclei with DAPI, a dye specific to DNA. This comprehensive staining process allowed detailed observation of protein localisation, cytoskeletal structures, and cell nuclear integrity.

Details on the specific concentration of buffers are summarised in Table 3.6 and described specifically in subsequent chapters.

*Table 3.6 Antibody Host and Dilution Utilised. Details on the host species and dilution factors used for each antibody in the experiments.*

| | Antibody/Stain | Host | Dilution |
|---|---|---|---|
| **Primary** | Active-YAP1 | Rabbit | 1:100 |
| | Cx43 | Mouse | 1:500 |
| | y-H2AX | Mouse | 1:800 |
| **Secondary** | Anti-rabbit Alexa Fluor 488 | Goat | 1:500 |
| | Anti-mouse Alexa Fluor 488 | Goat | 1:100 |
| | Anti-mouse Alexa Fluor 568 | Goat | 1:1000 |
| | Anti-rabbit CY5 | Goat | 1:500 |
| | Anti-mouse CY5 | Goat | 1:500 |

Following the staining procedure, a final wash with PBS was performed, and the coverslips or 3D hydrogels containing the cells were then prepared for microscopic examination. This 'mounting' process involved using a specialised mounting medium to help preserve the fluorescence emitted by the stained cells, which acts as an adhesive to attach the coverslip securely onto the microscope slide. The procedure involved carefully dispensing a drop of ProLong Diamond/Glass Anti-Fade onto the microscope slide, and the coverslip, with the cells facing downwards, was then gently lowered onto the slide, ensuring that the mounting medium formed a thin, even layer between the coverslip and the slide. To prevent dehydration of the samples, the edges of the coverslips were sealed with a thin layer of clear nail polish. Once the nail polish had dried, the slides were stored at 4 °C until they were ready to be imaged.

## 3.8 IMAGING METHODS, PROCESSING AND PIPELINES

### 3.8.1 YAP Nucleus-to-Cytoplasm Ratio

YAP1 is a primary marker of mechanotransduction and signal transduction processes. In the context of cellular stress and signalling, YAP1 undergoes dynamic localisation changes, moving between the cytoplasm and nucleus. This translocation is significant: when localised in the nucleus, YAP1 functions as a transcriptional co-activator, influencing the expression of genes involved in cell proliferation, apoptosis, and other vital cellular functions. Conversely, its presence in the cytoplasm indicates a different set of cellular states and activities, often linked to the retention or inactivation of YAP1's transcriptional activity.

To quantify YAP distribution within cells, an image analysis pipeline was developed using the CellProfiler software (Carpenter et al., 2006; McQuin et al., 2018; Stirling et al., 2021). This method allowed for the measurement of YAP fluorescence intensity in both nuclear and cytoplasmic regions. For each cell, the integrated intensity of YAP staining was calculated as follows:

- **Integrated nuclear intensity** was obtained by summing the fluorescence intensity of YAP within the nucleus, segmented using DAPI staining.
- **Integrated cytoplasmic intensity** was determined by summing the fluorescence intensity in the cytoplasmic region, defined as the area surrounding the nucleus after excluding nuclear pixels.

By adapting the methodologies outlined by Sero & Bakal (2017) a systematic image analysis workflow (Figure 3.7), was implemented using CellProfiler to characterise YAP localisation in both 2D and 3D experiments. The general workflow involved the following steps:

1. Input of Confocal Image: As shown in the first panel of Figure 3.7(1), confocal microscopy images were imported into CellProfiler. Channels were identified for DAPI (nucleus), F-actin (cytoplasmic structure), and YAP (nuclear and cytoplasmic localisation). For 3D samples, z-stacks were imported to capture volumetric data.
2. Object Identification: Illustrated in the second panel of Figure 3.7(2), nuclei were segmented based on DAPI staining, and cells were segmented using F-actin staining. For 2D samples, cytoplasmic regions were determined by subtracting the segmented nuclei from the cell area. In 3D samples, the cytoplasmic regions were determined by subtracting the segmented nuclei from the total cell volume, allowing for a full 3D segmentation of nuclear and cytoplasmic compartments.
3. Measurements: Integrated fluorescence intensity of YAP was calculated for both the nuclear and cytoplasmic compartments. This integrated intensity accounts for the total fluorescence

signal within each compartment (Figure 3.7(3). For both 2D and 3D samples the nuclear-to-cytoplasmic YAP ratio was calculated for each cell using the formula:

$$\text{Nuc/Cyto } YAP\ Ratio\ = \frac{Integrated\ Nuclear\ YAP\ Intensity}{Integrated\ Cytoplasmic\ YAP\ Intensity} \text{(Eq. 3)}$$

4. Output: Figure 3.7(4) reflects the output from the analysis, providing the nuclear-to-cytoplasmic YAP ratio, which was used to assess YAP translocation under different experimental conditions. In both 2D and 3D samples, a ratio greater than 1 indicated nuclear localisation, while a ratio less than 1 indicated cytoplasmic retention. For 3D samples, the analysis considered the volumetric data to provide a comprehensive measure of YAP distribution within the 3D cellular environment.

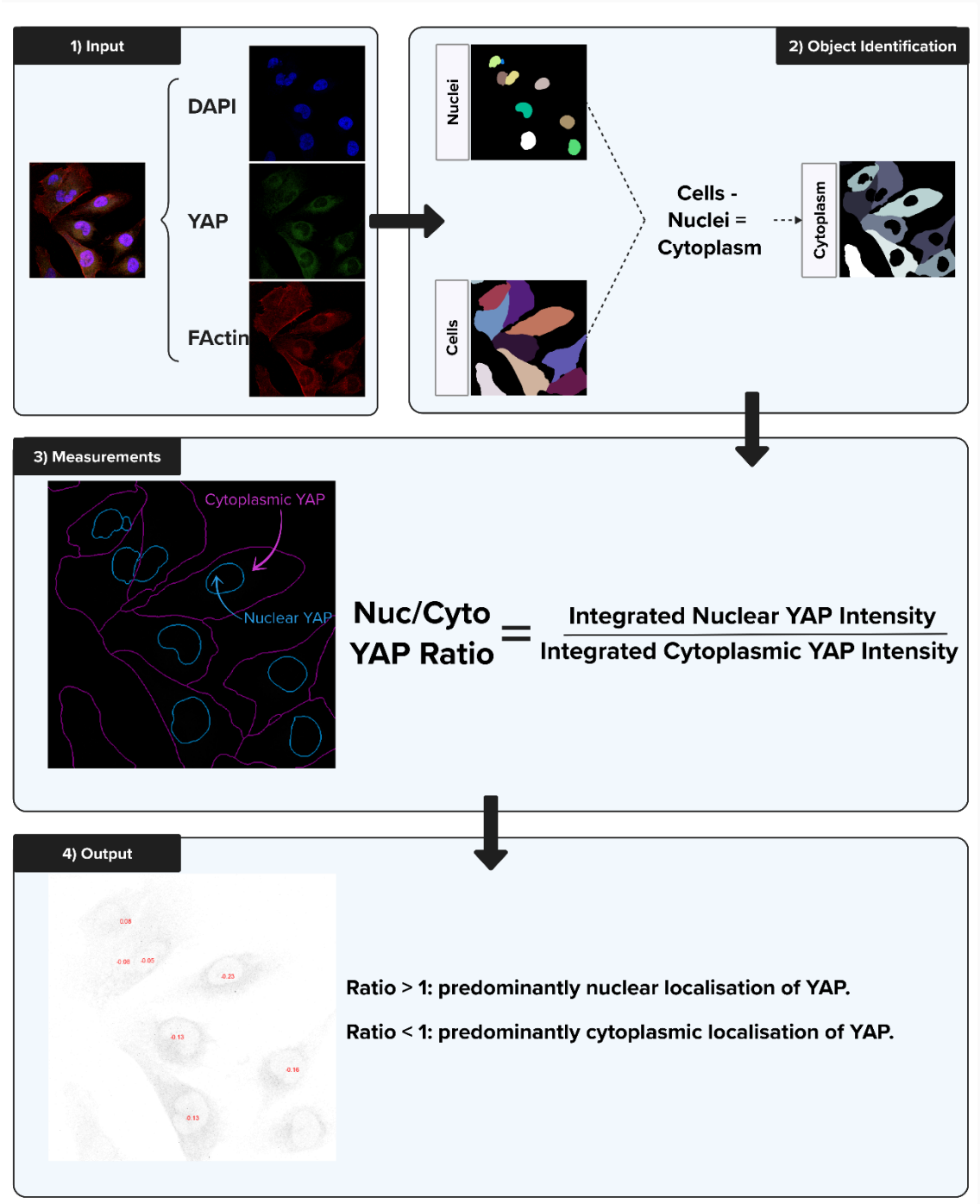


*Figure 3.7 Workflow for Intracellular YAP Localisation Analysis Using CellProfiler. (1) Input: Confocal images were processed to identify fluorescence channels corresponding to nuclei (DAPI), cell structure (F-Actin), and YAP localisation. (2) Object Identification: Nuclei and cellular outlines were segmented, and cytoplasmic regions were determined by excluding nuclear areas from the cell outlines. (3) Measurements: Integrated fluorescence intensities of YAP within nuclear and cytoplasmic compartments were measured and used to calculate the nuclear-to-cytoplasmic ratio. (4) Output: Ratios indicated YAP localisation; values greater than 1 denoted predominantly nuclear localisation, values less than 1 signified cytoplasmic localisation, and values around 1 indicated balanced distribution between nuclear and cytoplasmic regions.*

### 3.8.2 Cellular Morphology

CellProfiler was utilised to quantify cellular morphology to analyse F-actin staining. Image preprocessing techniques are initially applied to enhance the visibility of F-actin filaments, a key cytoskeleton component. This step is crucial for accurately identifying and isolating individual cells within the digital images. Following preprocessing, advanced image segmentation algorithms are employed to delineate cells as distinct objects based on the intensity and distribution of F-actin staining. This segmentation allows for the precise measurement of various morphological parameters, including cell area, perimeter, and the specific attributes of F-actin distribution within the cell, such as filament density and alignment.

This comparative analysis illuminates the impact of microgravity and radiation on cellular morphology, offering insights into the structural adaptations cells undergo in response to these stressors. Using CellProfiler for object identification and quantification, the study achieves high accuracy in measuring morphological changes, facilitating a deeper understanding of cellular responses and adaptations. This methodological approach underscores the importance of precise morphological quantification in elucidating the complex dynamics of cellular structure under stress conditions, contributing valuable data to the broader field of cellular biology and mechanobiology.

*Table 3.7 Parameters Assessed for Morphology Analysis. Key parameters evaluated in the morphology analysis, detailing aspects such as cell shape, area, perimeter, and structural features relevant to experimental outcomes.*

| Parameters | Definition | Indication of Values |
|---|---|---|
| **Area** | The area represents the two-dimensional space occupied by the cell or nucleus. | The area provides basic quantitative information about the size of the cell or nucleus, which can be crucial for understanding cell growth, division, and health. |
| **Eccentricity** | Eccentricity measures the deviation of the shape from a perfect circle. It quantifies the elongation of an object. | Values range from 0 (a perfect circle) to 1 (a line segment), with higher values indicating more elongated shapes. |
| **Solidity** | Solidity is the ratio of the shape's area to its convex hull's area. The convex hull is the smallest convex shape that completely encloses the shape. | Higher solidity values (closer to 1) indicate a shape closer to being completely convex, suggesting fewer indentations or protrusions. Lower values indicate a more irregular shape. |

The image analysis workflow employing the CellProfiler software, depicted in Figure 3.8, was followed to characterise cellular and nuclear morphology. The workflow was adapted from established methodologies to measure morphological features such as area, eccentricity, and solidity. This workflow enabled the precise quantitative analysis of cell morphology, which is critical for understanding cellular responses to various conditions and treatments. The steps include:

1. Input of Confocal Image: Displayed in the first panel of Figure 3.8 (1), confocal microscopy images were imported into CellProfiler. Channels for DAPI and F-Actin were identified, setting the stage for subsequent morphological assessments.
2. Object Identification: The second panel of Figure 3.8(2) illustrates the segmentation process, where nuclei were identified using DAPI staining and F-Actin staining to identify the cell outline. This step was crucial for distinguishing between individual cells and their nuclei.
3. Measurements: The third panel of Figure 3.8(3) details the measurement phase, where the number of pixels (2D) in each region was counted to determine area, and geometric properties were analysed to compute the eccentricity and solidity of the cells.
4. Output: The final panel of Figure 3.8(4) presented the outcome of the morphological analysis. Each cell's area, eccentricity, and solidity values were calculated to provide insights into cellular shape, structure, and cytoskeletal integrity.

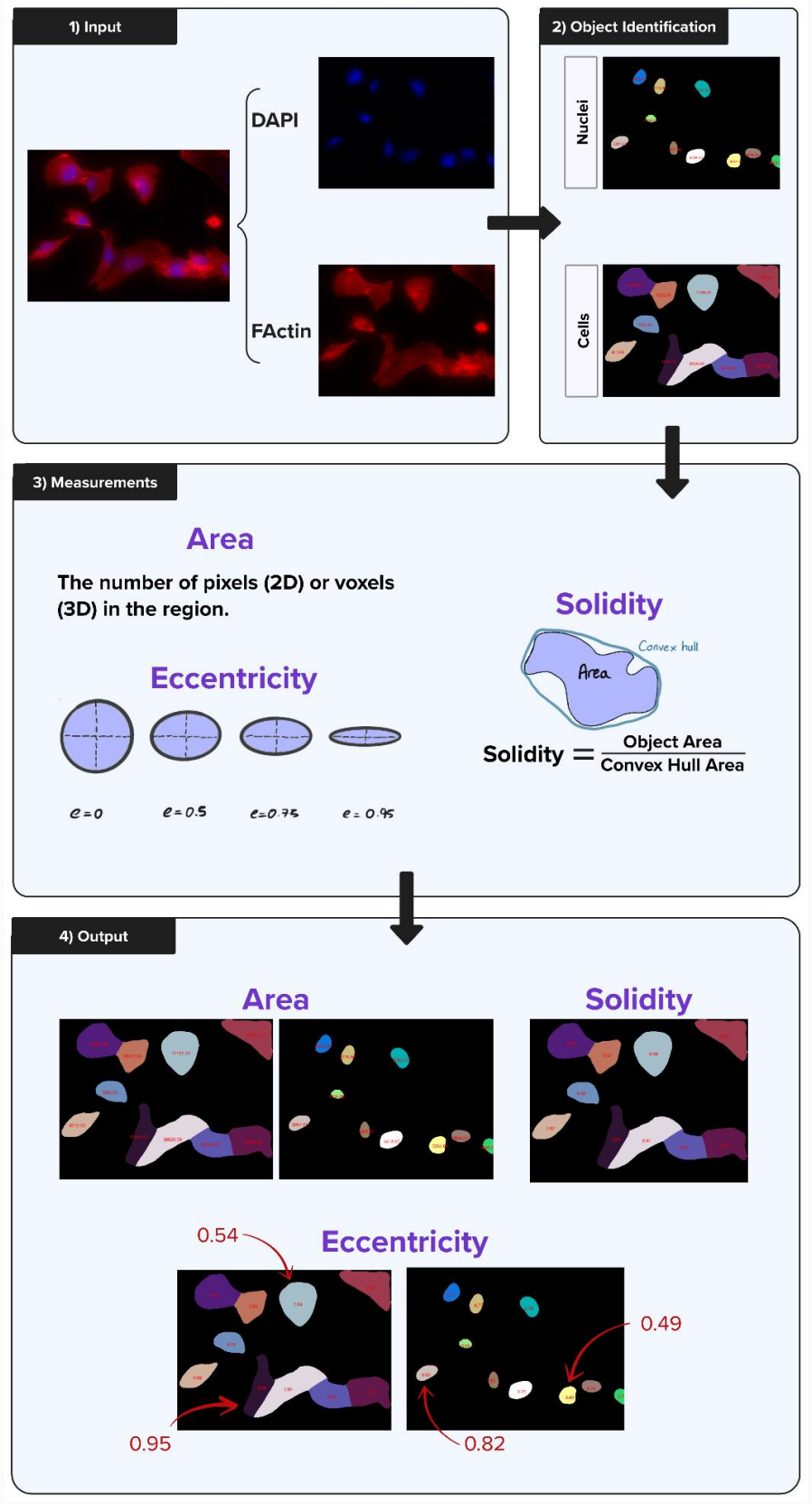


*Figure 3.8 Workflow for Cellular Morphology Analysis Using CellProfiler (1) Input: Confocal images were processed for DAPI and F-Actin fluorescence to delineate nuclei and cell structures. (2) Object Identification: Isolated nuclei were segmented, and cell perimeters were defined. (3) Measurements: Morphological features such as area, eccentricity, and solidity were quantified. (4) Output: Derived metrics provided insights into cell shape and structural integrity, with area reflecting cell size, eccentricity indicating shape elongation, and solidity measuring contour regularity.*

### 3.8.3 DNA Damage and DSB Repair Time

DNA damage protein H2AX expression was analysed using immunocytochemistry techniques. The choice of γ-H2AX as the marker for DNA double-strand breaks was deliberate and grounded in its established significance in radiobiology. γ-H2AX is a phosphorylated form of the histone protein H2AX, which becomes rapidly and specifically phosphorylated at the sites of DNA double-strand breaks induced by ionising radiation. This phosphorylation event forms discrete foci within the cell nucleus, making it a reliable and sensitive indicator of DNA damage.

For 2D images, γ-H2AX foci were manually counted to ensure precise evaluation of DNA damage. Cells were imaged under 100X magnification using a fluorescence microscope, and the γ-H2AX foci appeared as distinct bright spots within the nuclei, corresponding to sites of DNA damage. Each cell was assessed individually, and the total number of foci per nucleus was counted manually.

For 3D datasets, the quantification of γ-H2AX foci was performed using Fiji. The 3D stacks of z-sections were imported into Fiji, and γ-H2AX foci were detected using the software's automated segmentation tools "3D Objects Counter" plugins. The segmentation was carefully calibrated to detect foci based on intensity thresholds, ensuring that only true foci were counted while excluding background noise.

## 3.9 STATISTICAL ANALYSIS

The statistical analysis in this study was tailored to suit the distribution and nature of the experimental data. Different tests were used based on the data characteristics and the specific research questions being addressed.

### 3.9.1 Normality Assessment: Shapiro-Wilk Test

Before selecting appropriate statistical tests, it was crucial to determine the distribution of the data. The Shapiro-Wilk test was employed for this purpose. This test is particularly suitable for small to medium-sized datasets and effectively detects departures from normality. A significance level of $p < 0.05$ was used to determine non-normality.

### 3.9.2 Non-Parametric Test: Kruskal-Wallis Test

Given the non-normally distributed data, as confirmed by the Shapiro-Wilk test, the Kruskal-Wallis test was employed for analysis. This non-parametric test was used instead of one-way ANOVA when the data did not meet the normality assumption. It is ideal for comparing medians across more than two groups.

### 3.9.3 Parametric Tests: One-Way ANOVA, Two-Way ANOVA, and Student's t-test

When data is normally distributed, the following parametric tests are utilised:

- One-way ANOVA: Used for comparing the means of more than two independent groups - when exploring a single independent variable.
- Two-Way ANOVA: Employed when there are two independent variables, it's necessary to understand their interaction and individual effects on the dependent variable.
- Student's t-test: Utilized to compare the means of two independent groups. It is appropriate when the study involves only two groups or conditions.

### 3.9.4 Significance Threshold

In this study, the threshold for statistical significance was set at $p < 0.05$, reflecting a standard convention in statistical analysis that the probability of the observed results occurring by chance is less than 5%. To communicate the levels of statistical significance in the results, the following notation was used: * for $p \leq 0.05$, indicating moderate significance; ** for $p \leq 0.01$, denoting high significance; *** for $p \leq 0.001$, signifying very high significance; and **** for $p \leq 0.0001$, representing extremely high significance.

# Chapter 4 -

# Investigating Mechanotransduction: Cardiomyocyte Responses to Simulated Microgravity and Radiation In 2D

## 4.1 INTRODUCTION

This chapter investigates cardiomyocyte cellular responses under simulated microgravity (s-μG) and radiation (IR) within a two-dimensional (2D) environment. Utilising a 2D environment for preliminary studies provides a simplified and controlled model that is pivotal for dissecting the basic mechanisms of cellular responses before advancing to more intricate three-dimensional (3D) cultures or *in vivo* models. This approach is instrumental in optimising experimental methods to facilitate the simulation and assessment of s-μG and radiation effects on cardiomyocytes. The simplified nature of 2D cultures allows for clearer observations of changes in cellular morphology, gene expression, and other stress responses compared to the complex variables introduced by 3D models (Murphy & Atala, 2014; Z. Wang et al., 2018)

Cardiomyocytes respond to abnormal environmental conditions like those simulated in this study by undergoing various adaptive changes. These responses may include alterations in gene expression patterns, changes in cell morphology, adjustments in metabolic activity, and variations of signalling pathways involved in cell survival and function. Mechanotransduction pathways enable cardiomyocytes to sense and respond to mechanical forces like those experienced under microgravity and radiation, regulating essential cellular functions such as growth, differentiation, and remodelling. (Ingber, 2006)

## 4.2 AIM AND OBJECTIVES

This chapter focused on Aim 1, which seeks to elucidate the fundamental cellular mechanisms and responses to environmental stressors, contributing valuable insights to space medicine and cellular mechanobiology. The objectives were designed to comprehensively assess changes in proliferation, viability, gene expression, DNA damage, and mechanotransduction in 2D cultures under s-μG, IR, and their combined effects.

Aim 1: To Sequentially and Comprehensively Evaluate Cardiomyocyte Responses Under Simulated Microgravity, Radiation, and Their Combined Impact Exposure in a 2D Environment.

Objectives for Aim 1:

1. To characterise the response of cardiomyocytes to s-μG by evaluating its effects on cardiomyocyte proliferation, viability, and gene expression changes, providing a foundational understanding of how cells adapt to microgravity conditions.
2. To define the response of cardiomyocytes to IR by characterising their dose-dependent response to IR, focusing on DNA damage and repair mechanisms, using γH2AX as a biomarker to understand the extent and dynamics of DNA repair processes.
3. To investigate the combined effects of s-μG and IR on cardiomyocytes by leveraging the foundational insights from Objectives 1 and 2 to evaluate alterations in proliferation, viability, gene expression, and DNA damage when cells are subjected to both stressors concurrently.
4. To examine mechanotransduction pathways and morphological changes in cardiomyocytes under the combined influence of s-μG and IR, specifically focusing on YAP translocation between the nucleus and cytoplasm and the resulting cellular morphological adaptations.

## 4.3 METHODS

This section presents the methods employed to systematically investigate AC-16 cardiomyocytes' responses to s-μG and IR stressors within a 2D environment, describing a structured approach that aligns with the research aims and objectives - illustrated in Figure 4.1.

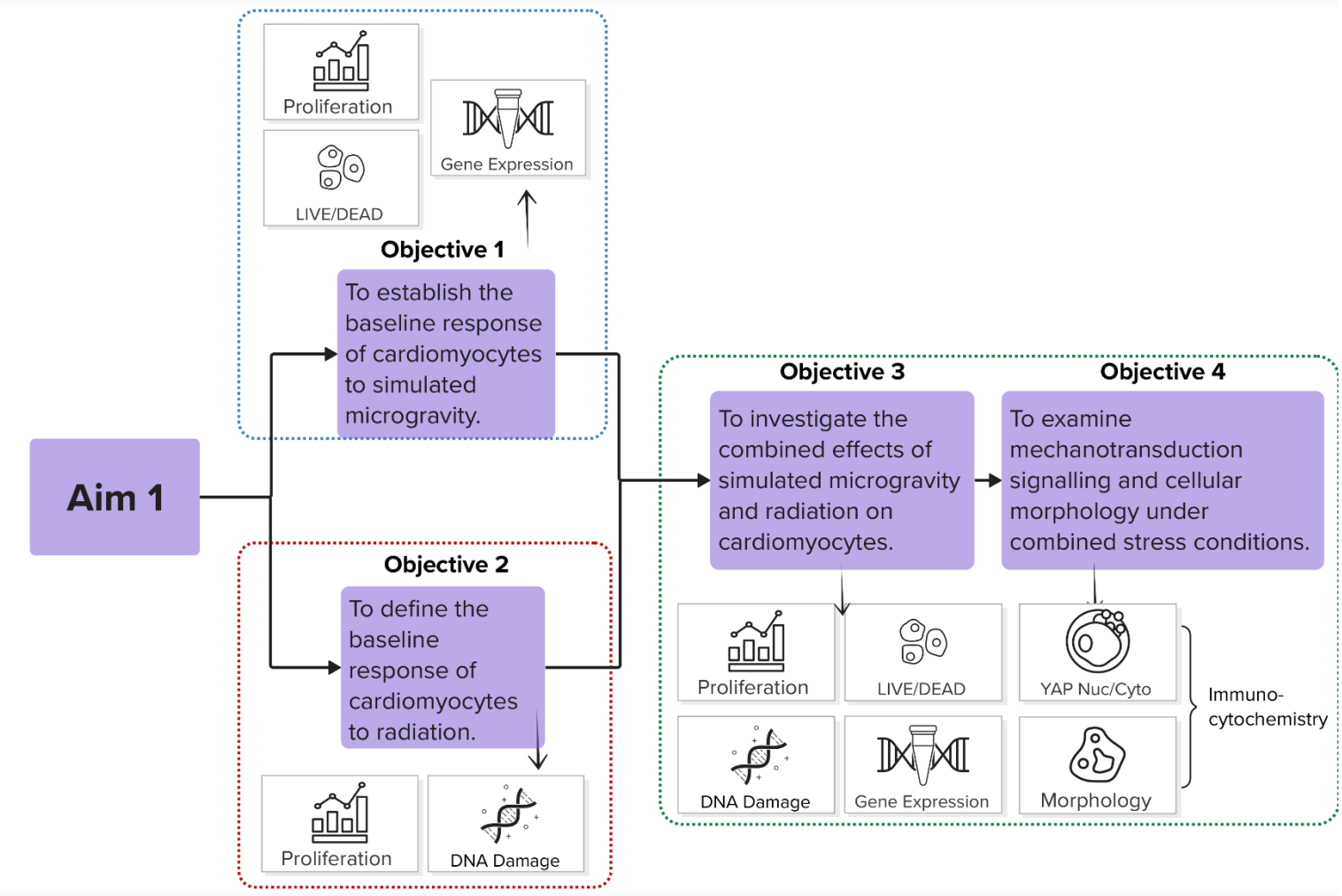


*Figure 4.1 Flow Chart Illustrating Methods Utilised in this Chapter that Corresponds to the Objectives.*

### 4.3.1 Characterization of Cardiomyocytes Proliferative Capacity

This experiment was designed to characterise the impact of s-μG, IR, and their combination on the proliferative capacity of cardiomyocytes – using a resazurin-based assay PrestoBlue™ Cell Viability Reagent, as detailed in Section 3.6.1. The experimental setup and timeline for characterising the proliferative capacity of cardiomyocytes for each exposure condition are described below and summarised in Table 4.1

*Table 4.1 Summary of 2D Proliferation Experiments on AC-16 Cardiomyocytes. This table summarises the 2D proliferation experiments conducted to evaluate the effects of varying s-μG exposure durations and IR doses on AC-16 cardiomyocyte proliferation.*

| 2D Proliferation Experiment Summary | | | |
|---|---|---|---|
| | **Exposure to s-μG** | **Radiation Dose** | **Combination of s-μG and IR** |
| **Experimental Conditions (Independent Variables)** | 6 hours of s-μG exposure<br>24 hours of s-μG exposure<br>48 hours of s-μG exposure<br>72 hours of s-μG exposure | 0Gy 0.5Gy 1Gy<br>2Gy 3Gy 4Gy<br>5Gy 6Gy 8Gy<br>10G 12Gy | Static control: 0Gy 1Gy 2Gy 4Gy 6Gy<br>s-μG treated: 0Gy 1Gy 2Gy 4Gy 6Gy |
| **Cell Numbers (Independent Variables)** | 625 cells per well<br>1250 cells per well<br>2500 cells per well<br>5000 cells per well | | 625 cells per well<br>1250 cells per well<br>2500 cells per well |
| **Observed Timepoint (Independent Variables)** | Start of the experiment (time 0)<br>6 hours following initial mounting on RPM<br>24 hours following initial mounting on RPM<br>48 hours following initial mounting on RPM<br>72 hours following initial mounting on RPM | 24 hours post-irradiation<br>96 hours post-irradiation<br>120 hours post-irradiation<br>144 hours post-irradiation<br>168 hours post-irradiation | 96 hours following initial mounting on RPM.<br>72 hours post-irradiation |

From the obtained RFU, the data were then processed, as described in Section 3.6.1. The processed data were then subjected to two-way ANOVA statistical analysis to compare multiple groups, ensuring the identification of statistically significant differences in proliferation under various conditions. In cases where significant differences were observed, Dunnet's post-hoc tests were utilised to identify specific duration-dependent effects.

#### *4.3.1.1 Simulated Microgravity*

For the initial characterisation of cells responses to s-μG, AC-16 human cardiomyocytes cells were seeded in 96-well plates at concentrations ranging from 625 to 5000 cells per well and cultured overnight at 37 ° C and 5% (v/v) $CO_2$ to allow attachment. Additional wells within the same 96-well plates were filled solely with media serving as controls for any background noise during the subsequent proliferation assay. These control wells are commonly referred to as "blank" wells. The exposure of cells to s-μG was then executed following the procedures detailed in Section 3.5.2. Following the preparation and sealing to facilitate exposure to the RPM, the approach outlined in Section 3.5.2.4 was followed. Subsequently, the 96-well plates were affixed to a metal plate and secured using loops to secure them onto the RPM. Following each specified exposure period, the PrestoBlue™ Cell Viability Reagent was employed to determine the proliferative capacity of the AC-16 cardiomyocytes, as outlined in section 3.6.1.

#### *4.3.1.2 Irradiation*

The initial characterisation of the radiation dose response of AC-16 cardiomyocytes involved the exposure of cells to a range of X-ray radiation doses using the X-RAD 320 biological irradiator. Cells were exposed to radiation doses between 0.5 Gy and 12 Gy, as outlined in Table 4.4.3.1. The primary objective of this experiment was to ascertain how AC-16 cardiomyocytes respond to varying radiation doses and to identify the specific dose levels that result in significant differences in the observed outcomes.

In this experiment, a separate flask was used for each radiation dose, and the flasks were irradiated individually with a dose rate of 100 cGy/minute. After IR, the cell monolayer of each flask was trypsinised. The cell was counted (Section 3.5.1.3 and Section 3.5.1.4), and 2500 cells/mL suspension was obtained for each flask and radiation dose. To seed the cells for further analysis, 200 μL of the cell suspension was dispensed into each well of a 96-well plate, resulting in a final concentration of 500 cells per well. For the assessment at each designated time point, one 96-well plate was allocated. The radiation dose response of AC-16 cardiomyocytes was evaluated over one week, with measurements taken at specific intervals—namely, at 24 hours, 96 hours, 120 hours, 144 hours, and 168 hours post-IR. These measurements were conducted using the PrestoBlue™ Cell Viability Reagent, as outlined in Section 3.6.1 of Chapter 3.

The resulting RFU were plotted against time (hours) to quantify the proliferation rates and growth of AC-16 cardiomyocytes after irradiation. A timepoint was selected from these data in which all treatments were as close to an exponential growth phase as possible (i.e., 144 h), and the RFU

replotted against log dose (Gy), with 95% CIs. The lethal dose, 50% (LD50), was determined by fitting a sigmoidal log-inhibitor versus response model to these data.

#### *4.3.1.3 Combination of Simulated Microgravity and Irradiation*

This experiment investigated the combined effects of s-μG and varying radiation doses on AC-16 cardiomyocyte proliferation. It was designed to determine if the combination of s-μG and different radiation doses results in observable differences in cell proliferation. Adjustments were made to the timeline based on findings from initial experiments focusing on individual exposure variables described in Section 3.5.2.3. Based on initial dose-response findings, a smaller radiation dose range of 0 Gy to 6 Gy was selected for its effectiveness in experiments combining s-μG and IR.

Cells at varying densities were seeded in a 96-well strip plate featuring 12 individual strip columns of eight rows each. As these strips were detachable, six strips of eight wells were placed on a static control plate, while the other six strips of eight were put on another well plate. The plate intended for s-μG and IR were subsequently attached to a metal plate and fastened onto the RPM by the procedure described in Section 3.5.2.4. After 24 hours of acclimatisation to s-μG conditions for the cells on the RPM, the cells were irradiated at the respective doses. Post-radiation, the cells were continuously exposed to s-μG or continued as static control for an additional 72 hours, making the total duration to s-μG 96 hours and 72 hours post-IR. At the endpoint, the strips from the static control plate and the RPM-mounted plate were combined back into one plate, as depicted in Figure 4.2. PrestoBlue™ Cell Viability Reagent was then used to assess the proliferation described in section 3.6.1.

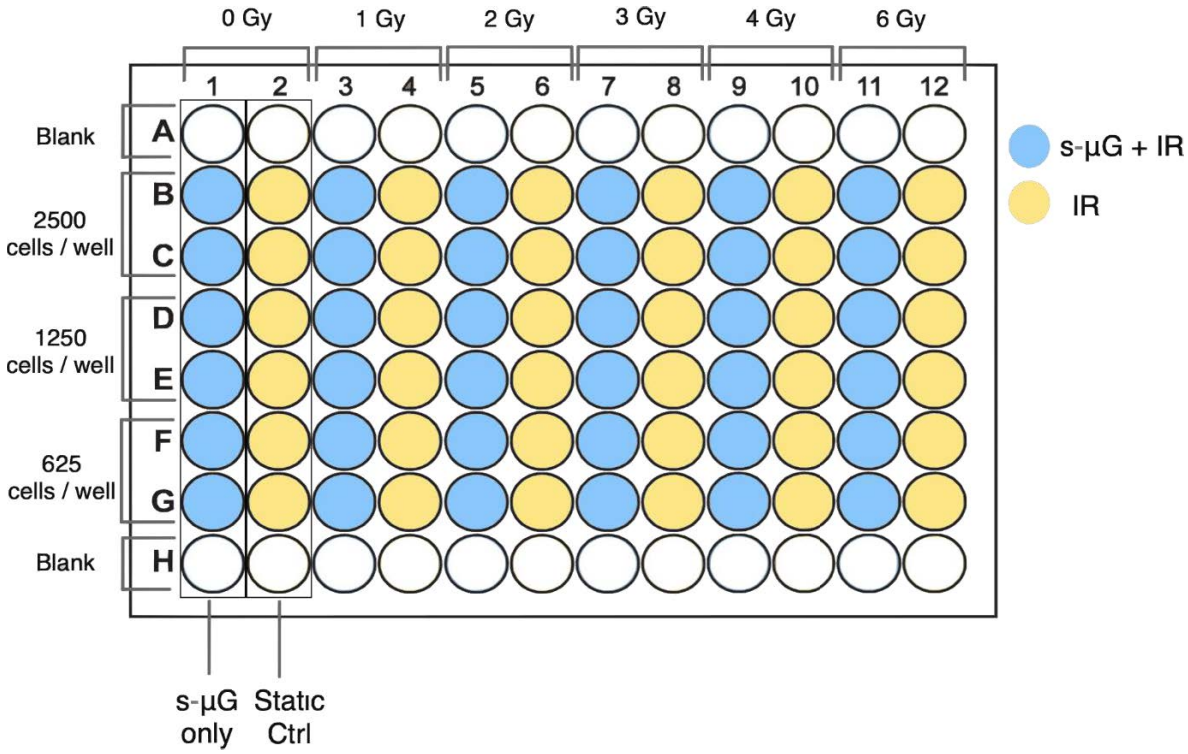


*Figure 4.2 96-Well Plate Layout for 2D Proliferation Assay with s-µG and IR Combination. Each column corresponds to a specific radiation dose, ranging from 0 to 6 Gy, while rows represent different starting cell densities, with the top and bottom rows as blanks. Blue-coloured wells indicate cells treated with both s-µG and IR, and yellow-coloured wells represent cells treated with IR only. The static control (Ctrl) is displayed in the first two columns, where cells were not subjected to either IR or s-µG, providing a reference point for treatment effects.*

### 4.3.2 Cardiomyocytes Viability

In the study of AC-16 cardiomyocyte responses to s-µG, a comprehensive investigation was conducted to determine whether changes in proliferative capabilities were due to altered cellular functions or cell death. To differentiate between live and dead cells, the LIVE/DEAD assay was employed, with subsequent capture of fluorescent images for detailed analysis (Section 3.6.2).

Initial experiments assessed cell viability over 0, 6, 24, 48, and 72 hours under s-µG conditions. Subsequently, a combination of s-µG and IR exposure used a more specified and relevant radiation dose (2Gy) at the 72-hour point only. A summary of experiments used to assess viability is described in Table 4.2. The procedure described in section 3.6.2 was followed at each assessment time point to evaluate cell viability using the Live/Dead assay. The images obtained were analysed with FIJI (ImageJ) software alongside a customised macro (detailed in Appendix B) designed for batch image processing.

*Table 4.2 Summary of 2D Viability Experiments on AC-16 Cardiomyocytes. This table summarises the viability experiments conducted to assess the effects of s-μG and s-μG + IR exposure on AC-16 cardiomyocytes.*

| 2D Viability Experiment Summary | | | | |
|---|---|---|---|---|
| **Experimental Conditions (Independent Variables)** | **Duration of exposure to s-μG** | **Combination of s-μG and IR** | | |
| | 6 hours of s-μG exposure<br>24 hours of s-μG exposure<br>48 hours of s-μG exposure<br>72 hours of s-μG exposure | Static control | 0Gy | 2Gy |
| | | s-μG conditions | 0Gy | 2Gy |
| **Observed Time (Independent Variables)** | Start of the experiment (time 0)<br>6 hours following initial mounting on RPM<br>24 hours following initial mounting on RPM<br>48 hours following initial mounting on RPM<br>72 hours following initial mounting on RPM | 72 hours post-irradiation | | |

The processed data were then subjected to Kruskal-Wallis statistical of cell viability variations chosen due to non-normally distributed data confirmed by Shapiro-Wilk tests. In cases where significant differences were observed, Dunn's multiple comparisons tests were utilised to identify specific differences in conditions.

### 4.3.3 Cardiac Gene Expression using RT-QPCR

In the exploration of cardiac mechanotransduction, experiments were focused on evaluating the expression of genetic markers responsive to mechanical stimuli. RT-qPCR analysis was employed to facilitate the detection and amplification of RNA. The genes are listed in Table 3.6.1. Corresponding primer sequences for these genes are detailed in Table 3.6.2 for reference.

Cells were seeded in T25 flasks filled to capacity to mitigate the impact of shear stress on the cells from the media during rotation on the RPM. Initially, the study explored varied durations of s-μG to comprehend alterations in gene expression under this singular stressor. The initial phase concentrated solely on s-μG and investigated the impact of different exposure periods: 0 hours, 6 hours, 24 hours, 48 hours, and 72 hours. Subsequently, the investigation integrated radiation exposure within the established 72-hour exposure period to understand the combined effects (with and without radiation) of these stressors on gene expression patterns and cellular responses. A total s-μG exposure period of 72 hours and 48 hours post-IR was investigated following a modified timeline to incorporate the 24 hours of s-μG adaptation (Section 3.5.2.4)

The methods in Section 3.6.3.2 were followed to prepare the samples for RT-qPCR. Briefly, at the desired time of investigation, the samples were lysed, and lysates were stored at -80°C. RNA was

extracted using the RNeasy Mini Kit, and the quality and quantity of RNA was determined and then reverse transcribed into cDNA at a 25 ng/uL concentration using the iScript™ cDNA Synthesis Kit. RT-qPCR was subsequently performed using SYBR Green PCR Master Mix. Gene expressions were expressed as log2 fold change for quantification and visualisation. Statistical evaluation of gene expression changes over time, comparing conditions of s-μG and the static control, was carried out using two-way ANOVA with Šídák's multiple comparisons tests or Tukey's test multiple comparisons. The analysis was conducted using ΔΔCt values to mitigate biases associated with log-transformed data.

### 4.3.4 Assessing DNA Damage and DNA Strand Breaks Repair Time

DNA damage protein H2AX expression was analysed using ICC techniques described in Section 3.6.4. Briefly, cells were seeded on 13mm coverslips and incubated at 37°C in 5% (v/v) $CO_2$ in air to attach overnight. For the initial assessment of IR on its own, cells underwent radiation exposure the following day at a dose of 2Gy to induce DNA damage. For experiments focusing on the combination of s-μG and IR, the cells were irradiated following 24 hours of s-μG adjustment period. This allowed the cells to adapt to the microgravity effect before irradiation.

For all experiments, cells were fixed at 10 minutes, 1 hour, 4 hours, and 24 hours to capture the temporal aspect of DNA damage response. A non-irradiated control (0Gy/0-hour) was included to provide a reference for comparison. The cells were subjected to a detailed ICC protocol at each time point (Section 3.6.4). This included fixation with 4% (v/v) PFA for 10 minutes at room temperature. The coverslips were washed with PBS and stored in PBS at 4°C until antibody labelling was performed. Once all the required time points were acquired, the cells were permeabilised with 0.5% (v/v) TritonX-100 for 3 minutes and then washed with PBS twice at room temperature. Coverslips were then incubated with 30uL of γH2AX (1:800) primary antibody diluted in 4% (w/v) BSA in PBS blocking buffer for approximately 45 minutes at 37°C. AlexaFluor488 Goat anti-Mouse (1:100) diluted in 4% (w/v) BSA was used as a secondary antibody and incubated with cells for approximately 25 minutes at 37°C. After the labelling, coverslips were washed with PBS twice at room temperature, dried by dabbing it on kimwipes to remove excess liquid, and mounted onto glass slides with ProLong Diamond Anti-Fade with DAPI for nuclear counterstaining. Slides were stored at 4°C until imaged using an Olympus D73 fluorescent microscope. For each time point, stained cell foci from at least 50 cells were counted from randomly chosen FOV. These were then averaged to indicate the severity of DNA damage experienced by the cells.

Statistical data analysis involved two-way ANOVA and post-hoc analyses using Sidak's multiple comparisons test.

### 4.3.5 Assessing Mechanotransduction Response via Immunocytochemistry

ICC was employed to identify and quantify alterations in the expression and localisation of key mechanotransduction components to determine any changes in cellular function, particularly in mechanotransduction pathways (as specified in Chapter 3, Section 3.6.4).

The experimental setup for 2D experiments involved affixing 13mm round coverslips to the bottom of a 24-well plate. Prior to use, coverslips were cleaned and sterilised through immersion in ethanol, followed by air-drying in a sterile environment. High-vacuum silicone grease was delicately applied onto the bottom surface of the coverslips to create a thin, even layer and gently placed onto 24-well plates (one coverslip for each well) using sterile forceps, ensuring proper adhesion and the absence of excess grease beyond the coverslip edges. This method provided a secure attachment of the coverslips whilst exposing them to s-μG and IR. Cells were seeded on the coverslips at 10,000 cells/ well and allowed to attach overnight. The following day, the set-up to mount on the RPM was followed (Section 3.5.2.4)

During each designated assessment interval, cells were first fixed using a 4% (v/v) PFA solution for 20 minutes at room temperature. Following fixation, the cells were permeabilised with a 0.5% (v/v) Triton X-100 solution in PBS for 20 minutes. Subsequently, a blocking step was carried out using a 1% (w/v) BSA solution in PBS, in which the cells were immersed for one hour at room temperature. After blocking, the cells were incubated with 50uL of primary antibodies concurrently targeting YAP1 (1:200) diluted in 1% (w/v) BSA. This incubation occurred overnight at 4°C. Post-primary antibody incubation, the coverslips with adherent cells were washed three times with PBS to remove unbound antibodies and then incubated with Anti-Rabbit Alexa Fluor 488 (1:200) fluorescently labelled secondary antibodies diluted in 1% (w/v) BSA. Further to antibody staining, the cells on the coverslips were stained with iFluor 594 Phalloidin (1:1000) for F-Actin visualisation and DAPI (1:1000) for nuclear counterstaining. Incubation with iFluor 594 Phalloidin and DAPI was conducted at room temperature for 20 minutes and 10 minutes, respectively. The mounting procedure described in Chapter 3.6.4 was followed to prepare the coverslips for imaging.

Slides were imaged using a DV Elite widefield fluorescent microscope and a 60X oil objective. This provided qualitative and quantitative results to investigate the difference in expression between the effect of s-μG and IR. Quantitatively, the experiment involved measuring the intensity of YAP staining in the nucleus and in the cytoplasm to determine its nucleus-to-cytoplasm ratio for each cell. Additionally, utilising F-actin and DAPI staining as masks, changes in cellular morphology were quantified to shape descriptors.

Image processing included background subtraction and intensity normalisation across experimental sets to ensure consistency in the fluorescence signals. The detailed quantitative analysis of YAP localisation and cellular morphology is provided in the Section 3.8.

### 4.3.6 Summary

Graphical summaries of the experimental timelines followed in this study are illustrated below in Figure 4.3, Figure 4.4 and Figure 4.5. These figures collectively encapsulate the methodical sequence of events and the investigative scope of the study, offering a visual summary of the experimental approaches undertaken to analyse the cellular responses of cardiomyocytes to spaceflight-relevant stressors.

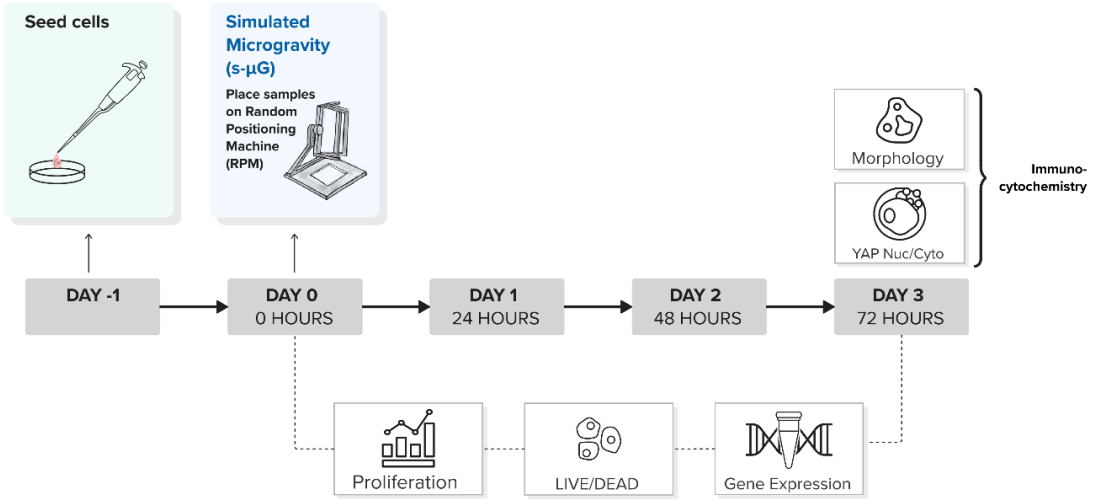


*Figure 4.3 Experimental Timeline for Assessing s-µG Effects on Cardiomyocytes. The timeline outlines the sequence from cell seeding to subsequent analyses at specified time points.*

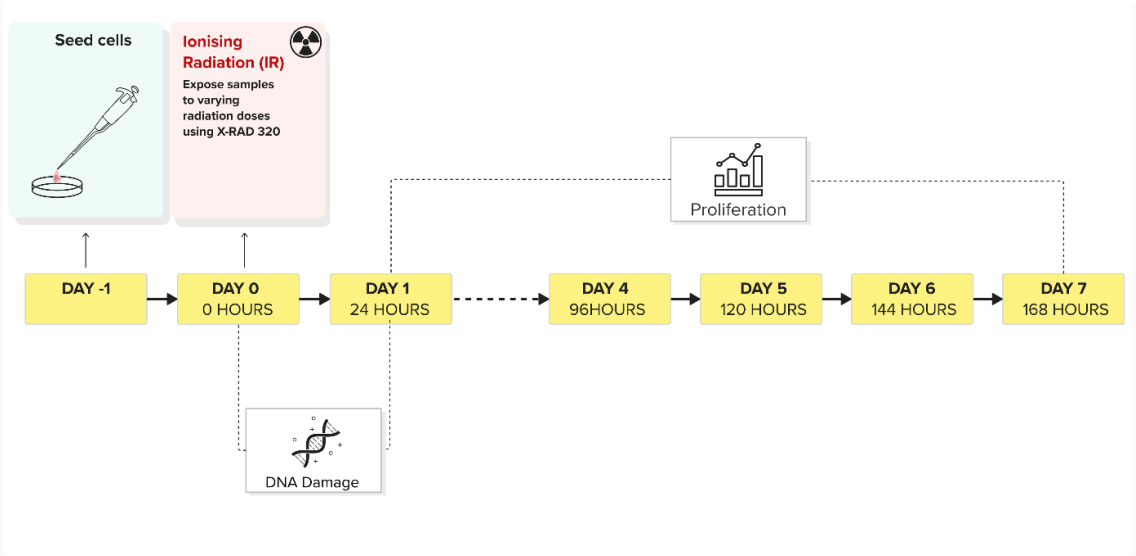


*Figure 4.4 IR Exposure Experimental Timeline for Proliferation and DNA Integrity Analysis. This timeline charts the procedure from cell seeding to DNA damage assessment at early time points, followed by proliferation evaluation over a 7-day period.*

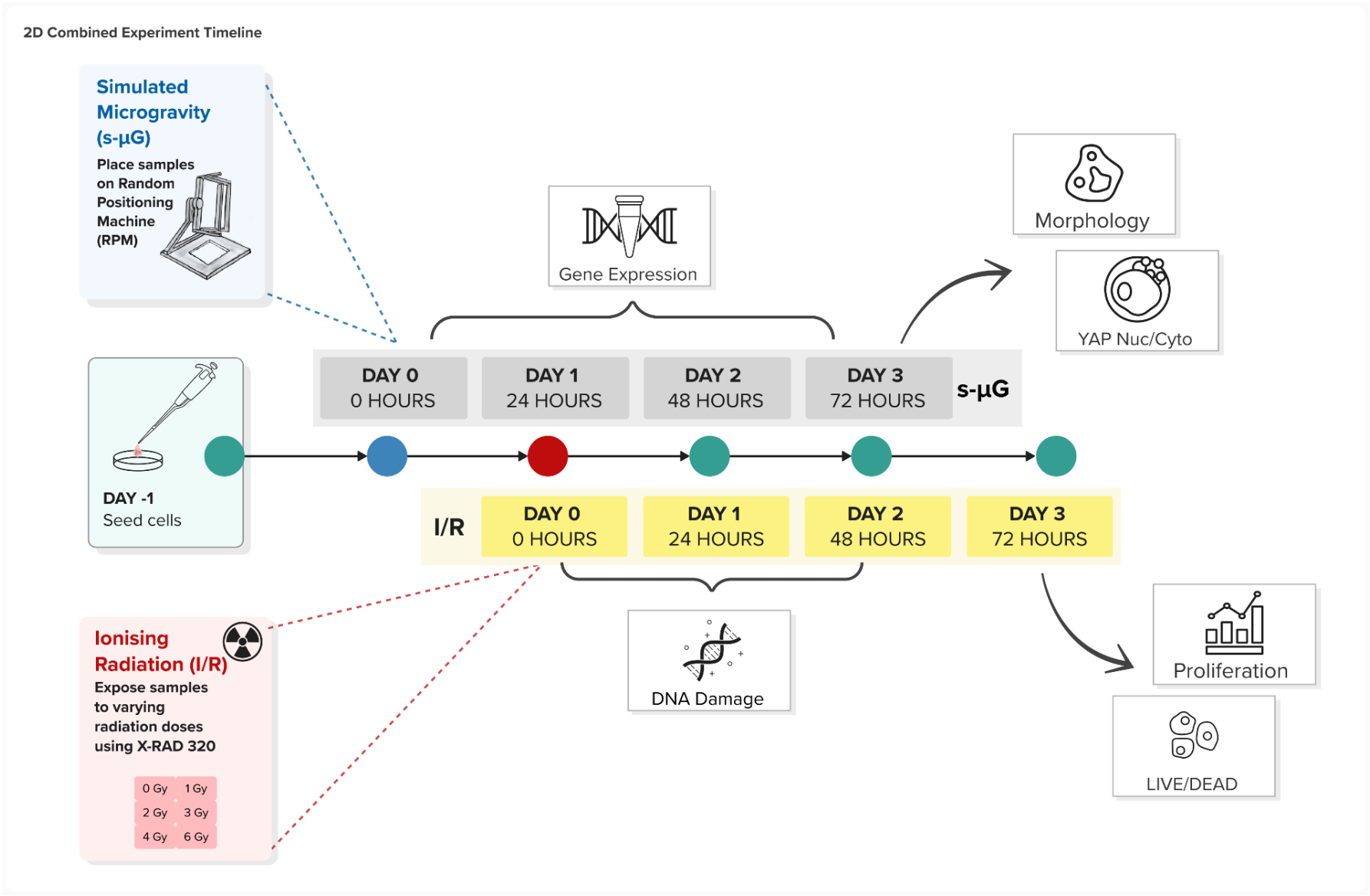


*Figure 4.5 Combined Experimental Timeline for AC-16 Cardiomyocyte Exposure to s-µG and IR. This timeline illustrates the sequential exposure of AC-16 cardiomyocytes to s-µG and IR, detailing key experimental stages and time points. This figure integrates the protocols from Figures 4.3-5 and 4.3-6, depicting a holistic approach to analysing the effects of combined stressors on cellular responses.*

## 4.4 RESULTS

### 4.4.1 Simulated Microgravity Alters Proliferation Rates of AC-16 Cardiomyocytes Across Various Seeding Densities

The first experiment to assess the response of AC-16 human cardiomyocytes to s-μG was to discern the impact of microgravity on the cells' proliferative capabilities. AC-16 human cardiomyocytes were seeded at densities of 625, 1250, 2500, and 5000 cells per well in a 96-well plate. Their proliferation was measured over 72 hours at 6, 24, 48, and 72 hours after placing it on the RPM, as described in Section 3.5.2.1. Utilising the PrestoBlue assay, the proliferation data was measured and blank subtracted, subsequently referred to as Corrected RFU.

In the proliferation study under s-μG, data from the 625 and 1250 cells per well densities were not presented in the main results due to technical limitations in discerning true biological responses from background fluctuations. The control wells at these densities exhibited a flat growth pattern, failing to demonstrate the expected increase in cell numbers over time. This suggests that the recorded activity might predominantly be background noise. Consequently, these data have been omitted from the main analysis to avoid misinterpretation of the results. To determine if there was a significant difference in the rate of cell proliferation between s-μG and control, the slopes of the linear regression lines was compared, and the corresponding regression analysis are shown in Table 4.3 and Table 4.4. Figure 4.6 depicts the resulting proliferation rates under s-μG for 5000 and 2500 cells per well.

*Table 4.3 Regression Analysis Results for 5000 Cells/Well. Note: Values in parentheses represent 95% confidence intervals.*

| Parameter | Ctrl | s-μG |
|---|---|---|
| **Y-Intercept** | 606.5 (95% CI: 27.06 to 1186) | 905.0 (95% CI: 584.8 to 1225) |
| **Slope** | 15.72 (95% CI: 1.325 to 30.12) | -5.828 (95% CI: -13.78 to 2.127) |
| **R-squared** | 0.8010 | 0.6444 |
| **Degrees of Freedom** | 3 | 3 |

*Table 4.4 Regression Analysis Results for 2500 Cells/Well. Note: Values in parentheses represent 95% confidence intervals.*

| Parameter | Ctrl | s-μG |
|---|---|---|
| **Y-Intercept** | 376.8 (95% CI: 95.83 to 657.7) | 460.4 (95% CI: 138.8 to 782.1) |
| **Slope** | 7.543 (95% CI: 0.5627 to 14.52) | 3.180 (95% CI: -4.812 to 11.17) |
| **R-squared** | 0.7977 | 0.3483 |
| **Degrees of Freedom** | 3 | 3 |

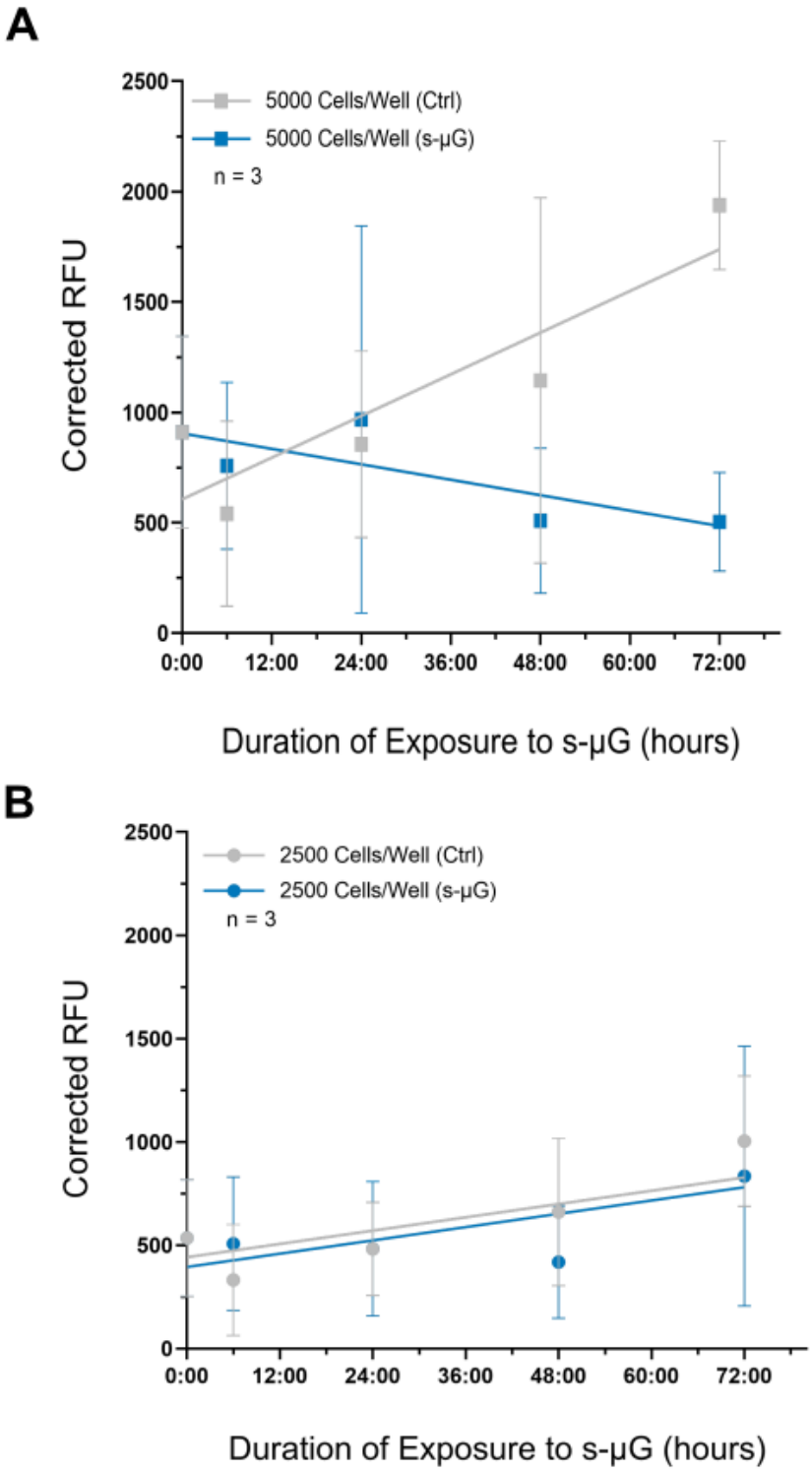


*Figure 4.6 Proliferation Rates of AC-16 Cardiomyocytes Under s-µG vs. Ctrl. Proliferation of AC-16 cardiomyocytes in 2D cultures, quantified using the PrestoBlue assay and background corrected, is expressed in Corrected RFU for (A) 5000 cells per well and (B) 2500 cells per well initial seeding density. Error bars, representing SD, are based on N = 3 biological replicates. Solid lines indicate the linear regression fits for each group. Statistical analyses were performed using regression analysis to compare slope differences between conditions (Table 4.3 and Table 4.4).*

The analysis for 5000 cells/well demonstrated a significant difference in the slopes of the regression lines between the control and s-µG groups, as indicated by a p=0.0059. The positive slope for the

control group (15.72) suggests an increase in cell proliferation over time, while the negative slope for the s-μG group (-5.828) indicates a decrease in cell proliferation. This suggests that exposure to s-μG has a suppressive effect on cell proliferation compared to the control condition.

For 2500 cells/well, p=0.2386 indicates no significant difference in the slopes between the control and s-μG groups. Both groups have positive slopes (7.543 for Control and 3.180 for s-μG), suggesting that cell proliferation increases over time under both conditions. The slopes are relatively similar, implying that exposure to s-μG does not significantly affect the proliferation rate at this cell density.

### 4.4.2 AC-16 Cardiomyocyte Viability Remains High Under Simulated Microgravity Despite Proliferation Changes

In examining AC-16 cardiomyocyte responses to s-μG, cell viability was assessed to determine if changes in proliferative capabilities resulted from altered cellular function or increased cell death. Viability was assessed using the LIVE/DEAD cell viability assay, measuring the proportion of live and dead cells at 6, 24, 48, and 72 hours following s-μG exposure, with an initial cell seeding density set at 2500 cells per well. The LIVE/DEAD assay procedure in Section 3.6.2 was followed at each time point to obtain qualitative images and quantitative % of cell viability.

Initial qualitative observations of the AC-16 human cardiomyocytes at 6, 24, 48, and 72 hours following s-μG showed diminished cell densities and altered distribution patterns over time in the cells treated with s-μG (Figure 4.7A) demonstrated by the number of live cells (green fluorescence). The qualitative observation also showed that the quantity of dead cells (red fluorescence) remained relatively constant in both the static control and s-μG treated groups.

The Kruskal-Wallis uncovered statistically significant differences ($p < 0.0001$) between time, pointing to the impact of s-μG on cell viability over the duration of the experiment. Post-hoc analysis using Dunn's multiple comparisons test assessed changes in cell viability at post-treatment intervals (6h, 24h, 48h, and 72h) compared to time 0 to determine the periods during which statistical significance was observed. While no significant alterations in cell viability were detected earlier, a significant reduction was observed 72 hours post-treatment (p=0.0084), where the mean relative viability decreased to 75.9%.

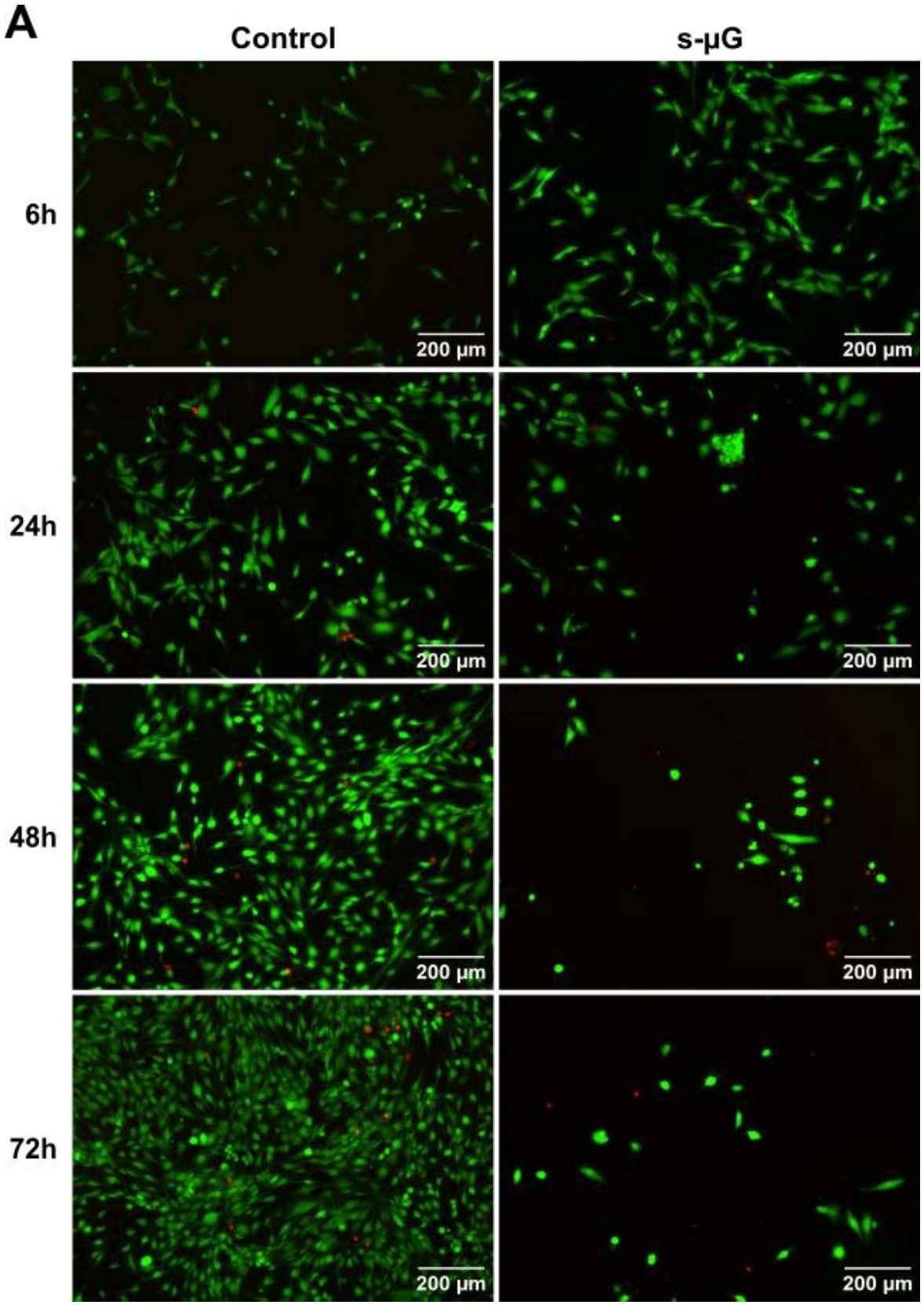


*Figure 4.7A Representative Immunofluorescence Images of AC-16 Cardiomyocyte Viability under s-µG Conditions. Immunofluorescence images show the viability of AC-16 cells under control and s-µG conditions at 6, 24, 48, and 72 hours. The LIVE/DEAD assay labelled cells with 1 µM calcein-AM for live cells and 4 µM Propidium Iodide for dead cells. Images were captured using an EVOS FL microscope with a 20X objective and processed. Cells in the GFP channel (green) were counted as live cells, and those in the Texas Red (red) channel were counted as dead cells using a custom macro. The scale bar represents 200 µm.*

**B**

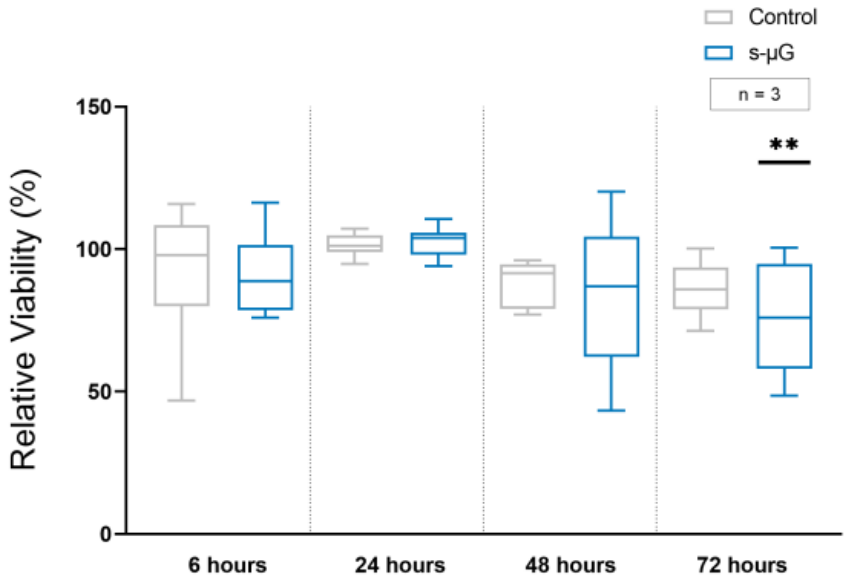


**C**

| Data Analyz | 6h (Ctrl) | 6h (s-µG) | 24h (Ctrl) | 24h (s-µG) | 48h (Ctrl) | 48h (s-µG) | 72h (Ctrl) | 72h (s-µG) | Total |
|---|---|---|---|---|---|---|---|---|---|
| LIVE | 2748 | 2647 | 4818 | 4468 | 5199 | 2374 | 6469 | 1035 | 29758 |
| DEAD | 212 | 221 | 246 | 310 | 1482 | 288 | 654 | 1080 | 4493 |
| Total | 2960 | 2868 | 5064 | 4778 | 6681 | 2662 | 7123 | 2115 | 34251 |

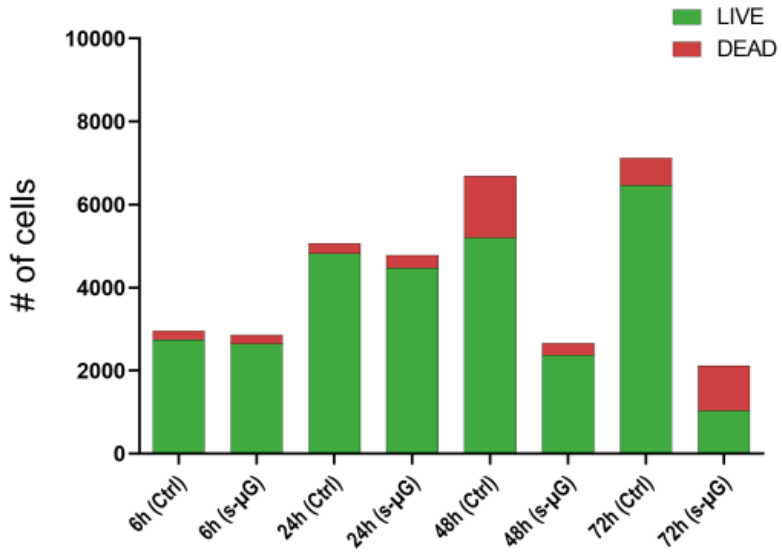


*Figure 4.7(B) Viability (%) of AC-16 Cardiomyocytes in 2D under s-µG Conditions. Relative viability (%) of AC-16 cells over various durations of s-µG exposure, generated from immunofluorescent image assessments (N = 3, FOV > 10) processed with a custom FIJI macro. (C) Cell counts are provided to contextualise the resulting cell density. Viability data for s-µG were normalised to control conditions at each time point, and data were plotted and analysed using GraphPad PRISM. Statistical analysis was performed using the Kruskal-Wallis test, selected due to non-normally distributed data confirmed by Shapiro-Wilk tests ($p < 0.05$). Significant differences among groups were identified, further analysed with Dunn's multiple comparisons test. Significance level: *** ($p \leq 0.001$).*

### 4.4.3 Gene Expression in AC-16 Cardiomyocytes Shows Resilience to Microgravity

Considering the findings on the proliferation and viability of cardiomyocytes under s-μG, a crucial observation emerged. Despite a reduction in proliferative capabilities, overall cell density, and distribution, it became evident that a proportion of the cells remained viable under s-μG conditions. To delve deeper into this alteration in functionality, a comprehensive investigation was conducted into the gene expression profile of the cells. The hypothesis centred around the notion that this functional shift could be attributed to changes in mechanotransduction within the cells. As a primary focus, genes associated with the regulation of developmental processes and responses to mechanical stimuli were examined.

Brightfield microscopy facilitated the observation of AC-16 cardiomyocyte morphology across different durations of exposure to s-μG (Figure 4.8.) Images were taken concurrently with RNA sample collection at intervals of 0, 6, 24, 48, and 72 hours post s-μG application. The images, captured with a 20x objective on an EVOS M5000 microscope, depicted the emergence of cell aggregates, denoted by red arrows, on the samples subjected to s-μG, illustrating the impact of s-μG on cell distribution and density. Furthermore, the cell size/aggregate significantly increased over time under exposure to s-μG. Evidently, from these images, the cells not subjected to s-μG continued proliferating to eventually fill up the FOV over the 72 hours. Acquired before RNA extraction, these images established a morphological reference point corresponding to the subsequent gene expression analysis.

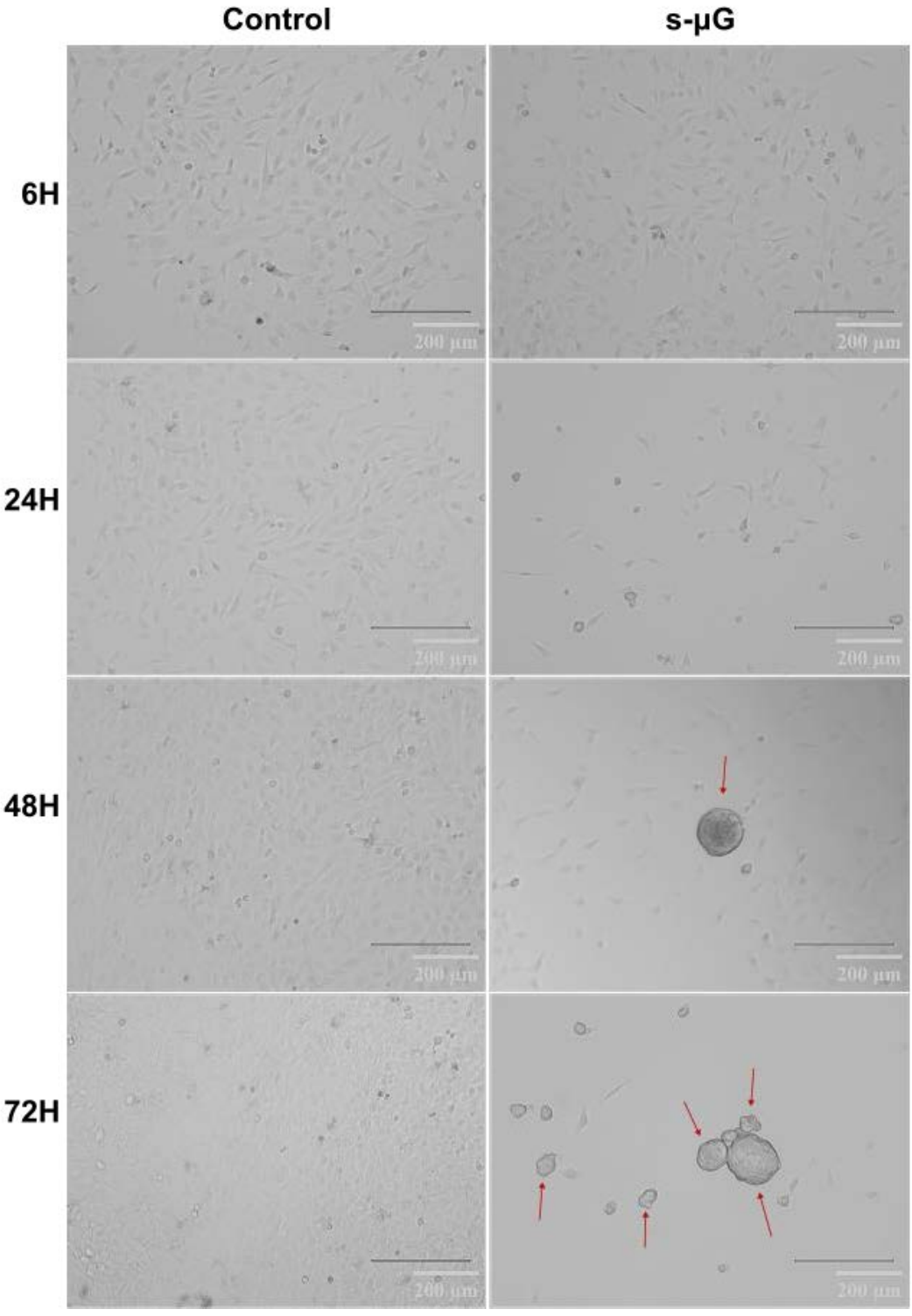


*Figure 4.8 AC-16 Cardiomyocyte Morphological Dynamics Under s-µG at Various Time Points. Brightfield images captured with an EVOS M5000 Imaging System at 20X magnification, illustrating AC-16 cardiomyocyte morphology and distribution in response to s-µG at 0, 6, 24, 48, and 72 hours. Red arrows indicate cell aggregates, highlighting cellular conformation and clustering phenomena under s-µG conditions prior to RNA extraction and gene expression analysis. The scale bar represents 200 µm.*

For gene expression analysis, RT-qPCR was conducted on the cDNA samples employing SYBR Green PCR Master Mix. The gene expression pattern of these genes was visually and statistically

assessed at 6 hours, 24 hours, 48 hours and 72 hours to understand the dynamic response under different experimental conditions. The results were presented as log2 fold change values, with samples compared to the initial measurement at 0 hours (see Section 4.3.3 for more details).

In the assessment of YAP1 expression, no significant differences were detected between s-μG and control groups at any examined time point. The p-values remained above 0.05, reflecting no significant change in gene expression. The expression pattern of Cx43 remained unaltered in response to s-μG when compared to the control across the time series. This was evidenced by overlapping means in dot plots and supported by non-significant p-values from Šídák's test. RHOA gene expression analysis paralleled the trends observed in other genes, with no significant deviations from control conditions noted at any time points, as indicated by the dot plot distribution and supported by the statistical analysis. The expression analysis of RAC2 revealed a consistent pattern with prior genes, with no significant differences in expression levels following s-μG treatment across the time points, as demonstrated by the dot plots and statistical tests. The comparative analysis of CDH2 expression also showed no significant differences between s-μG treated and control samples, with the dot plot means closely aligned across all time points and statistical analysis confirming these observations.

**A**

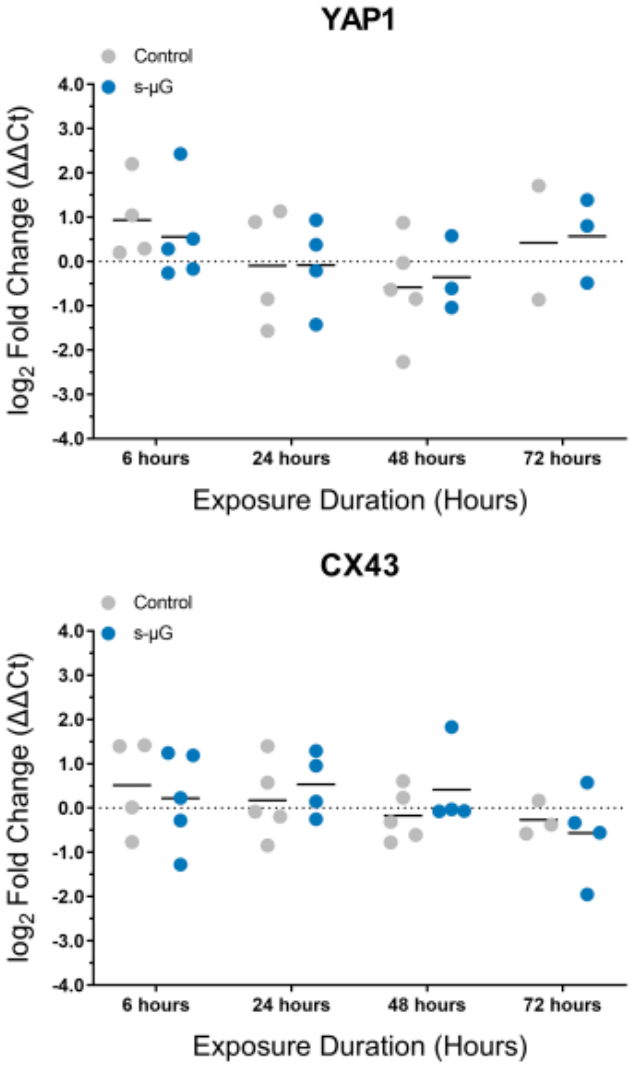
YAP1
Control
s-μG
log2 Fold Change (ΔΔCt)
4.0
3.0
2.0
1.0
0.0
-1.0
-2.0
-3.0
-4.0
6 hours
24 hours
48 hours
72 hours
Exposure Duration (Hours)
CX43
Control
s-μG
log2 Fold Change (ΔΔCt)
4.0
3.0
2.0
1.0
0.0
-1.0
-2.0
-3.0
-4.0
6 hours
24 hours
48 hours
72 hours
Exposure Duration (Hours)

**B**

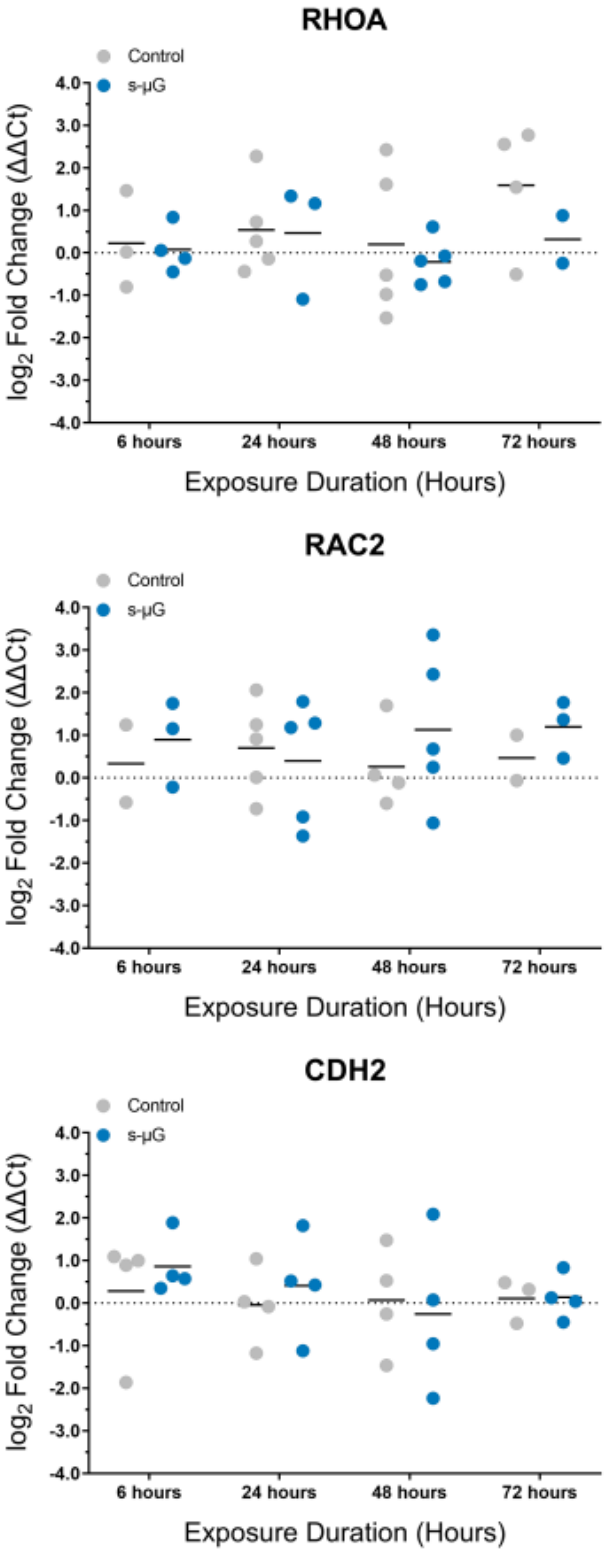


*Figure 4.9 Log2 Fold Change in Gene Expression of AC-16 Cardiomyocytes in 2D. Log2 fold change in gene expression for genes related to (A) signal transduction and communication and (B) cell structure and motility. The x-axis represents exposure durations, and the y-axis indicates gene expression log2 fold change compared to the control group (0-hour, pre-experiment sample). Gene expression fold change was determined using the 2^-ΔΔCt method. Each plotted dot shows the log2 value for individual experiments, with the mean for each group indicated by a solid line. A log2 fold change of 0 (dotted line) represents no change from the initial expression level. Statistical analysis was performed on ΔΔCt values using two-way ANOVA (N = 5) with Šídák's multiple comparisons test.*

### 4.4.4 Radiation Dose-Dependently Influences AC-16 Cardiomyocyte Proliferation

Prior to investigating the combined effects of s-μG and IR, characterisation of AC-16 cardiomyocyte responses to IR alone was necessary. The impact of a range of radiation doses on the proliferation capability of AC-16 cardiomyocytes was investigated over 7 days post-IR, enabling the visualisation of trends in cell proliferation over time and across increasing radiation doses (Figure 4.10). The visual representation did not include significance levels to maintain the clarity and readability of the graph presented in Figure 4.10. For a comprehensive breakdown of statistical analyses, including significance levels, refer to Appendix E - Table 1.

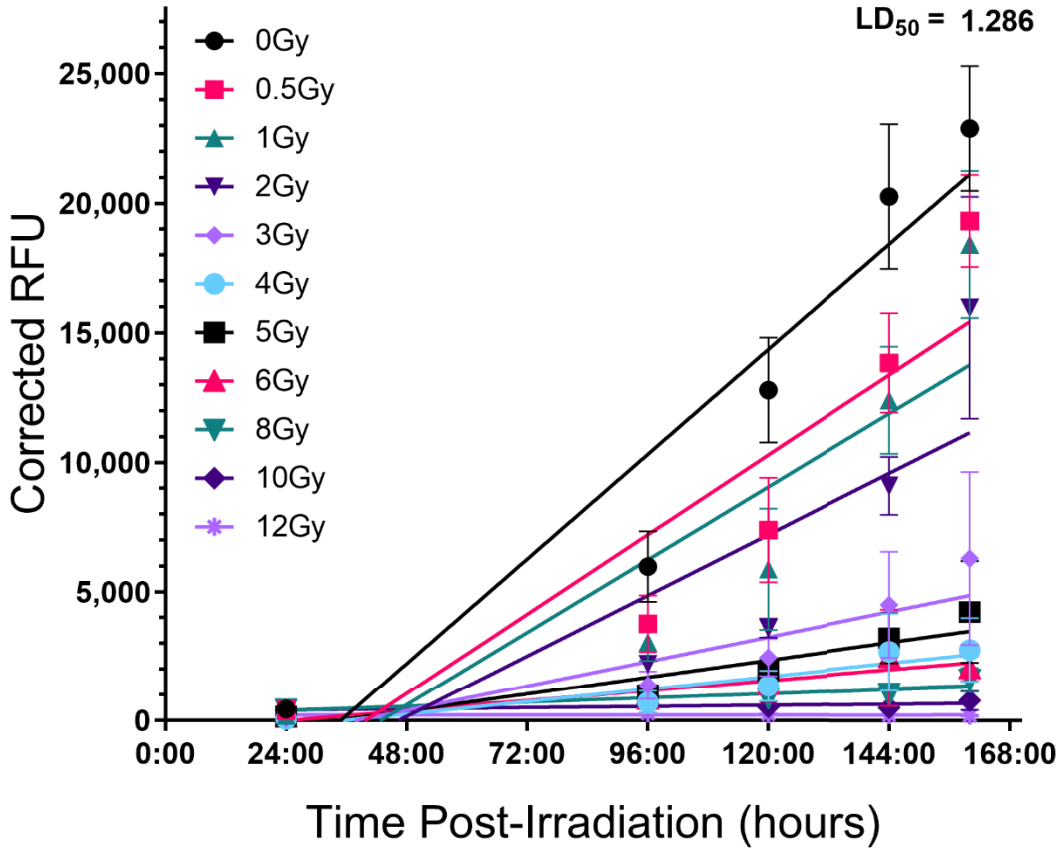


*Figure 4.10 Proliferation of AC-16 Cardiomyocytes Post X-Ray Irradiation. AC-16 cardiomyocytes were irradiated with varying X-ray doses (0 Gy - 12 Gy), and proliferation was assessed over one week using PrestoBlue (RFU). The x-axis represents time post-irradiation, and the y-axis shows corrected RFU values. Solid lines indicate linear regression fits for each dose group, illustrating dose-dependent proliferation rates. Statistical significance was analysed using a two-way ANOVA with Dunnett's test; details are summarised in Appendix E.*

To evaluate the dose-dependent effects of IR on AC-16 cardiomyocyte proliferation, the slopes of the linear regression lines for each radiation dose were compared. The corresponding regression analysis results are presented in Table 4.5. The analysis of the IR experiment shows a significant dose-dependent effect on the proliferation rates of AC-16 cardiomyocytes. An F-test yielded $p<0.0001$,

indicating significant differences in the slopes of regression lines across IR doses. The F-statistic of 72.73 (DFn = 10, DFd = 451) confirms that proliferation rates vary significantly with dose.

*Table 4.5 Regression Analysis Results for the Dose-Dependent Effects of Irradiation on AC-16 Cardiomyocyte Proliferation.*

| Dose (Gy) | Y-Intercept (95% CI) | Slope (95% CI) | R-squared | Degrees of Freedom (DF) |
|---|---|---|---|---|
| **0** | -5876 (-8312 to -3440) | 168.6 (148.1 to 189.1) | 0.8647 | 43 |
| **0.5** | -5096 (-7569 to -2623) | 128.1 (107.1 to 149.2) | 0.7828 | 42 |
| **1** | -5008 (-7787 to -2229) | 117.1 (92.79 to 141.5) | 0.714 | 38 |
| **2** | -4532 (-7351 to -1713) | 97.80 (73.55 to 122.0) | 0.6243 | 40 |
| **3** | -1491 (-2793 to -189.4) | 39.48 (28.05 to 50.90) | 0.556 | 39 |
| **4** | -715.6 (-1434 to 3.162) | 20.25 (14.01 to 26.48) | 0.5184 | 40 |
| **5** | -928.9 (-1700 to -157.4) | 27.31 (20.61 to 34.00) | 0.6296 | 40 |
| **6** | -396.5 (-1149 to 356.4) | 16.30 (9.764 to 22.83) | 0.3886 | 40 |
| **8** | 227.1 (-39.89 to 494.0) | 6.858 (4.610 to 9.105) | 0.4682 | 43 |
| **10** | 365.0 (179.4 to 550.6) | 1.928 (0.3659 to 3.491) | 0.1259 | 43 |
| **12** | 213.3 (137.9 to 288.8) | 0.05171 (-0.5835 to 0.6869) | 0.0006 | 43 |

At high doses (8 Gy, 10 Gy, 12 Gy), the slopes approach zero or become negative (e.g., slope = 0.05171 for 12 Gy), indicating minimal proliferation or cell death. These doses have low R-squared values (e.g., 0.0006 for 12 Gy), suggesting poor model fit due to increased variability or negligible proliferation, reflecting unpredictable or severely inhibited cell behavior. For low to moderate doses (0.5 Gy to 5 Gy), there is a progressive decrease in slopes, indicating reduced proliferation rates compared to the control (0 Gy). Higher R-squared values (e.g., 0.7828 for 0.5 Gy) suggest a better fit, implying that proliferation inhibition is more consistent at these doses. The control group (0 Gy) had the highest slope (168.6) and a strong R-squared (0.8647), indicating robust proliferation without IR.

The data was also fitted to the Gompertz growth model further to analyse the impact of radiation on cell proliferation. The growth was reported as interrupted for doses between 2 Gy and 6 Gy, indicating a significant deviation from the expected growth pattern and that the IR adversely affected the cells. Further analysis was conducted to assess the response of AC-16 cardiomyocytes by focusing on the 144-hour time point post-IR Figure 4.11. A three-parameter logistic model fitted the log-transformed radiation doses to the observed cellular responses. This approach facilitated the determination of the LD50 value — the radiation dose at which cell proliferation is halved — which was found to be 1.286 Gy. The R-squared value of 0.9047 indicated that the IR effects accounted for over 90% of the variance observed in the response data.

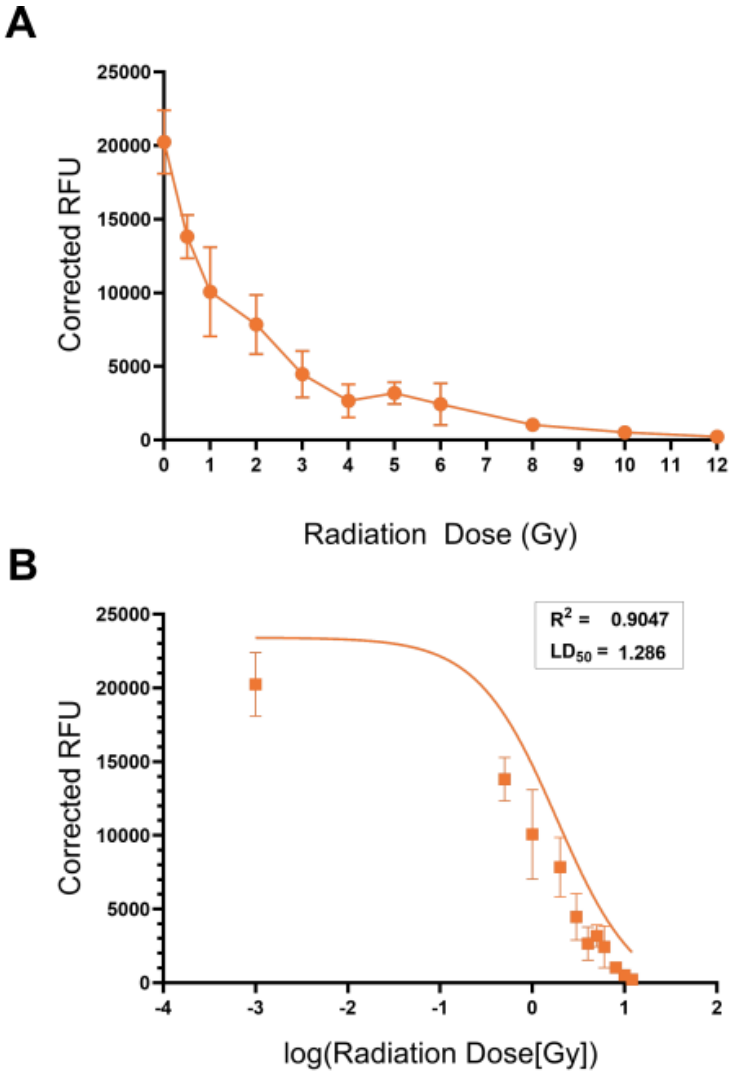


*Figure 4.11 Proliferation and Dose-Response Analysis of AC-16 Cardiomyocytes Post-IR. (A) Proliferation of AC-16 cardiomyocytes at 144 hours post-IR, modelled using the Gompertz growth model across various radiation doses (0 Gy to 12 Gy), with proliferation quantified as Corrected RFU. Error bars represent SD based on N = 3 biological replicates. (B) Dose-response analysis of AC-16 cardiomyocytes at 144 hours post-IR, using a three-parameter logistic model. Log-transformed radiation doses were fitted to the observed proliferation data to evaluate cellular responses. The model estimates the radiation dose required to reduce cell proliferation by 50%, calculated at 1.286 Gy. Error bars represent SD (n=3).*

### 4.4.5 Dose-Dependent DNA Damage Indicated by γ-H2AX in AC-16 Cardiomyocytes

The next characterisation stage involved assessing DNA damage in response to IR by detecting the amount of γ-H2AX foci. For the detection of γ-H2AX foci, the immunochemistry procedure described in Section 3.6.6 was followed. Immunofluorescence analysis was then conducted to visualise the amount of γ-H2AX foci within the nucleus of AC-16 cardiomyocytes to assess the extent of DNA damage in response to IR.

Visual observations of control groups and cells treated with 0.5 Gy and 2 Gy IR (Figure 4.12-A and Figure 4.12-B respectively) revealed minimal γ-H2AX signal in the non-irradiated controls, indicating low levels of DNA damage. Upon exposure to 0.5 Gy IR, an increase in γ-H2AX fluorescence was observed from 10 minutes of exposure time, reflecting induced DNA damage (Figure 4.12-A) A more pronounced response was evident in cells treated with 2 Gy IR, where the cells exhibited a substantial increase in the intensity of green foci and a notable increase in foci density, highlighting extensive DNA damage after the 10-minute exposure time (Figure 4.12-B). This is consistent with a higher level of DNA damage induced by the greater radiation dose. The co-localization of γ-H2AX foci with DAPI in the merged images confirmed the nuclear origin of the DNA damage.

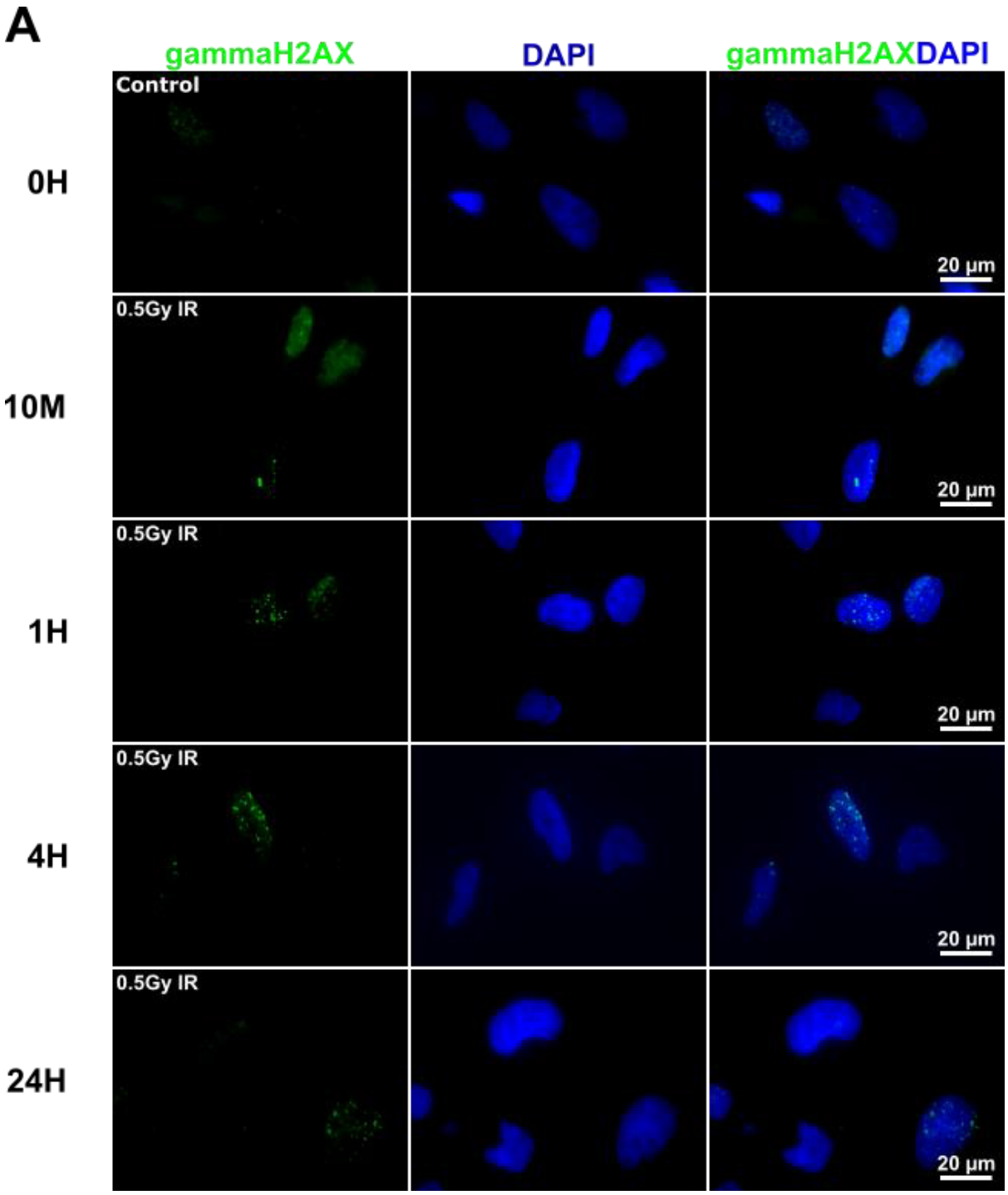


*Figure 4.12 (A) Representative Immunofluorescence Image of AC-16 Cardiomyocytes Exposed to 0.5 Gy Radiation. AC-16 cardiomyocytes were irradiated with a dose of 0.5 Gy and subsequently fixed at different time intervals (0 hour – non-irradiated, 10 minutes, 1 hour, 4 hours, and 24 hours) to assess the DNA damage response. Cells were stained with mouse anti-γH2AX (1:800) primary antibody and AlexaFluor488 Goat anti-Mouse (1:100) secondary antibody, with nuclei counterstained using DAPI at 1 µg/ml. Images were captured using an Olympus D73 fluorescent microscope with a 100X oil objective. Foci from at least 50 cells were manually counted from randomly chosen FOV. The scale bar represents 20 µm.*

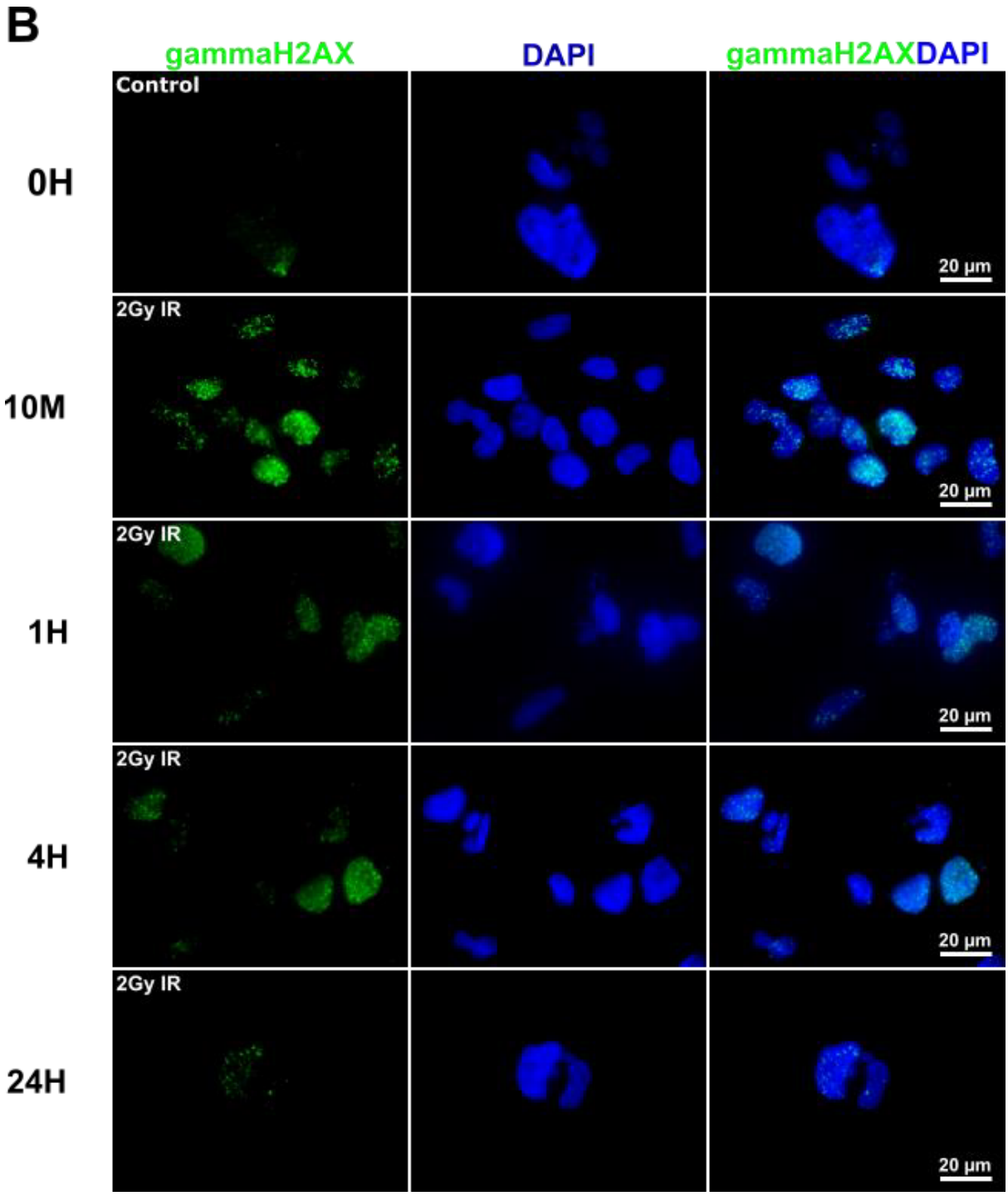


*Figure 4.12 (B) Representative Immunofluorescence Image of AC-16 Cardiomyocytes Exposed to 2 Gy Radiation. AC-16 cardiomyocytes were irradiated with doses of 0.5 Gy and 2 Gy, then fixed at various time intervals (0 hour – non-irradiated, 10 minutes, 1 hour, 4 hours, and 24 hours) to assess the DNA damage response. Cells were stained with mouse anti-γH2AX (1:800) primary antibody and AlexaFluor488 Goat anti-Mouse (1:100) secondary antibody, with nuclei counterstained using DAPI at 1 µg/ml. Images were acquired using an Olympus D73 fluorescent microscope with a 100X oil objective. Foci from at least 50 cells were manually counted from randomly chosen FOV. The scale bar represents 20 µm.*

A quantitative analysis of these foci using immunocytochemistry was conducted at various time points (10 minutes, 1 hour, 4 hours, and 24 hours) under normal gravity conditions (static control). For cells exposed to the 0.5 Gy radiation dose, the initial mean value in the non-irradiated control was 2.93 foci per cell, used as a reference point for comparison. The cell response to IR exposure was swift, where ten minutes post-IR, the mean foci count was 19.72. This reduced slightly to approximately a mean foci count of 14 per cell at one hour. At the four-hour mark, the cells exhibited approximately 16 foci per cell. At 24 hours, it was back to around three foci per nucleus.

For the 2 Gy radiation, the non-irradiated control for the 2 Gy dose displayed an initial value of 3.64 foci per cell. At 10 minutes post-IR, the number of γ-H2AX foci per cell significantly increased to a mean of 73 foci per nucleus. At one hour post-IR, it gradually decreased to 53.33 and 25.467 at the 4-hour. By the 24-hour mark, the foci count had returned to 3.64.

The mean number of γ-H2AX foci per nucleus at both the 2 Gy and 0.5 Gy irradiated AC-16 cardiomyocytes at different time points were assessed for statistical significance using Two-Way ANOVA and the Šídák's multiple comparisons tests. At 10 minutes post-IR, a substantial increase in the mean difference was observed, with 53.61 γ-H2AX foci per nucleus in the 2 Gy IR group compared to the 0.5 Gy IR group. This difference was statistically significant ($p = 0.0382$). The trend continued at 1 hour, with a mean difference of 39.11, with the 2 Gy IR group having a higher mean value, which was also statistically significant ($p = 0.0064$). The other time points suggested no significant differences between the two groups.

These results demonstrate that the γ-H2AX foci dynamics vary significantly between the 2 Gy IR and 0.5 Gy IR-exposed AC-16 cardiomyocytes, where the range of DNA damage induced by the 0.5 Gy dose is comparatively low, and the repair mechanism appears less dynamic over 24 hours compared to the 2 Gy dose. This difference in damage and repair kinetics between the two doses contributed to the decision to proceed with the 2 Gy dose in subsequent experiments.

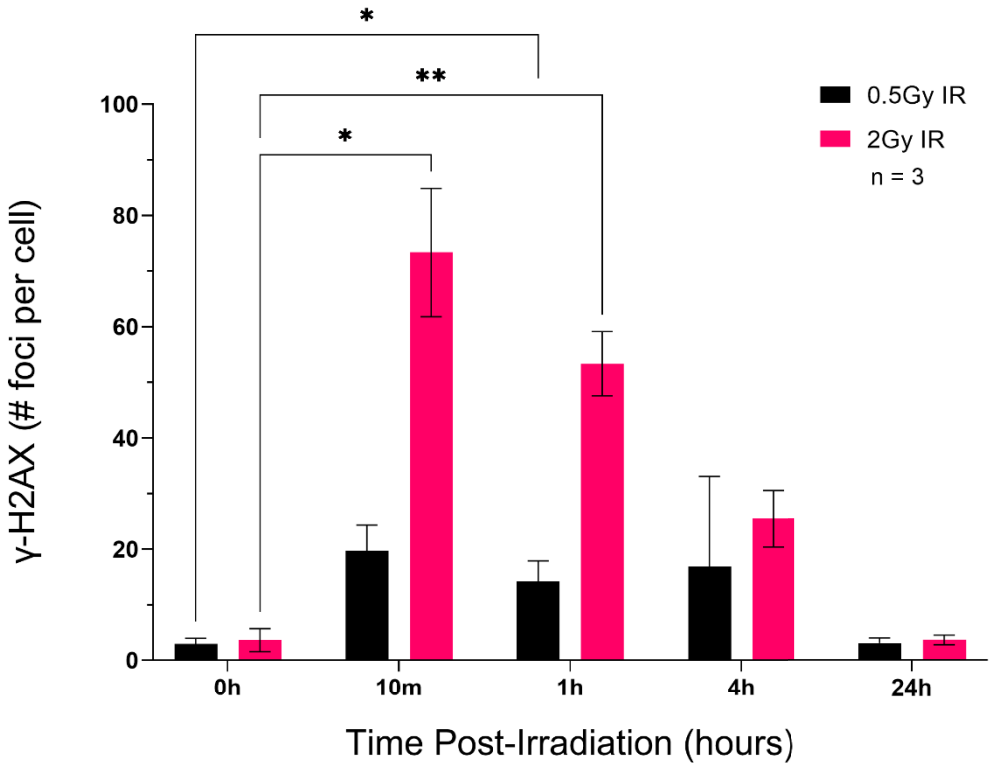


*Figure 4.13 Dynamics of γ-H2AX Foci per Nucleus in AC-16 Cardiomyocytes Post-Irradiation. AC-16 cardiomyocytes were observed for the appearance and quantification of γ-H2AX foci as a measure of DNA damage. The x-axis represents time post-irradiation (hours), and the y-axis shows the mean number of γ-H2AX foci per nucleus. Statistical analysis was conducted using two-way ANOVA (N = 3) and Šídák's multiple comparisons test. Significance levels: * ($p \leq 0.05$), ** ($p \leq 0.01$).*

### 4.4.6 Combined Simulated Microgravity and Radiation Exposure Impact AC-16 Cardiomyocyte Proliferation Differently Based on Cell Density

Following initial experiments of individual stressors, the investigation further explored the dynamics of AC-16 cardiomyocyte proliferation under the simultaneous influence of the combined conditions of IR and s-µG. The experimental timeline was adjusted based on initial findings to optimally measure the combined effects of s-µG and IR on cell growth (Section 4.3.1.3). The PrestoBlue™ Cell Viability Reagent was employed to quantify cell proliferation (Section 3.6.1).

In the combined s-µG and IR proliferation study, the main results did not include data for the 625 and 1250 cells per well densities. The control wells at these lower densities did not show the anticipated proliferation. This could be attributed to the assay's sensitivity limits in distinguishing between actual biological responses and background variation. To maintain the accuracy of the data interpretation, these results have been relegated to the Appendix. The main findings in Figure 4.14 focused on the 2500 cells per well density. The results indicated a lower mean proliferation in s-µG versus control, where the effect did not vary across radiation doses.

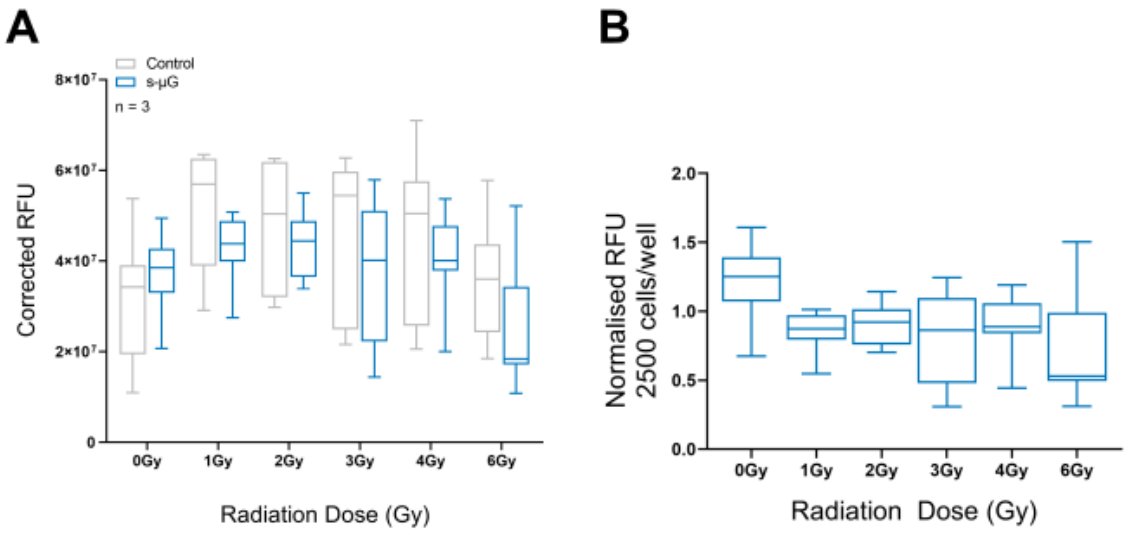


*Figure 4.14 Proliferation of AC-16 Cardiomyocytes in 2D under s-µG and IR Conditions. The proliferation of AC-16 human cardiomyocytes was measured to assess the combined impact of s-µG and IR. Radiation doses (Gy) are plotted on the x-axis, and RFU on the y-axis. GraphPad was used to plot (A) corrected RFU and (B) normalised RFU of cells with an initial seeding density of 2500 cells per well, exposed to both static control and s-µG with varied IR doses. Proliferation was assessed at 96 hours of s-µG and 72 hours post-IR using the PrestoBlue assay. Statistical analysis was performed with two-way ANOVA (N = 3) and Sidak's multiple comparison post hoc test to compare s-µG against control.*

A two-way ANOVA of AC-16 cardiomyocyte proliferation at 2500 cells per well under s-µG revealed radiation dose ($p=0.0002$) and s-µG exposure ($p=0.0347$) as significant factors affecting cell growth, with no significant interaction ($p=0.3615$). Sidak's multiple comparisons test revealed no statistically significant changes in proliferation across all tested radiation doses (1Gy to 6Gy) compared to the 0

Gy. Despite the lack of statistical significance, there is a consistent trend of reduced proliferation under s-μG conditions compared to the control, particularly noticeable at higher radiation doses (Figure 4.14A).

Normalisation of s-μG to control, depicted in Figure 4.14B and Šídák's multiple comparisons test showed no statistically significant differences. Although a trend of reduced proliferation with increasing radiation dose was observed, it did not reach significance.

In conclusion, under combined s-μG and IR conditions, AC-16 cardiomyocyte proliferation showed a consistent trend of reduced growth with increasing radiation doses, although statistical significance was not reached.

### 4.4.7 Compounded Reduction in AC-16 Cardiomyocyte Viability When Exposed to Both Simulated Microgravity and Radiation

Following the proliferation assay, the effects of s-μG, 2Gy IR and their combination on cell viability were assessed relative to the control group. This investigation followed an adjusted experimental timeline, detailed in Section 4.3.1.3. This protocol led to a total exposure to s-μG of 96 hours and a subsequent 72-hour post-IR treatment. Cell viability was evaluated using the LIVE/DEAD viability assay, as outlined in Section 4.3.2.

The immunofluorescent images indicated a qualitative decrease in cell count within the field of view for exposure conditions compared to the control, suggesting a reduction in total cell count due to the treatments (Figure 4.15A). Despite this, viability remained high for each field of view, implying that the remaining cells retained their viability. This indicates potential alterations in cell proliferation or migration patterns under s-μG and IR influence. Quantitative assessment normalised the viability measures from the treatment groups against the static control, accompanied by recording cell counts within the field of view to provide density context (Figure 4.15B and Figure 4.15C).

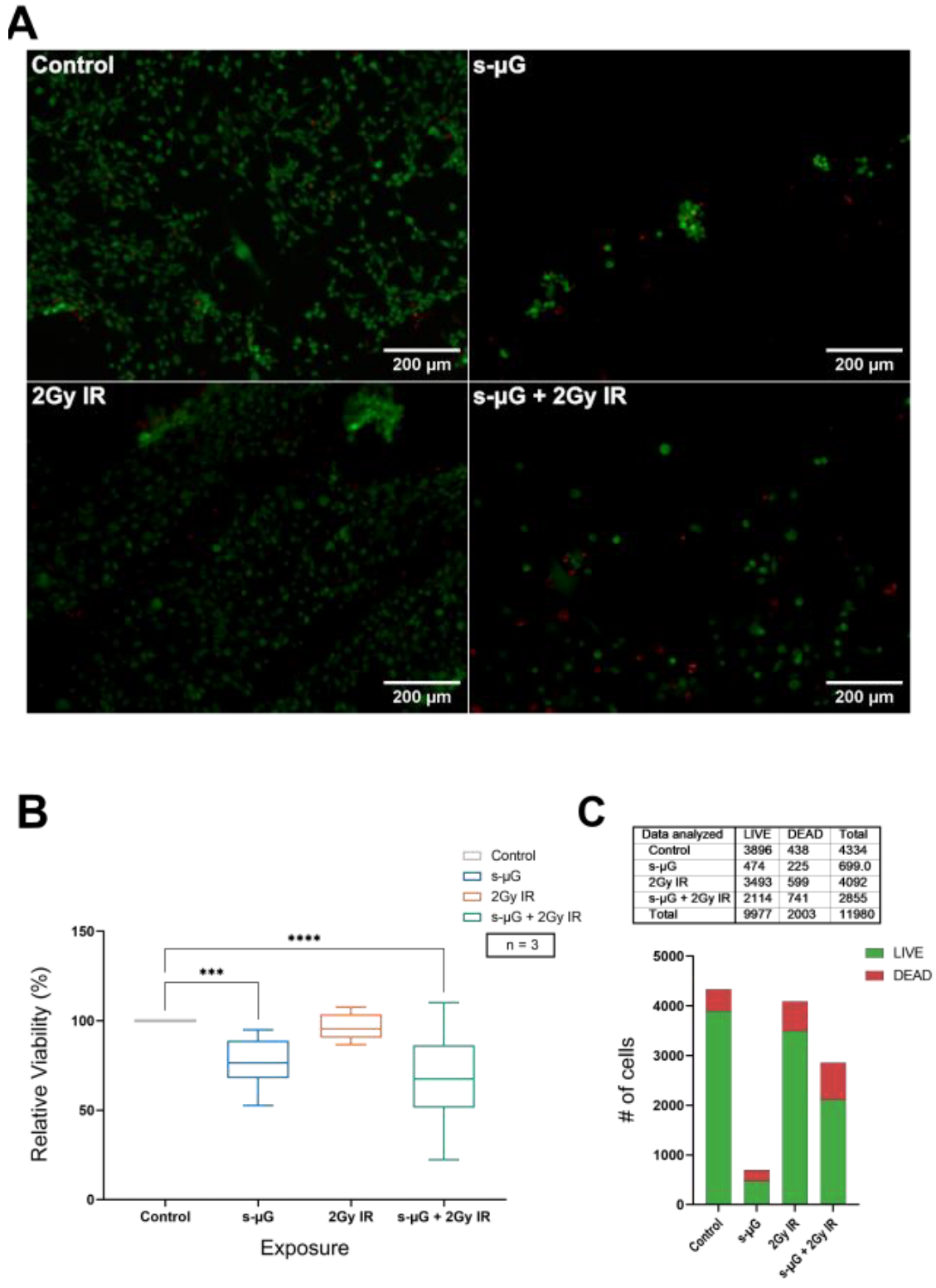


*Figure 4.15 AC-16 Cardiomyocyte Viability After s-µG and IR Assessed by LIVE/DEAD Assay. (A) Representative immunofluorescence image of AC-16 cardiomyocyte viability. Cells were labelled with 1 µM calcein-AM (live cells) and 4 µM Propidium Iodide (dead cells) and imaged using an EVOS FL microscope with a 20X objective. Cells in the GFP (green) channel were counted as live, and those in the Texas Red (red) channel were counted as dead. The scale bar represents 200 µm. (B) Average cell viability (%) under different exposure conditions, normalised to the static control. Data analysed using the Kruskal-Wallis test (N = 3) revealed significant differences among groups, further elucidated by Dunn's multiple comparisons test. Significance levels: *** ($p \leq 0.001$), **** ($p \leq 0.0001$). (C) Quantitative cell count for the LIVE/DEAD assay across treatment conditions with n = 11960, representing the total cell count across all replicates (N = 3).*

The Kruskal-Wallis test yielded a p-value of <0.0001, indicating significant variations among the four treatment groups. Further analysis via Dunn's multiple comparisons test revealed a significant reduction in cell viability in the s-μG group compared to the control ($p = 0.0001$) and between the combined s-μG and 2Gy IR treatment and control groups ($p < 0.0001$). In contrast, the viability impact of 2Gy IR alone did not show a significant difference from the control ($p > 0.9999$).

Overall, the qualitative reduction in cell density implies fewer cells due to treatments, yet viability remains high, suggesting altered proliferation. Quantitative analysis confirmed significant reductions in viability under s-μG and combined s-μG and 2Gy IR treatments, indicating their potential detrimental effects on cellular health.

### 4.4.8 No Significant Changes in Mechanotransduction-Related Gene Expression in AC-16 Cardiomyocytes Under Combined Stressors

Proliferation assays investigating the combined exposure of s-μG and IR indicated a cell density-dependent response to s-μG, with IR interactions showing no significant effect. Using LIVE/DEAD staining, viability assays demonstrated decreased viability under s-μG and s-μG + 2Gy IR. These preliminary findings set the stage for a more thorough molecular investigation into the cardiomyocytes' response to these environmental stressors, with RT-qPCR analyses focusing on genes related to mechanotransduction and developmental regulation, including YAP1, RHOA, RAC2, CDH2, and CX43.

The RT-qPCR experiments adhered to the amended timeline, detailed in Section 4.3.1.3, to adapt to the combination of s-μG and 2 Gy IR on AC-16 cardiomyocytes. RNA extraction from AC-16 cardiomyocytes was carried out 48 hours after 2 Gy IR treatment and 72 hours from the start of s-μG exposure. Gene expression analysis by RT-qPCR used SYBR Green PCR Master Mix to assess YAP1, RHOA, RAC2, CDH2, and CX43 under static control, s-μG, 2Gy IR and a combination of s-μG + 2Gy IR. The plotted $\log_2$ fold change values were based on normalisation to control, where 0 signifies no change from the static control.

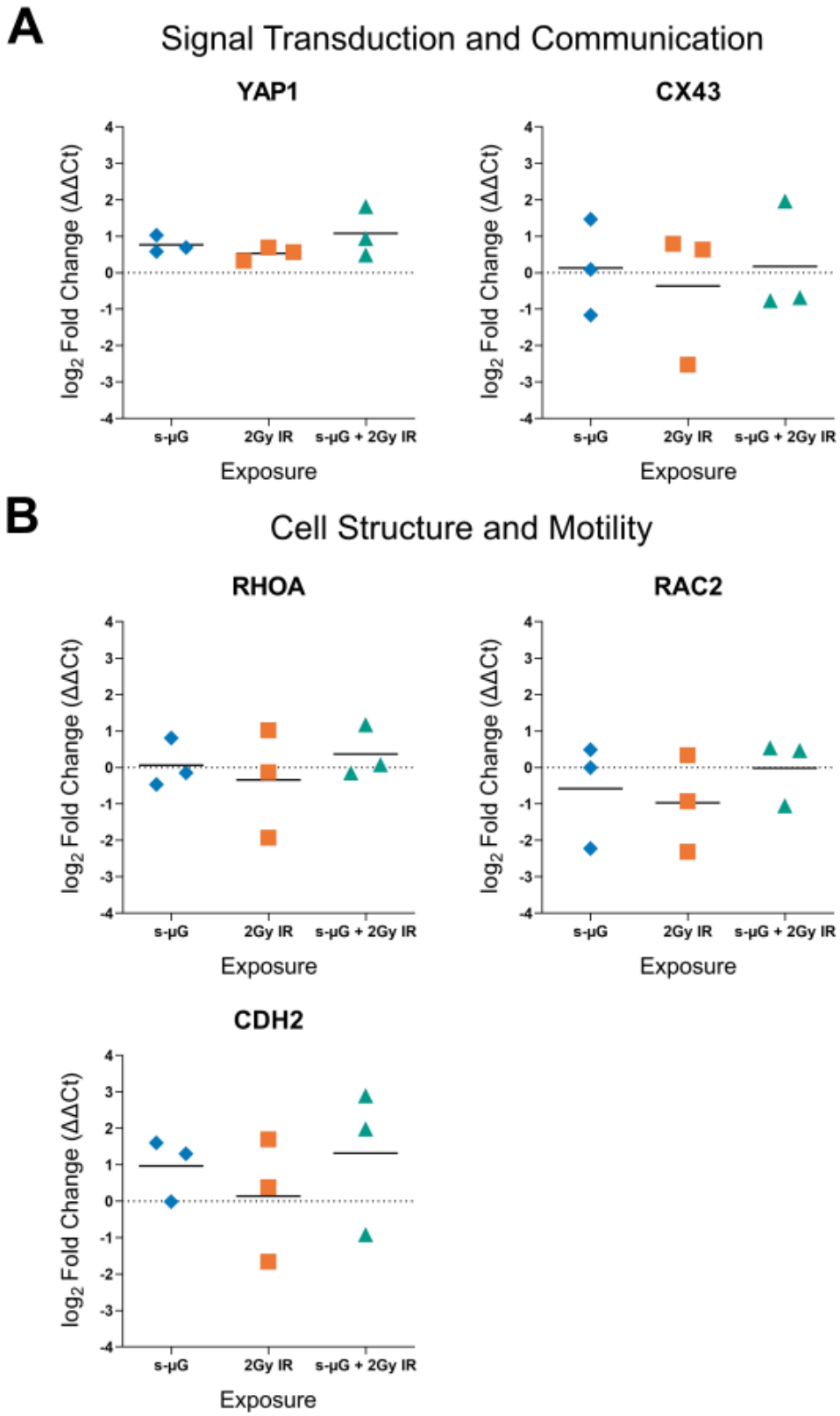


*Figure 4.16 Gene Expression Analysis of AC-16 Cardiomyocytes for Signal Transduction and Cell Structure Genes. Gene expression analysis for (A) signal transduction and communication and (B) cell structure and motility in AC-16 cardiomyocytes subjected to static control, s-μG, IR, and s-μG + IR. The x-axis represents exposure groups, and the y-axis shows gene expression as log2 fold change. The RT-qPCR protocol included a two-step cycle hold at 95˚C for 30 seconds, followed by 40 PCR cycles (95˚C for 5 seconds, 60˚C for 20 seconds), and a melt curve analysis. The 2^-ΔΔCt method was used to calculate gene expression fold change. Each plotted dot represents the log2 fold change for individual experiments, with the mean for each group indicated by a solid line. A log2 fold change of 0 (dotted line) represents no change from the control group. Statistical analysis was conducted on ΔΔCt values using two-way ANOVA (N = 5) with Šídák's multiple comparisons test.*

The analysis of $\log_2$ fold change across treatments (s-μG, 2Gy IR and s-μG +2Gy IR) revealed no significant differential expression for YAP1, Cx43, RHOA, RAC2 and CDH2. For YAP1, ANOVA highlighted no significant variation in expression across the different treatments, with a p-value of 0.8295. Similarly, CX43's expression showed no significant differences across treatments, with a p-value of 0.9744. RHOA's expression analysis also reported no significant changes among the treatments, as evidenced by ANOVA ($p = 0.9648$. RAC2 followed a similar trend, with no significant expression differences detected across treatments ($p = 0.8620$). Lastly, CDH2 expression analysis via ANOVA indicated no significant differences across treatments ($p = 0.7354$).

### 4.4.9 Efficient DNA Repair in AC-16 Cardiomyocytes with Combined Exposure to Simulated Microgravity and Radiation

The initial DNA repair study (section 4.4.5) on AC-16 cardiomyocytes revealed that the presence and subsequent repair dynamics of γ-H2AX foci differed significantly between cells exposed to 2 Gy IR and those exposed to 0.5 Gy IR. Consequently, the 2 Gy IR dose was chosen for subsequent experiments due to its ability to demonstrate DNA damage and repair.

Expanding upon the initial experiment, subsequent experiments included exposure to s-μG, resulting in the combination of s-μG + 2 Gy IR exposure on AC-16 cardiomyocytes. The observation period was extended to 48 hours for these experiments to assess potential cellular response or repair mechanism delays. Again, a 24-hour s-μG preconditioning was utilised for the combined treatment protocol, followed by 2 Gy IR (Section 4.3.1.3). 0 Gy control samples, not subjected to IR, were fixed before IR, while the remaining samples were irradiated with 2 Gy IR. Cells were fixed for analysis at designated time points, ensuring minimal disruption to the experimental setup and maintaining the integrity of the microgravity simulation.

Visual observations of γH2AX DNA damage foci between the 2 Gy IR group and the s-μG + 2 Gy IR group revealed noticeable differences in the cellular response to IR. The foci in the 2 Gy IR group displayed moderate fluorescence. They were less vibrant when compared to those in the s-μG + 2 Gy IR group, where the fluorescence was significantly brighter. In terms of size, the foci in the 2 Gy IR group were generally smaller and more dispersed. In contrast, the foci in the s-μG + 2 Gy IR group appeared larger, implying a more substantial accumulation of DNA repair complexes or more extensive DNA damage. These visual differences provide insights into the varied cellular responses to DNA damage under different experimental conditions, highlighting potential variations in the severity of damage or the efficiency of the repair mechanisms activated.

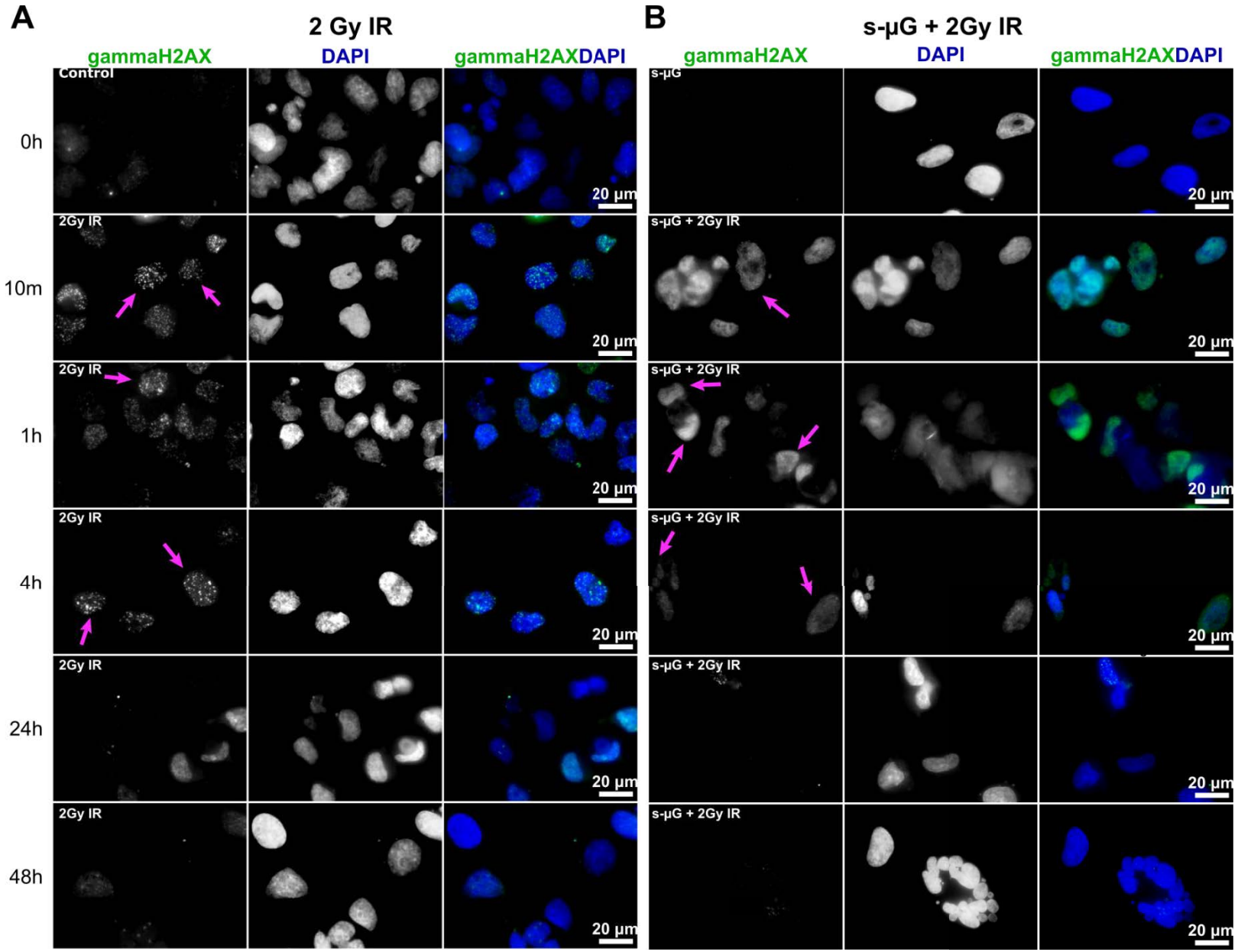


*Figure 4.17 Representative Immunofluorescence Image of AC-16 Cardiomyocytes Under Combined Exposure. AC-16 cardiomyocytes were irradiated with a 2 Gy dose and subsequently fixed at various time intervals (0 hour – non-irradiated, 10 minutes, 1 hour, 4 hours, 24 hours, and 48 hours) to assess the DNA damage response. Cells were stained with mouse anti-γH2AX (1:800) primary antibody and AlexaFluor488 Goat anti-Mouse (1:100) secondary antibody, with nuclei counterstained using DAPI at 1 µg/ml. Images were captured using an Olympus D73 fluorescent microscope with a 100X oil objective. Foci from at least 50 cells were manually counted from randomly chosen FOV. The scale bar represents 20 µm.*

Following the fixation and staining procedures described in Section 4.3.4, a quantitative analysis of γ-H2AX foci was performed. For the cells exposed to 2 Gy IR only, the non-irradiated control (0 hours) was established to be approximately 1 foci per cell, serving as the starting reference point. A substantial increase was observed at 10 minutes post-IR, with the number of γ-H2AX foci per cell reaching approximately 57. The response continued to intensify, peaking at approximately 77 foci per cell at the 1-hour mark. Subsequently, there was a reduction in foci count, declining to around 37 foci per cell at 4 hours, followed by a decrease to 6 foci per cell at 24 hours post-IR. This downward trend continued, reaching approximately 3 foci per cell by the 48-hour mark; for the cardiomyocytes exposed to s-μG + 2Gy IR, the foci count at 0 hours was established to be approximately 3 foci per cell. At 10 minutes post-IR, the foci count surged to approximately 70 foci per cell, and this count remained relatively stable at around 70 foci per cell at the 1-hour mark. However, it decreased to approximately 32 foci per cell at 4 hours post-IR, and a further decrease in foci count to 5 foci per cell at 24 hours, followed by a slight increase to 6 foci per cell by the 48-hour time point.

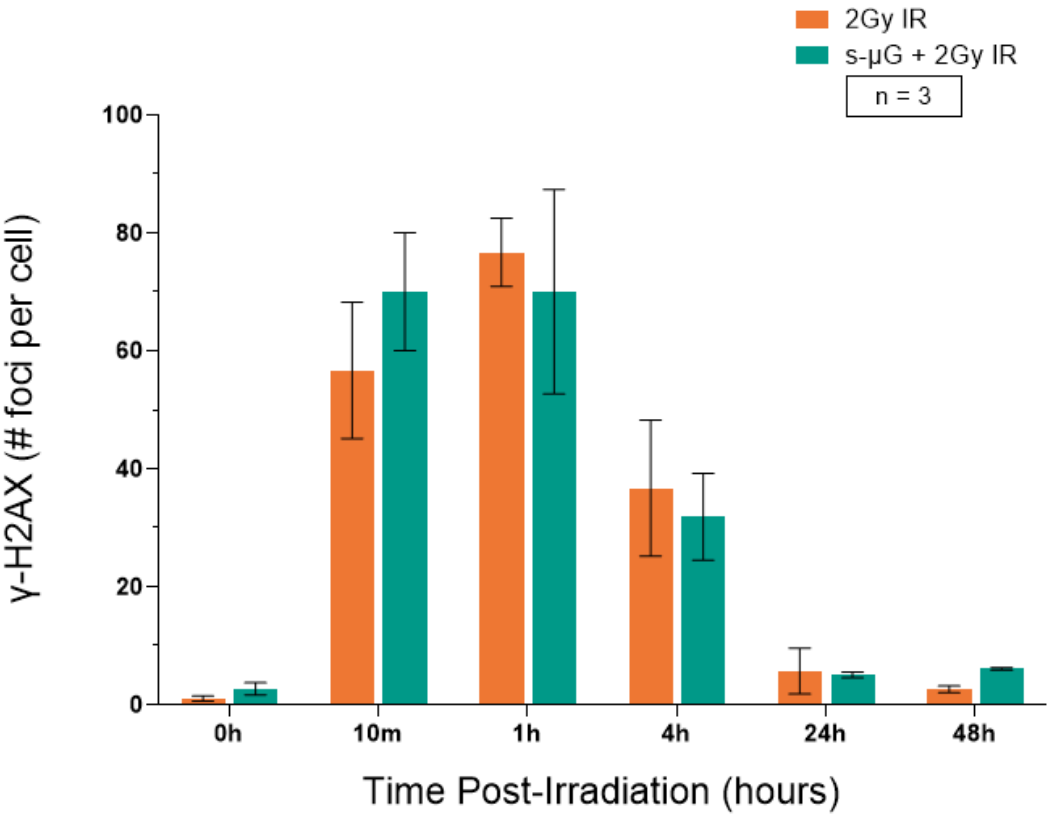


*Figure 4.18 γ-H2AX Foci per Nucleus in AC-16 Cardiomyocytes Post Combined Exposure. Quantitative analysis of γ-H2AX foci in AC-16 cardiomyocyte nuclei over a 48-hour period. The x-axis represents time post-irradiation (hours), and the y-axis shows the mean number of γ-H2AX foci per nucleus. Statistical analysis was performed using two-way ANOVA (N = 3) with Šídák's multiple comparisons test to compare s-μG and s-μG + 2 Gy IR at each time point.*

The mean number of γ-H2AX foci per nucleus between the 2 Gy IR group and s-μG + 2Gy IR group were assessed for statistical significance using Two-Way ANOVA and the Šídák's multiple comparisons test. Results demonstrated no statistically significant differences between the mean values of the treatment groups for each observed time.

The comprehensive study on AC-16 cardiomyocytes exposed to the combination of s-μG and IR has elucidated significant insights into cellular DNA damage and repair mechanisms. Adding s-μG exposure intensified the observed DNA damage responses, as evidenced by brighter and larger γ-H2AX foci than the 2 Gy IR group alone. Over the observation period, both groups demonstrated a peak in foci count shortly after IR exposure, which gradually declined, indicating active DNA repair processes. However, despite apparent foci intensity and size differences, statistical analysis revealed no significant differences between the exposure groups.

### 4.4.10 YAP Translocation: Insight into Mechanotransduction

In a comprehensive exploration of YAP signalling within AC-16 cardiomyocytes, a series of controlled experiments were conducted to examine the intracellular distribution of YAP, focusing on its localisation in response to s-μG and IR, both as single variables and in tandem. The distribution of YAP between the nucleus and cytoplasm was quantified and compared under various stress conditions to determine its mechanosensitive behaviour.

Initially, the investigation was conducted at 72 hours for cells subjected to static conditions and s-μG, compared to a control group at 0 hours. Immunofluorescent images of AC-16 cardiomyocytes were captured and analysed as described in 4.3.5.1, to observe the effects of s-μG alone. Utilising Dunn's multiple comparisons test, mean rank differences in YAP localisation were evaluated after 72 hours under static and s-μG conditions, compared to an initial control at 0 hours (Figure 4.21A). This investigation found no significant alteration in YAP's nuclear/cytoplasmic ratio in cells maintained under static conditions for 72 hours relative to the control group at 0 hours ($p = 0.0751$). In contrast, the s-μG group exhibited a pronounced increase in the nuclear localisation of YAP after 72 hours compared to the control group ($p < 0.0001$). Furthermore, direct comparison between the static and s-μG groups at 72 hours revealed a highly significant ($p < 0.0001$) nuclear localisation of YAP, reinforcing the observation that s-μG exerts a distinct influence on YAP localisation compared to static conditions.

The subsequent phase of the experiment introduced IR to the array of stress conditions, once again obtaining an immunofluorescence image of AC-16 cardiomyocytes 72 hours post-exposure to s-μG and 48 hours post-IR (Figure 4.20). As depicted in Figure 4.21B, YAP localisation was quantified to investigate the intracellular dynamics of YAP as an indicator of cellular mechanosensitivity and stress response. The data revealed a statistically significant increase in the nuclear localisation of YAP when cells were exposed to s-μG ($p < 0.0001$) and IR ($p < 0.0001$) independently, compared to the control group. Interestingly, when the combined s-μG and IR group was compared to the control group, no significant difference in the nuclear localisation of YAP was observed ($p = 0.1095$).

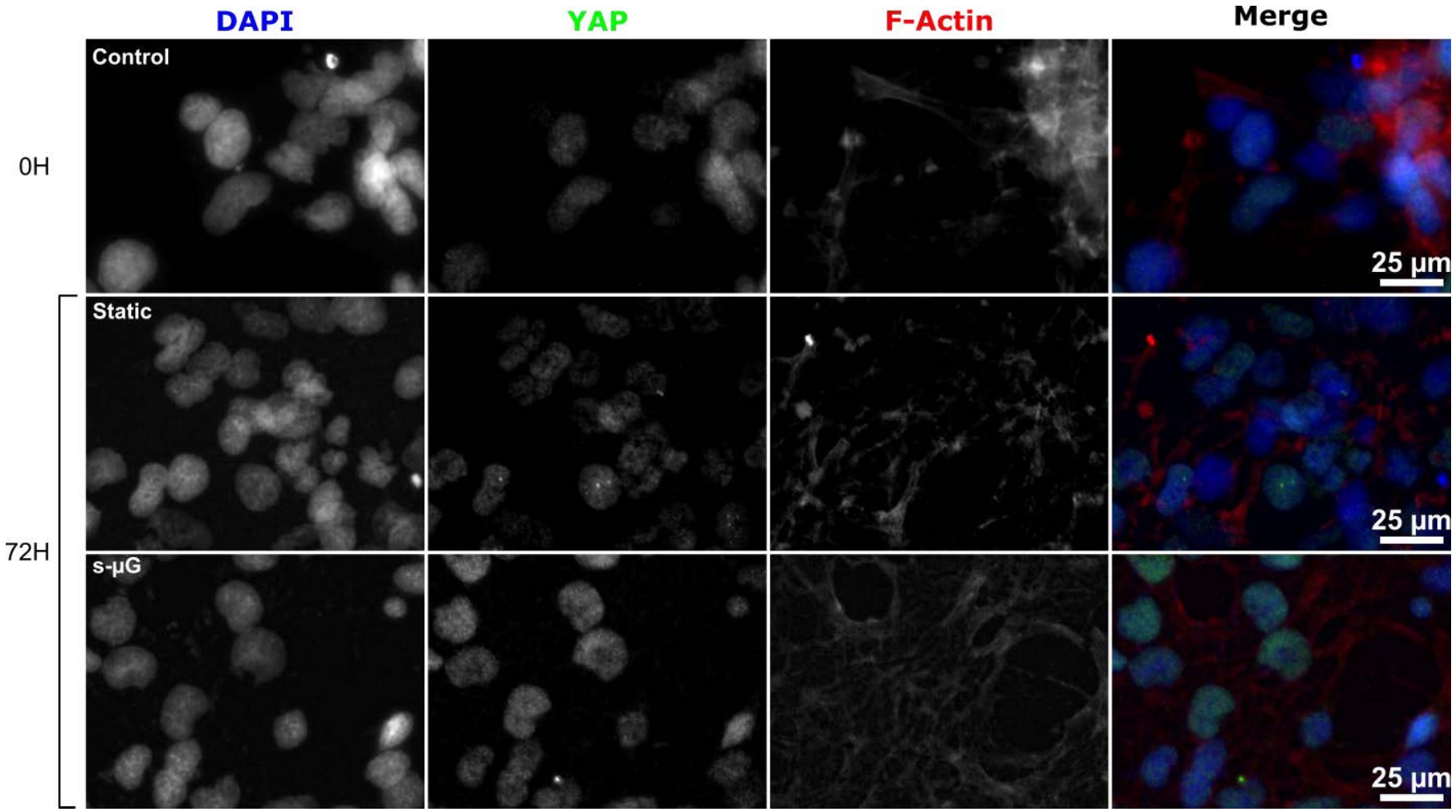


*Figure 4.19 YAP Localization in AC-16 Cardiomyocytes Subjected to s-µG. A representative immunofluorescence image shows YAP localization in AC-16 human cardiomyocytes after 72 hours of exposure to static conditions and s-µG, compared to a 0-hour control. YAP was detected using a primary antibody at 1:200 concentration with an Anti-Rabbit Alexa Fluor 488 secondary antibody at 1:100 dilution (YAP appears green). F-Actin was stained red with iFluor 594 Phalloidin at 1:1000 dilution, and nuclei were counterstained blue with DAPI at 1:10000 dilution. Images were captured using a DV Elite widefield fluorescent microscope with a 40X dry objective. Foci from at least 50 cells were captured from randomly selected FOV. The scale bar represents 50 µm.*

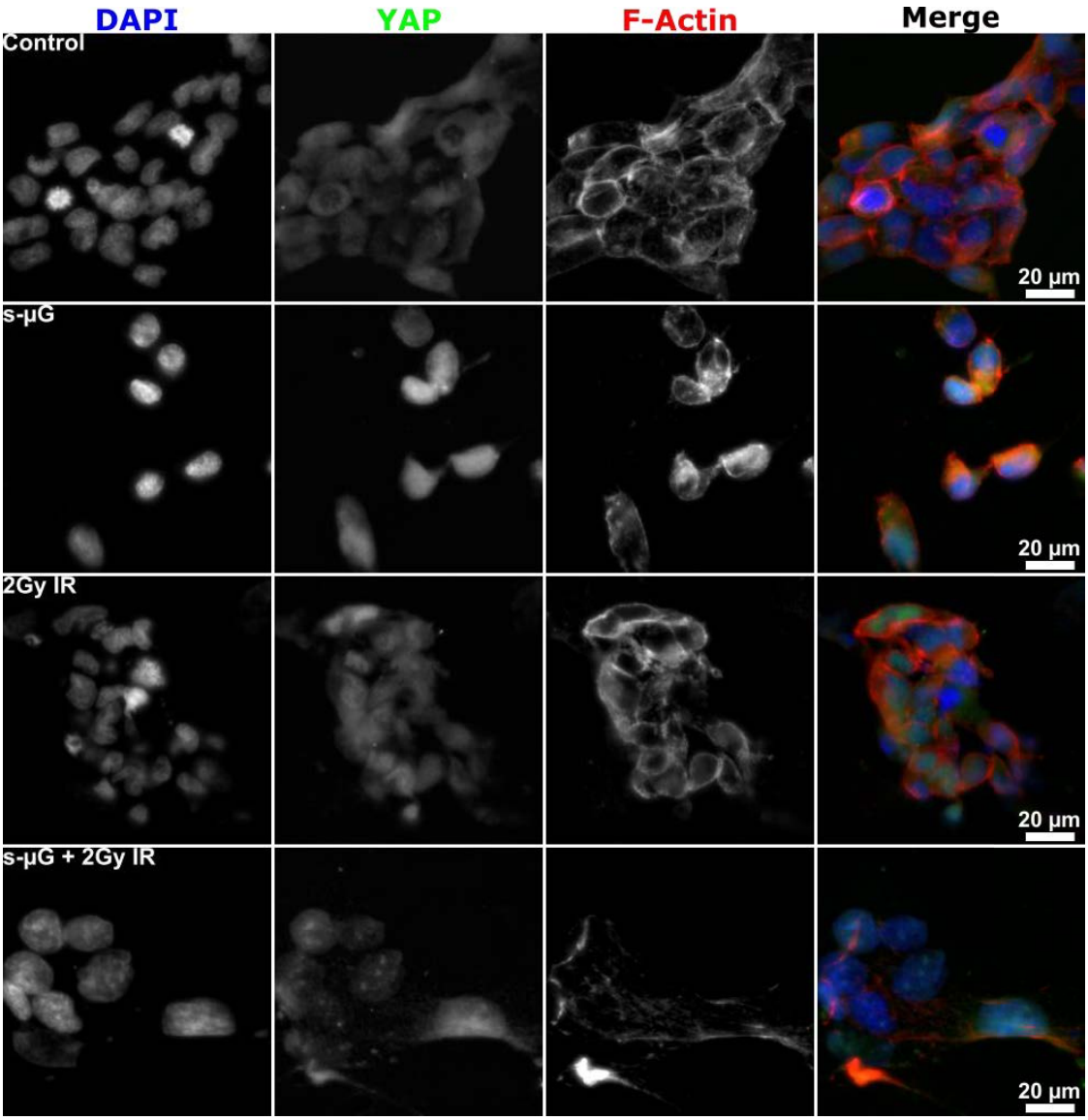


*Figure 4.20 YAP and Cx43 Localization in AC-16 Cardiomyocytes Under s-µG and IR. AC-16 cardiomyocytes were subjected to static control, s-µG, IR, and combined s-µG+IR for 72 hours. YAP and Cx43 localization was visualized using primary antibodies at 1:200 and 1:500, with Anti-Rabbit Alexa Fluor 488 and Anti-Mouse CY5 secondary antibodies at 1:100 to identify YAP (green) and Cx43 (magenta). F-Actin (red) was stained with iFluor 594 Phalloidin (1:1000), and nuclei (blue) were counterstained with DAPI (1:10000). Images were captured using a DV Elite widefield fluorescent microscope with a 40x dry objective, and foci from at least 50 cells were captured from randomly chosen FOV. The scale bar represents 20 µm.*

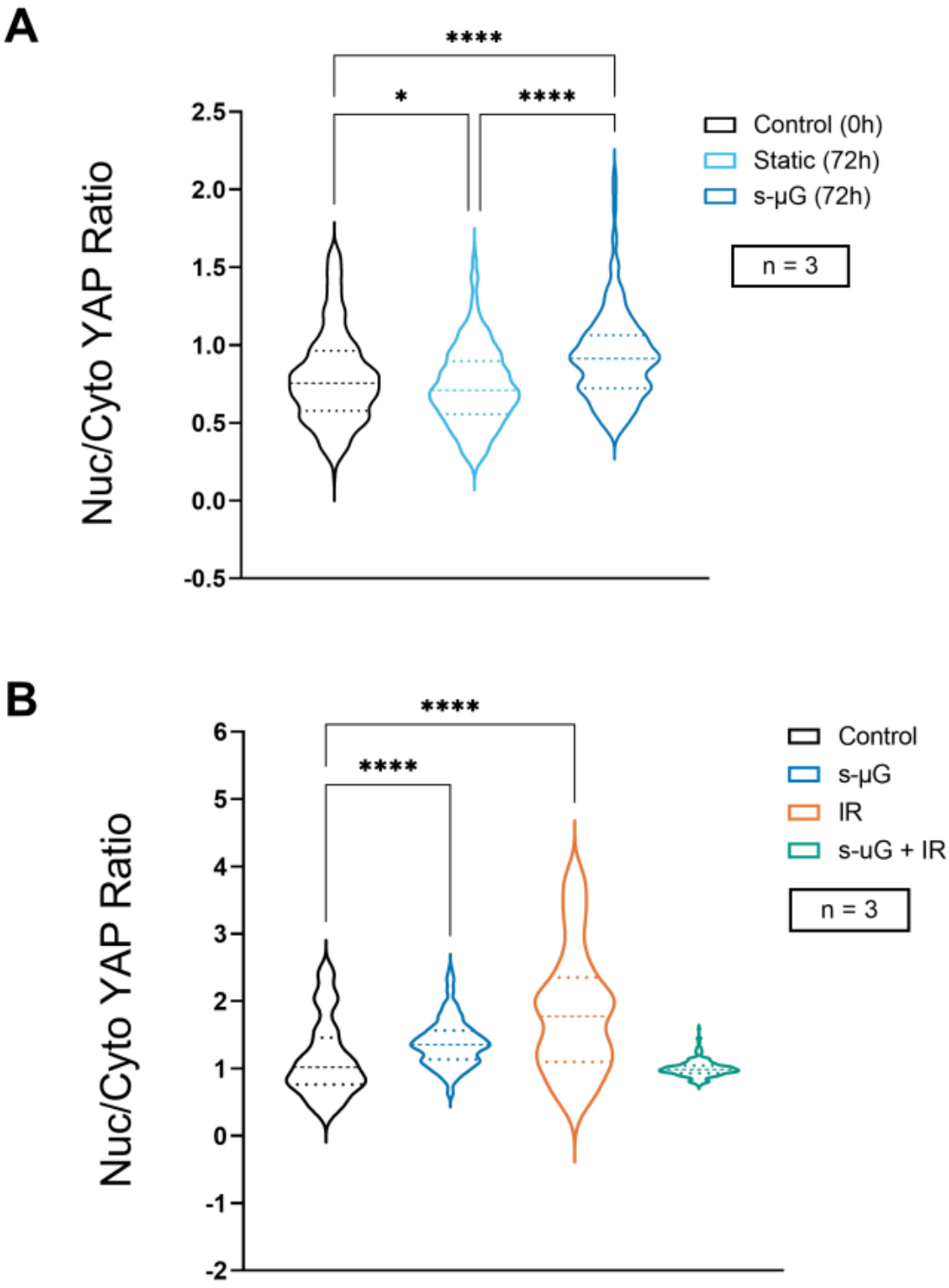


*Figure 4.21 YAP Intracellular Localization in AC-16 Cardiomyocytes Under Varied Conditions. Quantitative analysis of YAP localization in AC-16 cardiomyocytes. (A) Cells subjected to static conditions and s-µG for 72 hours, compared to the control group at 0 hours. (B) Cells subjected to s-µG, IR, combined s-µG and IR, and control condition for 72 hours. Analysis was based on the ratio of integrated nuclear fluorescence intensity to integrated cytoplasmic fluorescence intensity. Statistical analysis was conducted using the Kruskal-Wallis test (N = 3), followed by Dunn's multiple comparisons test to identify significant differences between groups. Significance is denoted by * ($p \leq 0.05$) and **** ($p \leq 0.0001$).*

### 4.4.11 Changes in AC-16 Cardiomyocyte Morphology Reflect Cellular Adaptation to Simulated Microgravity and Radiation Stress

After exploring YAP signalling dynamics and its localisation sensitivity within AC-16 cardiomyocytes exposed to s-μG and 2 Gy IR, the study expanded to evaluate the broader impact of these stressors on cellular morphology, connecting the complex mechanotransduction responses to visible structural changes.

Brightfield imaging before immunofluorescence fixation was performed to document the initial cellular morphology and distribution of AC-16 cardiomyocytes. Figure 4.22 presents the response of AC-16 cardiomyocytes to 2Gy IR alone and in combination with s-μG at 1, 4, 24, and 48 hours post-IR. At 1 hour post-IR, the cells treated with 2Gy IR alone showed that AC-16 cardiomyocytes maintained their typical morphology. Cells subjected to both s-μG and 2Gy IR also showed no immediate changes, although a slight reduction in cell number was observed. At 4 hours post-IR, the 2 Gy IR-treated cells continued displaying a normal phenotype. In contrast, the cells under combined stress began to show changes in distribution, with a tendency to group rather than spread evenly, as seen in the IR-only treated samples. At 24 hours after IR, the 2 Gy IR-treated cells maintained a largely healthy appearance with a subtle increase in cells at each field of view, suggesting ongoing cell proliferation. Conversely, cell clustering became apparent in the s-μG + 2Gy IR group. By 48 hours after IR, the 2 Gy IR-treated cells displayed evidence of proliferation, with a more crowded field of view. On the other hand, the cells under the combined influence of s-μG and 2 Gy IR exhibited pronounced cell clustering and visible morphological alterations. These changes demonstrated that s-μG addition altered cell growth patterns and distribution.

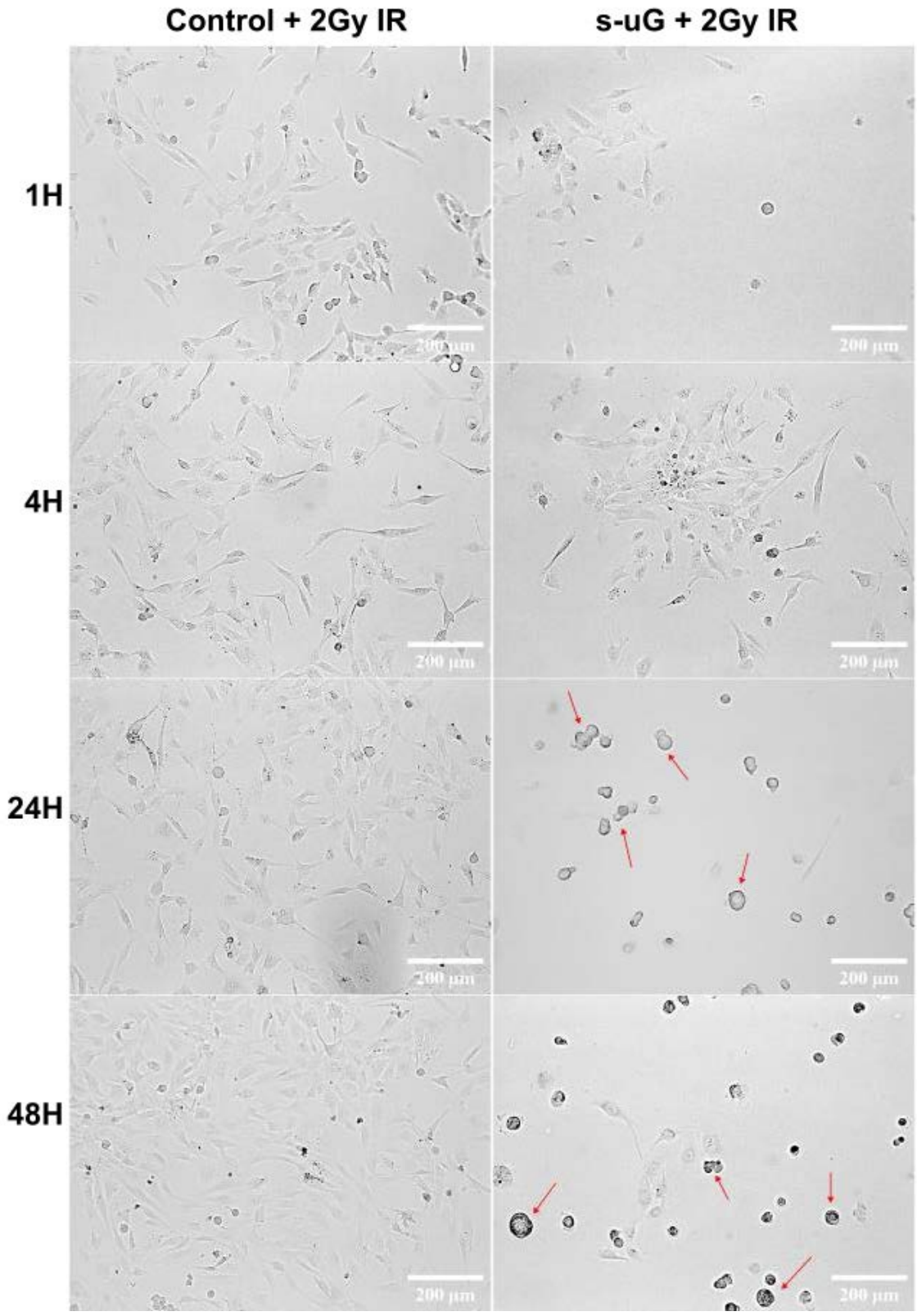


*Figure 4.22 Representative Brightfield Image of AC-16 Cardiomyocytes at Varying Durations of s-µG and Post-IR Conditions.Brightfield images captured with an EVOS M5000 Imaging System at 20x magnification, showing AC-16 cardiomyocyte morphology and distribution in response to s-µG and IR at 1,4,24,48 hours post-IR. Red arrows indicate cell aggregates, revealing cellular conformation and clustering phenomena under s-µG conditions before RNA extraction and gene expression analysis. The scale bar represents 200µm.*

The study on the immunofluorescent stained samples incorporated three key morphological parameters: area, eccentricity, and solidity, further described in Chapter 3, Section 3.6.5.3. Briefly, the area of the cells provided data on size changes indicative of growth, division, or morphological alterations. Eccentricity, measuring the elongation of cells, highlighted alterations in cell shape. Lastly, solidity measures the smoothness of the cell's outline, indicating the presence of protrusions or indentations.

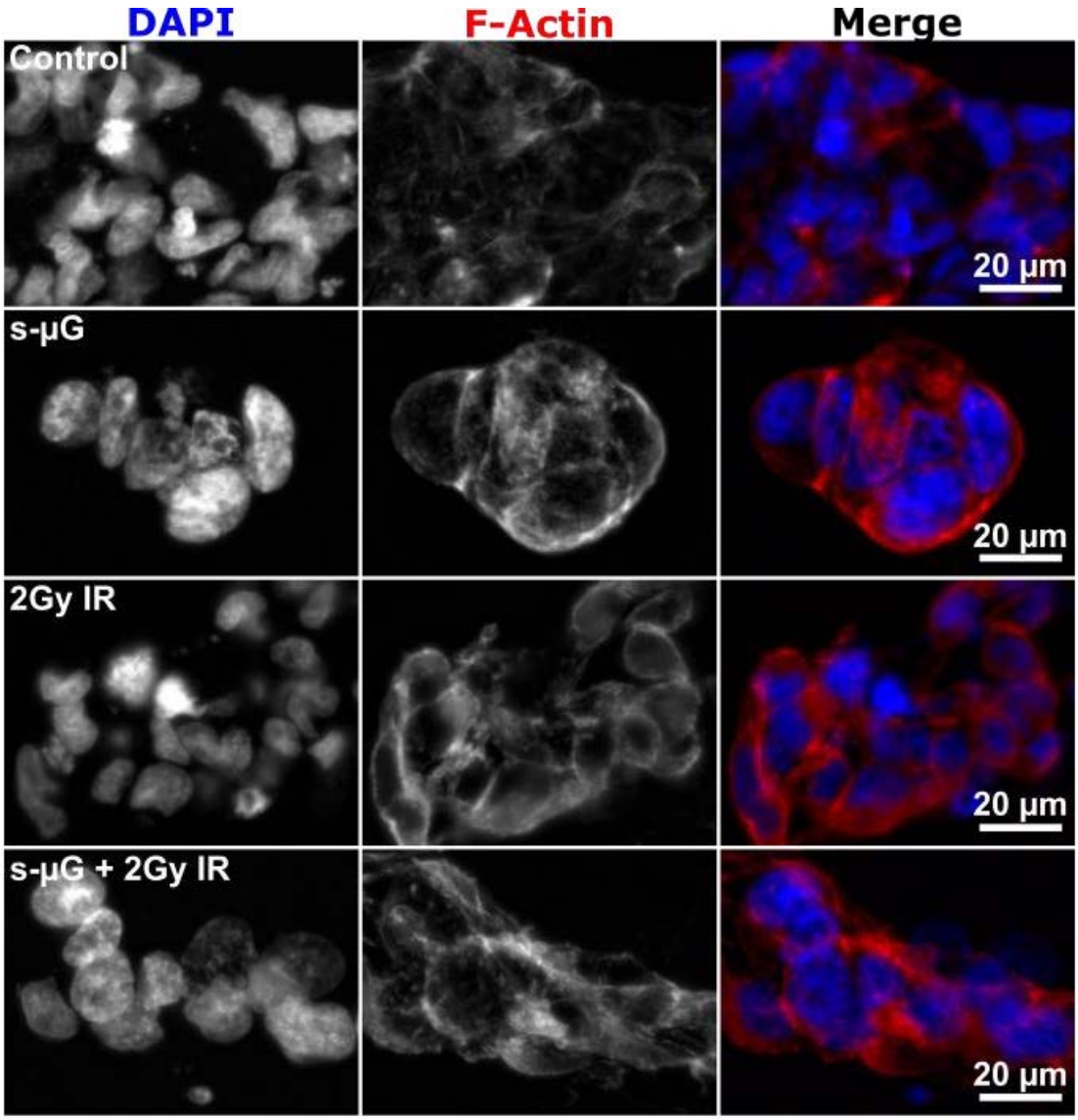


*Figure 4.23 Representative Immunofluorescence Image of AC-16 Cardiomyocyte Morphology Under Control, s-μG, IR, and s-μG+IR Conditions. F-Actin (red) was stained with iFluor 594 Phalloidin (1:1000), and nuclei (blue) were counterstained with DAPI (1:10000). Images were captured using a Leica confocal microscope with a 60x oil objective, with at least 5 randomly chosen FOV. The scale bar represents 20 μm.*

Significant variations were identified using the Kruskal-Wallis test to evaluate differences in cell area, eccentricity, and solidity among the four treatment groups: Control, s-μG, IR, and combined s-μG + IR ($p < 0.0001$). Dunn's multiple comparisons test revealed that both s-μG and s-μG + IR significantly increased cellular area compared to control (s-μG vs. Control, $p < 0.0001$; s-μG + IR vs. Control, $p < 0.0001$). Cells exposed to s-μG had a median area of 327.3 μm² (25th–75th percentile: 268.1–387.5 μm²), while those under s-μG + IR reached a median area of 351.2 μm² (25th–75th percentile: 308.1–419.7 μm²), both significantly larger than control cells, which had a median area of 261.9 μm² (25th–75th percentile: 205.1–316.0 μm²). In contrast, cells exposed to IR alone did not significantly differ in area from control (median 281.5 μm², 25th–75th percentile: 183.3–389.7 μm², $p = 0.3799$).

Despite the enlargement observed under s-μG and s-μG + IR, these treatments did not lead to significant changes in cell eccentricity ($p = 0.5626$). Median eccentricity values under s-μG and s-μG + IR were 0.7845 (25th–75th percentile: 0.7331–0.8189) and 0.7672 (25th–75th percentile: 0.7171–0.8024), respectively, which were not significantly different from control cells (median 0.7674, 25th–75th percentile: 0.6479–0.8391). Similarly, cells exposed to IR alone showed no significant difference in eccentricity compared to control (median 0.7693, 25th–75th percentile: 0.6325–0.8668, $p = 0.3799$).

Cell solidity was significantly reduced in both s-μG and s-μG + IR groups compared to control, indicating increased shape irregularity (s-μG vs. Control, $p < 0.0001$; s-μG + IR vs. Control, $p < 0.0001$). Median solidity values were 0.9269 (25th–75th percentile: 0.9154–0.9372) for s-μG and 0.9270 (25th–75th percentile: 0.9059–0.9414) for s-μG + IR, both significantly lower than the control group's median solidity of 0.9568 (25th–75th percentile: 0.9369–0.9719). In contrast, cells treated with IR alone had a median solidity of 0.9508 (25th–75th percentile: 0.9111–0.9751), which did not significantly differ from the control ($p = 0.2669$).

The analysis of nuclear area revealed significant enlargement in the s-μG and s-μG + IR groups compared to control ($p < 0.0001$). Nuclei in the s-μG group had a significantly larger area than those in the control group, with a median area of 239.7 μm² (25th–75th percentile: 214.1–268.3 μm²; $p < 0.0001$). Similarly, nuclei in the s-μG + IR group displayed a significant increase in area compared to control, with a median of 243.0 μm² (25th–75th percentile: 214.7–278.7 μm²; $p < 0.0001$). Control nuclei had a smaller median area of 138.0 μm² (25th–75th percentile: 94.72–207.1 μm²). Nuclei exposed to IR alone did not significantly differ in area from the control (median 156.4 μm², 25th–75th percentile: 106.2–194.5 μm²; $p > 0.9999$), indicating that radiation alone does not significantly affect nuclear size.

Nuclear eccentricity also showed significant differences among groups ($p < 0.0001$). Nuclei under s-μG exhibited a reduced eccentricity with a median value of 0.6693 (25th–75th percentile: 0.6324–

0.7266), indicating a more circular shape compared to control nuclei, which had a median eccentricity of 0.7415 (25th–75th percentile: 0.6265–0.8423). The reduction in eccentricity under s-μG was statistically significant ($p = 0.0375$). Similarly, nuclei in the s-μG + IR group also showed significantly reduced eccentricity, with a median value of 0.6336 (25th–75th percentile: 0.6118–0.6764), compared to control ($p < 0.0001$). In contrast, IR alone did not significantly affect nuclear eccentricity compared to control, with a median of 0.7461 (25th–75th percentile: 0.5601–0.8436) ($p > 0.9999$).

Overall, the study demonstrated that s-μG and combined s-μG + IR treatments significantly influenced both cell and nuclear morphology, leading to increased cell and nuclear areas and decreased cell solidity and nuclear eccentricity. IR alone, however, showed no significant effects on these parameters compared to control conditions, highlighting the distinct morphological adaptations induced by simulated microgravity and combined stress conditions.

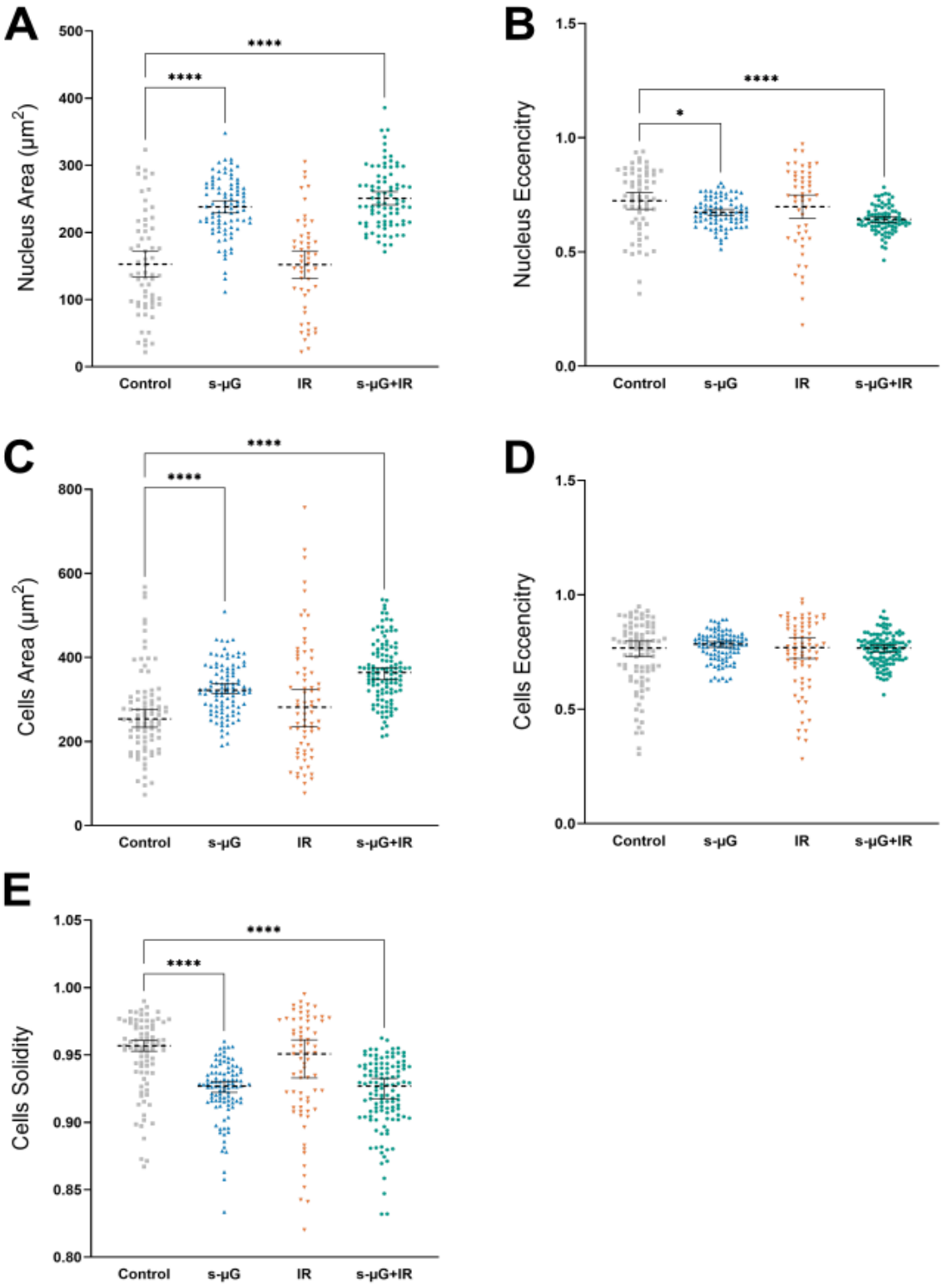


*Figure 4.24 Quantification of AC-16 Cardiomyocytes Morphological Changes. Dot plots representing single-cell morphological changes in AC-16 cardiomyocytes at 72 hours post-treatment, showing (A) nuclei area (µm²), (B) nuclei eccentricity, (C) cellular area (µm²), (D) cellular eccentricity, and (E) cellular solidity for cells subjected to static conditions, s-µG, IR, and combined s-µG+IR. Statistical analysis was conducted using the Kruskal-Wallis test (N = 3), with Dunn's multiple comparisons test to identify significant differences between groups. Significance levels: * ($p \leq 0.05$), **** ($p \leq 0.0001$).*

## 4.5 DISCUSSION

This chapter aimed to evaluate AC-16 Cardiomyocyte responses to s-μG, radiation, and their combined impact in a 2D environment. The result section of this chapter comprehensively explored the responses of AC-16 cardiomyocytes to s-μG, IR, and their combined effects by following the aim and objectives set out at the beginning of this research project.

A summary of the relevant sections and the objectives they cover are shown in Figure 4.25. To contextualise these findings within the broader landscape of cellular biology and space medicine, this discussion aims to integrate the observed cellular behaviours presented in the results (Section 4.4) — spanning changes in proliferation, viability, gene expression, DNA damage repair, and mechanotransduction signalling—into a cohesive understanding of AC-16 cardiomyocyte responses to s-μG, radiation, and their combined impact in a 2D environment.

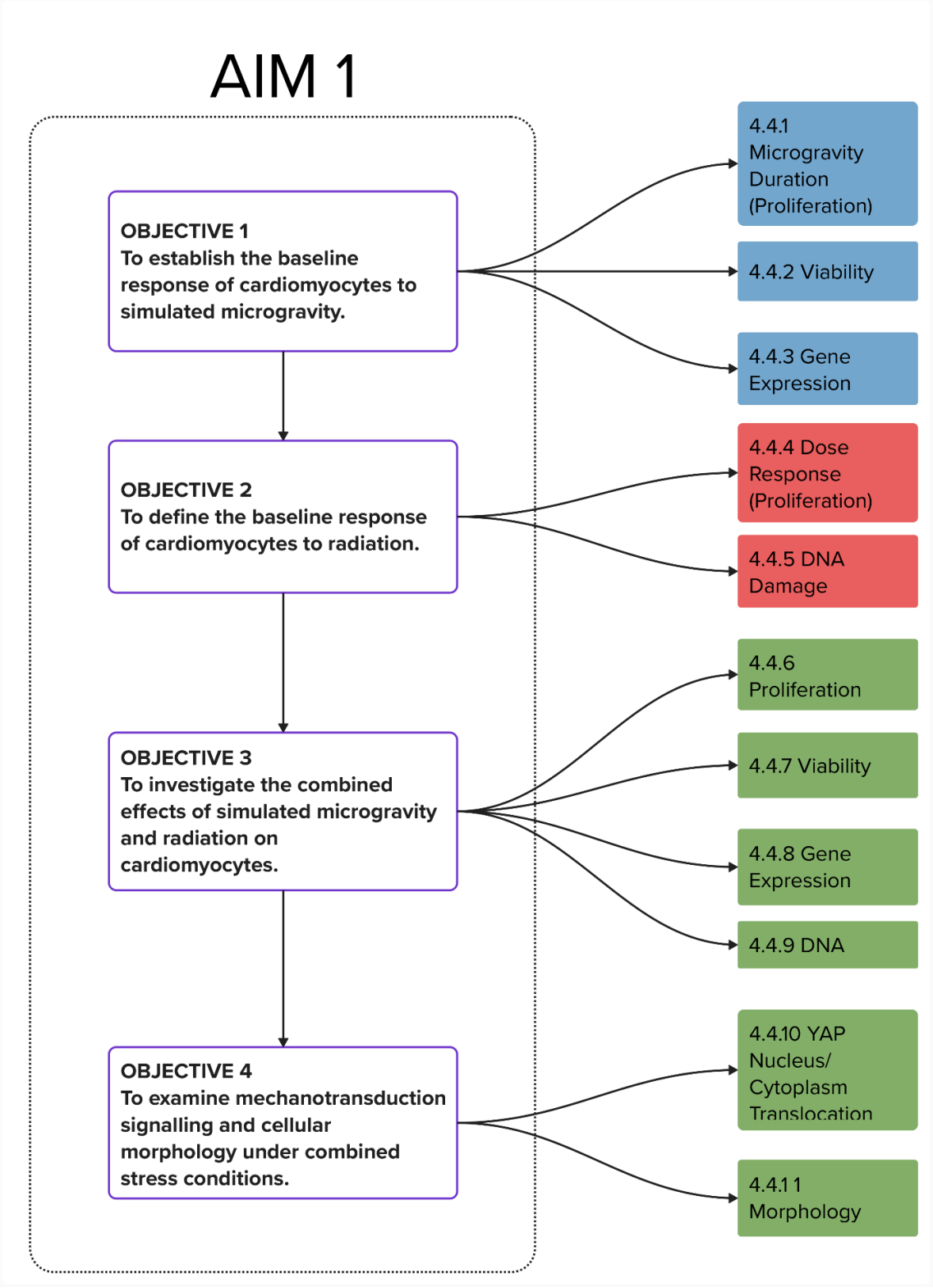


*Figure 4.25 Summary Mindmap that Captures the Objectives in Aim 1 and the Corresponding Section of the Chapters that Fulfills Those Objectives.*

### 4.5.1 Evaluating Cardiomyocyte Responses to Simulated Microgravity: Proliferation, Viability, and Gene Expression Analysis

Objective 1 of this study set out to establish the reference response of cardiomyocytes to s-μG, focusing on proliferation, viability, and gene expression changes. The results revealed varied responses at different seeding densities under s-μG, though these variances were not statistically significant. Nonetheless, the observed fluctuations suggest that s-μG still affects cellular metabolic activity, indicating an interaction between the microgravity environment and cell proliferation processes. Given that the results were normalised to static control, it was observed that at higher seeding densities, cells exposed to s-μG demonstrated increased proliferation compared to the static control at the same observation times. Over time, however, this trend reversed, with the proliferation of cells under s-μG decreasing below control levels. Supporting this observation, the LIVE/DEAD viability assay employed in this study showed a significant decrease in viability after 72 hours of s-μG exposure. The decrease in cell proliferation and viability at later stages mirrors the findings in differentiated skeletal muscle, macrophages, murine osteoblasts, and human male germ cells exposed to s-μG conditions. (Guarnieri et al., 2021; Morabito et al., 2017, 2020; L. Shi et al., 2021)

The differing observations in Figures 4.9 and 4.10 underscore the impact of culture format on AC-16 cardiomyocyte responses to s-μG. Figure 4.9, which utilized a 96-well plate format for the LIVE/DEAD assay, did not show cell aggregation, with significant reductions in viability observed over time. This result is likely due to the confined environment of the 96-well plate, which may limit cell-cell interactions and expose cells to higher shear stress. In contrast, Figure 4.10 demonstrates cell aggregation in a flask environment, where a larger culture surface area and medium volume were used. The flask was necessary for PCR experiments to ensure sufficient cell numbers for RNA extraction and subsequent gene expression analysis. However, this requirement introduces variability, as different culture conditions can influence cell behavior. This inconsistency represents a limitation of the study, suggesting that future experiments should aim to standardize culture conditions across all assays where possible or explore alternative methods to reduce variability between different experimental setups. Standardizing the culture environment could help provide more consistent and comparable results regarding cell viability, proliferation, and gene expression under s-μG conditions.

Interestingly, the effects of s-μG on cell proliferation and viability have been demonstrated to differ in stem cells and cardiomyocytes derived from pluripotent stem cells. Rampoldi et al (2022) demonstrated enhanced cell proliferation that supports the efficient production of cardiomyocytes with optimal characteristics – suggesting a beneficial aspect of microgravity on human induced pluripotent stem cell (hiPSC)-derived cardiomyocytes. Similarly, Jha et al (2016) found that the integration of 3D culture techniques with s-μG exposure also boosts the viability, proliferation, and differentiation of cardiac progenitors from hiPSCs, further supporting the notion that microgravity

can positively influence stem cell-derived cardiomyocytes. However, contrary to these findings, the study by Wang et al (2019) highlighted a reduction in proliferation due to cell cycle arrest in hematopoietic stem cells (HSCs) under microgravity conditions. This finding aligns with observations of decreased proliferation linked to cell cycle arrest in various cell types. (Guarnieri et al., 2021; Morabito et al., 2017, 2020; L. Shi et al., 2021)

AC-16 human cardiomyocyte cells responded to s-μG, which aligns with their mature, differentiated status, showing decreased proliferation and viability similar to other differentiated cells. (Guarnieri et al., 2021; Morabito et al., 2017, 2020; L. Shi et al., 2021) This response can be attributed to the inherent limitations of mature cells in adapting to the distinct stressors introduced by microgravity, constraining their ability to modulate cellular processes effectively in response to the atypical conditions of microgravity. hiPSC-CMs demonstrated a more favourable response to s-μG, likely due to their developmental stage (Jha et al., 2016). Their enhanced proliferation and differentiation under microgravity conditions suggest that the unique environmental stresses and mechanical forces of s-μG could be conducive to heart cell development. The distinct behaviour of AC-16 and hiPSC-CMs under s-μG conditions, therefore, calls for further investigation to fully unravel the complexities of cardiomyocyte adaptation to microgravity and the importance of taking the cellular origin and stage of development into consideration when evaluating the impact of microgravity on cardiomyocytes. However, it is interesting to note that the consistency of cell cycle arrest as a mechanism affecting cell proliferation also highlights its significance in the response of both stem cells and differentiated cells to microgravity.

Despite alterations in proliferation and viability, the findings of this study indicate that gene expression related to mechanotransduction, and stress response remains stable in AC-16 cardiomyocytes. This stability contrasts with other studies documenting significant gene expression alterations in cardiac cells under microgravity conditions. For example, Kumar et al (2021) and Rudimov et al (2017) reported that exposure to spaceflight and s-μG led to modifications in genes related to the cell cycle, apoptosis, redox balance, cell motility, and proliferation in ventricular tissue from mice and cultured endothelial cells, respectively. Additionally, research conducted by Camberos et al (2019) and Guarnieri et al (2021) On CPCs and research (2019) on hiPSC-CM exposed to space microgravity collectively demonstrated upregulated genes involved in cell proliferation, survival, cardiac differentiation and contraction. The lack of gene expression changes in AC-16 cardiomyocytes suggests that the observed adaptations to s-μG might be mediated through other mechanisms, such as alterations in metabolic pathways, DNA methylation, and intracellular communication. (Singh et al., 2010; Wise et al., 2021; H. Zhang et al., 2020) Given the inconsistent findings involving the responses of AC-16 cardiomyocytes from this study and other studies involving exposure of various cells, including cardiomyocytes, to microgravity, further and comprehensive analysis is necessary to understand the reasons behind the differences.

One limitation of this study is the potential overestimation of cell viability due to the exclusion of detached, non-viable cells from the analysis. Cells that detached from the well-plate during exposure to s-μG and ionizing radiation were not collected from the culture media or analyzed for viability. This could result in an artificial increase in the observed cell viability, as only attached cells were counted. Future studies should consider collecting and analyzing detached cells from the culture media to provide a more comprehensive assessment of cell viability under these conditions.

In conclusion, these findings collectively achieved Objective 1, providing a comprehensive understanding of the impact of s-μG on AC-16 cardiomyocyte proliferation, viability, and the stability of gene expression. These results serve as a foundational dataset for characterising the response of AC-16 human cardiomyocytes to s-μG.

### 4.5.2 Characterizing Cardiomyocyte Responses to Ionizing Radiation: DNA Damage and Repair Dynamics

Objective 2 aimed to characterise the AC-16 cardiomyocytes' response to radiation. A significant decrease in proliferation was observed in AC-16 cardiomyocytes from 96 hours post-IR for doses of 1 Gy and higher. This finding further emphasises the vulnerability of cardiomyocytes to radiation-induced proliferative inhibition. The study monitored γ-H2AX, a marker of DNA double-strand breaks, foci over 24 hours post-IR and revealed an immediate and substantial DNA damage response following IR, which gradually declined. This finding indicates the activation of DNA repair mechanisms with most DSBs repaired within 24 hours of radiation exposure, indicating an efficient DNA repair response to radiation-induced damage, consistent with existing literature (Frieß et al., 2015). Additionally, the study observed significant dose-dependent variations in γ-H2AX foci dynamics between cardiomyocytes exposed to 2 Gy versus 0.5 Gy IR, demonstrating a dose-dependent DNA damage and repair response, aligning with the findings from prior research. (Frank et al., 2014; Ugenskiene et al., 2009; Venkateswarlu et al., 2015)

The significant reduction in cell proliferation at higher doses and the evident DNA damage indicated by γ-H2AX foci formation highlights the detrimental effects of radiation exposure on cardiomyocyte health. The determination of LD50 values, alongside a thorough investigation into DNA repair mechanisms, established a quantitative benchmark for evaluating cardiomyocyte sensitivity to radiation. These results, therefore, not only achieved Objective 2 by defining the reference response of cardiomyocytes to radiation but also laid the groundwork for further research in this study on the combined impacts of microgravity and radiation, ultimately contributing to our understanding of cardiovascular health and risks in spaceflight environments.

### 4.5.3 Exploring the Effects of Simulated Microgravity and Radiation on Cardiomyocyte Function

Building on the findings from Objectives 1 and 2, Objective 3 sought to use the results and knowledge gathered from Objectives 1 and 2 to identify the effects of s-μG and IR on different cellular outputs. Contrary to initial expectations of pronounced adverse outcomes from the dual application of stressors, statistical analysis did not demonstrate a significant interaction between radiation and cellular proliferation rates with or without the application of s-μG. Nonetheless, it was identified that the interaction between treatment modalities and seeding density significantly impacted cellular proliferation, indicating a dependency of the cellular response to s-μG on the density of the cell population. This finding aligns with the absence of statistical significance in interaction effects. Yet, a discernible trend towards reduced proliferation under s-μG conditions was observed, especially at elevated radiation doses, suggesting a nuanced influence of s-μG on cell metabolism. This observation is consistent with the outcomes of Objective 1, which primarily focused on the response of cells to s-μG in isolation.

Building on this study, the analysis of cell viability demonstrated a significant reduction in cell viability due to s-μG, whereas 2Gy IR did not demonstrate any significant reduction. However, there was a noticeable decrease in cell viability when combined, with the cells' survival decreasing by about 25%. Aligning with findings from prior studies (Moreno-Villanueva et al., 2018; Tan et al., 2020), the findings from this study corroborate the notion that IR increases the cells' sensitivity to s-μG. The reduction in cell viability highlights a compounded effect significantly greater than the stressors alone, emphasising the need to explore further the cellular mechanisms in environments where both stressors are present.

Despite these observations of altered proliferation and reduced viability, gene expression analyses under combined stress conditions mirrored the stability in response to s-μG alone. This stability again highlights the potential involvement of alternative regulatory mechanisms, similar to what was previously discussed in Section 4.5.1, mechanisms that may operate at the post-transcriptional level or through modifications in metabolic pathways, which maintain the integrity of gene expression patterns even under compounded environmental stress. (Singh et al., 2010; Wise et al., 2021; H. Zhang et al., 2020)

The consistency of gene expression stability under various experimental conditions—under s-μG alone and in conjunction with IR—highlights the intricate nature of cellular stress adaption. It suggests that while AC-16 cardiomyocytes are sensitive to changes in their environment, as indicated by the changes in proliferation and viability, they also have a robust mechanism to stabilise gene expression in the face of these environmental stressors. This resistance to genetic changes necessitates

additional research into the cellular and molecular mechanisms that allow such an adaptive response. Understanding these mechanisms is crucial for understanding the cellular response to spaceflight environments and devising measures to reduce the negative impacts of such environmental stressors on human health during long-duration space missions.

The results from this study on the combined effects of s-μG and 2 Gy IR on AC-16 cardiomyocytes aimed to examine the implications of the addition of s-μG on the observed DNA damage and repair dynamics, as dictated by the presence and number of γ-H2AX foci. Similar to the preliminary experiment (Section 4.4.5) and other studies, the marked increase in γ-H2AX foci after IR exposure peaked at 1 hour. Subsequently, it declined, illustrating the cells' capacity for repair. The initial higher count of γ-H2AX foci in cells subjected to combined s-μG and 2 Gy IR and their subsequent repair trajectory indicates an exacerbated but manageable DNA damage under these conditions. (Frank et al., 2014; Frieß et al., 2015; Ugenskiene et al., 2009; Venkateswarlu et al., 2015)

The absence of statistical difference in DNA repair efficiency between treatment groups across various time points suggests that the AC-16 cardiomyocytes possess a robust DNA repair mechanism that is not significantly compromised by the additional stress of s-μG. This observation suggests a potential resilience and raises intriguing questions about the cellular and molecular mechanisms that facilitate this resilience. This may have significant implications for human health in space and must be investigated further.

By thoroughly investigating the effects of combined s-μG and 2 Gy IR exposure on cardiomyocyte proliferation, viability, gene expression, and DNA repair dynamics, this research successfully addressed Objective 3. Using the knowledge gained from Objectives 1 and 2, the research effectively planned and conducted tests to investigate the effects of s-μG and IR. This strategy made it possible to create an experiment with an optimal design that closely examined the reaction of the cardiomyocytes by employing fine-tuned timings and parameters. Furthermore, the findings identified an effect on the cell's viability whilst not significantly impacting proliferation, gene expression and DNA damage mechanism.

### 4.5.4 Assessing Mechanotransduction Signalling and Morphological Changes in Cardiomyocytes Under Combined Stress Conditions

Building on Objective 3, which examined the response of AC-16 cardiomyocytes to combined s-μG and IR, Objective 4 sets out to further examine mechanotransduction signalling and cellular morphology under s-μG and IR. YAP localisation plays a pivotal role in the cell's mechanotransduction response, with its nuclear presence promoting cell growth through the

activation of growth-related genes and its cytoplasmic localisation signalling a halt in growth by restricting access to DNA and gene activation processes.

Preliminary experiments to characterise AC-16 cardiomyocytes to s-μG alone provided a critical reference point, highlighting the sensitivity of AC-16 cardiomyocytes to changes in their mechanical environment. These experiments emphasised the impact of s-μG on YAP localisation, with significant differences observed when comparing s-μG-treated cells to both the pre-experiment 0-hour control and static conditions over 72 hours. This shift in YAP localisation to the nucleus reflects the cell's attempt to adapt to the altered mechanical environment, and given YAP's role in regulating genes essential for cell growth and survival, its nuclear localisation would normally lead to activation of genes that amplify the cellular response to environmental cues. (Bertini et al., 2009; Franklin et al., 2020; Kwon et al., 2022; Panciera et al., 2017; Piccolo et al., 2014; Pocaterra et al., 2020; Shreberk-Shaked & Oren, 2019; B. Zhao et al., 2010)

After the initial experiment, the influence of combining s-μG and IR on YAP localisation was examined over a period incorporating 72 hours of s-μG followed by 48 hours of IR. The results indicated a notable increase in YAP's nuclear presence when exposed to s-μG and IR independently, with a more profound increase due to IR. The significant nuclear accumulation of YAP in cells exposed to IR independently highlights the role of YAP as a mediator in the cellular response to genotoxic stress. Interestingly, when cells were exposed to both s-μG and IR, the expected additive effect on YAP localisation was not observed. Instead, YAP distribution was comparable to the control, indicating that the combination of s-μG and IR triggers a unique cellular response that changes YAP behaviour differently than when each stressor is applied in isolation.

Numerous studies have consistently shown that the nuclear localisation of the YAP protein influences gene expression without changing the expression of its encoding gene, YAP1. This distinction underlines a separation between the protein's function and its gene's expression levels, showcasing how mechanical cues from the cellular environment direct YAP's activity as a transcriptional co-activator. These findings highlight YAP's role in enabling cells to adaptively respond to their environment rather than through direct autoregulation of its gene expression. (Bertini et al., 2009; Franklin et al., 2020; Kwon et al., 2022; Panciera et al., 2017; Piccolo et al., 2014; Pocaterra et al., 2020; Shreberk-Shaked & Oren, 2019; B. Zhao et al., 2010) The absence of changes in YAP1 gene expression, despite increased nuclear localisation of YAP, further confirmed the notion mentioned earlier in section 4.5.1, where the observed differences in responses could be attributed to regulatory mechanisms employing post-transcriptional and post-translational modifications to preserve cellular functionality under microgravity. (Zevolis et al., 2022).

As mechanical cues from the cellular environment modulate YAP translocation, it is a critical link to understanding the importance of cellular morphology and shape analysis in mechanobiology. The spatial positioning of YAP, influenced by factors such as matrix stiffness and cell geometry, underscores the role of cellular architecture in dictating functional outcomes. (Das et al., 2016; Lin et al., 2014; Major et al., 2019; Sero & Bakal, 2017; Xin et al., 2011; Y. Zhang et al., 2021)Thus, investigating cell shape and morphology changes provides insight into the mechanotransductive pathways activated or suppressed in response to mechanical stimuli and how they ultimately impact gene expression, cellular behaviour, and fate decisions.

The next stage of this study examined the impact of s-μG, IR, and their combination s-μG+IR on AC-16 cardiomyocytes, focusing on cellular and nuclear morphology through measurements of area, eccentricity, and solidity.

The morphological analysis revealed that both s-μG and s-μG + IR treatments significantly increased cellular and nuclear areas, suggesting cell enlargement under microgravity conditions. This finding is consistent with previous studies, such as those by Barravecchia et al., who also observed increased cellular and nuclear areas in endothelial cells following spaceflight exposure (Barravecchia et al., 2021). The lack of significant changes in cellular and nuclear areas in response to IR alone indicates that microgravity, rather than radiation, plays a more dominant role in influencing cell and nuclear enlargement under these experimental conditions.

The decrease in cell solidity observed in the s-μG and s-μG + IR groups suggest a reduction in structural integrity. This reduction in solidity points towards increased cellular flexibility and decreased mechanical stiffness, highlighting the potential impact of microgravity on cytoskeletal dynamics. In contrast, IR alone had a minimal effect on cell solidity, further emphasizing the unique influence of microgravity on cellular architecture.

Interestingly, despite the changes in solidity and area, cell eccentricity remained largely consistent across all treatments, with cells maintaining their overall shape and elongation under environmental stressors. This is likely due to robust cytoskeletal networks, including actin filaments, microtubules, and intermediate filaments that preserve cell geometry. This cytoskeletal integrity allows cardiomyocytes to maintain their elongated morphology even when experiencing structural changes. However, the nucleus responds differently, with significant reductions in nuclear eccentricity observed under s-μG and s-μG + IR, while exposure to IR alone does not significantly alter nuclear shape. These findings suggest that microgravity uniquely disrupts the mechanical stability of the nucleus, leading to changes in nuclear morphology that are distinct from the cellular response.

Studies have shown that microgravity alters the tension exerted by perinuclear actin fibers, which are critical for nuclear positioning and stability (Radstake et al., 2023; Thiel et al., 2019). This disruption leads to a more rounded nuclear shape and reflects a decoupling of nuclear and cellular mechanics, where the cell maintains its overall shape while the nucleus becomes more circular(Khatau et al., 2012; Y. Li et al., 2015; Ye et al., 2014). The softening of the nuclear lamina under microgravity further reduces nuclear rigidity, emphasizing nucleus sensitivity to mechanical unloading (Bahnamiri & Roller, 2021; Stiekema et al., 2020).

A key mechanism behind these changes involves the LINC (Linker of Nucleoskeleton and Cytoskeleton) complex, which mechanically couples the nucleus to the cytoskeleton (Fu, 2024; Touchstone et al., 2019). Disruption of the LINC complex under microgravity impairs the transmission of mechanical signals, making the nucleus more susceptible to deformation, which can affect gene expression and cellular function (Neelam et al., 2020). Combined with the effects of radiation, these changes can compromise nuclear architecture, as evidenced by increased chromosome aberrations (Hada et al., 2018).

The altered mechanical properties of the nucleus have significant implications for cardiomyocyte function, particularly in mechanotransduction. Mechanotransduction is essential for regulating cardiomyocyte contractility, gene expression, and adaptation to mechanical stress. The reduction in nuclear eccentricity under s-μG and s-μG + IR could disrupt these pathways, impairing the cell's ability to respond to mechanical cues like stretch and pressure, which are critical for cardiac function.

In conclusion, the differential changes in cellular and nuclear eccentricity highlight the complex response of cardiomyocytes to mechanical stressors, where cellular morphology is preserved, but the nucleus undergoes significant alterations. These findings emphasize the importance of considering both nuclear and cellular morphology when assessing cardiomyocyte function under altered mechanical conditions, providing insights into the adaptation and vulnerability of cardiac cells in spaceflight and clinical settings.

## 4.6 KEY FINDINGS

- Cardiomyocytes exhibited varied responses in proliferation, viability, and gene expression under s-μG, with initial increases in proliferation at higher seeding densities and a significant decrease in viability after 72 hours.
- Post-IR, AC-16 cardiomyocytes showed reduced proliferation from 96 hours at doses ≥1 Gy, with immediate substantial DNA damage marked by γ-H2AX foci, largely repaired within 24 hours, demonstrating effective, dose-dependent DNA repair dynamics.
- Combined s-μG and 2 Gy IR exposure did not significantly alter proliferation interactions but reduced cell viability by 25%, indicating that combined stressors exacerbate cell sensitivity and overall detrimental effects.
- Significant nuclear YAP accumulation under s-μG and IR highlighted its role in stress adaptation, with marked morphological changes. These changes included increased cell and nuclear areas and decreased solidity under combined conditions.

## 4.7 KEY LIMITATIONS

- Each experiment assessing proliferation, mechanotransduction, and DNA damage used only one marker, limiting the depth and robustness of findings.
- The use of AC-16 cells, which lack contractility and striations, limits the ability to model native cardiac tissue behaviour.
- The 2D experiments did not replicate *in vivo* cardiomyocyte density, potentially impacting cellular communication and mechanotransduction.
- The segmentation methods may not fully capture detailed cell morphology and organisation, affecting data interpretation.
- The study did not collect culture media to assess detached, non-viable cells, which were not accounted for in cell viability analysis.

For a more detailed discussion and potential resolutions to these limitations, please refer to Section 7.4.

# Chapter 5 -

# Investigating Responses Of 3D Collagen Hydrogel Heart Model Exposed to Simulated Microgravity and Radiation

## 5.1 INTRODUCTION

In Chapter 5, the investigation of cardiomyocyte responses transitioned from experiments conducted within two-dimensional (2D) environments to more complex three-dimensional (3D) cultures embedded in collagen matrices. This chapter sought to link the fundamental knowledge acquired from 2D settings and the dynamic reactions observed within 3D collagen hydrogel models, which more closely resemble the natural cardiac environment, providing a more authentic environment to observe cellular behaviour and interactions under simulated microgravity (s-μG) and radiation (IR).

Collagen-based hydrogels have been identified as promising tools to facilitate the 3D organisation of AC-16 human cardiomyocytes, utilised in numerous studies, where collagen hydrogels were utilised as biomimetic scaffolds by mimicking the mechanical and physical properties of the cardiac ECM. (Duan et al., 2011; Edalat et al., 2019; Gishto et al., 2015; Rashedi et al., 2017). Continuing the focus on proliferation, viability, gene expression, DNA damage, and mechanotransduction, this progression into 3D cultures aimed to uncover the intricate mechanisms of cardiomyocyte adaptability and their responses to IR and s-μG. Additionally, it highlighted the significance of model selection in research, emphasising the importance of 3D modelling in advancing our comprehension of cellular biology and its implications for experimental design and research methodologies.

## 5.2 AIM AND OBJECTIVES

This chapter shifted the focus towards the second aim, which centred on developing a tissue-engineered 3D collagen model to analyse microgravity and radiation's effects on cardiomyocytes comprehensively. This aim aimed to provide a more physiologically relevant understanding of cardiomyocyte responses within a 3D environment, thus bridging the gap between traditional 2D studies and the complex realities of the cardiac microenvironment.

Aim 2: To Develop a 3D Collagen Model and Comprehensively Evaluate the Impact of Simulated Microgravity, Radiation and Their Combination on Cardiomyocytes in a 3D Environment.

Objectives for Aim 2:

1. To develop and validate a 3D collagen-based hydrogel focusing on scaffold optimisation for cell embedding and functionality for studying cardiomyocyte responses.
2. To investigate how s-μG and IR individually and in combination influence cell behaviour in 3D, focusing on mechanotransduction involving YAP1 and DNA damage assessment with γH2AX in the 3D model
3. To evaluate differences in cardiomyocyte reactions to s-μG, IR, and their combination in 2D versus 3D environments to understand the impact of dimensional context on cellular behaviour and stress responses.

## 5.3 METHODS

This section of Chapter 5 presents the methods utilised to prepare the collagen hydrogel embedding the AC-16 cardiomyocytes and methods employed subsequently to investigate AC-16 cardiomyocytes' responses to s-μG and IR stressors within a 3D environment, describing a structured approach that aligns with the research aims and objectives - illustrated in Figure 5.1.

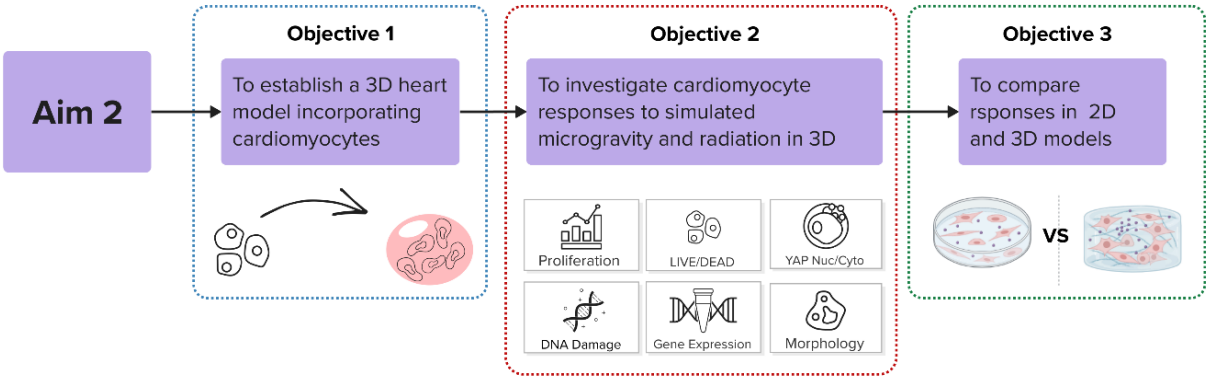


*Figure 5.1 Flow Chart Illustrating Methods Utilised in this Chapter that Corresponds to the Objectives.*

### 5.3.1 Preparation of AC-16 Cardiomyocytes in Collagen Hydrogels

Considering the limitations of 2D cell cultures in mimicking physiological conditions, a shift to a 3D environment was pursued to investigate potential differences in cell behaviours. The preparation of the collagen hydrogel embedded with AC-16 cardiomyocytes commenced with the cultivation of cells to confluency in a T175 flask under standard conditions (37°C, 5% (v/v) $CO_2$ in air), as detailed in Chapter 3, Section 3.5.1. Upon reaching approximately 80% confluency, the culture medium was aspirated, and cells were rinsed with 10 mL PBS to eliminate residual media. Subsequently, 5 mL of Trypsin was added to facilitate cell detachment during a 5-minute incubation at 37°C. Following confirmation of cell detachment under a brightfield microscope, 5 mL of complete culture media was added to neutralise the trypsin. The resulting cell suspension containing AC-16 cardiomyocytes was collected in a sterile 15 mL centrifuge tube and centrifuged at 500 g for 5 minutes at room temperature. The supernatant, comprising waste media and trypsin, was discarded, leaving behind AC-16 cardiomyocyte cell pellets. Cell counting (Chapter 3, Section 3.5.1.4) was performed, and cell aliquots were prepared in media at $1x10^6$ cells. $mL^{-1}$

The stock collagen, neutralising solution and PBS were handled under sterile conditions at 4°C on ice, ensuring their preservation throughout the process. Determination of the required collagen volume preceded the experiment. Aseptically, one part of the chilled neutralisation solution was transferred to a sterile 50 mL centrifuge tube, followed by adding nine parts of Rat Tail Collagen, totalling 10 parts. Gentle mixing and avoiding vortexing to prevent unintended disruption of the

collagen mixture achieved a homogenous solution. With the provided stock collagen concentration of 4 mg. $mL^{-1}$, neutralised collagen reached a 3.6 mg. $mL^{-1}$ concentration. To attain the target concentration of 3 mg. $mL^{-1}$, precise volumes of media-containing cells were meticulously added to the neutralised collagen solution, employing a ratio of 200 µL of media per mL of the collagen solution.

The resulting collagen mixture containing AC-16 cardiomyocyte cells in a final concentration of 3 mg. $mL^{-1}$ was then dispensed into designated culture wells. As the collagen hydrogel was viscous, the 200uL pipette tip with the end removed using scissors allowed for a larger extrusion hole. Following this, the samples underwent incubation (37°C, 5% (v/v) $CO_2$ in air) at room temperature for 30 minutes, followed by 37°C for 30 minutes (refer to Section 6.4.1.3), facilitating gel formation. Subsequently, complete culture media was added to each well, and the 3D collagen cells were further incubated overnight, ensuring their readiness for experimentation the following day.

### 5.3.2 Proliferation of AC-16 Cardiomyocytes in 3D Collagen Model

Initial experiments on s-µG exposure involved 6, 24, 48, and 72 hours in 3D hydrogels. Concurrent experiments combining s-µG and IR focused solely on a 72-hour duration and radiation doses ranging from 0 Gy to 6 Gy. This specific range was selected based on previous findings demonstrating its effectiveness in treatment comparisons. Details of these experimental parameters are summarised in Table 5.3.1.

*Table 5.1 Summary of 2D Proliferation Experiments on AC-16 Cardiomyocytes.*

*Summary of experiments assessing the effects of varying s-µG exposure durations and IR doses on AC-16 cardiomyocyte proliferation.*

<table>
<tr><th colspan="4">3D Proliferation Experiment Summary</th></tr>
<tr><td rowspan="2">Experimental Conditions (Independent Variables)</td><td>Duration of exposure to s-µG</td><td colspan="2">Combination of s-µG and IR</td></tr>
<tr><td>6 hours of s-µG exposure<br>24 hours of s-µG exposure<br>48 hours of s-µG exposure<br>72 hours of s-µG exposure</td><td>Static control<br>s-µG treated</td><td>0Gy 1Gy 2Gy<br>4Gy 6Gy<br>0Gy 1Gy 2Gy<br>4Gy 6Gy</td></tr>
<tr><td>Observed Timepoint (Independent Variables)</td><td>Start of the experiment (time 0)<br>6 hours following initial mounting on RPM<br>24 hours following initial mounting on RPM<br>48 hours following initial mounting on RPM<br>72 hours following initial mounting on RPM</td><td colspan="2">96 hours following initial mounting on RPM.<br>72 hours post-IR</td></tr>
</table>

A volume of 20uL of the collagen hydrogel containing AC-16 human cardiomyocytes was dispensed into specialised 96-well plates with detachable strips. Following overnight incubation at 37°C and 5% (v/v) $CO_2$ to allow cellular adjustment, the cells were prepared according to the described methodology in Section 3.5.2.4. Each well was securely sealed using silicone plugs and covered with a gas-permeable hydrophobic porous sealing film to facilitate exposure to s-μG, IR, or their combination as described in Chapter 3, Section 3.5.2.

To assess the impact of s-μG, IR, and their combination on the proliferative capacity of AC-16 human cardiomyocytes in a 3D collagen hydrogel, a modified PrestoBlue™ Cell Viability Reagent assay based on the procedures detailed in Section 3.6.1 was utilised. Post-incubation, fluorescence and absorbance measurements were taken only from the solution that had been incubated with the 3D collagen hydrogel to eliminate any interference from the matrix by carefully transferring the hydrogel containing the AC-16 cardiomyocytes to a new well plate and performing a Live/Dead viability assay on them (further described in Section 5.3.3). Experimental controls comprised wells filled solely with 3D collagen matrices without cells and blank wells to account for inherent background fluorescence and absorbance. Subsequent data processing and data normalisation followed the methodology described in Section 3.6.1.

The processed data underwent Kruskal-Wallis analysis to assess variations in cell viability, a choice informed by the non-normal distribution of data as confirmed by Shapiro-Wilk tests. Where significant differences were detected, Dunn's multiple comparison tests were applied to pinpoint the specific variations between conditions.

### 5.3.3 Viability in 3D Collagen Model

To evaluate AC-16 cardiomyocyte cell viability alterations within the 3D hydrogel environment and responses to the combination of s-μG and IR, s-μG + IR were specifically administered with a radiation dose of 2 Gy and assessed after 72 hours of s-μG. To distinguish between live and dead cells, the LIVE/DEAD assay was employed, with subsequent capture of fluorescent images for detailed analysis, as outlined in Section 3.6.2. Viability data were normalised to the control group, which consisted of cells in 3D collagen matrices unexposed to s-μG or IR, to enable comparisons.

Due to the non-normal data distribution, confirmed by Shapiro-Wilk tests with p-values less than 0.05, the Kruskal-Wallis test was selected for statistical evaluation to identify significant differences in cell viability among the conditions tested across different groups.

### 5.3.4 Gene Expression Analysis using qRT-PCR.

Further examination into the impact of s-μG and IR on gene expression within a 3D cellular environment, the choice of these specific genes is rooted in their pivotal roles in cardiomyocytes' structural organisation, cellular communication, and adaptive mechanisms. YAP1's central role in orchestrating cellular growth and adaptation holds significance within the complex spatial arrangement of cardiomyocytes in 3D, where alterations in YAP1-mediated gene expression due to microgravity and radiation profoundly shape structural responses crucial for cellular adaptation in this intricate context. Similarly, RHOA's pivotal regulation of cytoskeletal dynamics within the 3D structure of cardiomyocytes influences cellular architecture and contractility, which is pivotal for comprehending how altered gravity and radiation influence cellular organisation and function in a 3D setting. Further genes, such as RAC2, emerge as essential within this 3D environment due to their involvement in cellular migration and repair mechanisms, offering insights into tissue repair dynamics. Concurrently, the disruption of CX43-mediated intercellular communication within the 3D cardiomyocyte arrangement significantly affects cellular synchronisation and coordination. Meanwhile, CDH2's role in cell adhesion and mechanosensing deeply influences cellular connectivity and structural integrity in this 3D setting. The selection of these genes for 3D gene expression analysis in response to microgravity and radiation provides a comprehensive understanding of how these stressors influence essential cellular functions and structural integrity within the complex cardiomyocyte framework.

To assess gene expression changes in AC-16 human cardiomyocytes within a 3D collagen matrix subjected to s-μG and IR, the protocol outlined in Section 3.6.3.2 was employed. The genes selected for analysis were consistent with those studied in the 2D experiments (Table 3.6.1. and Table 3.6.2)

AC-16 human cardiomyocytes were seeded in a collagen matrix in 24-well plates (Section 5.3.1). Following 72 hours of s-μG exposure and 48 hours post-IR, 3D hydrogels were enzymatically degraded using collagenase at 37°C to disintegrate the collagen matrix. This was complemented by mechanical disruption using a 21G syringe, ensuring complete cellular release. The resultant mixture was then centrifuged to remove the collagenase supernatant and isolate the cells.

The methods in Section 3.6.3.2 were followed to prepare the samples for RT-qPCR. Briefly, the samples were lysed at the desired time of investigation, and the lysates were stored at -80°C. RNA was extracted using the RNeasy Mini Kit, and the quality and quantity of RNA was determined and then reverse transcribed into cDNA at a 25 ng/uL concentration using the iScript™ cDNA Synthesis Kit. RT-qPCR was subsequently performed using SYBR Green PCR Master Mix.

Log2 fold change was used for gene expression quantification and visualisation. Statistical analysis compared the treatment conditions to the static control and was carried out using two-way ANOVA with Šídák's multiple comparisons tests or Tukey's multiple comparisons. The analysis was conducted using ΔΔCt values to mitigate biases associated with log-transformed data.

### 5.3.5 DNA Damage in 3D Collagen Model

ICC was conducted to assess the expression of DNA damage protein H2AX, a marker for DNA strand breaks in AC-16 cardiomyocytes embedded within a 3D collagen hydrogel. Cells were seeded into a 24-well plate and incubated overnight at 37°C in 5% (v/v) $CO_2$, as described in section 5.3.1. The experimental timeline was adjusted for combined s-μG and IR exposure to acclimatise cells to s-μG conditions; samples designated for s-μG treatment were placed on the RPM 24 hours before radiation exposure. After this 24-hour acclimatisation period, cells were exposed to 2 Gy radiation. The subsequent culture continued either in static or s-μG conditions.

At 0 hours, 10 minutes, 1 hour and 24 hours, the 3D hydrogels underwent a detailed ICC protocol. Briefly, the 3D collagen hydrogels were fixed with 4% (v/v) PFA for 20 minutes at room temperature. The fixed hydrogels were then rinsed twice with PBS and stored in PBS at 4°C until further processing. Once ready, ICC procedures, as detailed in Section 3.6.4, were then initiated. Cell permeabilisation involved treatment with 0.5% (v/v) TritonX-100 for 10 minutes and two PBS washes at room temperature. Hydrogels were subsequently incubated with 4% (w/v) BSA for 30 minutes at room temperature with gentle shaking to ensure non-specific binding. The blocking solution was then replaced with 80 uL of γH2AX primary antibody (1:800; Invitrogen) diluted in 4% (w/v) BSA in PBS buffer, and hydrogels were then incubated overnight at 4°C. The following day, the primary antibody solution was removed, and the hydrogels were subsequently washed with PBS twice at room temperature and, following this, incubated with 80 uL AlexaFluor488 Goat anti-Mouse (1:100; ab150117 abcam) secondary antibody for approximately one hour at room temperature with gentle shaking. Post-secondary antibody incubation, DAPI, was used to counterstain the nucleus, with incubation at room temperature for 10 minutes. Following labelling, the hydrogels were gently washed twice with PBS at room temperature on a shaker for 5 minutes during each wash.

The labelled 3D collagen samples were transferred to specialised chamber slides suitable for confocal microscopy imaging. ProLong™ Glass Antifade Mountant was meticulously applied for sample preservation. Coverslips were gently placed over the samples, and the slides were appropriately sealed and stored at 4°C until confocal microscopy fluorescence imaging was performed.

Statistical data analysis involved two-way ANOVA and post-hoc analyses using Sidak's multiple comparisons test.

### 5.3.6 Assessing Mechanotransduction Response via Immunocytochemistry in 3D

ICC was used to assess the expression and localisation of mechanotransduction components, particularly YAP1, within 3D collagen hydrogels to understand changes in cellular function and mechanotransduction pathways. This methodology builds on the general methods described in Chapter 3 (Section 3.6.4) and follows a similar workflow as described in Chapter 4 but adapted for 3D cell cultures.

The experimental setup for 3D experiments involved embedding cells in collagen hydrogels, with the collagen matrices prepared following the procedure outlined in Section 3.5.2.5. At designated time points, the 3D cultures were fixed using 4% (v/v) PFA for 20 minutes at room temperature. Following fixation, cells were permeabilised with 0.5% (v/v) Triton X-100 in PBS for 30 minutes. After permeabilisation, cells were blocked with 1% (w/v) BSA in PBS for one hour at room temperature. The primary antibody targeting YAP1 (1:200 in 1% (w/v) BSA in PBS) was then applied to the hydrogels and incubated overnight at 4°C. Post-primary antibody incubation, the hydrogels were washed three times with PBS to remove unbound antibodies. Secondary antibodies (Alexa Fluor 488, 1:200) were then applied for one hour at room temperature with gentle shaking to ensure even diffusion into the collagen matrix. Cells were additionally stained with iFluor 594 Phalloidin (1:1000) for F-actin and DAPI (1:1000) for nuclear counterstaining, with incubation times of 20 and 10 minutes, respectively. After staining, the 3D hydrogels were transferred to specialised chamber slides and mounted with ProLong™ Glass Antifade Mountant. Coverslips were placed over the samples and the slides were sealed for storage at 4°C.

Samples of cells embedded in 3D hydrogels were imaged using a LEICA confocal microscope, with z-stacks acquired to capture the full 3D structure of the cells within the hydrogels. Image processing included background subtraction and intensity normalisation across experimental sets to ensure consistency in the fluorescence signals.

### 5.3.7 Summary

Graphical summaries of the experimental timelines followed in this study are illustrated below in Figure 5.2. These figures collectively encapsulate the methodical sequence of events and the investigative scope of the study, offering a visual summary of the experimental approaches undertaken to analyse the cellular responses of cardiomyocytes to spaceflight-relevant stressors.

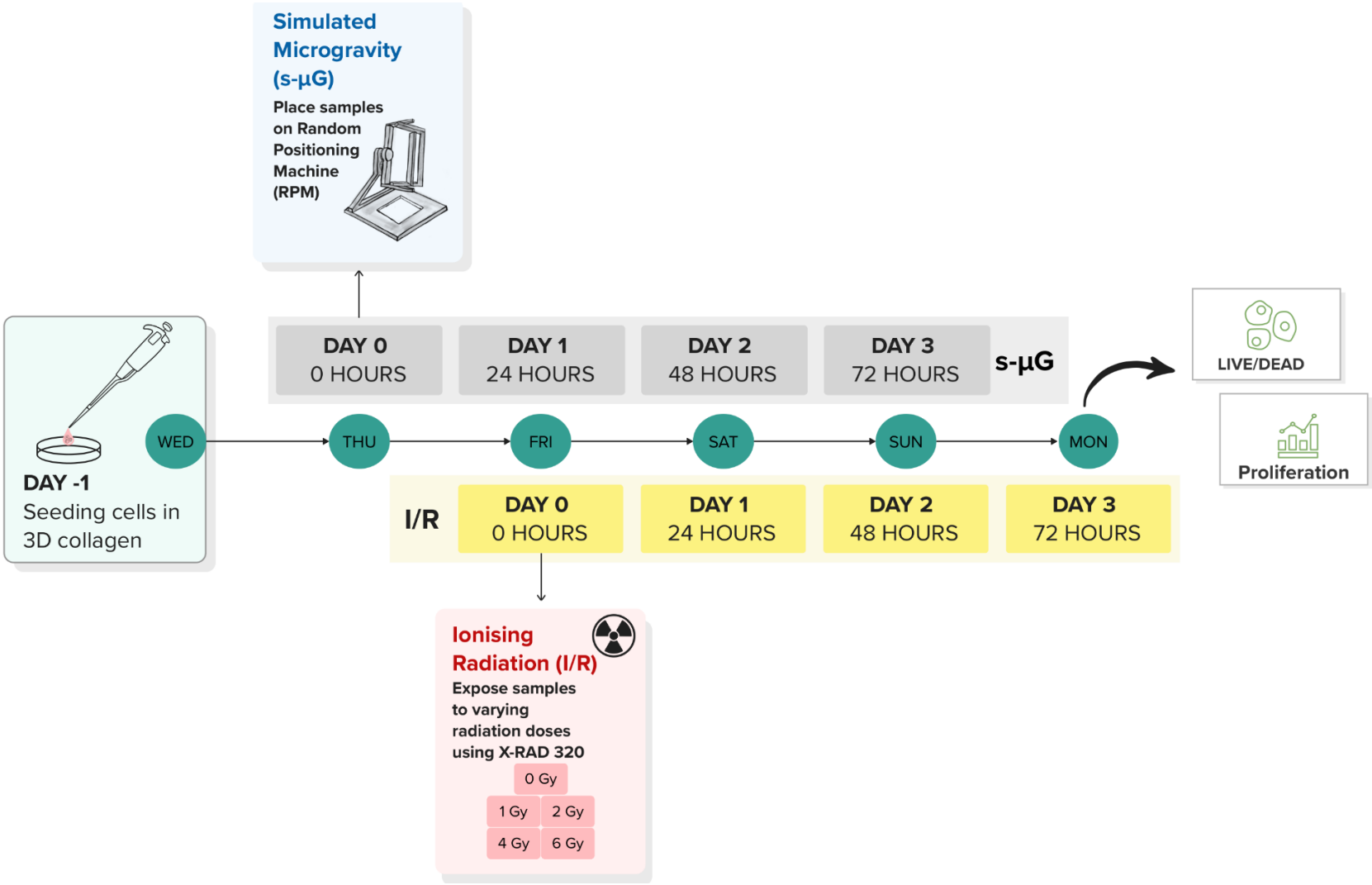


*Figure 5.2 Combined Experimental Timeline for AC-16 Cardiomyocyte Exposure to s-µG and IR in 3D Collagen Hydrogel.*

## 5.4 RESULTS

### 5.4.1 Proliferation of Cardiomyocytes Embedded in 3D Collagen When Exposed to s-μG and Radiation.

The investigation of AC-16 cardiomyocyte's proliferative response within a 3D culture was initially conducted under s-μG and static control conditions across a 72-hour interval. Figure 5.3A visualises the RFU data over the time course, indicating that while there is a trend of increasing RFU in the s-μG group compared to the static control, this increase does not represent a significant deviation from the control proliferation rates, confirmed by two-way ANOVA ($p = 0.5838$). After the increase in proliferation rate for the s-μG samples, the line trends downward, suggesting a decrease in proliferation rate and no significant impact of s-μG on cardiomyocyte proliferation within a 72-hour observation window. Furthermore, Dunnett's multiple comparisons test, which examined changes within the s-μG condition at various time points (0, 6, 24, 48, and 72 hours), revealed no significant changes in RFU. This is reflected in the p-values: 0.7020 at 6 hours, 0.7096 at 24 hours, and 0.9901 at 72 hours compared to pre-treatment 0 hours control. This is supported by the graph of normalised RFU value presented in Figure 5.3B, where the normalised values return to approximately one, indicating no difference between the s-μG and static control samples.

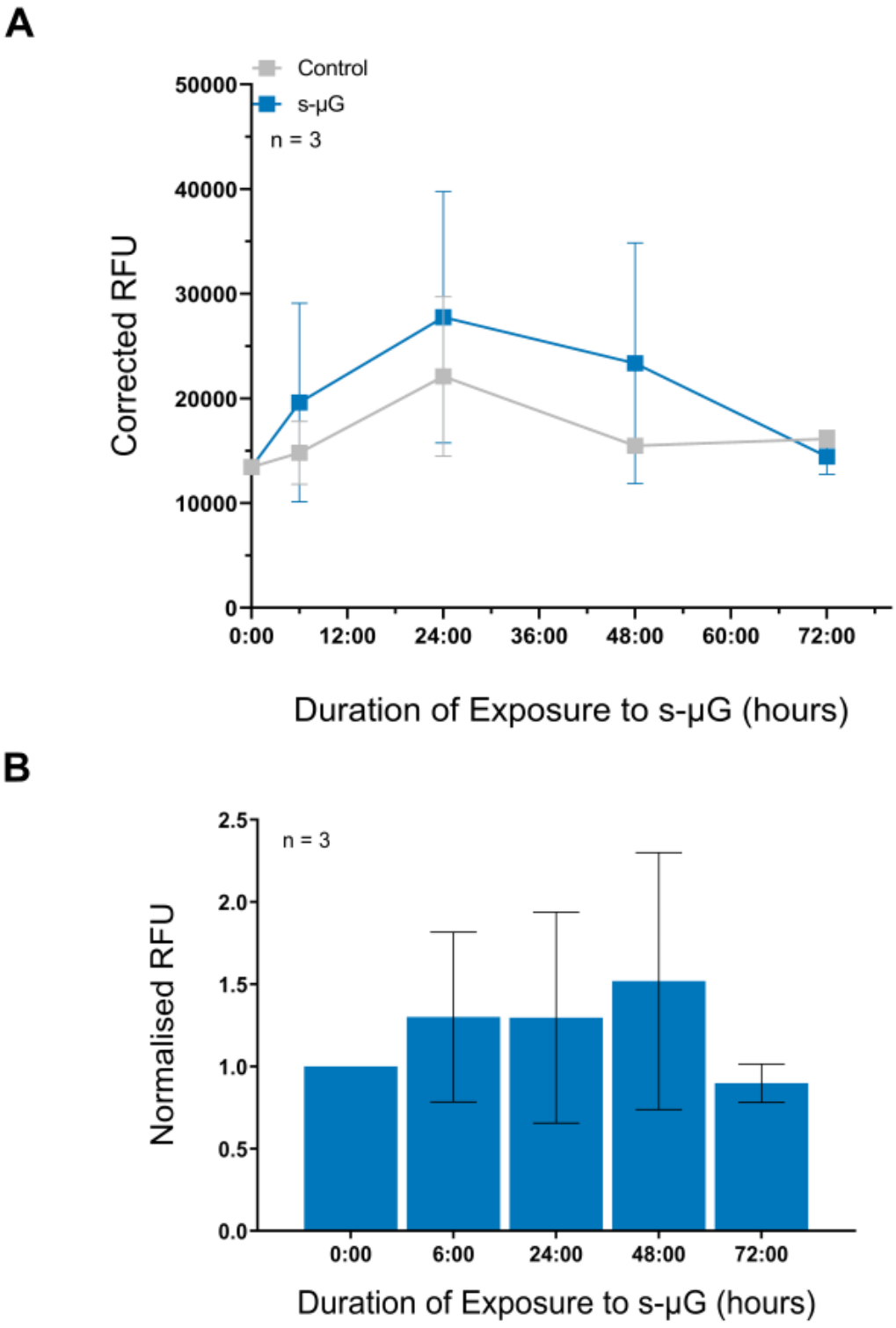


*Figure 5.3 Proliferation Rate of AC-16 Cardiomyocytes in 3D Collagen Matrix Under Ctrl and s-μG.Proliferation of AC-16 cardiomyocytes within a 3D collagen matrix under control (Ctrl) and s-μG conditions, quantified using the PrestoBlue assay. (A) Corrected RFU for Ctrl and s-μG showing the trend over time, and (B) Normalised RFU (s-μG/Ctrl) at time intervals of 0, 6, 24, 48, and 72 hours. A normalised value of 1 indicates equivalent RFU between conditions; values above 1 suggest increased proliferation under s-μG, while values below 1 indicate reduced proliferation relative to control. Error bars represent SD based on N = 3 replicates. Statistical analysis included two-way ANOVA to assess interaction effects, with Dunnett's tests evaluating significant proliferation changes from the initial measurement at time 0.*

Building upon the investigation of AC-16 cardiomyocyte proliferation under s-μG alone, the subsequent investigation looked at the combined effects of s-μG and IR. Figure 5.4 illustrates the outcome of this assessment, representing the proliferation responses expressed as RFU to different doses of IR under s-μG compared to control conditions in a 3D culture environment.

Analyses utilising two-way ANOVA revealed no significant interaction between IR doses (1Gy to 6Gy) and conditions ($p = 0.6244$), nor were significant effects observed from IR doses or s-μG conditions alone (p-values of 0.6244 and 0.0583, respectively). However, the p-value for the s-μG conditions approached the significance threshold, suggesting an observable trend that may justify additional research, potentially with an increased sample size or expanded experimental design. Dunnett's multiple comparisons test, which further analysed the effect within each condition (control and s-μG) at different IR doses, corroborated the lack of statistically significant differences. None of the IR doses significantly affected cardiomyocyte proliferation in the control condition compared to the unirradiated control (all $p > 0.9999$). Within the s-μG group, there was an increase in RFU with higher IR doses, with a notable increase at 2Gy ($p = 0.2142$); however, these differences did not reach statistical significance.

The results of these experiments on the proliferation of AC-16 cardiomyocytes within a 3D collagen hydrogel indicate that the AC-16 cardiomyocytes did not exhibit significant differences in proliferation under s-μG conditions compared to the control across the 72-hour experimental duration. The combined effect of s-μG and IR on the proliferation of AC-16 cardiomyocytes cultured in 3D also did not yield statistically significant changes across the doses tested. However, the trend towards significance in the conditions factor ($p = 0.0583$) and the observable mean differences in the s-μG group suggest that there may be a biological effect that could become more apparent under different experimental conditions or with a more sensitive assay.

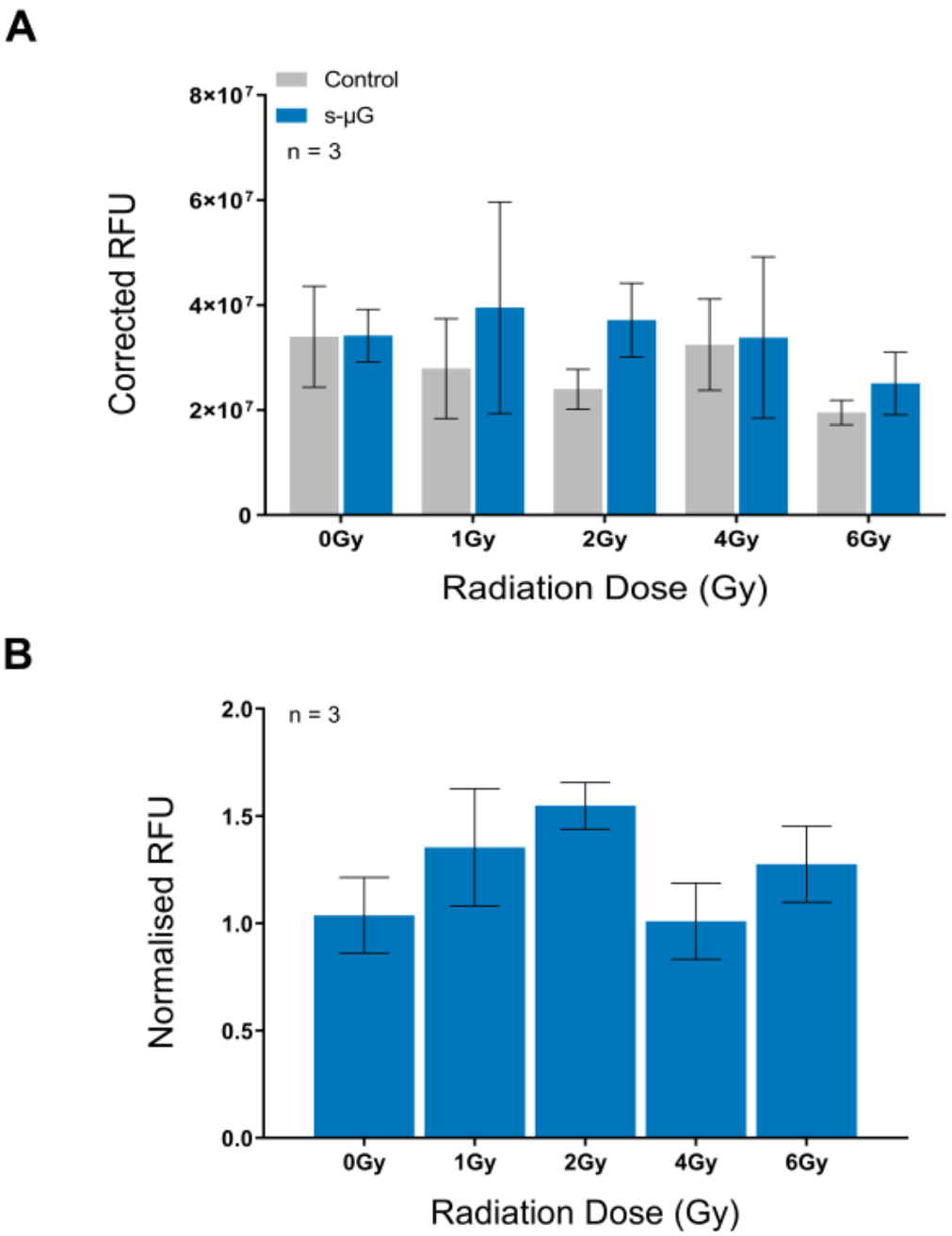


*Figure 5.4 Proliferation of AC-16 Cardiomyocytes in 3D Collagen Matrix Under s-μG and IR. Proliferation of AC-16 cardiomyocytes within a 3D collagen matrix under s-μG and IR conditions was quantified to assess combined effects. The PrestoBlue assay measured proliferation at 96 hours post-s-μG exposure and 72 hours post-IR. (A) Corrected RFU for Ctrl and s-μG across IR doses, and (B) Normalised RFU (s-μG/Ctrl) across IR doses (0 Gy, 1 Gy, 2 Gy, 4 Gy, and 6 Gy). A normalised value of 1 indicates equivalent RFU between conditions; values above 1 suggest increased proliferation under s-μG, while values below 1 indicate reduced proliferation relative to control. Error bars represent SD, with statistical analysis performed using two-way ANOVA (N = 3), followed by Dunnett's multiple comparison post hoc test to compare s-μG conditions against the control.*

### 5.4.2 Microgravity And Ionising Radiation Combination Markedly Decreased Viability in A 3D Environment

The viability of AC-16 cardiomyocytes within a 3D collagen hydrogel was investigated under s-μG, IR, and a combination of both (s-μG + 2Gy IR). Cell viability was quantified by LIVE/DEAD assay as detailed in Section 3.6.2, which facilitated the capture of immunofluorescence images represented in Figure 5.5A.

Investigations conducted 72 hours post-IR exposure indicated a statistically significant variance among the groups ($p=0.0006$) by the Kruskal-Wallis statistic test (Figure 5.5B). Dunn's multiple comparisons test identified significant disparities between certain treatment conditions. The comparison between s-μG + 2Gy IR and the static control group exhibited a substantial mean rank difference of -13.83 ($p = 0.0022$). The combined exposure of s-μG and 2Gy IR resulted in a significant decrease in cell viability compared to s-μG alone, as evidenced by a substantial mean rank difference of -14.13 ($p = 0.0031$).

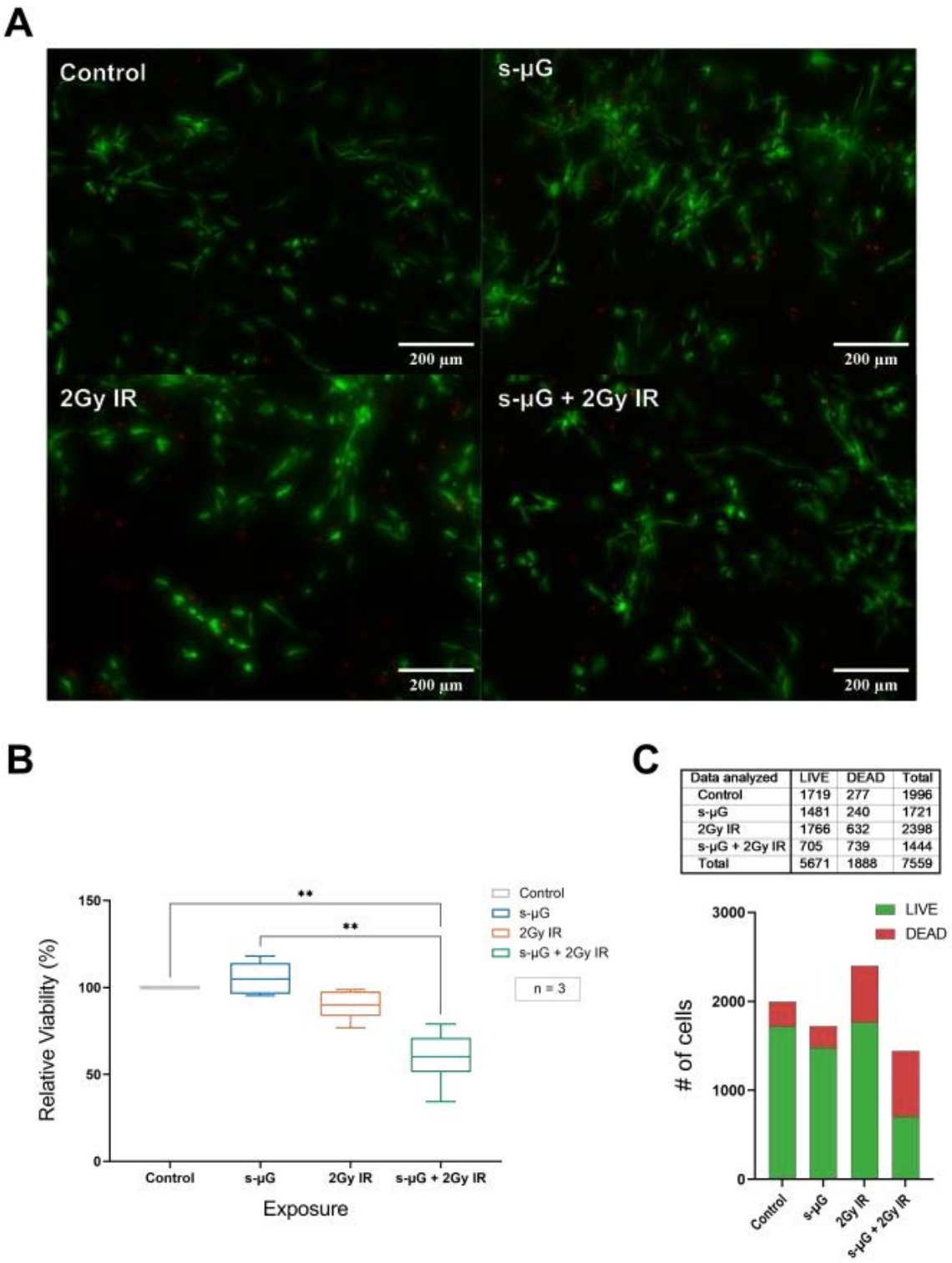


*Figure 5.5 Representative Immunofluorescence Images and Viability of AC-16 Cardiomyocytes in 3D Collagen Hydrogel Post-IR. (A) Representative immunofluorescence images of AC-16 cardiomyocytes embedded in a 3D collagen hydrogel 72 hours post-IR. Cells were labelled with Calcein AM and Propidium Iodide to distinguish live and dead cells, imaged using an EVOS FL microscope at a 20x objective and analysed via GFP (green) and Texas Red (red) channels. The scale bar represents 200 µm. (B) The resultant viability data, normalised to control, were plotted using GraphPad Prism. Statistical analysis using the Kruskal-Wallis test (N = 3) revealed significant differences among groups, further analysed by Dunn's multiple comparisons test. Significance level: ***p < 0.001.*

### 5.4.3 Gene Expression When Cardiomyocytes Are In 3D Collagen.

Following the findings on the proliferation and viability of AC-16 cardiomyocytes cultured within a 3D collagen matrix, notable differences were observed compared to 2D adhered cells. Under s-μG, the 3D structure facilitated a distinct cellular arrangement and distribution, potentially influencing cell-cell and cell-matrix interactions differently from 2D cultures.

For gene expression analysis in the 3D collagen matrix, RT-qPCR was conducted on cDNA samples using SYBR Green PCR Master Mix. Gene expression was assessed at 6, 24, 48, and 72 hours, with results in Figure 5.6 showing the mean log2 fold changes for each group, normalised to measurements at 0 hours (refer to Section 4.3.3 for additional details).

For YAP1, the expression analysis revealed minor differences between s-μG and control conditions at various time points, with the most noticeable deviation at 6 hours showing a mean difference of 1.413. However, these changes did not reach statistical significance, as indicated by Šídák's test. Cx43 expression exhibited minimal fluctuations from the initial reference point, with a peak variation at 24 hours (mean difference of 0.9279), yet none were statistically significant. RHOA expression under s-μG showed a maximum mean difference of 0.9884 at 24 hours compared to control, but similar to the other genes, these changes were insignificant. RAC2 analysis indicated slight variations with the maximum mean difference of 0.6761 at 72 hours; however, these were also insignificant. CDH2 showed the most variability at 72 hours with a mean difference of 0.9295, yet like the others, it remained statistically nonsignificant.

Overall, measurable differences in gene expression for specific genes were observed at various time points; however, none of these changes reached statistical significance when comparing s-μG treated samples to controls. This observation suggests that the 3D collagen matrix may stabilise gene expression under s-μG conditions.

**A**

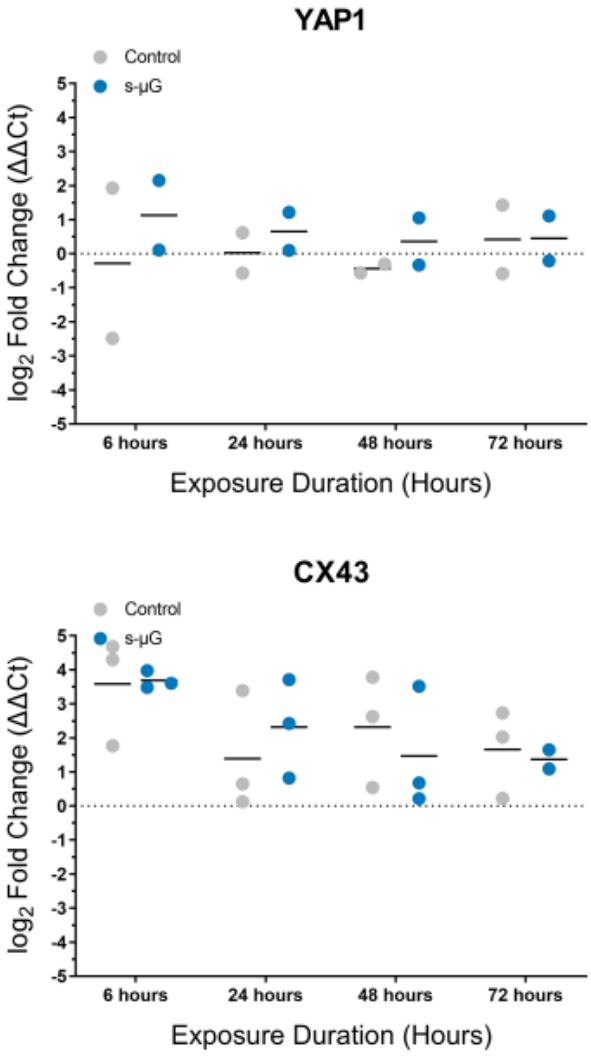
YAP1
Control
s-µG
log2 Fold Change (ΔΔCt)
5
4
3
2
1
0
-1
-2
-3
-4
-5
6 hours
24 hours
48 hours
72 hours
Exposure Duration (Hours)
CX43
Control
s-µG
log2 Fold Change (ΔΔCt)
6 hours
24 hours
48 hours
72 hours
Exposure Duration (Hours)

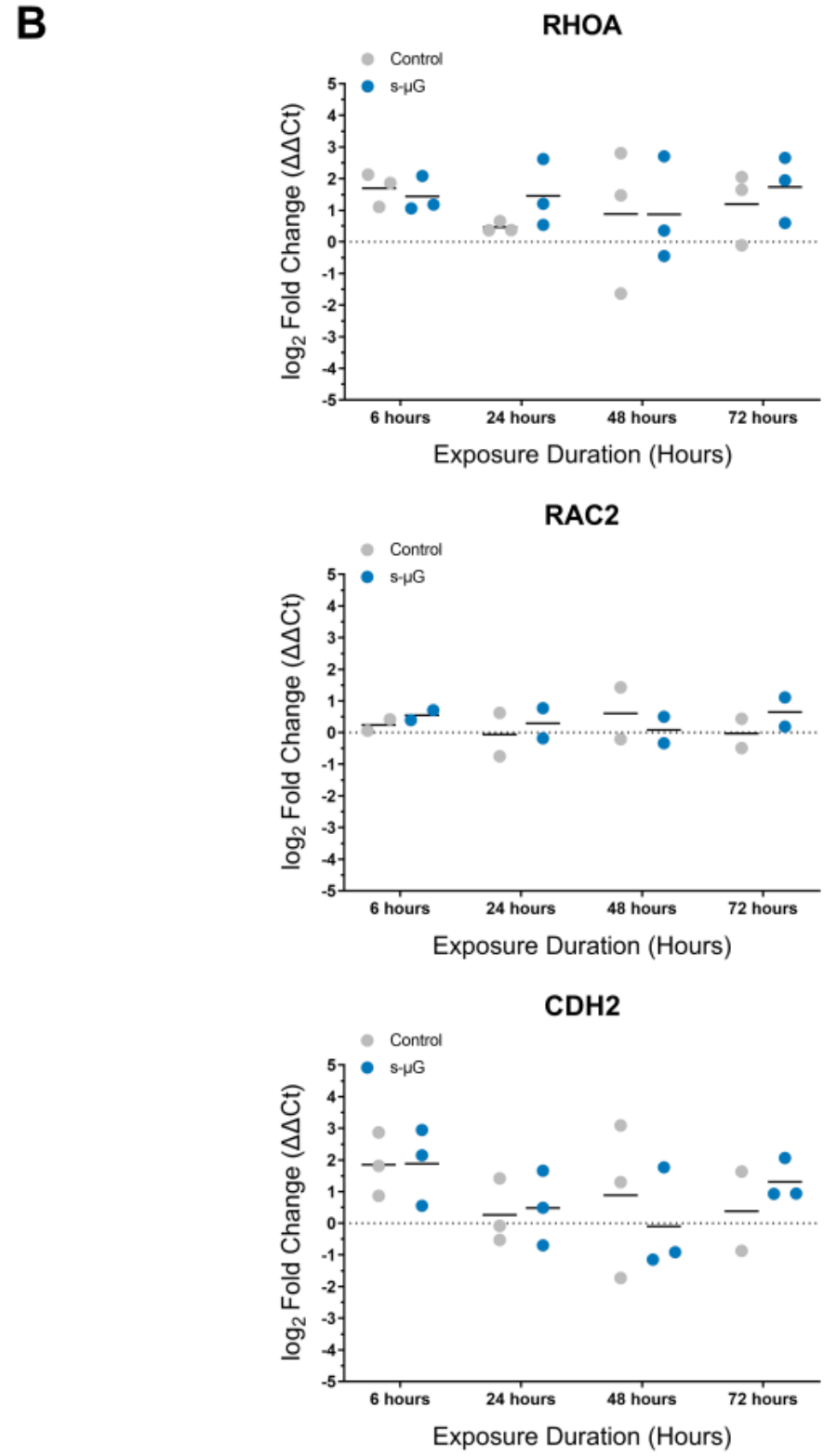


*Figure 5.6 Log2 Fold Change of AC-16 Cardiomyocytes in 3D Collagen Hydrogel for Gene Expression. Log2 fold change of gene expression in AC-16 cardiomyocytes within a 3D collagen hydrogel for genes related to (A) signal transduction and communication and (B) cell structure and motility. The x-axis represents exposure durations, while the y-axis shows the log2 fold change relative to the control group (0-hour). RT-qPCR followed a two-step cycle protocol with an initial hold at 95°C for 30 seconds, followed by 40 PCR cycles (95°C for 5 seconds, 60°C for 20 seconds), and concluded with a melt curve analysis. The 2^-ΔΔCt method was used to determine gene expression fold changes. Each dot represents the log2 value for individual experiments, with the group mean depicted by a solid line.*

AC-16 cardiomyocytes embedded in a 3D collagen hydrogel and exposed to combined s-μG and 2 Gy IR showed significantly lower cell viability than s-μG alone or static control. However, the proliferation assays showed no significant alterations in response to the combined stresses, indicating that cardiomyocyte proliferation remained resilient. To investigate this further, RT-qPCR with an adjusted timeline (Section 4.3.1.3) was employed to address the effects of combined s-μG and 2 Gy IR on AC-16 cardiomyocytes in 3D culture.

Statistical analysis showed no significant difference in the expression of the genes YAP1, CX43, RHOA, RAC2, and CDH2 across treatments in a 3D collagen matrix (Figure 5.7). Tukey's multiple comparisons test found that YAP1 expression did not differ substantially between treatments, with a p-value of 0.9296. Similarly, CX43 expression did not alter significantly across treatments (p-value = 0.9996). RHOA expression was constant throughout treatments, as evidenced by a p-value of 0.9850. A similar pattern was seen for RAC2, with no significant expression differences ($p = 0.9850$). Furthermore, Tukey's test revealed no significant variations in CDH2 expression between treatments ($p = 0.9838$).

The gene expression analysis of AC-16 cardiomyocytes cultured in a 3D collagen matrix for various s-μG durations and under s-μG and IR revealed no significant changes in the expression of key regulatory genes YAP1, CX43, RHOA, RAC2, and CDH2.

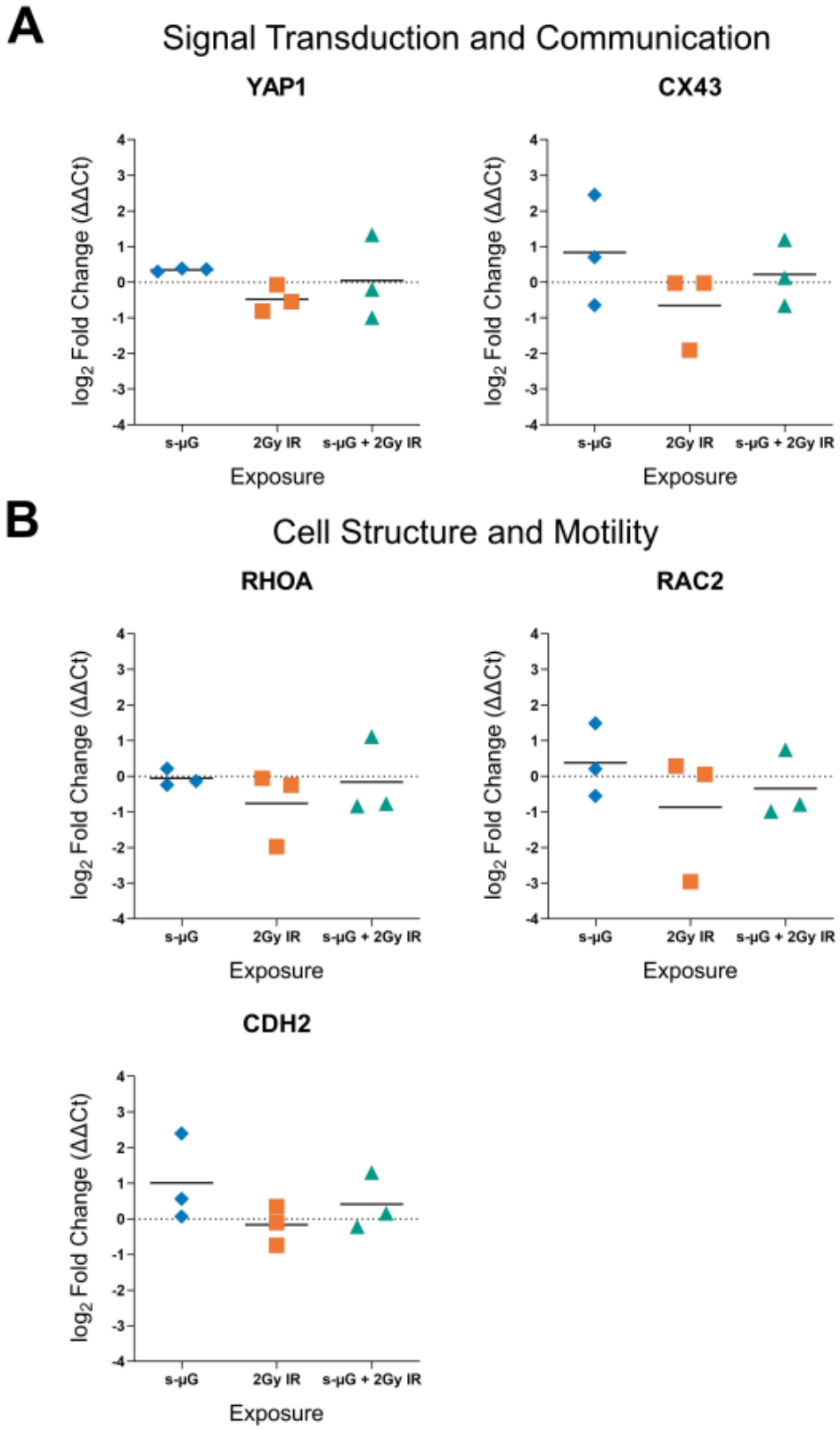


*Figure 5.7 Gene Expression Analysis of AC-16 Cardiomyocytes in 3D Collagen Matrix Under Static, s-μG, IR, and s-μG + IR. Gene expression analysis for (A) signal transduction and communication and (B) cell structure and motility. The x-axis represents exposure groups, while the y-axis shows the log2 fold change in gene expression. Fold changes were calculated using the 2^-ΔΔCt method. Each dot represents the log2 fold change for individual experiments, with the group mean depicted by a solid line. A log2 fold change of 0, indicated by a dotted line, signifies no variation from the control group. Statistical analysis was performed on ΔΔCt values using two-way ANOVA (N = 3) with Šídák's multiple comparisons test.*

### 5.4.4 Characterisation of DNA Damage Response in 3D Cultured AC-16 Cardiomyocytes

The following section characterises the DNA damage response in 3D cultured AC-16 cardiomyocytes upon IR exposure by detecting γ-H2AX foci formation. The immunochemistry procedure described in Section 3.6.6 was employed for γ-H2AX foci detection, followed by immunofluorescence analysis to visualise the foci within the nuclei of AC-16 cardiomyocytes cultured in 3D collagen ECM.

The response to IR was assessed by analysing the variable across different time points, as depicted in Figure 5.8. The time points investigated were 0 hours, 10 minutes, 1 hour, and 24 hours post-IR exposure. Statistical analysis was performed using one-way ANOVA, which revealed a significant difference among the treatment groups ($p = 0.0030$).

Quantitative analysis indicated distinct variations in the mean values across the different time points. At 0 hours, the mean value was 0.5454, serving as the reference for comparison. Following IR exposure, a significant increase was observed at 10 minutes (mean = 4.046), reflecting an immediate response to radiation. This elevated response persisted at 1 hour (mean = 3.243) but decreased substantially by 24 hours (mean = 1.081), suggesting a gradual recovery over time. Further analysis using Tukey's multiple comparison tests highlighted significant differences between specific time points. Notably, the comparison between 10 minutes and 0 hours yielded a mean difference of 3.501 ($p = 0.0049$), and between 1 hour and 0 hours, the mean difference was 2.698 ($p = 0.0215$), indicating significant increases. Conversely, the comparison between 24 and 0 hours did not show a significant difference (mean difference = 0.5361, $p = 0.8712$). The mean difference between 24 hours and 10 minutes was -2.965 ($p = 0.0130$), demonstrating a significant decrease.

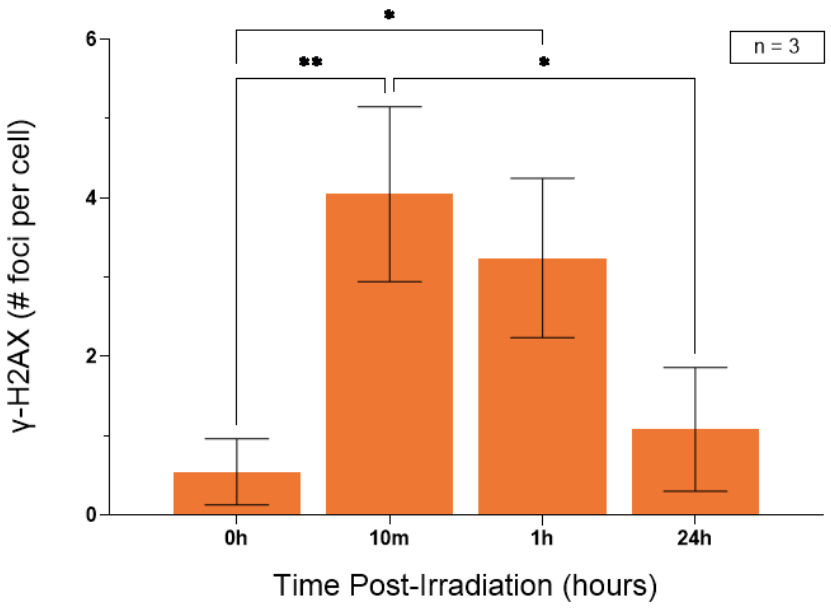


*Figure 5.8 Quantification of γ-H2AX Foci in AC-16 Cardiomyocytes in 3D Culture Post-IR. AC-16 cardiomyocytes in 3D culture were observed for the appearance and quantification of γ-H2AX foci, indicating the extent of DNA damage induced by a 2 Gy IR dose. The x-axis represents time post-IR (hours), and the y-axis shows the mean number of γ-H2AX foci per nucleus. Measurements were taken at 0 hours, 10 minutes, 1 hour, and 24 hours post-IR. Error bars represent the SD. Statistical analysis was conducted using one-way ANOVA followed by Tukey's multiple comparisons test. Significance levels: * ($p \leq 0.05$), ** ($p \leq 0.01$).*

These results suggest that the response to IR is rapid, with a peak at 10 minutes post-exposure, followed by a decline over the subsequent 24 hours. This pattern indicates that the cellular mechanisms activated by IR are most pronounced shortly after exposure, with a gradual reduction as recovery processes ensue.

The next phase of the study involved assessing the DNA damage response in AC-16 cardiomyocytes cultured in 3D under s-μG conditions, both with and without exposure to IR and quantifying γ-H2AX foci formation once again. A 24-hour s-μG preconditioning was utilised for the combined treatment protocol, followed by 2 Gy IR exposure described in Section 4.3.1.3. Control samples, not subjected to irradiation (0 Gy), were fixed before irradiation, while the remaining samples were irradiated with 2 Gy IR. Cells were fixed for analysis at designated time points, ensuring minimal disruption to the experimental setup and maintaining the integrity of the microgravity simulation.

Measurements were taken at 0 hours, 10 minutes, 1 hour, and 24 hours post-IR exposure. Statistical analysis using two-way ANOVA revealed significant effects, as shown in Figure 5.9. The two-way ANOVA indicated a significant interaction between time and treatment ($p = 0.0068$), with p-values of 0.0181 and 0.0095, respectively. Šídák's multiple comparisons test further validated these findings. The mean number of γ-H2AX foci per nucleus at 0 hours was 1.235 for the 2 Gy IR only group and

0.9339 for the s-μG + 2 Gy IR group, with no significant difference between the groups (p = 0.9940). At 10 minutes post-IR, there was a substantial increase in γ-H2AX foci in the s-μG + 2 Gy IR group, with a mean of 4.884 foci compared to 0.8108 foci in the 2 Gy IR group. This difference was statistically significant (mean difference = 4.073, p = 0.0042). At 1 hour post-IR, the s-μG + 2 Gy IR group maintained elevated foci levels with a mean of 3.262, significantly higher than the 0.5679 foci observed in the 2 Gy IR group (mean difference = 2.694, p = 0.0422). By 24 hours post-IR, the mean number of foci in the s-μG + 2 Gy IR group decreased to 0.06647, while the 2 Gy IR group had a mean of 1.014 foci, with no significant difference between the two groups (mean difference = -0.9472, p = 0.7286).

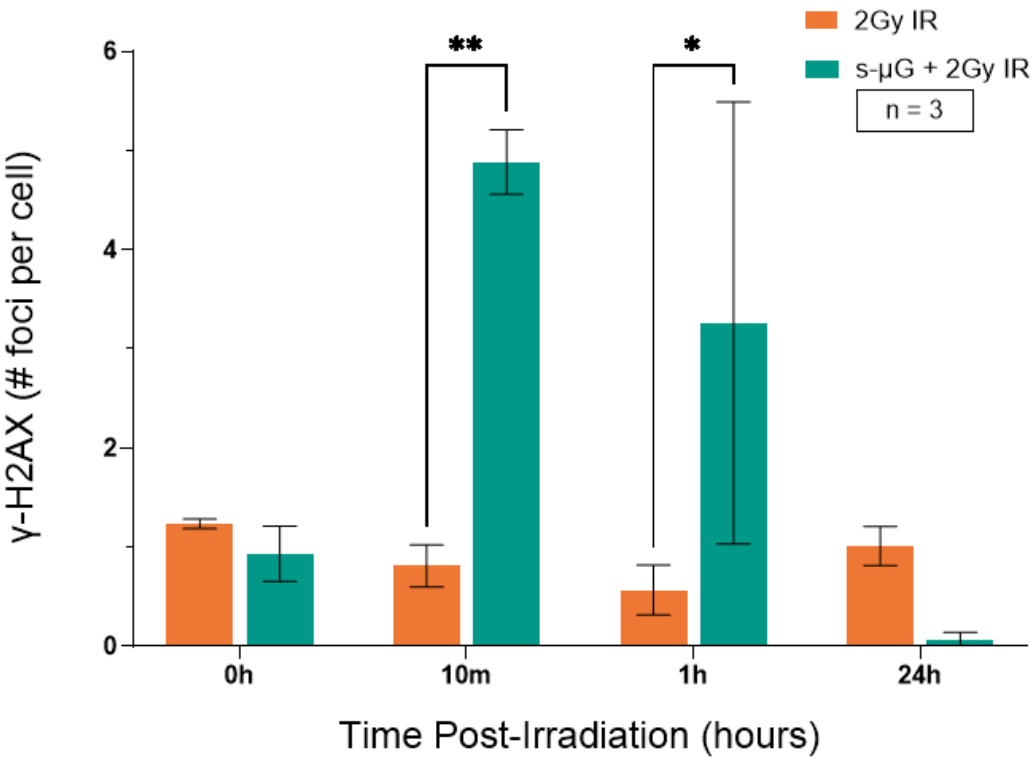


*Figure 5.9 Quantification of γ-H2AX Foci Formation in 3D Cultured AC-16 Cardiomyocytes 2 Gy IR Under s-μG With and Without s-μG. AC-16 cardiomyocytes in 3D culture were observed for γ-H2AX foci formation, indicating DNA damage under s-μG conditions with and without a 2 Gy IR dose. The x-axis represents time post-IR (hours), and the y-axis displays the mean number of γ-H2AX foci per nucleus. Measurements were taken at 0 hours, 10 minutes, 1 hour, and 24 hours post-IR. Error bars represent the SD. Statistical analysis was conducted using two-way ANOVA. Significance levels: * (p ≤ 0.05), ** (p ≤ 0.01).*

These results, illustrated in Figure 5.9, indicate that the response to IR under s-μG is rapid and substantial, with a peak in DNA damage observed at 10 minutes post-exposure. This elevated level of DNA damage persists at 1 hour but shows a significant reduction by 24 hours, suggesting the activation of DNA repair mechanisms over time and by the 24 hour mark.

In conclusion, the data from these analyses provide comprehensive insights into the dynamics of the response to IR, particularly under s-μG conditions. The initial part of the analysis focused on characterising cardiomyocytes in a 3D environment to provide a reference point for assessing the impact on cells encapsulated in collagen. Significant changes were observed at specific time points post-exposure, highlighting a time-dependent response to IR. Following this initial experiment, the dynamics of γ-H2AX foci formation under s-μG conditions revealed an initial surge in DNA damage followed by a gradual repair process. The significant interaction between time and treatment underscores the dynamic nature of the cellular response. These findings, depicted in Figures 5.8 and 5.9, corroborated the statistical analysis and supported the conclusion of a time-dependent response to IR in s-μG environment.

### 5.4.5 Glimpse into YAP Translocation in 3D Cardiomyocytes Model

Building upon the insights garnered from 2D culture experiments, we expanded our investigation into the effects of s-μG and IR on YAP signalling within 3D cultures of AC-16 cardiomyocytes.
Figure 5.10 illustrates the localization of YAP under control, s-μG, IR, and combined s-μG + IR conditions. In control conditions, YAP is distributed between the nucleus and cytoplasm, reflecting a Nuc/Cyto ratio near 1. Under s-μG, YAP predominantly localizes to the nucleus, corresponding to an increased Nuc/Cyto ratio (>1). In the IR condition, YAP also shows predominantly nuclear localization, though slightly less than s-μG alone. In the combined s-μG + IR condition, YAP is primarily cytoplasmic, indicating a lower Nuc/Cyto ratio (<1).

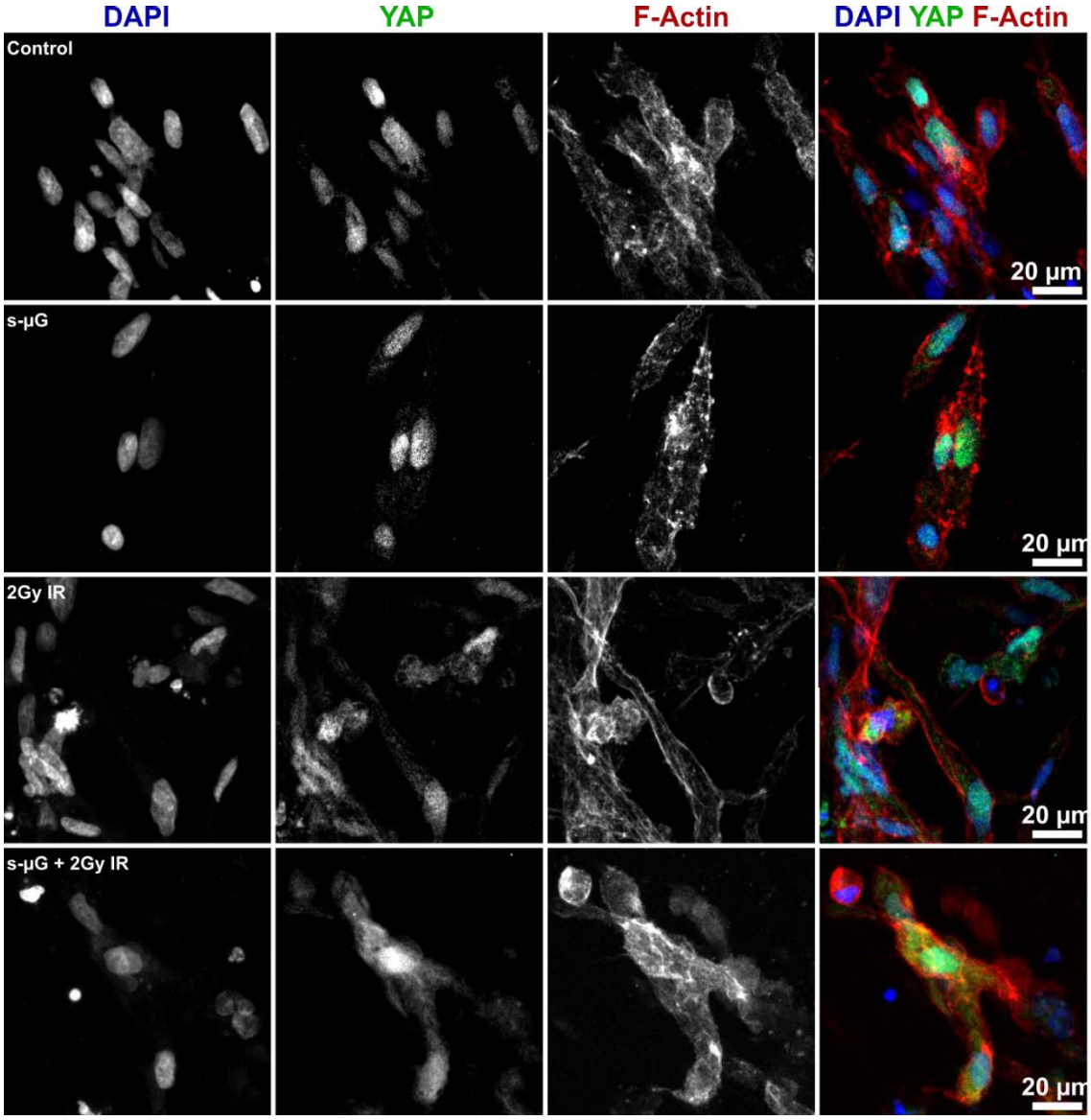


*Figure 5.10 YAP Localization in AC-16 Cardiomyocytes Cultured in 3D Collagen Hydrogel Under s-μG and IR.AC-16 cardiomyocytes were embedded in a 3D collagen hydrogel and subjected to control conditions, s-μG, IR, and combined s-μG + IR for 72 hours. YAP localization was assessed using primary antibodies targeting YAP (1:200), detected with Anti-Rabbit Alexa Fluor 488 secondary antibodies (1:100) to visualize YAP (green). F-Actin (red) was stained with iFluor 594 Phalloidin (1:1000), and nuclei (blue) were counterstained with DAPI (1:10000). Images were acquired using a LEICA confocal microscope with a 60x oil objective, focusing on cells within the hydrogel matrix. Representative images were captured from at least 50 cells across randomly selected FOV. Scale bar = 20 μm.*

To quantitatively assess these observations, a Kruskal-Wallis test was performed to compare the effects of the four treatments—Control, s-μG, IR, and s-μG + IR—on YAP localization (Figure 5.11). The analysis revealed significant differences among the medians of the treatment groups ($p < 0.0001$, Kruskal-Wallis statistic = 53.22), indicating a significant impact of the treatments on the measured parameter. Dunn's multiple comparisons test further compared each treatment group to the Control.

The s-μG treatment showed a mean rank difference of -12.07 from the Control, but this was not statistically significant ($p > 0.9999$). Similarly, the IR treatment did not significantly differ from the Control, with a mean rank difference of -21.92 ($p = 0.6919$). In contrast, the combined s-μG + IR treatment demonstrated a highly significant decrease in nuclear YAP localization compared to the Control, with a mean rank difference of -108.2 ($p < 0.0001$).

These findings confirm that while s-μG and IR individually promote nuclear localization of YAP, their combination significantly shifts YAP localization towards the cytoplasm, as visually represented in Figure 5.10 and quantitatively supported by the statistical analysis in Figure 5.11.

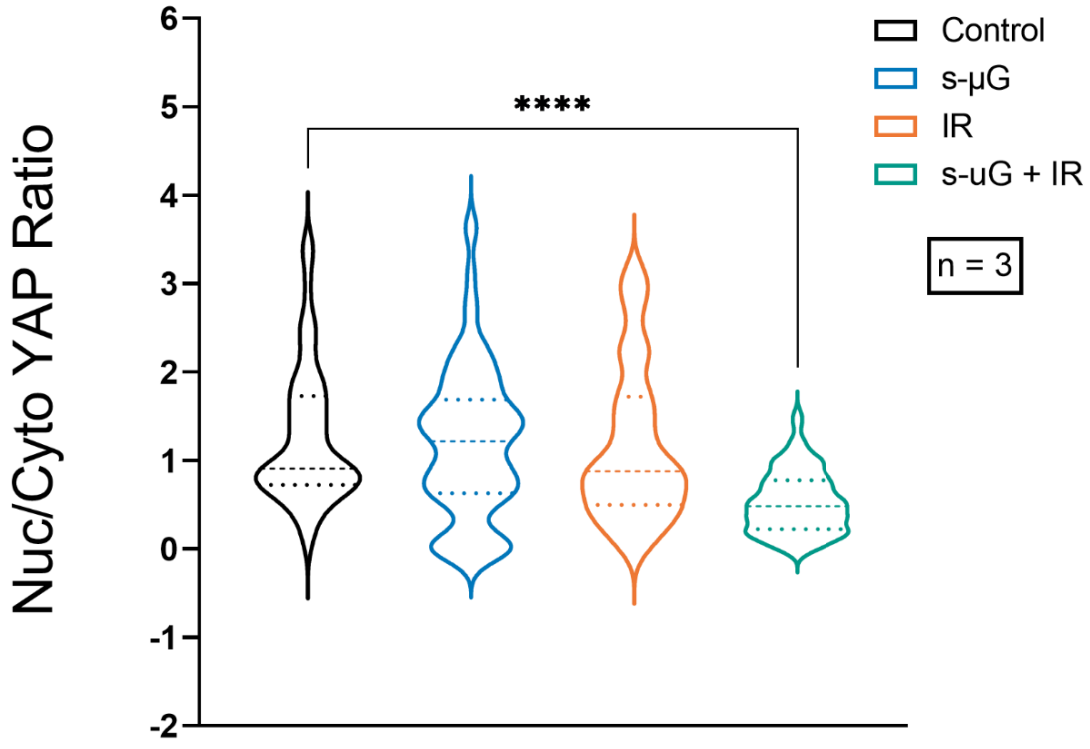


*Figure 5.11 YAP Intracellular Localization in 3D Encapsulated AC-16 Cardiomyocytes Under s-μG, IR, and Combined Conditions. Analysis of YAP localization in 3D encapsulated AC-16 cardiomyocytes subjected to s-μG, IR, combined s-μG + IR, and control conditions for 72 hours. Localization was quantified as the ratio of integrated nuclear fluorescence intensity to integrated cytoplasmic fluorescence intensity (Nuc/Cyto YAP Ratio). Violin plots represent data distribution across experimental groups. Statistical analysis was conducted using the Kruskal-Wallis test (N = 3), followed by Dunn's multiple comparisons test. Significance is denoted by **** ($p \leq 0.0001$).*

## 5.5 DISCUSSION

This chapter aimed to evaluate AC-16 cardiomyocyte responses to s-μG, IR, and their combined impact in a 3D environment. The results section of this chapter comprehensively explored the responses of AC-16 cardiomyocytes embedded in 3D collagen ECM to s-μG, IR, and their combined effects by following the aim and objectives set out at the beginning of this research project.

A summary of the relevant sections and the objectives they cover are shown in Figure 5.10. To contextualise these findings within the broader landscape of cellular biology and space medicine, this discussion aims to integrate the observed cellular behaviours presented in the methods (Section 5.3.1) and results (Section 5.4)—spanning changes in proliferation, viability, gene expression, DNA damage repair, and mechanotransduction signalling—into a cohesive understanding of AC-16 cardiomyocyte responses to s-μG, radiation, and their combined impact in a 3D environment. Differences in responses between 2D and 3D environments were further discussed to address Objective 3.

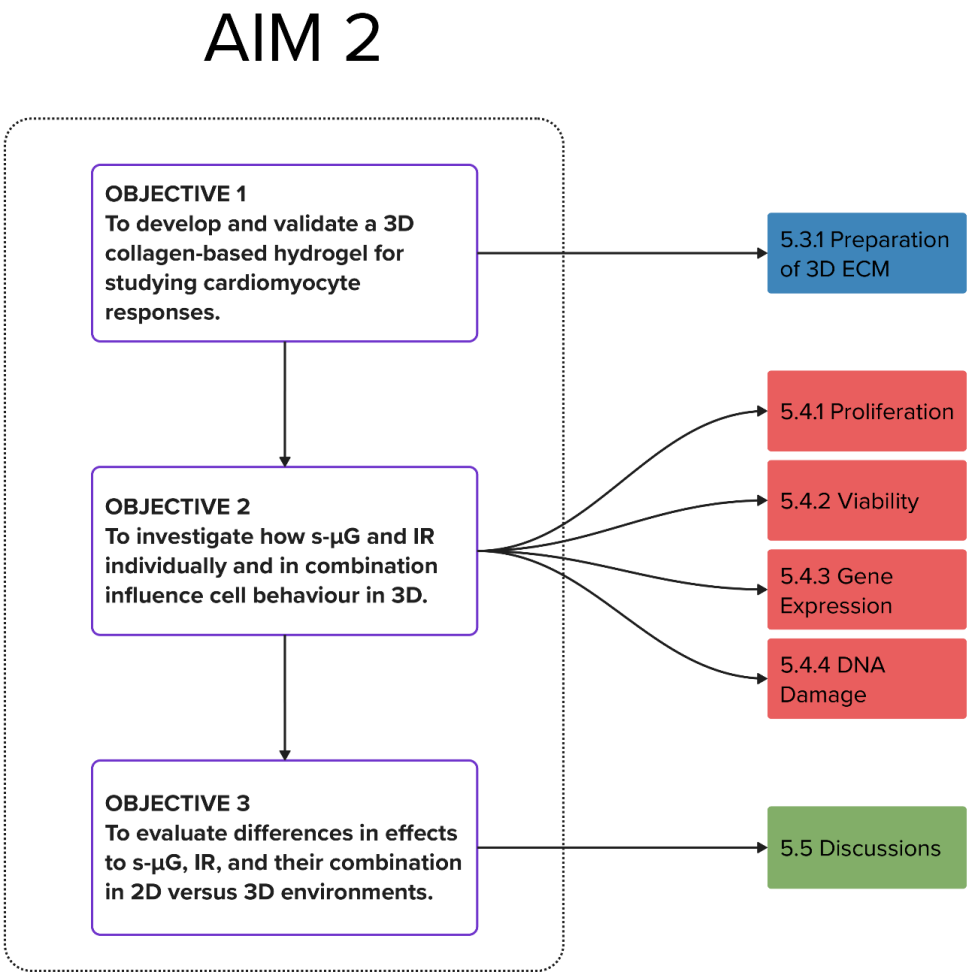


*Figure 5.12 Summary Mindmap that Captures the Objectives in Aim 2 and the Corresponding Section of the Chapters that Fulfills Those Objectives.*

### 5.5.1 Development and Validation of a 3D Collagen-Based Hydrogel for Cardiomyocyte Responses

The transition from traditional 2D cultures to a 3D environment was undertaken to more accurately mimic the *in vivo* cardiac microenvironment, which is essential for studying cardiomyocyte responses under various conditions including s-μG and IR. The optimisation process involved adjusting cell concentrations, refining the setting temperature, and varying collagen concentrations and embedding techniques to ensure uniform cell distribution and viability. These optimised methodologies are detailed in Chapter 5, Section 5.3.1.

Maintaining mechanical heterogeneity is an inherent challenge in collagen hydrogels. Our study assessed different polymerisation temperatures, including starting at 4°C, room temperature and 37°C. Subsequently, room temperature polymerisation followed by warming to 37°C was selected as the optimal approach. To further mitigate the heterogeneity challenges observed with room temperature polymerisation, a standard collagen concentration and neutralisation technique was employed across all batches. During optimisation, it was observed that the 3D hydrogel scaffold facilitated enhanced cell spreading, attributed to the environments ability to replicate the physical and mechanical properties of the cardiac ECM more accurately than 2D cultures. This allowed cardiomyocytes to interact more naturally with their surroundings, supporting attachment and function within the matrix. The development and validation process, including the effects on cell behaviour, are further described in Chapter 6, Section 6.4.1.3.

To validate the 3D collagen-based hydrogel, several parameters were assessed, including cell viability, proliferation, and functionality. The optimised collagen concentration provided a supportive environment for cardiomyocyte attachment, spreading, and interaction within the 3D matrix. Viability was assessed at various time points (0, 24, 48, and 72 hours) using calcein-AM and ethidium homodimer-1 staining to distinguish live and dead cells. Qualitative observations indicated enhanced functionality in 3D cultures compared to 2D conditions, suggesting that the 3D environment may better support cellular behaviours similar to *in vivo* conditions. An increased number of viable cells and enhanced proliferation were observed in the 3D cultures, as demonstrated in subsequent experiments (Figure 5.2). These findings underscore the importance of a 3D environment in maintaining cellular functions and resilience to stressors.

However, direct comparative data specifically quantifying cell viability between the two culture conditions were not obtained due to inherent methodological differences. These differences include variations in cell-matrix interactions and environmental stimuli unique to each setup, which complicate direct viability comparisons between 2D and 3D models.

The 3D collagen-based hydrogel demonstrated its utility in studying cardiomyocyte responses under various conditions. These findings are consistent with previous studies that highlight the advantages of 3D cultures in replicating the ECM and promoting cellular behaviors more closely aligned with *in vivo* conditions (Duan et al., 2011; Edalat et al., 2019; Gishto et al., 2015; Rashedi et al., 2017). Overall, the development and validation of the 3D collagen hydrogel achieved the objective of creating a functional scaffold for embedding cardiomyocytes.

### 5.5.2 Influence of Simulated Microgravity and Ionising Radiation on Cardiomyocyte Behaviour in a 3D Collagen Hydrogel

The shift to a 3D collagen hydrogel environment allowed for a more accurate simulation of physiological conditions compared to traditional 2D cultures, where AC-16 cardiomyocytes embedded in 3D collagen hydrogels exhibited significant changes in cell behaviour, including cell proliferation and viability. The 3D collagen matrix provides a more physiologically relevant context for cell-matrix and cell-cell interactions, which is crucial for maintaining normal cellular functions. (Duan et al., 2011; Edalat et al., 2019; Gishto et al., 2015; Rashedi et al., 2017).

From this study, the proliferation assay results of s-μG and the varying exposure duration, visualised in Figure 5.3 and Figure 5.4, demonstrated that the increase in RFU in the s-μG group compared to the static control was not statistically significant, confirmed by two-way ANOVA ($p = 0.5838$). This suggests that s-μG alone does not significantly impact cardiomyocyte proliferation within the 72-hour. These findings align with prior studies that have shown variable effects of microgravity on cell proliferation (Blaber et al., 2015; Lei et al., 2018). For instance, Blaber et al. (2015) observed that microgravity can have diverse effects on cell proliferation, depending on the cell type and experimental conditions. Similarly, Lei et al. (2018) noted that while some cell types exhibit reduced proliferation under microgravity, others show no significant change.

When examining the combined effects of s-μG and IR (Figure 5.4), two-way ANOVA analysis indicated no significant interaction between IR doses and conditions ($p = 0.6244$), nor were there significant effects from IR doses or s-μG conditions alone ($p = 0.6244$ and $p = 0.0583$, respectively). Despite the lack of statistically significant differences, the p-value close to the threshold for significance for the s-μG condition suggests a potential biological effect that may warrant further investigation with a larger sample size or more sensitive assays. Although not significant, the trend observed in the s-μG group indicates that microgravity conditions might prime the cells for altered responses to IR, a hypothesis supported by previous research demonstrating enhanced sensitivity of cells to radiation under microgravity (Moreno-Villanueva et al., 2017).

The viability assays, illustrated in Figure 5.5, revealed a significant reduction in cell viability in the s-μG + 2Gy IR group compared to the static control and s-μG alone, as determined by the Kruskal-Wallis test ($p = 0.0006$). Dunn's multiple comparisons test further confirmed significant viability decreases in the combined treatment group ($p = 0.0022$ and $p = 0.0031$, respectively). This finding indicates that the combined stress of s-μG and IR has a detrimental effect on cardiomyocyte viability, aligning with previous studies showing increased cellular sensitivity to combined microgravity and radiation exposure. (Kumari et al., 2009; Moreno-Villanueva et al., 2017; Tan et al., 2020). For example, Kumari et al. (2009) found that microgravity and radiation synergistically induce oxidative stress and apoptosis in various cell types. Similarly, Moreno-Villanueva et al. (2017) reported that the combination of these stressors exacerbates DNA damage and reduces cellular repair capacity. Tan et al. (2020) also highlighted the heightened vulnerability of cells to concurrent microgravity and radiation, leading to significant declines in cell viability. These studies collectively support the observed detrimental effects on cardiomyocyte viability under combined s-μG and IR conditions.
Gene expression analysis of key regulatory genes involved in signal transduction and cell structure (YAP1, CX43, RHOA, RAC2, CDH2) revealed no significant differences between the control and experimental conditions (Figure 5.6 and Figure 5.7). The lack of significant gene expression changes also aligns with the observed non-significant proliferation differences. However, it is essential to consider that gene expression changes might be subtle in 3D and require more sensitive detection methods or longer exposure times to become apparent.

γH2AX is a marker for DNA DSBs, providing insights into DNA damage extent and repair efficiency. Initially, the study investigated the cellular response to IR alone in AC-16 cardiomyocytes cultured in a 3D collagen matrix to provide a reference for comparison with traditional 2D cultures. Following IR exposure, a rapid increase in γ-H2AX foci was observed at 10 minutes post-exposure, suggesting an immediate cellular response to DNA damage. This rapid formation of γ-H2AX foci is consistent with previous studies showing swift H2AX phosphorylation following DSB induction by IR. Elevated γ-H2AX foci levels at 10 minutes and 1 hour post-IR exposure, in both the presence and absence of s-μG, indicate the activation of DNA damage signalling pathways immediately following radiation exposure. The subsequent decline in γ-H2AX foci by 24 hours post-IR exposure suggests active DNA repair mechanisms, with a residual level of foci indicating some persisting damage or slower repair processes. This pattern aligns with the well-documented kinetics of DNA repair, where γ-H2AX foci levels peak shortly after IR exposure and gradually decrease as the repair progresses (Habibi et al., 2021; Horn et al., 2011).

In the 3D collagen model, cells exposed to combined s-μG and IR showed a more pronounced γH2AX response than those exposed to either stressor alone (Figure 5.9). The substantial increase in γ-H2AX foci at 10 minutes and 1 hour post-IR exposure under s-μG + 2 Gy IR conditions, compared to s-μG alone, highlights the exacerbated DNA damage response under combined stress conditions.

This finding aligns with previous research indicating that microgravity can influence cellular stress responses and DNA repair mechanisms (Huang & Zhou, 2020; Kumari et al., 2009). Interestingly, by 24 hours post-IR exposure, the γ-H2AX foci levels in the s-μG + 2 Gy IR group decreased significantly. This suggests that DNA repair processes are eventually activated and functional despite the initial exacerbated response. This observation is critical as it implies potential adaptation mechanisms to mitigate prolonged DNA damage under combined IR and microgravity conditions. Furthermore, the addition of s-μG stress exacerbates DNA damage and challenges the cells' repair capacities. These findings align with existing literature, such as Li et al. (2015), Mangala et al. (2011), and T. Zhao et al. (2016), which highlight the compounding effects of microgravity and radiation on DNA integrity (N. Li et al., 2015; Mangala et al., 2011; T. Zhao et al., 2016).

Mechanotransduction pathways are critical in how cells sense and respond to mechanical stimuli. YAP1 is a key regulator in mechanotransduction, influencing gene expression in response to changes in the cellular environment. The morphological assessment and further YAP signalling component of the 3D hydrogel study will be completed after the submission of this thesis. The results of the ongoing analysis are briefly discussed here with the aims to provide initial insights into cardiomyocytes YAP localisation within the 3D collagen matrix.

Preliminary results indicated that s-μG and IR exposure led to alterations in YAP1 signalling within the 3D collagen matrix (Figure 5.11). Figure 5.11 illustrates these findings, showing the distribution of YAP nuclear/cytoplasmic localisation across treatment groups, where value above 0 suggest nuclear localisations, whilst value below 0 suggest cytoplasmic localisation. A one-way ANOVA assessing the effects of Control, s-μG, IR, and s-μG + IR revealed significant differences among the treatment groups ($p < 0.0001$). The Control group exhibited higher nuclear localisation of YAP, consistent with high basal mechanotransduction activity. s-μG conditions alone showed a modest but significant increase in YAP nuclear localisation ($p = 0.0372$) compared to the Control, aligning with reduced cellular tension. Meanwhile IR treatment alone did not show a significant difference ($p = 0.1119$). However, the combination of s-μG and IR demonstrated a highly significant decrease in YAP nuclear localisation ($p < 0.0001$), suggesting a potentially enhanced stress response mechanisms due to mechanical unloading and radiation stress.

Preliminary observations suggest that YAP nuclear and cytoplasmic localisation will be immensely impacted in the 3D environment. The morphological analysis within the 3D collagen matrix will provide more insight into the spatial dynamics of YAP localisation, offering a nuanced understanding of how these stressors influence cellular architecture and mechanotransduction pathways. Future work will complete these analyses to offer a comprehensive understanding of the cellular dynamics in response to s-μG and IR in a 3D environment.

### 5.5.3 Evaluating Differences in Cardiomyocyte Reactions in 2D vs. 3D Environments

This discussion evaluates the differences in cardiomyocyte reactions to s-μG and IR in 2D and 3D environments, integrating results from Chapters 4 and 5 of this thesis. Understanding the impact of dimensional context on cellular behaviour and stress responses is crucial for developing accurate models of the cardiac microenvironment. The effects of s-μG and IR on YAP1 signalling, cell proliferation, viability, and DNA damage responses were assessed in both 2D and 3D environments to understand the impact of dimensional context on cellular behaviour and stress responses.

In the 2D environment, the proliferation and viability of AC-16 cardiomyocytes under s-μG and IR were thoroughly investigated. The results indicated a significant decrease in cell proliferation and viability after 72 hours of s-μG exposure. The combination of s-μG and IR further exacerbated this reduction in viability, highlighting the increased stress imposed on cells under dual stress conditions. Gene expression analysis in 2D revealed no significant changes in YAP1 expression; however, there was a significant increase in the nuclear localization of YAP under both s-μG and IR conditions. This shift in YAP localization suggests an adaptive response to the altered mechanical environment and genotoxic stress, promoting the activation of growth-related genes necessary for cellular adaptation and survival (conditions. Figure).

Transitioning to the 3D environment, the study aimed to provide a more physiologically relevant context by embedding cardiomyocytes in a 3D collagen matrix. The viability of cardiomyocytes in the 3D hydrogel under s-μG, IR, and their combination was significantly affected. As shown in Figure 5.5-A, the LIVE/DEAD assay results revealed a statistically significant variance in cell viability among the different treatment groups. The combined exposure of s-μG and 2Gy IR resulted in a marked decrease in cell viability compared to s-μG alone, indicating that the 3D environment may amplify the cellular stress response to combined s-μG and IR (Figure 5.5-B). This suggests that the 3D environment potentially enhances the stress effects on cell viability compared to 2D cultures. Gene expression analysis in 3D indicated no significant changes in the expression of key regulatory genes (YAP1, CX43, RHOA, RAC2, and CDH2) in the 3D collagen matrix under s-μG and IR conditions (Figure 5.7).

The DNA damage response was another critical aspect evaluated in both environments. In 2D cultures, IR exposure led to substantial DNA damage, with a notable increase in γH2AX foci immediately following exposure and a gradual decline over 24 hours, indicating active DNA repair processes. The presence of γH2AX foci was significantly more intense under combined s-μG and IR conditions, suggesting an amplified DNA damage response compared to IR alone (Section 4.5). In the 3D environment, the DNA damage response exhibited distinct variations in γH2AX foci levels at different time points post-IR exposure, with an immediate increase in DNA damage followed by

a gradual repair process. This pattern was observed under both normal and s-μG conditions, with an exacerbated response when combined with IR exposure (Section 5.5.1). These findings suggest that the 3D environment enhances DNA repair activity compared to 2D cultures, providing a more supportive context for maintaining genomic integrity under combined stress conditions.

The observation that the number of γ-H2AX foci per cell is lower under 3D conditions compared to 2D (Figure 5.9 vs. Figure 4.19) can be attributed to several biological and methodological factors. In 2D cultures, cells may experience altered signalling pathways and increased DNA damage due to the flat substrate and mechanical stress, leading to higher γ-H2AX foci formation. In contrast, 3D matrices provide a more physiologically relevant environment with enhanced cell-cell and cell-matrix interactions, which may promote more efficient DNA repair. Additionally, the 3D spatial arrangement allows clearer differentiation of individual foci, reducing clustering that may inflate damage in 2D cultures (Hagiwara et al., 2017).

The comparison of 2D versus 3D responses revealed that both environments significantly impact YAP localisation, but the patterns and implications differ. In 2D, the mechanotransduction response is more straightforward, with clear nuclear localisation shifts in response to mechanical and radiation stressors. In contrast, the 3D environment presents a more complex interaction, with combined stressors eliciting different localisation patterns, suggesting that the spatial context and cellular architecture play a crucial role in mechanotransduction. These differences underscore the importance of considering the dimensionality of the cellular environment in studies of mechanotransduction and highlight the need for further research to fully elucidate these mechanisms in 3D contexts.

## 5.6 KEY FINDINGS

- s-μG showed no significant changes in cardiomyocyte proliferation or viability in 3D collagen matrix, but combined s-μG and IR significantly reduced cell viability by 25%.
- No significant differences in the expression of key regulatory genes (YAP1, CX43, RHOA, RAC2, CDH2) under s-μG and IR conditions.
- Rapid increase in γ-H2AX foci post-IR exposure indicated immediate DNA damage, with substantial repair by 24 hours. Combined s-μG and IR showed a more pronounced DNA damage response.
- Significant increase in YAP nuclear localisation under s-μG, while combined s-μG and IR resulted in a significant decrease in YAP nuclear localisation.
- Enhanced viability, mechanotransduction signalling, and DNA repair activity in 3D cultures compared to 2D, providing a more physiologically relevant context.

## 5.7 KEY LIMITATIONS

- There was no direct comparative assessment of cell viability between 2D and 3D cultures due to methodological differences, limiting quantitative comparisons.
- The imaging and analysis of 3D cultures are inherently challenging due to the thickness and complexity of the hydrogel environment.
- Similar to 2D experiments, single markers were used in 3D assessments, restricting the ability to fully capture cellular responses.
- The study did not fully characterise the mechanical properties of the 3D gels, which limits understanding of how these properties influence cellular responses.

For a more detailed discussion and potential resolutions to these limitations, please refer to Section 7.4.

# Chapter 6 -

# Development and Fabrication of Hybrid Heart-on-a-Chip

## 6.1 INTRODUCTION

Chapter 6 aims to advance the exploration of cardiac cell responses under space-like conditions by developing a 3D hybrid heart-on-a-chip model. Building on studies of cardiomyocytes in 2D environments (Chapter 4) and 3D hydrogel models (Chapter 5), this chapter integrates microfluidic technology with 3D bioprinting techniques to more accurately emulate the cardiac microenvironment.

As discussed in Section 1.5.3, recent advancements in cardiac modelling have leveraged 3D bioprinting and microfluidics to create physiologically relevant models that better replicate the human heart. Heart-on-a-chip models combine these technologies to recreate cardiac tissue architecture and function, providing controlled environments for studying cardiac function, disease mechanisms, and potential therapies (Gao et al., 2017; Jang, 2017).

Heart-on-a-chip models, including basic cardiac tissue chips and vascularized heart chips, offer precise control over physiological parameters like fluid flow and mechanical forces, essential for cardiac function(Chen et al., 2013; Ren et al., 2013). However, challenges remain, such as replicating the full complexity of *in vivo* heart tissue and achieving functional vascular networks necessary for sustained perfusion. The fabrication complexity and need for specialised equipment also pose limitation (F. Zhang et al., 2021).

3D bioprinting has advanced cardiac modelling by enabling the construction of complex tissues using hydrogel bioinks, allowing the precise spatial arrangement of multiple cell types, but achieving adequate vascularisation is still challenging (Z. Wang et al., 2018). As discussed in Section 1.5.3, strategies such as sacrificial materials, multi-axial nozzles, and self-assembly have been explored to enhance vascular formation, but fully functional vascular networks are still challenging to achieve (Gao et al., 2017).

This chapter explores a hybrid heart-on-a-chip model, integrating 3D bioprinting and microfluidics to arrange cardiomyocytes, endothelial cells, and fibroblasts within a dynamic microenvironment. The model aims to promote vascular-like structures that enhance nutrient delivery and physiological relevance (Gao et al., 2017; Y. S. Zhang et al., 2016). Although still in development, this approach seeks to address some limitations of current models and offers potential pathways for customisation to study specific cardiac pathologies and therapeutic responses. The ongoing work contributes to bridging the gap between static models and dynamic cardiac conditions, with future applications envisioned for understanding cardiac responses under spaceflight and other extreme environments.

## 6.2 AIMS AND OBJECTIVES

The third aim of this thesis is to develop an innovative hybrid heart-on-chip model engineered to mimic the complex cardiac microenvironment accurately. The ultimate goal is to establish a robust and reliable platform for a thorough investigation into the impact of space-like conditions on cardiac tissues.

Aim 3: To design, develop and fabricate a 3D hybrid heart-on-a-chip model that simulates the cardiac microenvironment.

Objectives for Aim 3

- To optimise 3D bioprinting techniques for cardiac tissues, including the 3D bioprinting methodologies and materials utilised to closely mimic the structure and function of cardiac tissues, ensuring compatibility with cardiomyocyte viability.
- To conduct biological assessments of the 3D bioprinted heart model by doing comprehensive evaluations of cell viability, proliferation, and functionality within the 3D bioprinted heart model under s-μG and IR to validate the model's biological fidelity.

## 6.3 METHODS

### 6.3.1 Cell Culture

The heart model incorporated three specific cell types: AC-16 human cardiomyocytes, adult human coronary artery endothelial cells (HCAEC), and adult human cardiac fibroblasts (HFCS). Specific information, including the complete culture medium used, can be found in Section 3.3. Cells were kept in a humidified atmosphere at 37°C with 5% (v/v) $CO_2$, with media changes every 3-4 days and passaging upon reaching approximately 80% confluence, employing aseptic techniques in class II biosafety cabinets.

### 6.3.2 Bioink Preparation and Parameters Optimization

To prepare the bio-ink precursors, gelatin and alginate concentrations were doubled to ensure a final 1:1 mixing ratio with cell suspensions, aiming to ease the cell encapsulation and mixing process and support cell viability post-printing. The preparation involved heating distilled water to 60°C and gradually adding gelatin and sodium alginate to achieve concentrations of i) 20% Gelatin (w/v), ii) 16% Gelatin + 8% Alginate (w/v), iii) 16% Gelatin + 4% Alginate (w/v), iv) 20% Gelatin + 8% Alginate (w/v), and v) 20% Gelatin + 4% Alginate (w/v).

The mixtures were stirred on a heated magnetic stirrer for two hours until fully dissolved. The resulting bio-inks were aliquoted into 10 mL volumes to avoid degradation from repeated thaw cycles and stored at 4°C. Before bioprinting and cell integration, aliquots were warmed to 37°C to optimise cell survival and printing efficacy.

A sequence of bioprinting experiments was executed employing a pneumatic extrusion-based 3D printer. These experiments were structured to methodically adjust bioprinting parameters such as pressure (kPa), temperature (°C), print speed (mm/s), pre-flow (ms), and post-flow (ms) to determine the optimal conditions for each specific bioink composition. This was essential to developing and choosing a sacrificial material, which would be utilised to create a vascular channel within the printed structure, subsequently liquefied and removed to establish a hollow channel conducive to endothelial cell lining.

For subsequent cell viability assessment, the investigation focused on two bio-ink formulations: a 10% gelatin solution and a composite solution of 10% gelatin with 2% alginate. These were chosen based on their superior rheological properties, which were conducive to precise extrusion and the maintenance of structural integrity post-printing.

HCAECs were cultured to 80% confluence, trypsinised, and resuspended in the selected bio-inks to achieve a final $1x10^6$ cells. $mL^{-1}$ concentration. Vascular channels were fabricated using a Cellink BioX 3D bioprinter with the optimised bio-inks under meticulously determined printing parameters. The constructs were incubated at 37°C in an atmosphere containing 5% $CO_2$ (v/v) in air post-fabrication. Cell viability was assessed at 0, 24-, 48-, and 72 hours post-printing, as described in Section 3.6.2. Briefly, cells were washed with PBS, stained with 1 μM calcein-AM and 4 μM ethidium homodimer-1, and incubated for 30 minutes at 37°C atmosphere containing 5% $CO_2$ (v/v) in air. Post-incubation, cells were washed with PBS to remove excess dye, and imaging was conducted using a fluorescent microscope. At least five FOVs were observed for each time point and treatment, capturing at least 50 cells per time to ensure a comprehensive viability assessment. Images acquired were analysed using FIJI (Image J) software, employing a custom macro for batch processing, as detailed in Appendix B.

Given the data's non-normal distribution, confirmed by Shapiro-Wilk tests ($p < 0.05$), non-parametric tests were selected for analysis. The Kruskal-Wallis test was used to compare cell viability percentages among different experimental groups and time points, with a significance threshold of $p < 0.05$ set to determine significant differences in viability under assessed conditions.

### 6.3.3 Collagen ECM Preparation and Optimization

The ECM was prepared using RatCol® Type I Collagen. Essential materials, including 10mg/ mL of the RatCol® Type I Collagen stock solution, sterile PBS, and neutralising solution, were chilled to prevent premature gelation. After determining the required volume of collagen, 1 part of the neutralising solution was transferred into a sterile mixing tube, and 9 parts of the rat tail collagen was subsequently added, giving a total of 10 parts. The stock concentration of the collagen was 4mg. mL-1, and after being neutralised, it is at 3.6mg. $mL^{-1}$. To obtain a 3 mg. $mL^{-1}$ concentration, 200uL of media containing 1.2 x $10^6$ cells were added for every mL of neutralised collagen solution. This dilution achieved a final cell concentration of 1 x $10^6$ cells $mL^{-1}$ in the ECM.

For experiments involving co-culture of AC-16 cardiomyocytes and HCF, cells were combined in a 2:1 ratio to obtain a total concentration of 1 x $10^6$ cells in 200 μL. This ratio ensured that two-thirds of the cell population consisted of AC-16 cardiomyocytes and one-third were HCFs. The addition of 200 μL of this cell suspension to 1 mL of neutralised collagen achieved a uniform final cell density of 1 x $10^6$ cells $mL^{-1}$ in the ECM. This consistency in cell density was maintained across all experimental conditions to facilitate accurate comparative analysis. For experiments conducted without HCFs, the concentration of AC-16 cardiomyocytes was equivalent to the total cell concentration, maintaining a final density of 1 x $10^6$ AC-16 cells. $mL^{-1}$ in the ECM.

Optimisation experiments include investigating the influence of collagen fibre size on the behaviour of embedded cells and utilising temperature variations during the polymerisation process to control fibre size within the collagen matrix. The experiment was divided into three distinct temperature treatment groups: large fibres (37°C for 1 hour), intermediate fibres (room temperature for 30 minutes followed by 37°C for 30 minutes), and small fibres (4°C for 30 minutes, room temperature for 15 minutes, and 37°C for 15 minutes). The effects of these different fibre sizes on cell morphology, proliferation, and migration within the collagen matrices were evaluated. Brightfield microscopy images were captured on Day 1, Day 4, and Day 8 post-embedding using an EVOS M5000 fluorescence microscope. Collagen fibre size and cell morphology were assessed qualitatively based on cell spreading and shape.

### 6.3.4 Hybrid Heart-on-Chip Device Fabrication

This section outlines the detailed process for constructing a hybrid Heart-on-Chip device, incorporating engineered model gaskets, hydrogel compositions for 3D cell co-culture, 3D bioprinting of vascular channels, and removing sacrificial material to establish a functional vascular network.

#### *6.3.4.1 Engineered model gasket*

Utilising CAD software (Solidworks, Dassault Systèmes), the gasket was meticulously designed to confine the bioprinted hydrogel structures within a predetermined area, reflecting the intended vascular channel geometry (Figure 6.1). A negative mould for the gasket was fabricated using a resin-based 3D printer (Form 2), from which a polydimethylsiloxane (PDMS) gasket was cast. The PDMS mixture, combined with a PDMS curing agent at a 10:1 ratio, was cured in an oven at 65°C for at least one hour. After curing, the gasket was carefully extracted, trimmed, and then plasma bonded to a glass slide. To facilitate the integration of the vascular model, 25G needles were inserted at both the inlet and outlet ends of the gasket.

*Figure 6.1 CAD Rendering of Negative Mould for PDMS Gasket Fabrication. Illustrates the CAD file for creating the negative mould for PDMS gasket casting, essential for confining bioprinted hydrogel structures within a specified area for intended vascular channel geometries. Developed using Solidworks (Dassault Systèmes) and printed with a Form 2 resin-based 3D printer.*

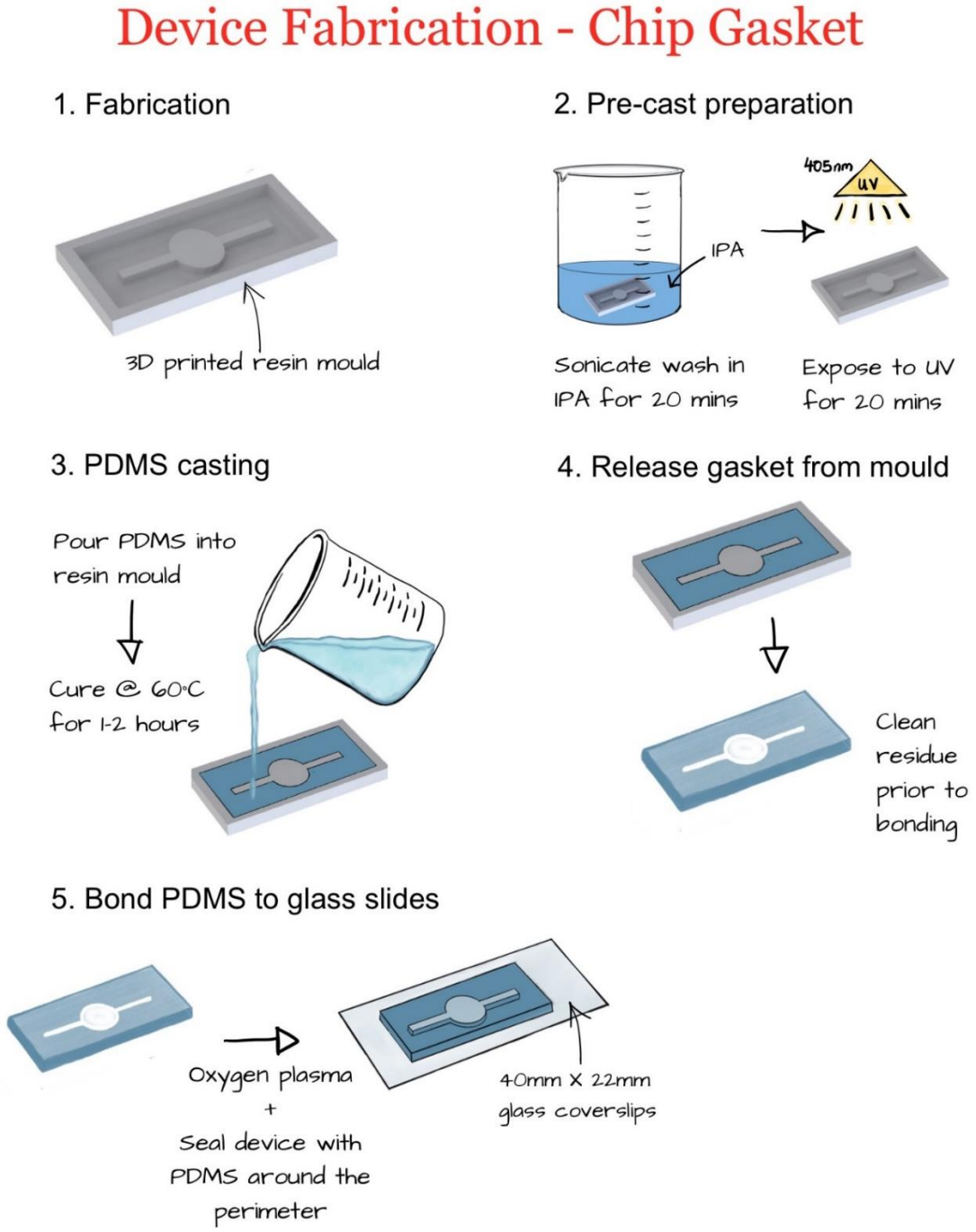


*Figure 6.2 Fabrication Process for a Polydimethylsiloxane (PDMS) Chip Gasket The fabrication process for a PDMS chip gasket involves five main steps: (1) Fabrication of a 3D-printed resin mould to shape the PDMS; (2) Preparation before casting, including sonication in IPA and UV exposure for cleanliness and surface activation; (3) PDMS casting into the resin mould, followed by curing at 60°C for 1-2 hours; (4) Release of the cured PDMS gasket from the mould, with cleaning to remove any residues; and (5) Bonding of the PDMS gasket to glass slides using oxygen plasma to ensure a sealed microfluidic device with a PDMS perimeter.*

#### *6.3.4.2 Hydrogel Composition and Fabrication for 3D Cells Co-Culture*

For cell encapsulation and cultivation within a 3D matrix, the ECM was formulated using RatCol® Type I Collagen (Advanced Biomatrix) at a final concentration of 3 mg. mL-1. Conversely, sacrificial vascular channels were created with a final composition of 10% (w/v) gelatin and 2% (w/v) alginate.

A stock solution of bio-ink precursor consisting of 20% (w/v) gelatin and 4% (w/v) alginate was prepared for cell encapsulation. This precursor hydrogel was preheated in a water bath for at least 30 minutes to ensure homogenous liquefaction and optimal temperature conditions. HCAECs were trypsinised, collected, and resuspended in MesoEndo cell growth medium to a concentration of $2x10^6$ cells in 500 μL. This cell suspension was then transferred to a 1.5 mL Eppendorf tube and thoroughly mixed with the bio-ink precursor at a 1:1 volume ratio (cell suspension to 20% gelatin + 4% alginate bio-ink precursor). This mixing resulted in a final bio-ink formulation containing $1x10^6$ cells. $mL.^{-1}$ in a 10% (w/v) gelatin and 2% (w/v) alginate solution, ready for the bioprinting process.

RatCol® Type I Collagen from Advanced Biomatrix prepared the ECM for cell encapsulation. Essential materials, including the collagen solution, sterile PBS, and neutralising solution, were chilled and kept on ice to prevent premature collagen gelation during the procedure. After determining the required volume of collagen, 1 part of the neutralising solution was transferred into a sterile mixing tube, and 9 parts of the rat tail collagen was subsequently added, giving a total of 10 parts. The stock concentration of the collagen was 4mg. mL-1, and after being neutralised, it is at 3.6mg. mL-1. This was stored on ice until the sacrificial vascular channel had been printed and the collagen ECM was ready to be cast. To obtain a 3 mg. mL-1 of neutralised collagen concentration, 200uL of $1x10^6$ cells in media were added for every mL of neutralised collagen. AC-16 cardiomyocytes and HCFs were collected and re-suspended into appropriate cell culture media at a ratio of 1:2 (HCFs: AC-16) within a volume of 200uL and mixed with 1mL of neutralised RatCol® Type I Collagen. This mixture was then mixed back and forth to ensure the homogenous mixture of the cells in the bioink was ready to use immediately.

#### *6.3.4.3 3D Bioprinting of Vascular Channels*

Sterilisation of the device setup preceded the 3D bioprinting phase, where the PDMS gasket, affixed to a glass slide, was exposed to UV light for 30 minutes for sterilisation, followed by two PBS washes of approximately 100μl that covered the whole negative structure. Collagen Type I coating at 50 μg/mL was added to the surface of the chip to promote cell attachment.

Employing a Cellink BioX 3D bioprinter, the vascular channels were printed using the sacrificial bioink 10% (w/v) gelatin and 2% (w/v) alginate bio-ink hydrogel. To print the sacrificial vascular channel within the gasket, a 27G needle was employed with precision to achieve the desired channel

size using the Cellink BioX 3D bioprinter system (Cellink, Sweden). The print parameters previously optimised —speed, pressure, and temperature—were meticulously controlled to achieve the precise dimensions and geometry of the vascular channels, ensuring the structural integrity and functionality of the printed channels. Printing parameters were set at a speed of 5 mm/s and a pressure range of 50-100 kPa at 30°C with a temperature-controlled print head. In contrast, the print bed was maintained at 8°C to facilitate the polymerisation of the 10% (w/v) gelatin and 2% (w/v) alginate hydrogel embedded with HCAEC. Given gelatin's ability to polymerise and solidify at lower temperatures, the hydrogel transitioned to a gel-like state upon reaching the print bed and completing the printing process.

Three vascular channel designs, VAS1, VAS2, and VAS3, each featuring a uniform 200 µm diameter channel, were initially designed to explore the effects of vascular geometries on fluid flow, shear stress, and endothelial cell behaviour. VAS1 was designed to simulate vascular dilation and constriction, with a channel leading to a large area and reconverging to a narrow exit, offering insights into blood flow dynamics in vascular anomalies. VAS2 branched into three separate channels and then merged back into one, aimed to examine the complexities of vascular branching and its implications for angiogenesis and vascular health. VAS3, the simplest design, featured a single channel bifurcating and reconverging, focusing on studying shear stress effects at bifurcation points on endothelial cells. VAS3 was selected for initial experimentation due to its simplicity and direct applicability in understanding the fundamental aspects of vascular flow dynamics and endothelial response to shear stress. This choice showcases a methodical approach to dissecting vascular biology and laying the groundwork for more complex future investigations.

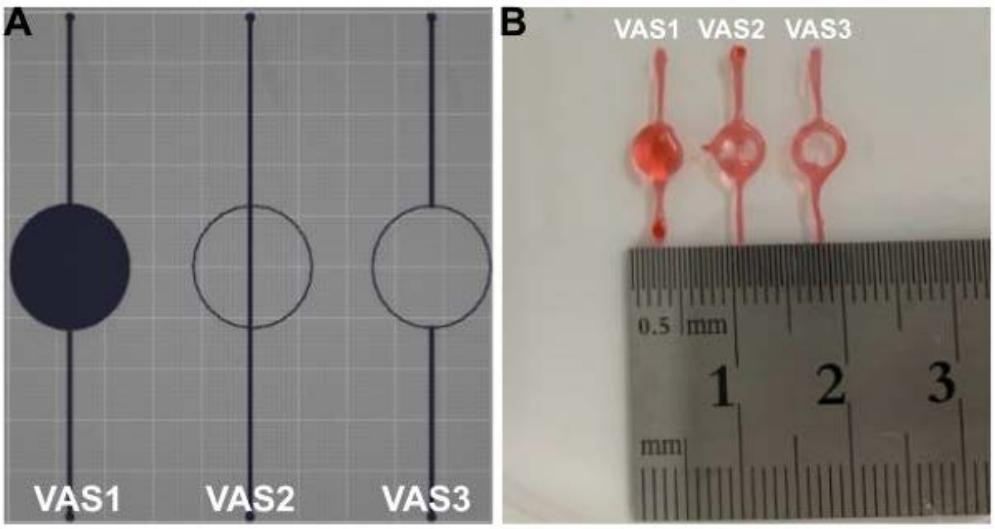


*Figure 6.3 CAD and Bioprinted Vascular Channel Designs: This figure showcases (A) CAD schematics alongside (B) their bioprinted counterparts, fabricated using sacrificial material for three distinct vascular channel designs. VAS1 features a 200 µm channel that widens and then narrows; VAS2 bifurcates a 200 µm channel into three branches and reconverges; VAS3 presents a straightforward bifurcation from a single 200 µm channel.*

Following printing the vascular channels, the ECM encapsulating AC-16 cardiomyocytes and hCFs within collagen were cast atop, encompassing the printed sacrificial channels and inlet/outlet needles. The device remained at room temperature throughout this procedure to enable the gradual polymerisation of the collagen, fostering the formation of larger collagen fibres (30 minutes at room temperature). Subsequently, the device was incubated at 37°C for 30 minutes to fully polymerise the collagen, which also resulted in the liquefaction of the sacrificial hydrogel. To facilitate the attachment of HCAECs to the inner wall of the channel under static conditions, the device was incubated for an additional two hours within a media bath at 37°C.

#### *6.3.4.4 Removal of sacrificial material*

The channel, previously filled with the sacrificial gel, was perfused, leaving behind a hollow structure indicative of the former vascular channel shape. Following incubation, the device was connected to a syringe pump by attaching the 25G needle to an empty syringe via a Tygon tube. The inlet was submerged in a reservoir containing culture medium. The introduction of the growth medium into the vascular channel facilitated the expulsion of the sacrificial material, now in a liquid state, from the channel, resulting in a hollow channel lined with HCAEC cells. Once the lumen was established, the growth medium was continuously circulated through the channel, promoting the full maturation of the HCAEC cells over 2 days.

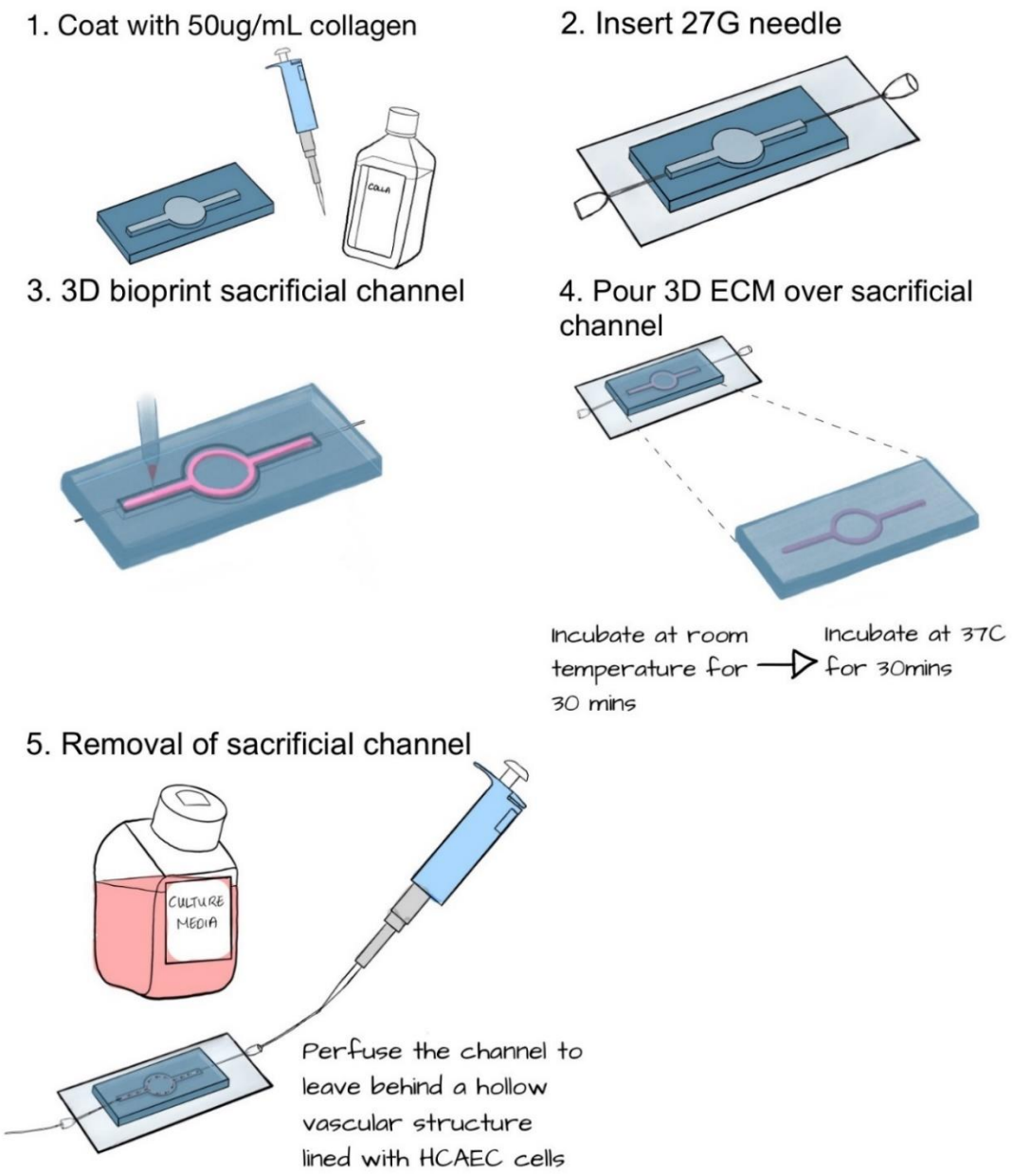


*Figure 6.4 Device Fabrication Process for Cell Incorporation in Microfluidic Channels. The fabrication process for incorporating cells into microfluidic channels includes: (1) Coating the device with 50 µg/mL collagen to prepare the surface; (2) Inserting a 27G needle to define the flow path; (3) 3D bioprinting of a sacrificial channel within the device; (4) Casting ECM over the bioprinted sacrificial channel to embed the cellular structure, followed by a two-stage incubation—first at room temperature for 30 minutes to allow initial polymerisation, then at 37°C for 30 minutes to complete polymerisation and initiate sacrificial material liquefaction; and (5) Removing the sacrificial channel through perfusion, leaving a hollow vascular structure lined with HCAEC cells, ready for subsequent biological studies.*

## 6.4 RESULTS

### 6.4.1 Optimisation and Evaluation of Materials and Devices

#### *6.4.1.1 Evaluation of Bioink Formulations and Printing Conditions*

In the initial experimental series that examined the print quality of various bio-ink compositions, five distinct formulations were evaluated under controlled conditions: a set temperature of 30°C and a consistent print speed of 5 mm/s. The pressures were varied from 20kPa to 120kPa to cater to the unique flow characteristics of each bioink (Table 6.1)

*Table 6.1 Results of Initial Printing Optimisation.*

| Bioink Composition | Pressure (kPa) | Temperature (°C) | Speed (mm/s) | Rating | Notes |
|---|---|---|---|---|---|
| 10% Gelatin | 50 | 30 | 5 |  | Consistent print with little adjustments... |
| 8% Gelatin + 4% Alginate | 50 | 30 | 5 |  | Patchy print |
| 8% Gelatin + 2% Alginate | 20 | 30 | 5 |  | Too liquid |
| 10% Gelatin + 4% Alginate | 120 | 30 | 5 |  | It's patchy, and the nozzle gets blocked easily. |
| 10% Gelatin + 2% Alginate | 100 | 30 | 5 |  | Close to true size, consistent prints |

The 10% gelatin bio-ink from the initial experiment exhibited the most promising results, achieving consistent and stable prints with minimal adjustments at a moderate pressure of 50 kPa.

The 8% gelatin + 4% alginate blend, printed at 50 kPa, resulted in patchy structures, indicating that the viscosity might not be conducive to a stable bioprinting process regardless of pressure adjustments ±20kPa.

The 10% gelatin + 4% alginate blend faced extrusion difficulties and frequent nozzle clogging at a higher pressure of 120 kPa, suggesting a need for viscosity modification.

The 8% gelatin + 2% alginate bioink, at a lower pressure of 20 kPa, was too fluid for effective printing, resulting in poor structural integrity.

On the other hand, the 10% gelatin + 2% alginate bioink performed well at 100 kPa, producing prints that nearly matched the intended size and exhibited consistent quality, warranting further exploration.

These results highlighted the delicate balance between bioink composition and printing parameters, with bioink viscosity and temperature sensitivity playing pivotal roles. This led to focused experiments, where refined parameters, such as varied pressures, temperatures, print speeds, and the new introduction of pre-flow and post-flow timings, were tested on selected bioink formulations identified as promising from the initial experiments —specifically 10% gelatin, 10% gelatin + 2% alginate, and 8% gelatin + 4% alginate (Table 6.4.2)

*Table 6.2 Results of Printing Optimisatio.*

| Bioink Composition | Pressure (kPa) | Temperature (°C) | Print Speed (mm/s) | Pre-flow (ms) | Post-flow (ms) | Rating | Notes |
|---|---|---|---|---|---|---|---|
| 10% Gelatin | 50 | 30 | 2 | | | 🟡 | Structure swelled |
| | 50 | 30 | 5 | | | 🟡 | Defined structure, a patch is missing |
| | 60 | 30 | 5 | | | 🟡 | Super flat, well-defined structure |
| | 100 | 30 | 3 | 150 | | 🟢 | Best one |
| | 100 | 30 | 4 | | | 🟡 | Good size, missing a patch |
| | 100 | 30 | 5 | | | 🟢 | Good consistency |
| | 75 | 32 | 5 | 250 | 500 | 🟡 | The print is not smooth; there are lumps in some areas. |
| 10% Gelatin + 2% Alginate | 80 | 28 | 8 | 400 | | 🟡 | Minimal swelling, good size, defined features |
| | 50 | 30 | 5 | 100 | 100 | 🟡 | Minimal swelling, good size, defined features |
| 8% Gelatin + 4% Alginate | 50 | 25 | 3 | | 100 | 🔴 | Multiple unsuccessful attempts at extrusion |
| | 25 | 28 | 2 | | | 🔴 | Undefined structure |
| | 40 | 28 | 5 | | | 🔴 | Less swelling but patchy |
| | 50 | 28 | 5 | | | 🔴 | Undefined shape (still too liquid) |
| | 50 | 30 | 3 | | | 🔴 | Print swelled (bioink is too liquid) |

For the 10% gelatin bio-ink, a range of pressures (25 kPa – 100kPa), print speeds (2 mm/s – 8mm/s), and temperatures were tested (28°C – 32°C), and pre-flow and post-flow timings were introduced. Lower print speeds led to swelling, while certain pressure-speed combinations produced defined structures with some gaps. The most optimal condition was at 100 kPa pressure with a 3 mm/s print speed and a pre-flow timing of 150 ms, generating the best print quality, where structures were defined, and no gaps were present in the final structure. However, adjusting the printing temperatures to slightly higher temperatures introduced issues, such as clump formation, underscoring the need for flow timing adjustments. Variations in print speed at this pressure displayed good size and consistency, with some parts of the structure missing, creating gaps in the desired vessel structure.

Printing at a speed of 5 mm/s at 50 kPa pressure produced a more defined structure, although some parts were missing again. Increasing the pressure to 60 kPa and maintaining the speed at 5 mm/s yielded a flat structure with good definition. The combination of a slightly increased temperature (32°C) and a pre-flow of 250 ms with a substantial post-flow of 500 ms resulted in a print that was not irregular and didn't clump, indicating the need for fine-tuning flow timings. Temperature changes also affected the print quality, as seen in the swelled structures at higher temperatures, despite adding flow timings.

The 10% gelatin + 2% alginate bio-ink responded well to a print speed of 8 mm/s at 80 kPa pressure and a lower temperature of 28°C, with a pre-flow of 400 ms, resulting in minimal swelling and well-defined features. A similar outcome was observed at a pressure of 50 kPa, temperature of 30°C, and balanced pre-flow and post-flow timings of 100 ms each, affirming the importance of coordinated flow timings in achieving print accuracy. The 10% gelatin + 2% alginate bio-ink was fine-tuned to achieve minimal swelling and well-defined features, indicating that the print speed and temperature adjustments were beneficial.

Conversely, the 8% gelatin + 4% alginate bio-ink remained problematic. Multiple attempts were unsuccessful in extruding the bioink at 50 kPa pressure and 25°C temperature. Increasing the temperature to 28°C and adjusting the print speed did not significantly improve the results, with prints still displaying undefined structures and patchiness. A print speed of 3 mm/s at 50 kPa and 30°C resulted in swelling, indicating that the bioink was still too fluid for effective printing.

When taken together with the visual evidence from Figure 6.4.1 and the comprehensive data, Table 6.4.1 and Table 6.4.2, the findings from this set of experiments illustrate the intricate interplay between bioink composition and printing parameters—further emphasising that achieving the desired print quality in 3D bioprinting necessitates meticulous pressure optimisation, temperature, and speed optimisation.

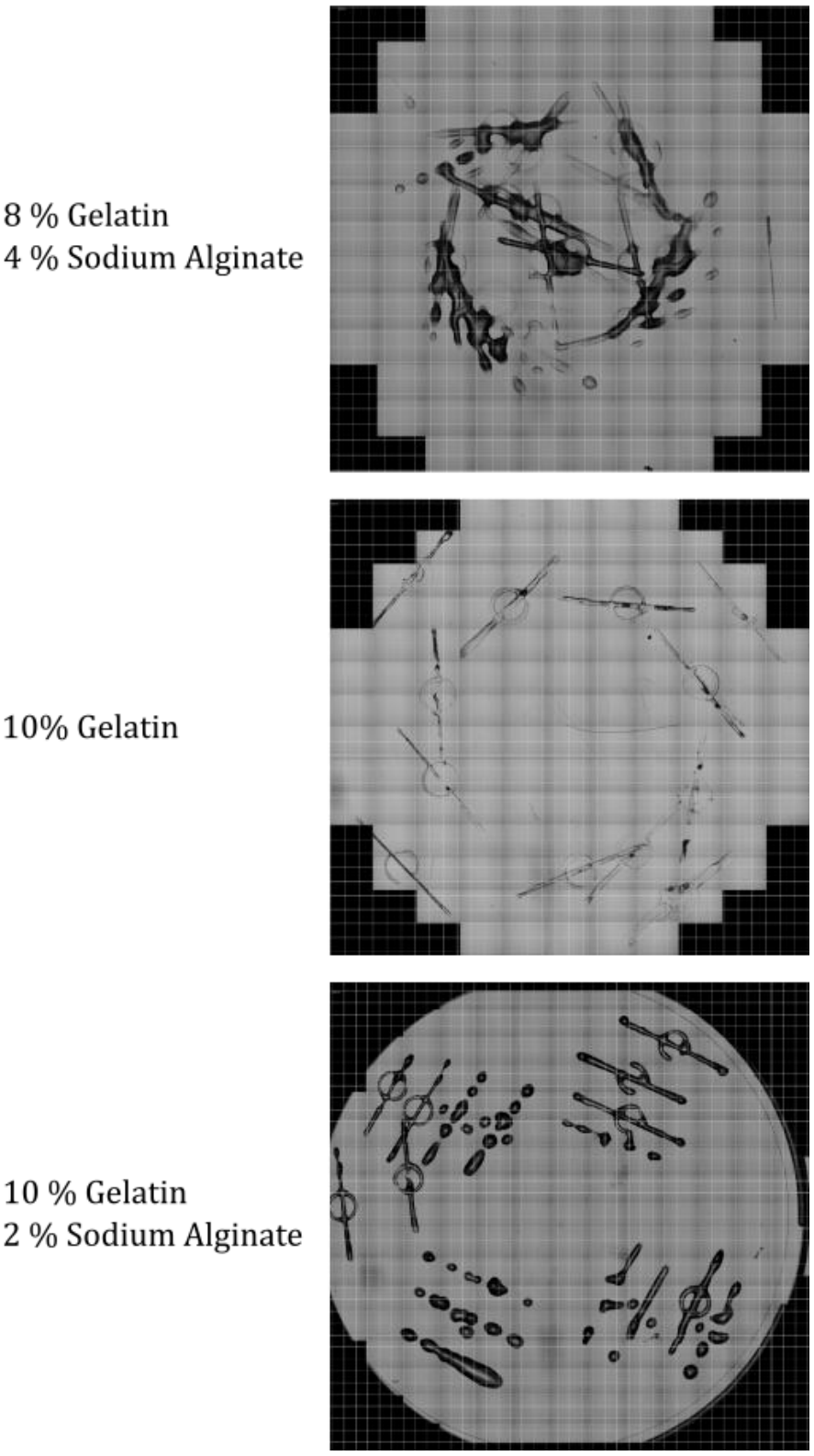


*Figure 6.5 Assessment of Print Quality Across Varied Bioink Compositions. The series of images from top to bottom represents the structural outcomes of bioprinted constructs using (1) 8% Gelatin + 4% Alginate, (2) 10% Gelatin, and (3) 10% Gelatin + 2% Alginate bioinks. The top image reveals challenges with the 8% Gelatin + 4% Alginate blend, including inconsistent printing and nozzle blockages at higher pressures. The middle image displays the 10% Gelatin bioink, showing uniform and stable printing at an optimised pressure of 50 kPa. The bottom image illustrates the 10% Gelatin + 2% Alginate bioink, which achieved satisfactory print quality at a higher pressure setting of 100 kPa.*

#### *6.4.1.2 Viability within Sacrificial Bioink*

After optimising the sacrificial bio-ink precursor composition and the printing parameters, the focus shifted to assessing the viability of HCAECs encapsulated within bioprinted constructs over 72 hours. This assessment targeted the two most promising bio-ink compositions: 10% gelatin and 10% gelatin with 2% alginate (Figure 6.6)

For constructs created with 10% gelatin bioink, a significant decrease in cell viability was observed at both 24 hours ($p=0.0040$) and 48 hours ($p<0.0001$) when compared to the 0-hour reference point. However, by 72 hours, the viability levels showed no significant deviation from the 0-hour measurement, indicating a stabilisation of cell conditions. In parallel, the constructs comprising 10% gelatin and 2% alginate bioink also experienced significant reductions in cell viability at 24 hours ($p=0.0038$) and 48 hours ($p=0.0122$). Similar to the gelatin-only constructs, by the 72-hour mark, the viability of cells in these constructs did not significantly differ from the initial measurements.

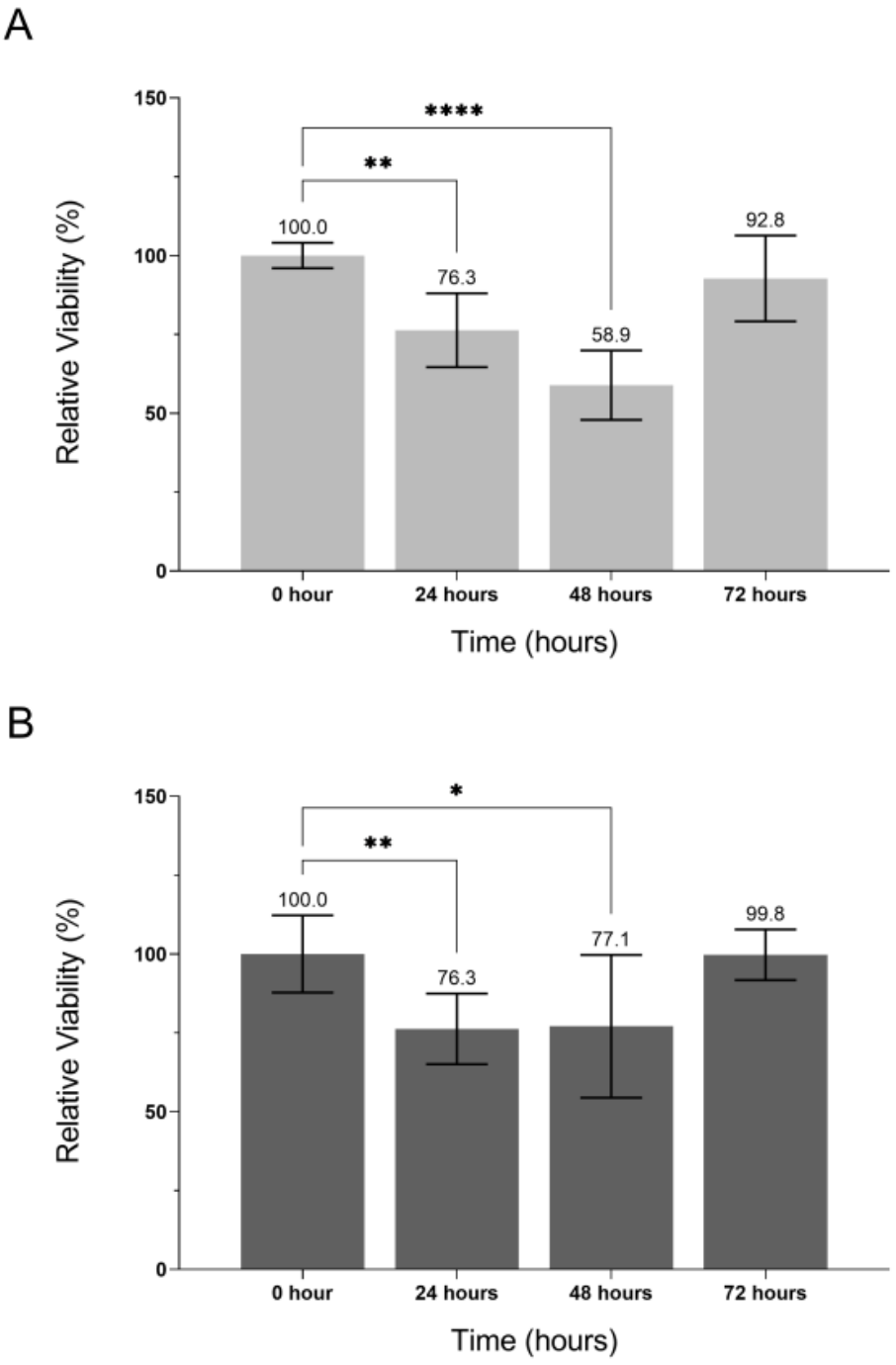


*Figure 6.6 Comparative Cell Viability in Bioprinted Constructs Over 72 Hours. (A) Viability of Human Coronary Artery Endothelial Cells (HCAECs) encapsulated in 10% gelatin bioink, illustrating significant reductions at 24 and 48 hours, with stabilisation by 72 hours. (B) Cell viability in constructs with 10% gelatin and 2% alginate bioink showed similar trends, with significant decreases at 24 and 48 hours, followed by stabilisation at the 72-hour mark. Statistical significance is indicated for comparisons against the initial 0 hours measurement. Significance levels: * ($p \leq 0.05$), ** ($p \leq 0.01$), **** ($p \leq 0.0001$).*

#### *6.4.1.3 Collagen Behaviour Modulated by Temperature*

The following experiment demonstrated significant variations in collagen fibre formation under differing temperature treatments. The approach involving initial cooling at 4°C, followed by a gradual warming process, resulted in larger and more visible collagen fibres formed when observed under brightfield microscopy. This finding starkly contrasted with the results obtained from the standard protocol, where collagen fibres remained largely invisible. An intermediate treatment, which entailed exposure to room temperature for 30 minutes before proceeding to the 37°C incubation, yielded moderately visible fibres.

Throughout the 8-day observation period, significant variations in cell morphology were observed across the different treatment groups. In the 37°C treatment group, cells remained rounded without noticeable morphological changes (Figure 6.7). Rounded cells, as seen in the 37°C treatment group, typically indicate minimal interaction with the substrate, which can limit cell proliferation and function. Cell proliferation was notably subdued in the 37°C treatment group, with minimal increases in cell numbers observed.

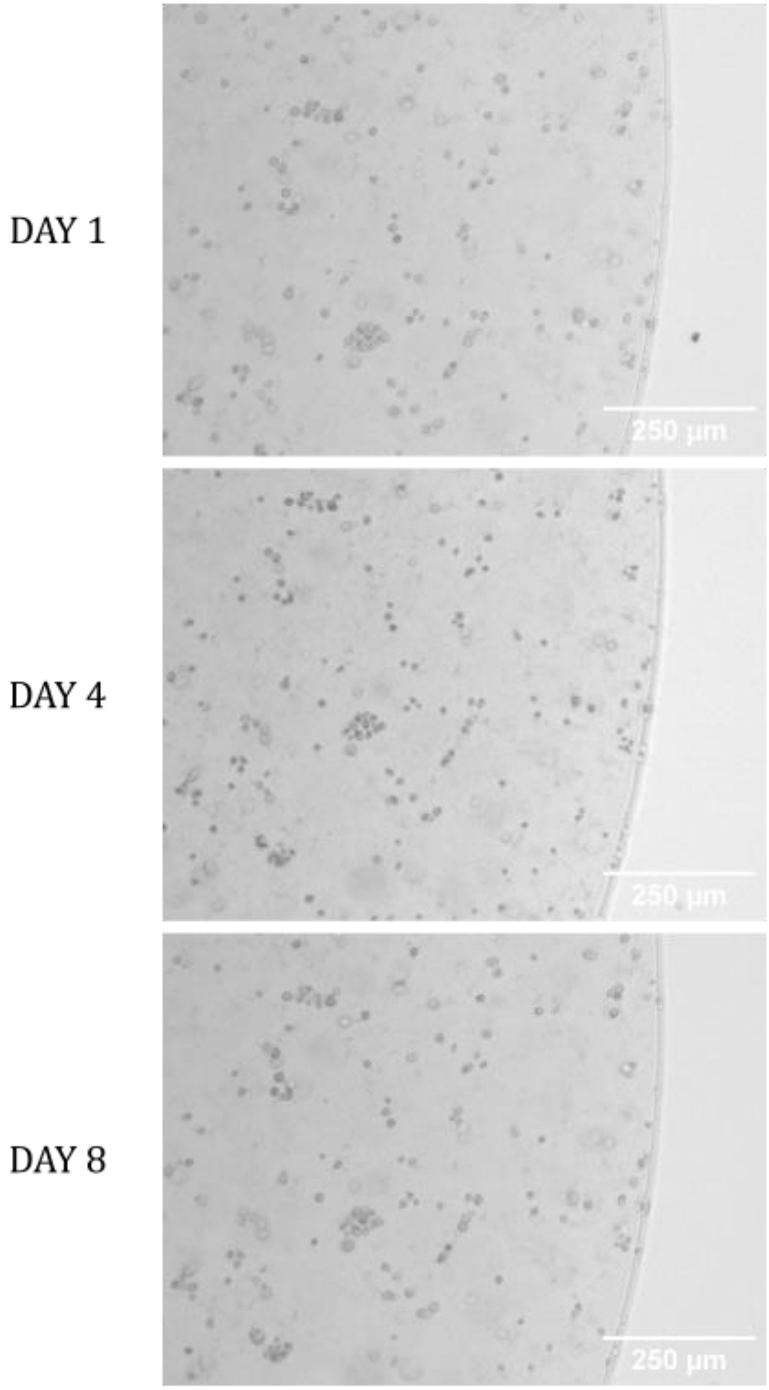


*Figure 6.7 Cell Behaviour and Collagen Fiber Visibility in the 37°C Treatment Group. This figure illustrates the outcome of embedding fibroblast cells within a collagen matrix followed by incubation solely at 37°C for 1 hour. Representative brightfield microscopy images taken on Day 1, Day 4, and Day 8 depicted the absence of visible collagen fibres and the morphology of embedded cells over time, highlighting minimal changes in cell count.*

In contrast, in the groups with larger and visible fibres (4°C and RT before 37°C), cells demonstrated marked changes in morphology over time, transitioning from round to more spread and elongated forms, indicative of enhanced interaction with the collagen matrix (Figure 6.8). The cells showed evidence of active cell proliferation within these collagen gels. By Day 8, the cell count had increased

within these groups, and cells were also observed migrating out of the collagen gel, highlighting a dynamic response to the structural properties of the collagen matrix.

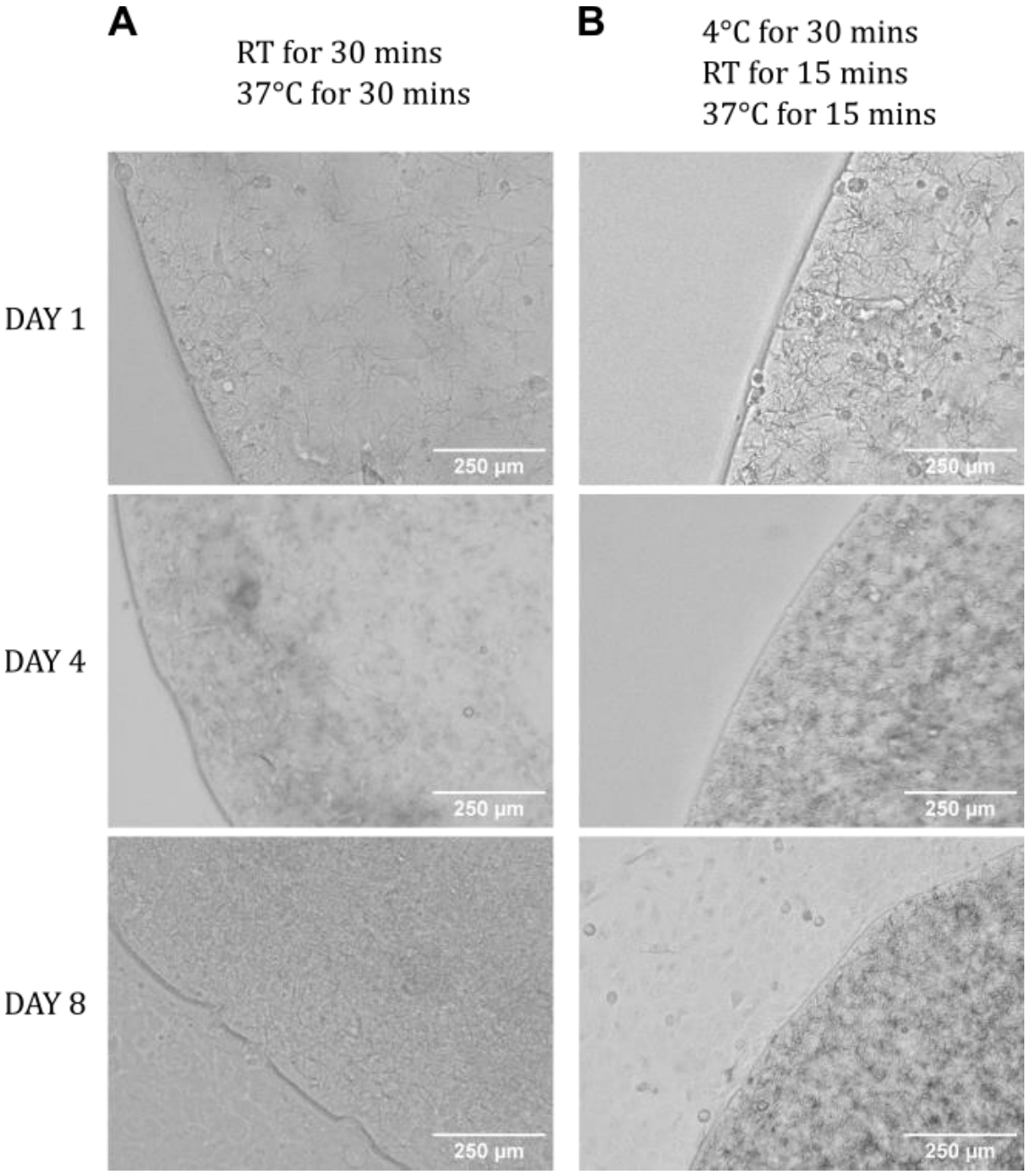


*Figure 6.8 Comparative Analysis of Cell Behaviour and Collagen Fiber Formation under Different Temperature Treatments. Panel A corresponds to the 4˚C treatment followed by incubation at 37˚C, whereas Panel B represents the protocol starting at 4˚C, transitioning to room temperature, and concluding with a 37˚C incubation. Each sub-panel includes brightfield microscopy images taken on Day 1, Day 4, and Day 8. Panel A (4˚C then 37˚C) demonstrates visible collagen fibre formation with moderate cell proliferation and morphological changes. Panel B (4˚C, RT, then 37˚C) shows pronounced collagen fibre visibility, significant cell proliferation, and extensive cell migration out of the collagen gel by Day 8.*

#### *6.4.1.4 Viability of AC-16 Cardiomyocytes and HCF in 3D Collagen*

The co-culture of AC-16 human cardiomyocytes with HCF in a 3D collagen matrix focused on investigating the complex interaction of heart cells' adaptive behaviours in a simulated ECM, providing insights into cardiac tissue dynamics. AC-16 cardiomyocytes, derived from human ventricular tissue, serve as a vital model for cardiac research, offering insights into heart function and disease mechanisms. The inclusion of HCF in the culture aimed to elucidate the role of fibroblasts in supporting cardiomyocyte function and contributing to the structural integrity of cardiac tissue.

In the following experiment, the viability and responses of AC-16 cardiomyocytes, when cultured with HCF in a 3D collagen matrix, were investigated. Observations commenced from Day 1, allowing sufficient time for the cells to adapt to the collagen matrix, providing a foundational understanding of their initial adaptation and subsequent dynamic changes. Initial observations indicated a uniform adaptation with uniform median values at 100% viability, suggesting effective cell adjustment and spreading from Day 1. However, a significant shift was observed by Day 3, where median values decreased to 95.4% viability, highlighting a range of cellular behaviours with statistical significance ($p<0.001$), as shown in Figure 6.9. This change underscores the evolving nature of cell-matrix and cell-cell interactions. By Day 5, a stabilisation was noted with median values returning to 100% viability, indicating a recovery or equilibrium in cellular adaptation, supported by a significant change from Day 3 ($p=0.0198$), yet showing no statistical difference from Day 1 ($p=0.2737$).

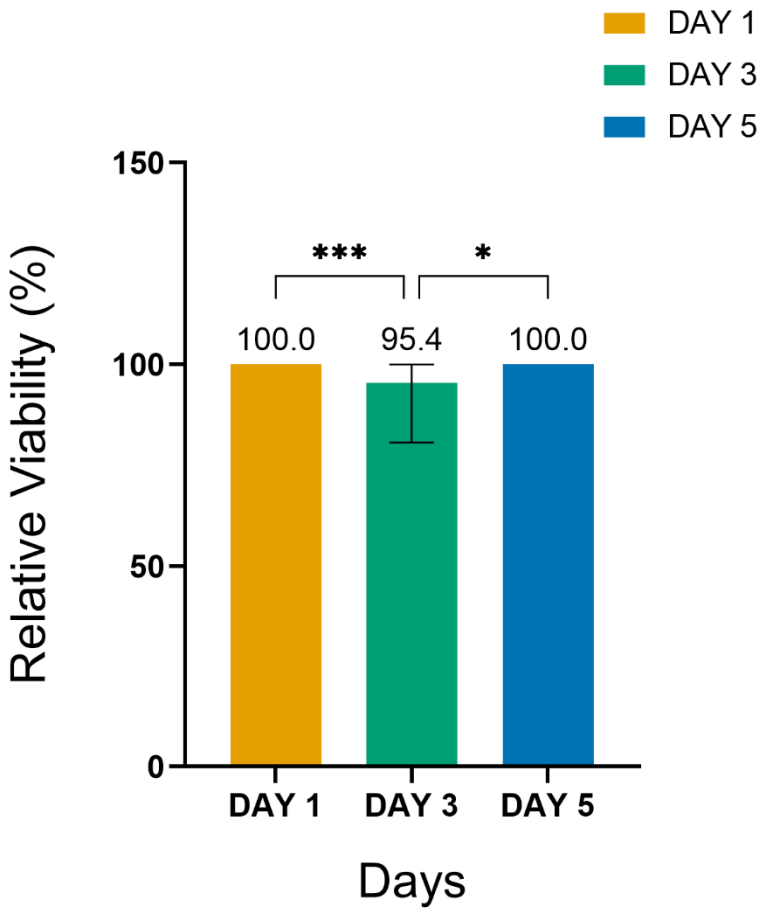


*Figure 6.9 Viability of AC-16 Human Cardiomyocytes Co-cultured with Human Cardiac Fibroblasts (HCF) in a 3D Collagen Matrix Over a Five-Day Period. Day 1 serves as a reference, showing uniform cell adaptation with median viability values at 100%. A noticeable decline to 95.4% median viability by Day 3 signifies a period of adjustment with significant cellular responses ($p < 0.0001$). By Day 5, viability returned to starting levels, indicating a recovery to initial adaptation states or a new equilibrium within the cellular environment ($p = 0.0198$ from Day 3; no significant difference from Day 1 with $p = 0.2737$). Significance level: * ($p \leq 0.05$), *** ($p \leq 0.001$).*

#### *6.4.1.5 Preliminary Formation of Vascular Channel*

The initial stages of the fabrication of the hybrid heart-on-chip device were dedicated to developing and refining a method for creating hollow vascular channels within the collagen ECM. This process involved strategically removing sacrificial material designed to emulate the intricate patterns of natural vasculature.

The initial findings from this study confirmed the successful perfusion and removal of the sacrificial material used to form vascular channels within a collagen matrix. This critical step validated the capability of the sacrificial channel to be entirely cleared out, leaving behind a hollow structure that mirrors the intended vascular patterns. Moreover, these results demonstrated the resilience of the collagen matrix, effectively withstanding the manipulations involved in the removal process and the shear flow introduced during perfusion.

The chosen vascular channel design included a channel with a 200 μm diameter that bifurcated and reconverged within the gasket (Figure 6.10). In these initial experiments, red dye was included in the sacrificial material to help distinguish the sacrificial material and the opaque collagen matrix. The contrast between the sacrificial material and the ECM can be seen. After the removal of sacrificial material by perfusion, the clear channel formation in the shape of VAS3 amidst the ECM, with traces of red dye observed diffusing into the ECM, emphasises the precision and effectiveness of the removal process. This visualisation highlights the precision of the channel creation process and suggested interactions between the vascular structure and the surrounding matrix, which is crucial for developing functional tissue constructs. Establishing these optimal conditions is a significant step toward endothelialising the channels, contributing greatly to the goal of replicating the structural and functional complexity of natural tissues in engineered constructs.

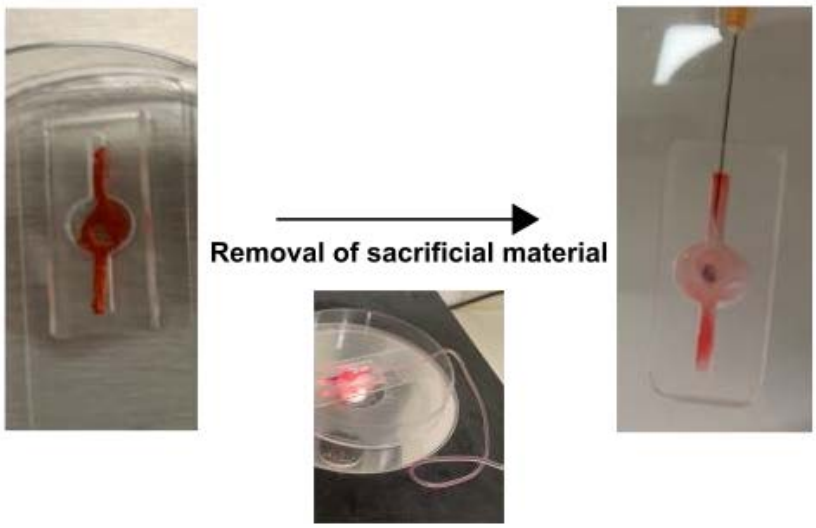


*Figure 6.10 Visualisation of the Engineered Vascular Channel within the Collagen ECM. A collagen ECM depicts the engineered vascular channel following the removal of sacrificial material. The channel design features a 200 μm diameter that bifurcates and reconverges, creating a clear pathway through the opaque collagen matrix. Red dye, initially integrated into the sacrificial material to trace the channel's formation, is visible as remnants within the ECM, indicating slight diffusion from the vascular channel.*

### 6.4.2 Cellular Responses – Initial Assessment

Following the optimisation of experimental parameters, the investigation advanced to evaluate the effects of experimental conditions (static control, s-μG, IR, and the combination of s-μG and IR) on components of the hybrid heart-on-chip. Including HCFs is essential for simulating the *in vivo* cardiac environment, thereby enhancing the physiological relevance of the experimental models. These fibroblasts are crucial for maintaining cardiac tissue structure and function, offering a more comprehensive understanding of cellular interactions under varied stress conditions.

This phase is integral to the broader application of these findings in the development of heart-on-chip technology. Such technology aims to replicate essential features of human heart function at a microscale, facilitating advanced studies on heart diseases and therapeutic strategies. By incorporating both cardiomyocytes and fibroblasts, the heart-on-chip model aims to elucidate mechanisms of cardiac fibrosis, resilience, and regeneration under stress, thus contributing significantly to advancements in cardiovascular research and potential clinical applications.

#### *6.4.2.1 Proliferation of combined AC-16 + HCF under combined stressors*

In the conducted analysis, Šídák's multiple comparisons tests were used to assess significant differences in cellular responses under various experimental conditions. These conditions involved AC-16 cardiomyocytes cultured alone (-HCF) or in conjunction with human cardiac fibroblasts (+HCF).

A statistically significant difference was observed in the static control exposed cells, with cells cultured without HCF exhibiting a lower proliferation rate, indicated by a p-value of 0.0005. This finding suggests that the presence of HCFs may enhance the proliferation of AC-16 cardiomyocytes under static conditions. Similarly, when the cardiomyocytes were exposed to s-μG, the impact of cells cultured without HCF was also significant, leading to a decreased proliferation rate in the -HCFs group compared to the +HCFs group, denoted by a p-value of 0.0009. This finding supports the notion that HCFs may be critical in modulating cardiomyocyte response to microgravity conditions. More pronounced effects were observed in the IR condition, which exhibited a highly significant difference with a p-value of less than 0.0001. The -HCFs group showed significantly lower proliferation rates compared to cells co-cultured with HCFs, indicating that the protective effects of HCFs may be particularly crucial in environments with ionising radiation. The combined stressors of s-μG + IR demonstrated a comparable level of statistical significance, with a p-value of less than 0.0001. The lower proliferation rates in the -HCFs group underline the potential synergistic impact of HCFs in mitigating the adverse effects of combined environmental stressors on cardiomyocyte function.

These results collectively demonstrate that the absence of HCFs consistently leads to reduced proliferation rates in AC-16 cardiomyocytes across various experimental conditions (Figure 6.11). The significant differences noted in each scenario underscore the integral role of HCFs in supporting cardiomyocyte adaptation and survival under stress.

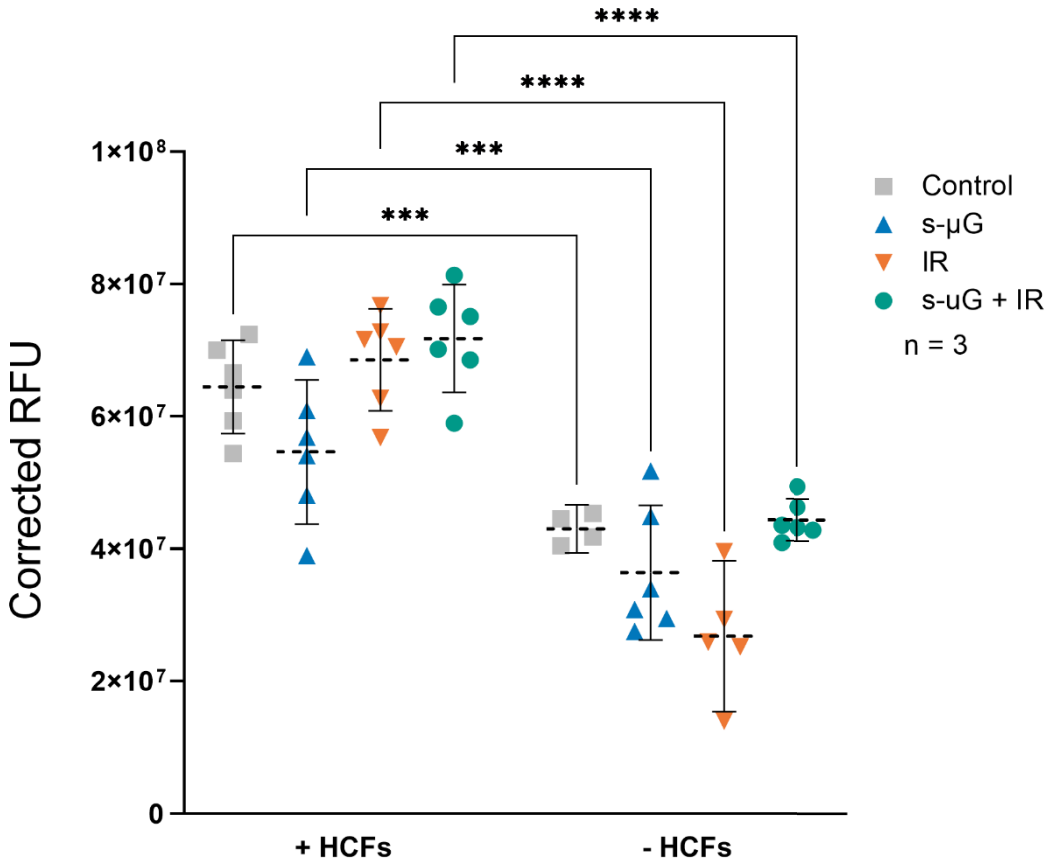


*Figure 6.11 Comparative analysis of cellular responses in AC-16 cardiomyocytes co-cultured with human cardiac fibroblasts (+HCF) and AC-16 cardiomyocytes cultured alone (-HCF) under various experimental conditions. The figure illustrates that in +HCF cultures, significant differences were only observed when comparing IR and its combination with s-μG to s-μG alone. Conversely, in -HCF cultures, significant changes were noted when comparing IR to ctrl and s-μG + IR to IR, highlighting the distinct impacts of IR and its enhancement by s-μG on cardiomyocytes cultured without fibroblasts. Significance level: * ($p \leq 0.05$), ** ($p \leq 0.01$) *** ($p \leq 0.001$), **** ($p \leq 0.0001$).*

#### *6.4.2.2 Advancements and Challenges in 3D Heart-on-a-Chip Fabrication*

The study aimed to develop an experimental model that closely simulated cardiac tissue's complex architecture and functional dynamics. The planned components of the model included a collagen ECM embedding AC-16 cardiomyocytes and human cardiac fibroblasts layered over a bioprinted scaffold channel of gelatin and alginate hydrogel, with endothelial cells embedded. This channel would eventually act as a vascular channel integrated within the cardiac model, achieving a hybrid 3D Heart-on-a-Chip. This structure mimics the vascularised heart, providing realistic simulations of cellular environments and interactions. The model was expected to facilitate detailed studies of the responses of the cardiovascular system under space conditions, including space microgravity and IR.

The planned objectives of the project were to optimise and establish a co-culture system of cardiomyocytes and fibroblasts within the ECM, optimise and use sacrificial materials to create vascular-like channels that could be made perfusable, introduce flow within these channels to

simulate blood flow and investigate mechanotransduction processes focusing on YAP nuclear translocation in response to mechanical stresses of space conditions.

In terms of achievements, the project successfully established the co-culture of cardiomyocytes and fibroblasts, achieving optimal concentration ratios that facilitated effective cellular interactions and proliferation. Incorporating cardiomyocytes and fibroblasts within the collagen ECM is critical for replicating the cardiac tissue's cellular composition and mechanical properties. The integration of sacrificial materials was also refined. The successful removal of the sacrificial material, leaving behind a perfusable vascular channel, demonstrated the bioprinting process's precision and the collagen matrix's robustness. This optimised methodology, which included optimising materials and 3D bioprinting parameters, represented another key achievement of this study. The model progressed to the assessment phase under previously defined experimental conditions—static control, s-μG, IR, and their combinations—to challenge the cells with environmental stressors mimicking those encountered in space exploration.

However, the project faced substantial disruptions that impacted further progress. The global pandemic restricted access to laboratory facilities, significantly reducing the time for experimental work. Additionally, supply chain disruptions during the pandemic caused delays in delivering critical materials and equipment for the research, further complicating the project's progression. The intermittent availability of supervisory support also posed significant challenges, with the need for timely guidance and feedback impeding effective problem-solving and decision-making.

In conclusion, progress was made on the development of the heart-on-a-chip model by successfully establishing the co-culture system and integrating vascular-like structures. However, the system's full integration and final testing were not pursued. Instead, prioritising the analysis and documentation of the data obtained took precedence over further experimental work. This adjustment in focus was necessary to ensure the thorough presentation and evaluation of the results achieved under the constraints encountered.

## 6.5 DISCUSSION

This thesis chapter presents the development and fabrication of a 3D hybrid heart-on-a-chip model, which simulates cardiac tissue architecture and dynamics. The model effectively mimics the vascularised heart structure by embedding cardiomyocytes and fibroblasts in a collagen ECM and incorporating a vascular channel of endothelial cells within a gelatin-alginate hydrogel scaffold. This innovative approach enhances the study of cellular interactions, enabling detailed investigations into cardiac cells' mechanical and physiological responses under various stress conditions, including space microgravity and radiation.

### 6.5.1 Optimisation and Evaluation of Materials and Methods for the Fabrication of the Hybrid Heart-on-Chip

The optimisation of materials and fabrication methods was crucial in developing the hybrid heart-on-a-chip model. Key to this process was understanding how the ECM's physical properties influence cellular behaviour. Fibrillogenesis, the process of collagen fibre formation, is sensitive to various physicochemical conditions, including temperature, which can significantly influence collagen fibre size, shape, and opacity. Literature has shown that lower temperatures or gradual warming promote the formation of larger, more visible fibres due to slower fibrillogenesis, facilitating orderly assembly, in stark contrast to the rapid, less organised fibril formation at the physiological temperatures of 37°C that typically results in smaller, less visible fibres (Raub et al., 2007; Yang et al., 2009). Cell interaction with the collagen matrix is crucial for various biological processes, including cell migration, proliferation, and morphogenesis.

This study observed considerable variation in cell interaction with the collagen matrix under different temperature treatments. At 37°C, the absence of visible collagen fibres correlated with minimal cell proliferation and significant morphological changes, suggesting diminished cell-matrix interaction (Figure 6.7). Conversely, collagen ECM polymerised initially at 4°C and room temperature before exposure to 37°C preserved visible collagen fibres (Figure 6.8). Enhanced cellular responses, such as morphological changes, increased proliferation, and migration, were noted, confirming that lower temperatures promote the formation of larger collagen fibres, facilitating greater cell attachment and migration. This finding supports the notion that the physical properties of ECM significantly impact cellular behaviour (Fraley et al., 2015).

Further viability assessments incorporating AC-16 cardiomyocytes and HCF into the collagen ECM revealed adaptive behaviours, highlighting the dynamic nature of cell-matrix and cell-cell interactions in 3D cultures. Initial declines in cell viability were observed within the first 48 hours post-printing, but stabilisation by 72 hours confirmed the ECM's supportive role in maintaining cellular function

over time. These findings emphasise the critical role of the ECM's physical properties in supporting cardiac tissue dynamics and underscore the need for precise optimisation of fabrication conditions.

The development of the hybrid heart-on-a-chip model also required extensive optimisation of the sacrificial bioink to ensure structural integrity and cellular compatibility. Among the tested bioinks, the 10% gelatin formulation consistently produced stable prints at moderate pressure (50 kPa). In contrast, the 8% gelatin + 4% alginate blend exhibited patchy and inconsistent structures, even with pressure adjustments, while the 10% gelatin + 4% alginate blend faced extrusion difficulties and nozzle clogging at higher pressures. The 10% gelatin + 2% alginate bioink performed optimally at 100 kPa, producing structures that maintained their intended size and quality, demonstrating its potential for further development in the heart-on-a-chip model.

Further experiments refined the printing conditions for the most promising bioinks: 10% gelatin and 10% gelatin + 2% alginate. Optimal conditions for the 10% gelatin bioink were achieved at 100 kPa pressure with a 3 mm/s print speed, delivering high-quality prints. For the 10% gelatin + 2% alginate blend, the best results were achieved at 80 kPa with an 8 mm/s print speed at 28°C, resulting in well-defined features with minimal swelling. These findings underscore the importance of optimising parameters such as pressure, temperature, and speed in achieving consistent, high-quality bioprints for the hybrid heart-on-a-chip model, as supported by visual evidence (Figure 6.5) and data (Tables 6.4.1 and 6.4.2).

Constructs made with the optimised bioinks demonstrated superior structural integrity and cellular compatibility, as confirmed by viability tests (Figure 6.6). Both formulations exhibited initial stress responses, with reduced cell viability at 24- and 48-hours post-printing, but stabilised by 72 hours. This adaptation highlights the blend's suitability for supporting immediate and long-term cellular function, which is critical for the heart-on-a-chip model's success. The decision to proceed with the 10% gelatin + 2% alginate blend was justified by its balanced performance in providing structural integrity and promoting cellular viability, making it a promising candidate for further development of the hybrid heart-on-a-chip.

These optimisation efforts underscore the need for tailored approaches to fabricating complex cardiac models. The integration of multiple cell types within a finely tuned ECM and scaffold environment reflects the dynamic interactions seen in native cardiac tissues, making the hybrid heart-on-a-chip a more physiologically relevant platform compared to traditional 3D models.

### 6.5.2 Biological Assessment of the 3D Bioprinted Heart Model under Simulated Microgravity and Ionising Radiation

Understanding the evolving nature of cell-matrix and cell-cell interactions is crucial in studying cardiac tissue dynamics in 3D cultures as the interplay between cells and their microenvironment, including the ECM, significantly influences cellular behaviour over time. (H. V. Almeida et al., 2021; Hirt et al., 2014). The 3D microenvironment provides structural and biochemical cues influencing cell-to-cell and cell-matrix interactions, promoting cardiomyocyte maturation and tissue functionality. (H. V. Almeida et al., 2021). In 3D cardiac constructs, interactions among different cell types, such as cardiomyocytes, fibroblasts and endothelial cells, are critical for modelling the complex cellular environment of the heart. (Sacchetto et al., 2020). This study demonstrated the feasibility of creating a dynamic and structurally complex 3D heart-on-a-chip model that integrates multiple cell types and replicates key aspects of the cardiac microenvironment. This model enables detailed investigations into how these cells cooperate and respond to environmental stressors such as s-μG and IR.

Preliminary findings highlight the protective role of HCFs in enhancing cardiomyocyte proliferation under s-μG and IR. Specifically, HCFs significantly improved cardiomyocyte proliferation rates across various stress conditions, including s-μG and IR. As detailed in Figure 6.9, the proliferation rates of AC-16 cardiomyocytes cultured with HCFs were notably higher than those cultured alone. Under static control conditions, cardiomyocytes without HCF showed a lower proliferation rate ($p = 0.0005$), highlighting the supportive role of HCFs. This trend continued under s-μG, where the presence of HCFs mitigated the reduction in cardiomyocyte proliferation ($p = 0.0009$). The most pronounced effects were observed under IR, where cardiomyocytes cultured without HCF exhibited significantly lower proliferation rates than those co-cultured with HCFs ($p < 0.0001$). This protective effect was also evident when cardiomyocytes were subjected to the combined stressors of s-μG and IR, with HCF helping to maintain higher proliferation rates ($p < 0.0001$). These results suggest that HCFs are crucial in supporting cardiomyocyte viability and function, particularly under conditions that mimic the environmental stressors encountered in space exploration.

These findings establish the feasibility of fabricating a stable and biologically compatible heart-on-a-chip model, highlighting its superior ability to replicate complex cellular interactions and responses compared to traditional 3D models. While 3D cultures with collagen-based matrices support cardiomyocyte alignment, migration, and enhanced tissue structure, they lack the dynamic conditions required to simulate the complex interactions experienced by cardiac tissues *in vivo*, particularly under unique space stressors such as microgravity and radiation.

Heart-on-a-chip models extend the capabilities of 3D models by providing a more controlled environment for studying cardiac tissue under conditions that replicate aspects of the native heart.

Although this study has not yet implemented fluid flow, the structural elements and cell compositions of the heart-on-a-chip platform lay the foundation for future incorporation of microfluidic elements. This development will further improve the model's ability to mimic *in vivo* cardiac mechanobiology, enhancing its value as a tool for understanding cellular responses to environmental changes.

## 6.6 KEY FINDINGS

- The optimisation of bioink compositions and printing parameters was crucial in achieving stable and consistent prints, with the 10% gelatin and 10% gelatin + 2% alginate bioinks emerging as the most promising formulations for 3D bioprinting.
- The viability of HCAEC encapsulated in bioprinted constructs showed initial decreases at 24 and 48 hours, stabilising by 72 hours, indicating a stress response followed by adaptation.
- Temperature modulation during collagen ECM preparation significantly influenced collagen fibre formation, with lower temperatures promoting the formation of larger, more visible fibres that enhanced cell attachment, spreading, and migration.
- Co-culturing AC-16 cardiomyocytes with HCF in a 3D collagen matrix revealed significant adaptive behaviours, with a notable decrease in cell viability on Day 3 and stabilisation by Day 5, highlighting the dynamic nature of cell-matrix interactions.
- The presence of HCFs was critical in enhancing the proliferation of AC-16 cardiomyocytes under static, s-μG, and IR conditions, underscoring their protective role in the cardiac microenvironment.
- The fabrication of vascular channels within the collagen ECM was achieved by strategically removing sacrificial material. Preliminary experiments on vascular channel designs demonstrated successful perfusion and removal of sacrificial materials, validating the capability of creating functional vascular structures within the collagen matrix.

## 6.7 KEY LIMITATIONS

- The planned inclusion of perfusion to simulate dynamic *in vivo* conditions was not fully implemented, reducing the model's physiological relevance.
- The heart-on-a-chip model lacks an endothelial lining, limiting its ability to mimic true vascular structures and affecting nutrient supply to cells.

For a more detailed discussion and potential resolutions to these limitations, please refer to Section 7.4.

# Chapter 7 -

## Conclusions

## 7.1 GENERAL RESULTS DISCUSSION

The primary aims of this thesis were to investigate the effects of s-μG and IR on cardiomyocytes using various models, including both 2D and 3D models and to develop advanced tissue-engineered models to mimic the cardiac microenvironment under space-like conditions. This final discussion synthesises the findings from the research, evaluates how the aims and objectives were met, and discusses the study's broader implications for understanding cardiovascular health risks associated with spaceflight.

In Chapter 4, the 2D models were employed to establish baseline responses of AC-16 cardiomyocytes to s-μG, revealing significant impacts on cellular proliferation and viability, with marked reductions observed after 72 hours of exposure, aligning with findings from other studies on differentiated cells under microgravity conditions (Morabito et al., 2020; L. Shi et al., 2021). Figure 4.6 and Figure 4.8 illustrates these changes, showing decreased cell viability and proliferation in s-μG conditions compared to controls. Gene expression analysis revealed stability in mechanotransduction and stress response genes, contrasting with other reports of significant alterations under microgravity (Kumar et al., 2021; Rudimov et al., 2017). This stability suggests alternative cellular adaptation mechanisms may be at play, such as metabolic pathway alterations and DNA methylation (Singh et al., 2010; Wise et al., 2021). The investigation into the effects of IR revealed significant dose-dependent DNA damage responses, as indicated by γ-H2AX foci formation (Figure 4.13). AC-16 cardiomyocytes exhibited substantial DNA damage immediately following IR exposure, with a gradual decline in γ-H2AX foci over 24 hours, suggesting efficient DNA repair mechanisms. These findings are consistent with existing literature, which reports similar DNA repair dynamics in response to radiation (Frieß et al., 2015). The combined effects of s-μG and IR were investigated to understand their combined impact on cardiomyocyte function. Contrary to expectations, statistical analysis did not demonstrate significant interaction effects between s-μG and IR on proliferation rates. However, a discernible trend towards reduced proliferation under combined stressor conditions was observed, particularly at higher radiation doses (Figure 4.14). These results suggest that while the combined effects may not be strongly synergistic, the presence of both stressors still exacerbates the reduction in cell proliferation.

In Chapter 5, the 3D collagen hydrogels were shown to support the embedding and functionality of AC-16 cardiomyocytes, with notable changes in cell behaviour compared to 2D cultures. While the morphological components of the 3D hydrogel study were not completed before the submission of this thesis, preliminary results indicated significant changes in cell behaviour under s-μG and IR conditions. The study found that s-μG conditions did not significantly impact cardiomyocyte proliferation within the 72-hour observation window, aligning with prior studies showing variable effects of microgravity on cell proliferation. Combined effects of s-μG and IR also did not show

significant changes in proliferation, though a trend towards significance for the s-μG condition suggests potential biological effects that warrant further investigation. Viability assays revealed a significant reduction in cell viability in the s-μG + 2Gy IR group compared to static control and s-μG alone, indicating that combined stressors exacerbate cell sensitivity and overall detrimental effects.

The γH2AX foci formation study demonstrated a rapid increase in γH2AX foci post-IR exposure, with a peak at 10 minutes, followed by a gradual decline over 24 hours, indicating active DNA repair processes. This was consistent with observations in 2D cultures but showed a more pronounced response in the 3D environment, highlighting the enhanced DNA repair capabilities supported by the 3D matrix (Figure 5.8). In the 2D culture (Figure 4.19), after exposure to 2 Gy IR, the γ-H2AX foci peaked at 73 foci per nucleus at 10 minutes, gradually decreasing to approximately 53 foci per nucleus at 1 hour, and dropping further to 3.64 foci per nucleus by 24 hours, indicating ongoing DNA repair. In contrast, the 3D culture (Figure 5.8) showed a peak of 4.884 foci per nucleus at 10 minutes post-IR exposure, reducing to 3.262 foci per nucleus at 1 hour, and 0.06647 foci per nucleus by 24 hours, suggesting a more efficient DNA repair process.This data demonstrates the enhanced DNA repair capabilities in the 3D matrix compared to 2D, as evidenced by the quicker resolution of γ-H2AX foci. Comparative analysis demonstrated that the 3D matrix facilitated a better DNA damage response and supported repair mechanisms more effectively, underscoring the importance of the 3D context in understanding cellular responses to combined environmental stressors. The 3D collagen model provided a more physiologically relevant platform, better mimicking the *in vivo* cardiac environment and highlighting the limitations of traditional 2D cultures.

YAP localisation analysis showed significant alterations under s-μG and IR conditions within the 3D collagen matrix. The s-μG and the IR treatment alone did not significantly differ from the Control. However, the combined s-μG + IR treatment caused a highly significant decrease in nuclear YAP localisation compared to the Control ($p < 0.0001$). These findings indicate that while s-μG and IR individually promote nuclear localization of YAP, their combination significantly shifts YAP localization towards the cytoplasm, as visually represented in Figure 5.10 and quantitatively supported by the statistical analysis in Figure 5.11. This shift in YAP localisation towards the cytoplasm indicates an enhanced cellular stress response under combined conditions in the 3D environment, suggesting that the presence of both stressors alters the mechanotransduction pathways more significantly than either stressor alone. In contrast, the 2D model findings, as outlined, demonstrated that both s-μG and IR individually led to a significant increase in nuclear YAP localisation compared to the control group, reflecting a heightened mechanosensitivity and stress response in the cells. However, when s-μG and IR were combined, no significant difference in nuclear localisation of YAP was observed compared to the control ($p = 0.1095$). This suggests that in 2D environments, the combined effects of s-μG and IR do not substantially alter the YAP localisation, possibly due to the limited mechanotransduction signalling capacity inherent in flat cultures.

The comparison highlights a critical difference: while 2D models reveal the independent effects of s-μG and IR on promoting nuclear YAP localisation, they fail to capture the combined stress response that is evident in 3D environments. The 3D model's ability to demonstrate a significant shift of YAP to the cytoplasm under combined stress suggests a more complex and physiologically relevant interaction between microgravity and radiation, which is not apparent in 2D cultures. This underscores the importance of using 3D models to better understand the integrated effects of multiple spaceflight stressors on cardiac mechanobiology, revealing cellular behaviours that are masked in simpler 2D systems.

Chapter 6 described developing an innovative hybrid heart-on-a-chip model to simulate the complex cardiac microenvironment. The optimisation of 3D bioprinting techniques was crucial for achieving stable and functional cardiac tissue constructs. Using bioinks, such as 10% gelatin and 10% gelatin + 2% alginate, provided promising results for 3D bioprinting, ensuring compatibility with cardiomyocyte viability and functionality (Figure 6.1). While fluid flow and perfusion were intended as key elements of this model, these components were not yet implemented, indicating an area for future development.

Biological assessments of the 3D bioprinted heart model revealed significant findings related to cell viability, proliferation, and functionality under s-μG and IR conditions. The results demonstrated the model's biological fidelity and potential as a platform for studying the impacts of space-like conditions on cardiac tissues. The presence of human cardiac fibroblasts within the model further enhanced cardiomyocyte survival and proliferation, highlighting the microenvironment's importance in cellular responses (Figure 6.11). This model holds promise for capturing the dynamic interactions of the cardiac microenvironment more accurately than static 3D cultures, albeit further work is needed to incorporate fluid flow to fully realise the model's capabilities.

Understanding cardiac mechanobiology—how heart cells sense and respond to mechanical stimuli—is critical for evaluating cardiovascular health risks associated with spaceflight and developing countermeasures. Each model system—2D, 3D, and heart-on-a-chip—offers distinct advantages that, when integrated, provide a more comprehensive understanding of cardiac mechanobiology in space-like conditions and on Earth.

2D cell cultures, where cardiomyocytes are grown on flat surfaces, have been widely used as a preliminary model due to their simplicity, cost-effectiveness, and ease of analysis. These models are valuable for studying basic cellular responses to microgravity and radiation, such as changes in cell proliferation, viability, and basic mechanotransduction pathways(Ferranti et al., 2014; Svejgaard et al., 2015). However, 2D models lack the complex cell-cell and cell-ECM interactions inherent to cardiac

tissue. This limits their ability to replicate the mechanical environment of the heart, reducing the physiological relevance of findings. For example, mechanotransduction signals that are crucial for cardiac function, such as those involving YAP/TAZ localisation, behave differently in 2D due to the absence of 3D context and tissue-specific architecture (Arun et al., 2019).Thus, while 2D models serve as an essential first step, they do not fully capture the mechanobiological dynamics of the heart, especially under the altered gravity and radiation exposure of space.

3D models, such as collagen hydrogels, represent a significant advancement over 2D systems by providing a more realistic environment that better mimics the structural and mechanical properties of cardiac tissue. This study using 3D collagen matrices demonstrated enhanced cellular responses, including improved DNA repair and altered mechanotransduction signalling compared to 2D models. For instance, the quicker resolution of γ-H2AX foci observed in the 3D collagen model in Chapter 5, suggests that the 3D environment supports more effective DNA repair mechanisms. Moreover, 3D models allow for the study of how microgravity and radiation impact complex cellular behaviours, such as the localisation and function of YAP/TAZ, which play a crucial role in cardiac adaptation to mechanical stress (Scott et al., 2021). The mechanotransduction pathways activated in 3D cultures are notably different from those in 2D systems. In 3D environments, cells experience varied mechanical cues that can influence their morphology and signalling pathways, leading to altered gene expression and cellular responses (Frtús et al., 2020; Guo et al., 2020; Sheth, 2024). These insights are invaluable not only for understanding cardiac responses to spaceflight but also for broader applications in cardiac disease research on Earth, where mechanical stress plays a significant role in conditions such as heart failure.

Heart-on-a-chip models combine 3D tissue engineering with microfluidics, offering the most advanced platform for studying cardiac mechanobiology. These models integrate multiple cell types, dynamic mechanical cues, and fluid flow, closely mimicking the *in vivo* cardiac environment (Kong et al., 2019). The ability to simulate both the biomechanical forces and microenvironmental conditions of the heart makes heart-on-a-chip models particularly well-suited for studying the combined effects of s-μG and radiation. Unlike static 3D models, heart-on-a-chip systems can recreate the dynamic aspects of the cardiac environment, providing insights into how cardiomyocytes respond to mechanical unloading and radiation simultaneously. For instance, the presence of fluid flow in heart-on-a-chip devices allows for the study of endothelial-cardiomyocyte interactions under s-μG, which is crucial for understanding vascular health in space (Kaiser & K Coulombe, 2015; Kong et al., 2019). Furthermore, the ability to manipulate the mechanical properties of the scaffolds and the surrounding microenvironment further enhances the relevance of these models for studying disease progression and therapeutic responses (Corbin et al., 2019; Sadeghi et al., 2017).

The integration of 2D, 3D, and heart-on-a-chip models offers a multi-scale approach to understanding cardiac mechanobiology under space-like conditions and on Earth. Each model provides unique insights into cellular responses to mechanical and environmental stressors, with 2D models serving as a foundational tool, 3D models enhancing our understanding of tissue-level interactions, and heart-on-a-chip systems providing the most accurate simulations of the cardiac microenvironment. This comprehensive approach is essential for advancing our knowledge of cardiac health risks associated with spaceflight and developing effective countermeasures, while also informing broader cardiovascular research and therapeutic development on Earth.

## 7.2 VALIDATION OF HYPOTHESIS: CARDIOMYOCYTE RESPONSES TO SIMULATED SPACEFLIGHT CONDITIONS

The research conducted in this thesis aimed to address the hypothesis that exposing cardiomyocytes to s-μG and IR in various models provides critical insights into the effects of spaceflight-like conditions on cardiac function and disease.

Results from Chapter 4 demonstrated that s-μG and IR individually impacted cardiomyocyte proliferation and viability, with significant DNA damage responses observed under IR exposure. These responses were crucial as a reference for understanding how cardiomyocytes react to spaceflight-like conditions in a 2D environment. The observed changes, particularly the DNA damage response, provided critical insight into how cardiomyocytes may react to the combined stressors of microgravity and radiation, laying the groundwork for subsequent experiments in more advanced 3D models. While proliferation was noted in AC-16 cardiomyocytes, which retain some proliferative capacity, it is important to recognise that adult cardiomyocytes *in vivo* typically have limited proliferation.

In Chapter 5, the development and validation of the 3D collagen-based hydrogel provided a more physiologically relevant environment for studying cardiomyocyte responses. The 3D model offered a superior environment for investigating other vital cellular processes, such as mechanotransduction and viability. The enhanced mechanotransduction observed in the 3D system reflects how cells respond to mechanical stimuli. Furthermore, the 3D model provided a more robust platform for observing significant changes in cell behaviour and DNA damage responses under the combined influence of s-μG and IR. These factors more closely mimic the *in vivo* cardiac microenvironment compared to traditional 2D models. This underscores the importance of using 3D cultures to understand complex cellular responses to space-like conditions, where traditional 2D models may fall short.

Chapter 6 aimed to further advance the hypothesis by developing a hybrid heart-on-a-chip model, optimising 3D bioprinting techniques, and performing biological s-μG and IR conditions. The findings from these experiments demonstrated the model's potential for studying the impacts of space-like conditions on cardiac tissues, supporting the hypothesis that 3D models provide a more accurate representation of the cardiac microenvironment and cellular responses to stressors.

These findings shed light on the impact of space on cardiac function and diseases, highlighting the potentially more physiologically relevant responses in advanced models compared to traditional 2D cultures. This validates the use of diverse and sophisticated models for studying cellular responses and underscores their importance in space biology and regenerative medicine. Future research should

aim to enhance these models further by incorporating dynamic elements such as fluid flow, mechanical stimuli, and cell-to-cell interactions, which are critical for accurately replicating *in vivo* conditions. These refinements would allow for a more comprehensive understanding of how microgravity and radiation influence the cardiovascular system.

Overall, the research presented in this thesis supports the hypothesis that exposing cardiomyocytes to s-μG and radiation across different cardiac models provides valuable insights into the effects of space on cardiac function and disease. The validation of the hypothesis was strengthened by the multi-model approach. Each model contributed uniquely to this understanding: 2D models offered foundational data on cellular responses, while 3D collagen hydrogels enhanced the study of mechanotransduction and DNA repair processes in a more physiologically relevant setting. The heart-on-a-chip model, though still in development, promises to offer the most accurate representation of cardiac microenvironments under spaceflight conditions, supporting the broader implications of this work for space biology and regenerative medicine.

## 7.3 LIMITATIONS OF MICROGRAVITY AND RADIATION SIMULATION

The use of s-μG conditions achieved with the RPM and the X-RAD 320 radiation system in this study provided valuable insights into the impact of microgravity and radiation on biological systems. However, certain limitations of these models need to be critically considered when interpreting the results, particularly regarding their reliability in replicating real spaceflight conditions.

In this study, s-μG conditions were achieved using RPM. As previously mentioned in Chapter 1, the RPM is an established ground-based device that mimics the microgravity environment encountered during spaceflight by continuously rotating samples along multiple axes. This rotational movement can disrupt normal cellular behaviour, as seen in the cellular mechanotransduction responses observed in this study. These changes are consistent with the cardiovascular deconditioning experienced by astronauts, suggesting that the RPM is a useful tool for modelling microgravity's impact on cellular function (Nguyen et al., 2021). Compared to other microgravity simulation methods, such as clinostats or RWV, the RPM provides a more realistic simulation of the constant orientation changes in microgravity, making it a versatile and reliable model for studying microgravity effects without the logistical and financial constraints of spaceflight experiments (ElGindi et al., 2022; Neelam et al., 2021). Despite its advantages, the RPM cannot perfectly replicate the complex and prolonged weightlessness conditions of space. Artifacts related to rotational forces and transient gravity exposure may influence cellular responses, introducing variability that would not occur in true microgravity conditions (Pala et al., 2023). Moreover, the RPM lacks the ability to simulate *in vivo* physiological changes such as fluid shifts and altered shear stress experienced by astronauts, limiting its capacity to model comprehensive spaceflight conditions. Despite these limitations, the RPM serves as a powerful tool for investigating how reduced mechanical loading affects biological systems, offering critical insights into the cellular adaptations to microgravity.

In this study, the X-RAD 320, an X-ray irradiation system that produces low-LET ionizing radiation at an energy level of 320 keV, was used to simulate radiation exposure conditions. X-rays are a form of low-LET radiation that results in DNA damage such as single-strand breaks (SSBs) and DSBs. This damage activates cellular repair mechanisms, which are typically straightforward (due to the dispersed nature of the damage), making X-rays a common choice for experimental studies (Autsavapromporn et al., 2013; Cartwright et al., 2015; Y. Li et al., 2012; Macaeva et al., 2021). However, the primary limitation of the X-RAD 320 is its inability to replicate high-LET radiation, such as heavy ions and protons, which are predominant in space. High-LET radiation produces densely ionising tracks that cause complex and clustered DNA damage, which is more difficult for cells to repair accurately, leading to a higher risk of mutations, genomic instability, and adverse

biological effects such as carcinogenesis and cardiovascular damage (Buonanno et al., 2015; E. H. Kim et al., 2017; Pang et al., 2016; Yu et al., 2010)

In conclusion, both the RPM and X-RAD 320 provide controlled and reproducible conditions, enhancing the reliability of experimental results. However, their inherent limitations in accurately simulating true spaceflight environments must be acknowledged. For example, RPM-induced s-μG conditions can still result in transient gravity exposure due to mechanical constraints, while X-RAD 320 cannot replicate the complex radiation field encountered in space (Buonanno et al., 2015; Miles et al., 2021). These factors necessitate careful interpretation of the data, recognising the potential biases introduced by these simulation models. Future studies should focus on integrating advanced simulation technologies, including high-LET radiation sources, to better capture the full spectrum of biological effects observed in space.

## 7.4 DISCUSSION OF STUDY LIMITATIONS

These limitations reflect the constraints of the study design and experimental setup. Addressing them in future research will enhance the depth, reliability, and applicability of findings related to cardiomyocyte responses under spaceflight-like conditions.

- Lack of normalisation for number of cells: In this study, no specific normalisation of the fluorescence signal (Corrected RFU) to cell number was performed. The assay results were based on the metabolic activity of the cells, as indicated by the reduction of resazurin to resorufin. This approach was chosen due to the experimental focus on relative changes in metabolic activity rather than absolute cell counts. However, normalising fluorescence readings to cell numbers would provide a more precise measure of cellular proliferation, accounting for variations in cell density. This has been identified as a limitation of the current study, and future experiments will aim to include cell counting or other normalisation methods to enhance the accuracy of proliferation assessments.
- Single markers: Throughout the study, single markers were used for assessing proliferation, mechanotransduction, and DNA damage in both 2D and 3D experiments. This approach limits the ability to capture the full complexity of these processes, potentially overlooking additional cellular pathways and responses. To enhance robustness, future studies should employ multiple markers or multiplexing techniques.
- Use of AC-16 Cells: AC-16 cells, used in this study, lack contractility and striations, making them more similar to myofibroblast-like cells rather than fully functional cardiomyocytes. This limitation affects the study's ability to model the contractile and mechanical behaviour of native cardiac tissue, particularly under stress conditions like s-μG and radiation.
- Low cell density in 2D: The cell density in 2D experiments was lower than that found *in vivo*, where cardiomyocytes are densely packed and in direct contact. This limitation could influence cellular communication and mechanotransduction, potentially affecting the validity of the observed cellular responses.
- Lack of comparison between 2D and 3D models: Direct comparisons of viability between 2D and 3D models were not performed due to methodological differences, limiting the ability to quantitatively compare these culture environments. Future studies should develop consistent evaluation protocols for direct comparison.
- Challenges in imaging, segmentation and analysis: The imaging and segmentation methods used in both 2D, and 3D experiments faced significant challenges due to the complexity of the cellular environments. These limitations can compromise data interpretation, highlighting the need for improved staining protocols, enhanced imaging modalities, and sophisticated segmentation algorithms, to accurately assess cellular interactions and morphological changes in future studies.

- Lack of mechanical characterisation of 3D gel: The mechanical properties of the 3D gels, such as stiffness and porosity, were not comprehensively characterised. These properties are critical in influencing cellular mechanotransduction pathways, and their lack of detailed characterisation limits the understanding of the cellular responses observed.
- Unrealised perfusion in Heart-on-a-Chip Model: The initial plan for dynamic perfusion was not fully implemented, reducing the model's physiological accuracy and limiting its ability to simulate *in vivo* conditions effectively. This affects the interpretation of cardiac mechanobiology under spaceflight conditions.

## 7.5 FUTURE DIRECTIONS

Future research will address study limitations to enhance the depth and applicability of findings related to cardiomyocyte responses under spaceflight conditions.

- Investigation of non-gene expression changes: The stability of gene expression related to mechanotransduction and stress response in AC-16 cardiomyocytes, despite physiological changes, points to the importance of non-genetic mechanisms in cellular adaptation to s-μG. Future research could focus on understanding how alterations in metabolic pathways, DNA methylation, and intracellular communication contribute to cell adaptation in microgravity. This could involve detailed studies on post-translational modifications, epigenetic modifications, and signalling pathways that are activated in response to microgravity.
- Comparative analysis of different cardiac cell types: Given the varied responses to s-μG observed in AC-16 cardiomyocytes compared to stem cells and other differentiated cells, conducting comparative analyses across different cell types and developmental stages could provide insights into the factors that confer sensitivity or resilience to microgravity. This could help identify specific characteristics or states that make certain cells more adaptable to the microgravity environment.
- Longer studies on cellular adaptations: To fully understand the long-term effects of microgravity on cellular functions, conducting longitudinal studies that track the changes in cell behaviour, gene expression, and adaptation mechanisms over extended periods of s-μG exposure could be valuable.
- Collection of culture media to assess the presence of detached, non-viable cells: Future studies should include the collection and analysis of culture media to assess the presence of detached, non-viable cells, which were not accounted for in the current study's viability assessments. This will provide a more comprehensive evaluation of cell survival under experimental conditions.
- Mechanical characterisation: Further characterisation of 3D gel properties, including stiffness and porosity, will enhance understanding of mechanotransduction pathways in cardiomyocytes.

Future work will also focus on completing the morphological signalling analyses in the 3D hydrogel study and further refining the hybrid heart-on-a-chip model. These efforts will provide a more detailed understanding of the cellular mechanisms underlying cardiomyocyte responses to spaceflight conditions. In summary, addressing these future directions can build on the foundational knowledge provided by this study, advancing our understanding of cellular adaptation to microgravity and its implications for space biology, human health during space missions, and potential biomedical applications on Earth.

## 7.6 CONCLUSION

This thesis has successfully addressed the initial aims and objectives, contributing to a deeper understanding of cardiomyocyte behaviour under spaceflight-like conditions. By employing 2D and 3D models, this research has highlighted key cellular responses to s-μG and IR, advancing our knowledge of how these stressors impact cardiac cells. The comprehensive evaluation of cellular responses, including proliferation, mechanotransduction, and DNA damage, underscores the complex interplay between mechanical and radiation-induced stress. While the heart-on-a-chip model remains in development, the findings to date have established a robust framework for refining this approach, ultimately aiming to replicate the physiological conditions of human cardiac tissue more accurately.

The study has provided valuable insights into the limitations and potential adaptations of cardiomyocytes in altered gravitational environments. Through the comprehensive evaluation of s-μG and IR effects on cardiomyocytes, both in 2D and 3D environments, this research has laid a strong foundation for future studies to mitigate cardiovascular health risks associated with space travel

# BIBLIOGRAPHY


A. Moes, M. J., Gielen, J. C., Bleichrodt, R.-J., W. Loon, J. J., M. Christianen, P. C., & Boonstra, J. (2010). Simulation of Microgravity by Magnetic Levitation and Random Positioning: Effect on Human A431 Cell Morphology. *Microgravity Science and Technology*. https://doi.org/10.1007/s12217-010-9185-x

Afshinnekoo, E., Scott, R. T., MacKay, M. J., Pariset, E., Cekanaviciute, E., Barker, R., Gilroy, S., Hassane, D., Smith, S. M., Zwart, S. R., Nelman-Gonzalez, M., Crucian, B. E., Ponomarev, S. A., Orlov, O. I., Shiba, D., Muratani, M., Yamamoto, M., Richards, S. E., Vaishampayan, P. A., … Beheshti, A. (2020). Fundamental Biological Features of Spaceflight: Advancing the Field to Enable Deep-Space Exploration. *Cell*, *183*(5), 1162–1184. https://doi.org/10.1016/j.cell.2020.10.050

Aleshcheva, G., Bauer, J., Hemmersbach, R., Slumstrup, L., Wehland, M., Infanger, M., & Grimm, D. (2016). Scaffold-free Tissue Formation Under Real and Simulated Microgravity Conditions. *Basic & Clinical Pharmacology & Toxicology*, *119*(S3), 26–33. https://doi.org/10.1111/bcpt.12561

Almeida, E. (n.d.). *The Effects of Microgravity on Cells*. 17.

Almeida, H. V., Tenreiro, M. F., Louro, A. F., Abecasis, B., Santinha, D., Calmeiro, T., Fortunato, E., Ferreira, L., Alves, P. M., & Serra, M. (2021). Human Extracellular-Matrix Functionalization of 3D hiPSC-Based Cardiac Tissues Improves Cardiomyocyte Maturation. *ACS Applied Bio Materials*, *4*(2), 1888–1899. https://doi.org/10.1021/acsabm.0c01490

Anıl-İnevi, M., Yaman, S., Yıldız, A. A., Meşe, G., Yalcin-Ozuysal, Ö., Tekin, H. C., & Özçivici, E. (2018). Biofabrication of in Situ Self Assembled 3D Cell Cultures in a Weightlessness Environment Generated Using Magnetic Levitation. *Scientific Reports*. https://doi.org/10.1038/s41598-018-25718-9

Antoni, D., Burckel, H., Josset, E., & Noel, G. (2015). Three-Dimensional Cell Culture: A Breakthrough in Vivo. *International Journal of Molecular Sciences*, *16*(3), Article 3. https://doi.org/10.3390/ijms16035517

Arun, R. P., Sivanesan, D., Patra, B., Varadaraj, S., & Verma, R. S. (2019). Simulated microgravity increases polyploid giant cancer cells and nuclear localization of YAP. *Scientific Reports*, *9*(1), 10684. https://doi.org/10.1038/s41598-019-47116-5

Auman, H. J., Coleman, H., Riley, H. E., Olale, F., Tsai, H.-J., & Yelon, D. (2007). Functional Modulation of Cardiac Form through Regionally Confined Cell Shape Changes. *PLoS Biology*, *5*(3), e53. https://doi.org/10.1371/journal.pbio.0050053

Australian Institute of Health and Welfare. (2024). *Heart, stroke and vascular disease: Australian facts*. https://www.aihw.gov.au/reports/heart-stroke-vascular-diseases/hsvd-facts

Autsavapromporn, N., Suzuki, M., Funayama, T., Usami, N., Plante, I., Yokota, Y., Mutou, Y., Ikeda, H., Kobayashi, K., Kobayashi, Y., Uchihori, Y., Hei, T. K., Azzam, E. I., & Murakami, T. (2013). Gap Junction Communication and the Propagation of Bystander Effects Induced by Microbeam Irradiation in Human Fibroblast Cultures: The Impact of Radiation Quality. *Radiation Research*. https://doi.org/10.1667/rr3111.1

Bahnamiri, M. M., & Roller, R. J. (2021). Mechanism of Nuclear Lamina Disruption and the Role of pUS3 in Herpes Simplex Virus 1 Nuclear Egress. *Journal of Virology*. https://doi.org/10.1128/jvi.02432-20

Baio, J., Martinez, A. F., Silva, I., Hoehn, C. V., Countryman, S., Bailey, L., Hasaniya, N., Pecaut, M. J., & Kearns-Jonker, M. (2018). Cardiovascular progenitor cells cultured aboard the International Space Station exhibit altered developmental and functional properties. *Npj Microgravity*, *4*(1), 13. https://doi.org/10.1038/s41526-018-0048-x

Barravecchia, I., De Cesari, C., Forcato, M., Scebba, F., Pyankova, O. V., Bridger, J. M., Foster, H. A., Signore, G., Borghini, A., Andreassi, M., Andreazzoli, M., Bicciato, S., Pè, M. E., & Angeloni, D. (2021). Microgravity and space radiation inhibit autophagy in human capillary endothelial cells, through either opposite or synergistic effects on specific molecular

pathways. *Cellular and Molecular Life Sciences*, *79*(1), 28. https://doi.org/10.1007/s00018-021-04025-z

Becker, J. L., & Souza, G. R. (2013). Using space-based investigations to inform cancer research on Earth. *Nature Reviews Cancer*, *13*(5), 315–327. https://doi.org/10.1038/nrc3507

Berardini, M. (2023). Simulated Microgravity Exposure Induces Antioxidant Barrier Deregulation and Mitochondria Enlargement in TCam-2 Cell Spheroids. *Cells*. https://doi.org/10.3390/cells12162106

Bertini, E., Oka, T., Sudol, M., Strano, S., & Blandino, G. (2009). YAP: At the crossroad between transformation and tumor suppression. *Cell Cycle*, *8*(1), 49–57. https://doi.org/10.4161/cc.8.1.7259

Blaber, E. A., Finkelstein, H., Dvorochkin, N., Sato, K. Y., Yousuf, R., Burns, B. P., Globus, R. K., & Almeida, E. A. C. (2015). Microgravity Reduces the Differentiation and Regenerative Potential of Embryonic Stem Cells. *Stem Cells and Development*, *24*(22), 2605–2621. https://doi.org/10.1089/scd.2015.0218

Boerma, M., Sridharan, V., Mao, X.-W., Nelson, G. A., Cheema, A. K., Koturbash, I., Singh, S. P., Tackett, A. J., & Hauer-Jensen, M. (2016). Effects of ionizing radiation on the heart. *Mutation Research/Reviews in Mutation Research*, *770*, 319–327. https://doi.org/10.1016/j.mrrev.2016.07.003

Brungs, S., Hauslage, J., & Hemmersbach, R. (2019). Validation of Random Positioning Versus Clinorotation Using a Macrophage Model System. *Microgravity Science and Technology*. https://doi.org/10.1007/s12217-019-9687-0

Buonanno, M., de Toledo, S. M., Howell, R. W., & Azzam, E. I. (2015). Low-Dose Energetic Protons Induce Adaptive and Bystander Effects That Protect Human Cells Against DNA Damage Caused by a Subsequent Exposure to Energetic Iron Ions. *Journal of Radiation Research*. https://doi.org/10.1093/jrr/rrv005

Burridge, K., & Chrzanowska-Wodnicka, M. (1996). FOCAL ADHESIONS, CONTRACTILITY, AND SIGNALING. *Annual Review of Cell and Developmental Biology*, *12*(1), 463–519. https://doi.org/10.1146/annurev.cellbio.12.1.463

Calvaruso, M., Militello, C., Minafra, L., Regina, V. L., Torrisi, F., Pucci, G., Cammarata, F. P., Bravatà, V., Forte, G. I., & Russo, G. (2021). Biological and Mechanical Characterization of the Random Positioning Machine (RPM) for Microgravity Simulations. *Life*. https://doi.org/10.3390/life11111190

Camberos, V., Baio, J., Bailey, L., Hasaniya, N., Lopez, L. V., & Kearns-Jonker, M. (2019). Effects of Spaceflight and Simulated Microgravity on YAP1 Expression in Cardiovascular Progenitors: Implications for Cell-Based Repair. *International Journal of Molecular Sciences*, *20*(11), 2742. https://doi.org/10.3390/ijms20112742

Camberos, V., Baio, J., Mandujano, A., Martinez, A. F., Bailey, L., Hasaniya, N., & Kearns-Jonker, M. (2021). The Impact of Spaceflight and Microgravity on the Human Islet-1+ Cardiovascular Progenitor Cell Transcriptome. *International Journal of Molecular Sciences*, *22*(7), 3577. https://doi.org/10.3390/ijms22073577

Cameli, M., Pastore, M. C., Campora, A., Lisi, M., & Mandoli, G. E. (2022). Donor shortage in heart transplantation: How can we overcome this challenge? *Frontiers in Cardiovascular Medicine*, *9*, 1001002. https://doi.org/10.3389/fcvm.2022.1001002

Camelliti, P., Al-Saud, S. A., Smolenski, R. T., Al-Ayoubi, S., Bussek, A., Wettwer, E., Banner, N. R., Bowles, C. T., Yacoub, M. H., & Terracciano, C. M. (2011). Adult human heart slices are a multicellular system suitable for electrophysiological and pharmacological studies. *Journal of Molecular and Cellular Cardiology*, *51*(3), 390–398. https://doi.org/10.1016/j.yjmcc.2011.06.018

Cao, R., Tian, H., Tian, Y., & Fu, X. (2023). A Hierarchical Mechanotransduction System: From Macro to Micro. *Advanced Science*, *n/a*(n/a), 2302327. https://doi.org/10.1002/advs.202302327

Carpenter, A. E., Jones, T. R., Lamprecht, M. R., Clarke, C., Kang, I. H., Friman, O., Guertin, D. A., Chang, J. H., Lindquist, R. A., Moffat, J., Golland, P., & Sabatini, D. M. (2006). CellProfiler: Image analysis software for identifying and quantifying cell phenotypes. *Genome Biology*, *7*(10), R100. https://doi.org/10.1186/gb-2006-7-10-r100

Carr, Z. A., Land, C. E., Kleinerman, R. A., Weinstock, R. W., Stovall, M., Griem, M. L., & Mabuchi, K. (2005). Coronary heart disease after radiotherapy for peptic ulcer disease. *International Journal of Radiation Oncology*Biology*Physics*, *61*(3), 842–850. https://doi.org/10.1016/j.ijrobp.2004.07.708

Cartwright, I. M., Bell, J. J., Maeda, J., Genet, M., Romero, A., Fujii, Y., Fujimori, A., Kitamuta, H., Kamada, T., Chen, D. J., & Kato, T. A. (2015). Effects of Targeted Phosphorylation Site Mutations in the DNA-PKcs Phosphorylation Domain on Low and High LET Radiation Sensitivity. *Oncology Letters*. https://doi.org/10.3892/ol.2015.2974

Caspi, O., Lesman, A., Basevitch, Y., Gepstein, A., Arbel, G., Habib, I. H. M., Gepstein, L., & Levenberg, S. (2007). Tissue Engineering of Vascularized Cardiac Muscle From Human Embryonic Stem Cells. *Circulation Research*, *100*(2), 263–272. https://doi.org/10.1161/01.RES.0000257776.05673.ff

Cazzaniga, A., Ille, F., Wüest, S. L., Haack, C., Koller, A., Giger-Lange, C., Zocchi, M., Egli, M., Castiglioni, S., & M. Maier, J. A. (2020). Scalable Microgravity Simulator Used for Long-Term Musculoskeletal Cells and Tissue Engineering. *International Journal of Molecular Sciences*. https://doi.org/10.3390/ijms21238908

Chapla, R., Hammer, J. A., & West, J. L. (2022). Adding Dynamic Biomolecule Signaling to Hydrogel Systems via Tethered Photolabile Cell-Adhesive Proteins. *ACS Biomaterials Science & Engineering*, *8*(1), 208–217. https://doi.org/10.1021/acsbiomaterials.1c01181

Chen, M. B., Srigunapalan, S., Wheeler, A. R., & Simmons, C. A. (2013). A 3D microfluidic platform incorporating methacrylated gelatin hydrogels to study physiological cardiovascular cell–cell interactions. *Lab on a Chip*, *13*(13), 2591. https://doi.org/10.1039/c3lc00051f

Chin, I. L., Hool, L., & Choi, Y. S. (2019). A Review of *in vitro* Platforms for Understanding Cardiomyocyte Mechanobiology. *Frontiers in Bioengineering and Biotechnology*, *7*, 133. https://doi.org/10.3389/fbioe.2019.00133

Christ, F., Gamble, J., Baranov, V., Kotov, A., Chouker, A., Thiel, M., Gartside, I. B., Moser, C. M., Abicht, J., & Messmer, K. (2001). Changes in microvascular fluid filtration capacity during 120 days of 6° head-down tilt. *Journal of Applied Physiology*, *91*(6), 2517–2522. https://doi.org/10.1152/jappl.2001.91.6.2517

Codelia, V. A., Sun, G., & Irvine, K. D. (2014). Regulation of YAP by Mechanical Strain through Jnk and Hippo Signaling. *Current Biology*, *24*(17), 2012–2017. https://doi.org/10.1016/j.cub.2014.07.034

Coleman, M. A., Sasi, S. P., Onufrak, J., Natarajan, M., Manickam, K., Schwab, J., Muralidharan, S., Peterson, L. E., Alekseyev, Y. O., Yan, X., & Goukassian, D. A. (2015). Low-dose radiation affects cardiac physiology: Gene networks and molecular signaling in cardiomyocytes. *American Journal of Physiology-Heart and Circulatory Physiology*, *309*(11), H1947–H1963. https://doi.org/10.1152/ajpheart.00050.2015

Corbin, E. A., Vite, A., Peyster, E., Bhoopalam, M., Brandimarto, J., Wang, X., Bennett, A. I., Clark, A., Cheng, X., Turner, K. T., Musunuru, K., & Margulies, K. B. (2019). Tunable and Reversible Substrate Stiffness Reveals a Dynamic Mechanosensitivity of Cardiomyocytes. *Acs Applied Materials & Interfaces*. https://doi.org/10.1021/acsami.9b02446

D'Agostino, M., Babin, A.-L., Zaffino, M., Frippiat, J.-P., Machouart, M., & Debourgogne, A. (2022). Simulated Microgravity Created Using a Random Positioning Machine Induces Changes in the Physiology of the Fusarium Solani Species Complex. *Microorganisms*. https://doi.org/10.3390/microorganisms10112270

Das, A., Fischer, R. S., Pan, D., & Waterman, C. M. (2016). YAP Nuclear Localization in the Absence of Cell-Cell Contact Is Mediated by a Filamentous Actin-dependent, Myosin II- and Phospho-YAP-independent Pathway during Extracellular Matrix Mechanosensing*. *Journal of Biological Chemistry*, *291*(12), 6096–6110. https://doi.org/10.1074/jbc.M115.708313

Del Re, D. P., Yang, Y., Nakano, N., Cho, J., Zhai, P., Yamamoto, T., Zhang, N., Yabuta, N., Nishimura, H., Pan, D., & Sadoshima, J. (2013). Yes-Associated Protein Isoform 1 (Yap1) Promotes Cardiomyocyte Survival and Growth to Protect Against Myocardial Ischemic Injury. *Journal of Biological Chemistry*. https://doi.org/10.1074/jbc.m112.436311

Delp, M. D., Charvat, J. M., Limoli, C. L., Globus, R. K., & Ghosh, P. (2016). Apollo Lunar Astronauts Show Higher Cardiovascular Disease Mortality: Possible Deep Space Radiation Effects on the Vascular Endothelium. *Scientific Reports*, *6*(1), 29901. https://doi.org/10.1038/srep29901

Demontis, G. C., Germani, M. M., Caiani, E. G., Barravecchia, I., Passino, C., & Angeloni, D. (2017). Human Pathophysiological Adaptations to the Space Environment. *Frontiers in Physiology*, *8*, 547. https://doi.org/10.3389/fphys.2017.00547

Di, X., Gao, X., Peng, L., Ai, J., Jin, X., Qi, S., Li, H., Wang, K., & Luo, D. (2023). Cellular mechanotransduction in health and diseases: From molecular mechanism to therapeutic

targets. *Signal Transduction and Targeted Therapy*, *8*(1), Article 1. https://doi.org/10.1038/s41392-023-01501-9

Dijkstra, C. E., Larkin, O., Anthony, P., Davey, M. R., Eaves, L., Rees, C., & Hill, R. (2010). Diamagnetic Levitation Enhances Growth of Liquid Bacterial Cultures by Increasing Oxygen Availability. *Journal of the Royal Society Interface*. https://doi.org/10.1098/rsif.2010.0294

Du, J., Zeng, L., Yu, Z., Chen, S., Chen, X., Zhang, Y., & Yang, H. (2022). A Magnetically Enabled Simulation of Microgravity Represses the Auxin Response During Early Seed Germination on a Microfluidic Platform. *Microsystems & Nanoengineering*. https://doi.org/10.1038/s41378-021-00331-5

Duan, Y., Liu, Z., O'Neill, J., Wan, L. Q., Freytes, D. O., & Vunjak-Novakovic, G. (2011). Hybrid Gel Composed of Native Heart Matrix and Collagen Induces Cardiac Differentiation of Human Embryonic Stem Cells without Supplemental Growth Factors. *Journal of Cardiovascular Translational Research*, *4*(5), 605–615. https://doi.org/10.1007/s12265-011-9304-0

Dupont, S., Morsut, L., Aragona, M., Enzo, E., Giulitti, S., Cordenonsi, M., Zanconato, F., Le Digabel, J., Forcato, M., Bicciato, S., Elvassore, N., & Piccolo, S. (2011). Role of YAP/TAZ in mechanotransduction. *Nature*, *474*(7350), Article 7350. https://doi.org/10.1038/nature10137

Edalat, S. G., Jang, Y., Kim, J., & Park, Y. (2019). Collagen Type I Containing Hybrid Hydrogel Enhances Cardiomyocyte Maturation in a 3D Cardiac Model. *Polymers*, *11*(4), Article 4. https://doi.org/10.3390/polym11040687

ElGindi, M., Sapudom, J., Laws, P., Garcia-Sabaté, A., Daqaq, M. F., & M. Teo, J. C. (2022). 3D Microenvironment Attenuates Simulated Microgravity-Mediated Changes in T Cell Transcriptome. *Cellular and Molecular Life Sciences*. https://doi.org/10.1007/s00018-022-04531-8

Engler, A. J., Carag-Krieger, C., Johnson, C. P., Raab, M., Tang, H.-Y., Speicher, D. W., Sanger, J. W., Sanger, J. M., & Discher, D. E. (2008). Embryonic cardiomyocytes beat best on a matrix with heart-like elasticity: Scar-like rigidity inhibits beating. *Journal of Cell Science*, *121*(22), 3794–3802. https://doi.org/10.1242/jcs.029678

Engler, A. J., Sen, S., Sweeney, H. L., & Discher, D. E. (2006). Matrix Elasticity Directs Stem Cell Lineage Specification. *Cell*, *126*(4), 677–689. https://doi.org/10.1016/j.cell.2006.06.044

Feger, B. J., Thompson, J. W., Dubois, L. G., Kommaddi, R. P., Foster, M. W., Mishra, R., Shenoy, S. K., Shibata, Y., Kidane, Y. H., Moseley, M. A., Carnell, L. S., & Bowles, D. E. (2016). Microgravity induces proteomics changes involved in endoplasmic reticulum stress and mitochondrial protection. *Scientific Reports*, *6*(1), 34091. https://doi.org/10.1038/srep34091

Ferranti, F., Caruso, M. L., Cammarota, M., Masiello, M. G., Scheri, K. C., Fabrizi, C., Fumagalli, L., Schiraldi, C., Cucina, A., Catizone, A., & Ricci, G. (2014). Cytoskeleton Modifications and Autophagy Induction in TCam-2 Seminoma Cells Exposed to Simulated Microgravity. *Biomed Research International*. https://doi.org/10.1155/2014/904396

Fraley, S. I., Wu, P., He, L., Feng, Y., Krisnamurthy, R., Longmore, G. D., & Wirtz, D. (2015). Three-dimensional matrix fiber alignment modulates cell migration and MT1-MMP utility by spatially and temporally directing protrusions. *Scientific Reports*, *5*(1), 14580. https://doi.org/10.1038/srep14580

Frank, S., Durante, M., Helm, A., & Ritter, S. (2014). *Cellular radiation response of mouse embryonic stem cell derived cardiomyocytes* (GSI-SR2013-BIOPHYSICS-20). GSI Helmholtzzentrum für Schwerionenforschung. https://doi.org/10.15120/GR-2014-1-BIOPHYSICS-20

Franklin, J. M., Ghosh, R. P., Shi, Q., Reddick, M. P., & Liphardt, J. T. (2020). Concerted localization-resets precede YAP-dependent transcription. *Nature Communications*, *11*(1), Article 1. https://doi.org/10.1038/s41467-020-18368-x

Freedman, B. R., Bade, N. D., Riggin, C. N., Zhang, S., Haines, P., Ong, K., & Janmey, P. A. (2015). The (Dys)functional Extracellular Matrix. *Biochimica Et Biophysica Acta (Bba) - Molecular Cell Research*, *1853*(11), 3153–3164. https://doi.org/10.1016/j.bbamcr.2015.04.015

Frieß, J. L., Heselich, A., Ritter, S., Haber, A., Kaiser, N., Layer, P. G., & Thielemann, C. (2015). Electrophysiologic and cellular characteristics of cardiomyocytes after X-ray irradiation. *Mutation Research/Fundamental and Molecular Mechanisms of Mutagenesis*, *777*, 1–10. https://doi.org/10.1016/j.mrfmmm.2015.03.012

Frtús, A., Smolková, B., Uzhytchak, M., Lunová, M., Jirsa, M., Hof, M., Jurkiewicz, P., Lozinsky, V. I., Wolfová, L., Petrenko, Y., Kubinová, Š., Dejneka, A., & Lunov, O. (2020). Hepatic Tumor Cell Morphology Plasticity Under Physical Constraints in 3D Cultures Driven by YAP–mTOR Axis. *Pharmaceuticals*. https://doi.org/10.3390/ph13120430

Fu, X. (2024). Targeting Nuclear Mechanics Mitigates the Fibroblast Invasiveness in Pathological Dermal Scars Induced by Matrix Stiffening. *Advanced Science*. https://doi.org/10.1002/advs.202308253

Fuentes, T. I., Appleby, N., Raya, M., Bailey, L., Hasaniya, N., Stodieck, L., & Kearns-Jonker, M. (2015). Simulated Microgravity Exerts an Age-Dependent Effect on the Differentiation of Cardiovascular Progenitors Isolated from the Human Heart. *PLOS ONE*, *10*(7), e0132378. https://doi.org/10.1371/journal.pone.0132378

Gallo, C., Ridolfi, L., & Scarsoglio, S. (2020). Cardiovascular Deconditioning During Long-Term Spaceflight Through Multiscale Modeling. *NPJ Microgravity*. https://doi.org/10.1038/s41526-020-00117-5

Gao, Q., Liu, Z., Lin, Z., Qiu, J., Liu, Y., Liu, A., Wang, Y., Xiang, M., Chen, B., Fu, J., & He, Y. (2017). 3D Bioprinting of Vessel-like Structures with Multilevel Fluidic Channels. *ACS Biomaterials Science & Engineering*, *3*(3), 399–408. https://doi.org/10.1021/acsbiomaterials.6b00643

Geiger, B., Spatz, J. P., & Bershadsky, A. D. (2009). Environmental sensing through focal adhesions. *Nature Reviews Molecular Cell Biology*, *10*(1), Article 1. https://doi.org/10.1038/nrm2593

Gibler, P., Gimble, J., Hamel, K., Rogers, E., Henderson, M., Wu, X., Olesky, S., & Frazier, T. (2021). Human Adipose-Derived Stromal/Stem Cell Culture and Analysis Methods for Adipose Tissue Modeling In Vitro: A Systematic Review. *Cells*, *10*(6), Article 6. https://doi.org/10.3390/cells10061378

Gishto, A., Farrell, K., & Kothapalli, C. R. (2015). Tuning composition and architecture of biomimetic scaffolds for enhanced matrix synthesis by murine cardiomyocytes. *Journal of Biomedical Materials Research Part A*, *103*(2), 693–708. https://doi.org/10.1002/jbm.a.35217

Grimm, D., Infanger, M., Westphal, K., Ulbrich, C., Pietsch, J., Kossmehl, P., Vadrucci, S., Baatout, S., Flick, B., Paul, M., & Bauer, J. (2009). A Delayed Type of Three-Dimensional Growth of Human Endothelial Cells Under Simulated Weightlessness. *Tissue Engineering Part A*, *15*(8), 2267–2275. https://doi.org/10.1089/ten.tea.2008.0576

Guarnieri, S., Morabito, C., Bevere, M., Lanuti, P., & Mariggiò, M. A. (2021). A Protective Strategy to Counteract the Oxidative Stress Induced by Simulated Microgravity on H9C2 Cardiomyocytes. *Oxidative Medicine and Cellular Longevity*, *2021*, e9951113. https://doi.org/10.1155/2021/9951113

Guo, Y., Du, S., Quan, S., Jiang, F., Yang, C., & Li, J. (2020). Effects of Biophysical Cues of 3D Hydrogels on Mesenchymal Stem Cells Differentiation. *Journal of Cellular Physiology*. https://doi.org/10.1002/jcp.30042

Habibi, M., Karyofyllis, P. K., Nikolakopoulou, A., Papagiannis, P., Karaiskos, P., Georgakilas, A. G., Hatzi, V. I., Malakos, I., Kollaros, N., Mastorakou, I., Voudris, V., & Terzoudi, G. I. (2021). The Use of Genotoxicity Endpoints as Biomarkers of Low Dose Radiation Exposure in Interventional Cardiology. *Frontiers in Public Health*, *9*. https://www.frontiersin.org/journals/public-health/articles/10.3389/fpubh.2021.701878

Hada, M., Ikeda, H., Rhone, J., Beitman, A., Plante, I., Souda, H., Yoshida, Y., Held, K., Fujiwara, K., Saganti, P., & Takahashi, A. (2018). Increased Chromosome Aberrations in Cells Exposed Simultaneously to Simulated Microgravity and Radiation. *International Journal of Molecular Sciences*, *20*(1), 43. https://doi.org/10.3390/ijms20010043

Hagiwara, Y., Niimi, A., Isono, M., Yamauchi, M., Yasuhara, T., Limsirichaikul, S., Oike, T., Sato, H., Held, K. D., Nakano, T., & Shibata, A. (2017). 3D-structured illumination microscopy reveals clustered DNA double-strand break formation in widespread γH2AX foci after high LET heavy-ion particle radiation. *Oncotarget*, *8*(65), 109370–109381. https://doi.org/10.18632/oncotarget.22679

Hargens, A. R., & Richardson, S. (2009). Cardiovascular adaptations, fluid shifts, and countermeasures related to space flight. *Respiratory Physiology & Neurobiology*, *169*, S30–S33. https://doi.org/10.1016/j.resp.2009.07.005

Herranz, R., Anken, R., Boonstra, J., Braun, M., Christianen, P. C. M., de Geest, M., Hauslage, J., Hilbig, R., Hill, R. J. A., Lebert, M., Medina, F. J., Vagt, N., Ullrich, O., van Loon, J. W. A., & Hemmersbach, R. (2013). Ground-based facilities for simulation of microgravity:

Organism-specific recommendations for their use, and recommended terminology. *Astrobiology*, *13*(1), Article 1. https://doi.org/10.1089/ast.2012.0876

Herron, T. J., Rocha, A. M. D., Campbell, K. F., Ponce-Balbuena, D., Willis, B. C., Guerrero-Serna, G., Liu, Q., Klos, M., Musa, H., Zarzoso, M., Bizy, A., Furness, J., Anumonwo, J., Mironov, S., & Jalife, J. (2016). Extracellular Matrix–Mediated Maturation of Human Pluripotent Stem Cell–Derived Cardiac Monolayer Structure and Electrophysiological Function. *Circulation: Arrhythmia and Electrophysiology*, *9*(4), e003638. https://doi.org/10.1161/CIRCEP.113.003638

Hirt, M. N., Hansen, A., & Eschenhagen, T. (2014). Cardiac Tissue Engineering: State of the Art. *Circulation Research*, *114*(2), 354–367. https://doi.org/10.1161/CIRCRESAHA.114.300522

Hodge, J. G., Robinson, J. L., & Mellott, A. J. (2023). Tailoring the secretome composition of mesenchymal stem cells to augment specific functions of epidermal regeneration: An *in vitro* diabetic model. *Frontiers in Medical Technology*, *5*. https://www.frontiersin.org/articles/10.3389/fmedt.2023.1194314

Horn, S., Barnard, S., & Rothkamm, K. (2011). Gamma-H2AX-Based Dose Estimation for Whole and Partial Body Radiation Exposure. *PLOS ONE*, *6*(9), e25113. https://doi.org/10.1371/journal.pone.0025113

Huang, R.-X., & Zhou, P.-K. (2020). DNA damage response signaling pathways and targets for radiotherapy sensitization in cancer. *Signal Transduction and Targeted Therapy*, *5*(1), 60. https://doi.org/10.1038/s41392-020-0150-x

Hughes-Fulford, M. (2011). To infinity … and beyond! Human spaceflight and life science. *The FASEB Journal*, *25*(9), 2858–2864. https://doi.org/10.1096/fj.11-0902ufm

Hughson, R. L., Helm, A., & Durante, M. (2018). Heart in space: Effect of the extraterrestrial environment on the cardiovascular system. *Nature Reviews Cardiology*, *15*(3), 167–180. https://doi.org/10.1038/nrcardio.2017.157

Hughson, R. L., Robertson, A. D., Arbeille, P., Shoemaker, J. K., Rush, J. W. E., Fraser, K. S., & Greaves, D. K. (2016). Increased postflight carotid artery stiffness and inflight insulin resistance resulting from 6-mo spaceflight in male and female astronauts. *American Journal of Physiology-Heart and Circulatory Physiology*, *310*(5), H628–H638. https://doi.org/10.1152/ajpheart.00802.2015

Infanger, M., Kossmehl, P., Shakibaei, M., Baatout, S., Witzing, A., Grosse, J., Bauer, J., Cogoli, A., Faramarzi, S., Derradji, H., Neefs, M., Paul, M., & Grimm, D. (2006). Induction of three-dimensional assembly and increase in apoptosis of human endothelial cells by simulated microgravity: Impact of vascular endothelial growth factor. *Apoptosis*, *11*(5), 749–764. https://doi.org/10.1007/s10495-006-5697-7

Ingber, D. E. (2003). Tensegrity I. Cell structure and hierarchical systems biology. *Journal of Cell Science*, *116*(7), 1157–1173. https://doi.org/10.1242/jcs.00359

Ingber, D. E. (2006). Cellular mechanotransduction: Putting all the pieces together again. *The FASEB Journal*, *20*(7), 811–827. https://doi.org/10.1096/fj.05-5424rev

J. Rowe, W. W. (2012). Correcting Magnesium Deficiencies May Prolong Life. *Clinical Interventions in Aging*. https://doi.org/10.2147/cia.s28768

Jang, J. (2017). 3D Bioprinting and In Vitro Cardiovascular Tissue Modeling. *Bioengineering*, *4*(4), 71. https://doi.org/10.3390/bioengineering4030071

Jiang, M., Wang, H., Liu, Z., Lin, L., Wang, L., Xie, M., Li, D., Zhang, J., & Zhang, R. (2020). Endoplasmic Reticulum Stress-dependent Activation of iNOS/NO-NF-κB Signaling and NLRP3 Inflammasome Contributes to Endothelial Inflammation and Apoptosis Associated With Microgravity. *The Faseb Journal*. https://doi.org/10.1096/fj.202000734r

Kaarj & Yoon. (2019). Methods of Delivering Mechanical Stimuli to Organ-on-a-Chip. *Micromachines*, *10*(10), 700. https://doi.org/10.3390/mi10100700

Kaiser, N. J., & K Coulombe, K. L. (2015). Physiologically Inspired Cardiac Scaffolds for Tailored<i>in Vivo</I>function and Heart Regeneration. *Biomedical Materials*. https://doi.org/10.1088/1748-6041/10/3/034003

Kamal, K. Y., Herranz, R., W. Loon, J. J., M. Christianen, P. C., & Medina, F. J. (2015). Evaluation of Simulated Microgravity Environments Induced by Diamagnetic Levitation of Plant Cell Suspension Cultures. *Microgravity Science and Technology*. https://doi.org/10.1007/s12217-015-9472-7

Kang, C.-Y., Zou, L., Yuan, M., Wang, Y., Li, T.-Z., Zhang, Y., Wang, J.-F., Li, Y., Deng, X.-W., & Liu, C.-T. (2011). Impact of simulated microgravity on microvascular endothelial cell apoptosis. *European Journal of Applied Physiology*, *111*(9), 2131–2138. https://doi.org/10.1007/s00421-011-1844-0

Khatau, S. B., Bloom, R., Bajpai, S., Razafsky, D., Zang, S. L., Giri, A., Wu, P. H., Marchand, J. A., Celedon, A., Hale, C. M., Sun, S. X., Hodzic, D., & Wirtz, D. (2012). The Distinct Roles of the Nucleus and Nucleus-Cytoskeleton Connections in Three-Dimensional Cell Migration. *Scientific Reports*. https://doi.org/10.1038/srep00488

Kim, E. H., Kim, M., Lee, K., Sai, S., Jeong, Y. K., Koh, J.-S., & Kong, C.-B. (2017). Effect of Low- And High-Linear Energy Transfer Radiation on in Vitro and Orthotopic in Vivo Models of Osteosarcoma by Activation of Caspase-3 and -9. *International Journal of Oncology*. https://doi.org/10.3892/ijo.2017.4102

Kim, J. H., Lee, G., Won, Y., Lee, M., Kwak, J.-S., Chun, C. H., & Chun, J. (2015). Matrix Cross-Linking–mediated Mechanotransduction Promotes Posttraumatic Osteoarthritis. *Proceedings of the National Academy of Sciences*, *112*(30), 9424–9429. https://doi.org/10.1073/pnas.1505700112

Kong, M., Lee, J., Yazdi, I. K., Miri, A. K., Lin, Y., Seo, J., Zhang, Y. S., Khademhosseini, A., & Shin, S. R. (2019). Cardiac Fibrotic Remodeling on a Chip With Dynamic Mechanical Stimulation. *Advanced Healthcare Materials*. https://doi.org/10.1002/adhm.201801146

Krause, L., Braun, M., Hauslage, J., & Hemmersbach, R. (2018). Analysis of Statoliths Displacement in Chara Rhizoids for Validating the Microgravity-Simulation Quality of Clinorotation Modes. *Microgravity Science and Technology*. https://doi.org/10.1007/s12217-017-9580-7

Kumar, A., Tahimic, C. G. T., Almeida, E. A. C., & Globus, R. K. (2021). Spaceflight Modulates the Expression of Key Oxidative Stress and Cell Cycle Related Genes in Heart. *International Journal of Molecular Sciences*, *22*(16), Article 16. https://doi.org/10.3390/ijms22169088

Kumari, R., Singh, K. P., & DuMond Jr., J. W. (2009). Simulated microgravity decreases DNA repair capacity and induces DNA damage in human lymphocytes. *Journal of Cellular Biochemistry*, *107*(4), 723–731. https://doi.org/10.1002/jcb.22171

Kwon, H., Kim, J., & Jho, E. (2022). Role of the Hippo pathway and mechanisms for controlling cellular localization of YAP/TAZ. *The FEBS Journal*, *289*(19), 5798–5818. https://doi.org/10.1111/febs.16091

Laflamme, M. A., & Murry, C. E. (2011). Heart regeneration. *Nature*, *473*(7347), 326–335. https://doi.org/10.1038/nature10147

LeBlanc, A., Schneider, V., Shackelford, L., West, S., Oganov, V., Bakulin, A., & Voronin, L. (2000). Bone mineral and lean tissue loss after long duration space flight. *Journal of Musculoskeletal & Neuronal Interactions*, *1*(2), 157–160.

Lee, S. M. C., Ribeiro, L. C., Martin, D. S., Zwart, S. R., Feiveson, A. H., Laurie, S. S., Macias, B. R., Crucian, B. E., Krieger, S., Weber, D., Grune, T., Platts, S. H., Smith, S. M., & Stenger, M. B. (2020). Arterial structure and function during and after long-duration spaceflight. *Journal of Applied Physiology*, *129*(1), 108–123. https://doi.org/10.1152/japplphysiol.00550.2019

Lei, X., Cao, Y., Zhang, Y., Qian, J., Zhao, Q., Liu, F., Zhang, T., Zhou, J., Gu, Y., Xia, G., & Duan, E. (2018). Effect of microgravity on proliferation and differentiation of embryonic stem cells in an automated culturing system during the TZ-1 space mission. *Cell Proliferation*, *51*(5), e12466. https://doi.org/10.1111/cpr.12466

Lesman, A., Gepstein, L., & Levenberg, S. (2010). Vascularization shaping the heart: Vascularization shaping the heart. *Annals of the New York Academy of Sciences*, *1188*(1), 46–51. https://doi.org/10.1111/j.1749-6632.2009.05082.x

Lewis, M. L., Reynolds, J. L., Cubano, L. A., Hatton, J. P., Lawless, B. D., & Piepmeier, E. H. (1998). Spaceflight alters microtubules and increases apoptosis in human lymphocytes (Jurkat). *The FASEB Journal*, *12*(11), 1007–1018. https://doi.org/10.1096/fasebj.12.11.1007

Li, L.-J., Zhong, L., Jiang, L., Chen, G., & Zou, L. (2010). B-Elemene Radiosensitizes Lung Cancer A549 Cells by Enhancing DNA Damage and Inhibiting DNA Repair. *Phytotherapy Research*. https://doi.org/10.1002/ptr.3367

Li, N., An, L., & Hang, H. (2015). Increased Sensitivity of DNA Damage Response-Deficient Cells to Stimulated Microgravity-Induced DNA Lesions. *PLOS ONE*, *10*(4), e0125236. https://doi.org/10.1371/journal.pone.0125236

Li, Y., Lovett, D. B., Zhang, Q., Neelam, S., Kuchibhotla, R. A., Zhu, R., Gundersen, G. G., Lele, T. P., & Dickinson, R. B. (2015). Moving Cell Boundaries Drive Nuclear Shaping During Cell Spreading. *Biophysical Journal*. https://doi.org/10.1016/j.bpj.2015.07.006

Li, Y., Qian, H., Wang, Y., & Cucinotta, F. A. (2012). A Stochastic Model of DNA Fragments Rejoining. *Plos One*. https://doi.org/10.1371/journal.pone.0044293

Lin, Z., von Gise, A., Zhou, P., Gu, F., Ma, Q., Jiang, J., Yau, A. L., Buck, J. N., Gouin, K. A., van Gorp, P. R. R., Zhou, B., Chen, J., Seidman, J. G., Wang, D.-Z., & Pu, W. T. (2014). Cardiac-Specific YAP Activation Improves Cardiac Function and Survival in an Experimental Murine MI Model. *Circulation Research*, *115*(3), 354–363. https://doi.org/10.1161/CIRCRESAHA.115.303632

Liu, C., Pei, M., Li, Q., & Zhang, Y. (2022). Decellularized extracellular matrix mediates tissue construction and regeneration. *Frontiers of Medicine*, *16*(1), 56–82. https://doi.org/10.1007/s11684-021-0900-3

Liu, C., Zhong, G., Zhou, Y., Yang, Y., Tan, Y., Li, Y., Gao, X., Sun, W., Li, J., Jin, X., Cao, D., Yuan, X., Liu, Z., Liang, S., Li, Y., Du, R., Zhao, Y., Xue, J., Zhao, D., … Li, Y. (2020). Alteration of calcium signalling in cardiomyocyte induced by simulated microgravity and hypergravity. *Cell Proliferation*, *53*(3). https://doi.org/10.1111/cpr.12783

Liu, M., Gao, H., Shang, P., Zhou, X., Ashforth, E., Zhuo, Y., Chen, D., Ren, B., Liu, Z., & Zhang, L. (2011). Magnetic Field Is the Dominant Factor to Induce the Response of Streptomyces Avermitilis in Altered Gravity Simulated by Diamagnetic Levitation. *Plos One*. https://doi.org/10.1371/journal.pone.0024697

Long, M., Wang, Y., Zheng, H., Shang, P., Duan, E., & Lü, D. (2015). Mechano-biological Coupling of Cellular Responses to Microgravity. *Microgravity Science and Technology*, *27*(6), 505–514. https://doi.org/10.1007/s12217-015-9464-7

Macaeva, E., Tabury, K., Michaux, A., Janssen, A., Averbeck, N., Moreels, M., De Vos, W. H., Baatout, S., & Quintens, R. (2021). High-Let Carbon and Iron Ions Elicit a Prolonged and Amplified P53 Signaling and Inflammatory Response Compared to Low-Let X-Rays in Human Peripheral Blood Mononuclear Cells. *Frontiers in Oncology*. https://doi.org/10.3389/fonc.2021.768493

Major, L. G., Holle, A. W., Young, J. L., Hepburn, M. S., Jeong, K., Chin, I. L., Sanderson, R. W., Jeong, J. H., Aman, Z. M., Kennedy, B. F., Hwang, Y., Han, D.-W., Park, H. W., Guan, K.-L., Spatz, J. P., & Choi, Y. S. (2019). Volume Adaptation Controls Stem Cell Mechanotransduction. *ACS Applied Materials & Interfaces*, *11*(49), 45520–45530. https://doi.org/10.1021/acsami.9b19770

Mangala, L. S., Zhang, Y., He, Z., Emami, K., Ramesh, G. T., Story, M., Rohde, L. H., & Wu, H. (2011). Effects of Simulated Microgravity on Expression Profile of MicroRNA in Human Lymphoblastoid Cells *. *Journal of Biological Chemistry*, *286*(37), 32483–32490. https://doi.org/10.1074/jbc.M111.267765

Manzano, A. I., W. Loon, J. J., M. Christianen, P. C., González-Rubio, J. M., Medina, F. J., & Herranz, R. (2012). Gravitational and Magnetic Field Variations Synergize to Cause Subtle Variations in the Global Transcriptional State of Arabidopsis in Vitro Callus Cultures. *BMC Genomics*. https://doi.org/10.1186/1471-2164-13-105

Mao, X. W., Nishiyama, N. C., Pecaut, M. J., Campbell-Beachler, M., Gifford, P., Haynes, K. E., Becronis, C., & Gridley, D. S. (2016). Simulated Microgravity and Low-Dose/Low-Dose-Rate Radiation Induces Oxidative Damage in the Mouse Brain. *Radiation Research*, *185*(6), 647–657. https://doi.org/10.1667/RR14267.1

Martino, F., Perestrelo, A. R., Vinarský, V., Pagliari, S., & Forte, G. (2018). Cellular Mechanotransduction: From Tension to Function. *Frontiers in Physiology*, *9*, 824. https://doi.org/10.3389/fphys.2018.00824

Mathur, A., Ma, Z., Loskill, P., Jeeawoody, S., & Healy, K. E. (2016). In vitro cardiac tissue models: Current status and future prospects. *Advanced Drug Delivery Reviews*, *96*, 203–213. https://doi.org/10.1016/j.addr.2015.09.011

McCain, M. L., & Parker, K. K. (2011). Mechanotransduction: The role of mechanical stress, myocyte shape, and cytoskeletal architecture on cardiac function. *Pflügers Archiv - European Journal of Physiology*, *462*(1), 89–104. https://doi.org/10.1007/s00424-011-0951-4

McGale, P., Darby, S. C., Hall, P., Adolfsson, J., Bengtsson, N.-O., Bennet, A. M., Fornander, T., Gigante, B., Jensen, M.-B., Peto, R., Rahimi, K., Taylor, C. W., & Ewertz, M. (2011). Incidence of heart disease in 35,000 women treated with radiotherapy for breast cancer in Denmark and Sweden. *Radiotherapy and Oncology*, *100*(2), 167–175. https://doi.org/10.1016/j.radonc.2011.06.016

McQuin, C., Goodman, A., Chernyshev, V., Kamentsky, L., Cimini, B. A., Karhohs, K. W., Doan, M., Ding, L., Rafelski, S. M., Thirstrup, D., Wiegraebe, W., Singh, S., Becker, T., Caicedo, J. C., & Carpenter, A. E. (2018). CellProfiler 3.0: Next-generation image processing for biology. *PLOS Biology*, *16*(7), e2005970. https://doi.org/10.1371/journal.pbio.2005970

Miles, D., Cao, N., Sandison, G. A., Stewart, R., Moffitt, G. B., Pulliam, T. H., Parvathaneni, U., Goff, P. H., Nghiem, P., & Stantz, K. M. (2021). *Differential Effects of High Versus Low Linear Energy Transfer (LET) Radiation on Type-I Interferon (IFNB) and TREX1 Responses*. https://doi.org/10.1101/2021.07.07.451516

Morabito, C., Guarnieri, S., Catizone, A., Schiraldi, C., Ricci, G., & Mariggiò, M. A. (2017). Transient increases in intracellular calcium and reactive oxygen species levels in TCam-2 cells exposed to microgravity. *Scientific Reports*, *7*(1), Article 1. https://doi.org/10.1038/s41598-017-15935-z

Morabito, C., Guarnieri, S., Cucina, A., Bizzarri, M., & Mariggiò, M. A. (2020). Antioxidant Strategy to Prevent Simulated Microgravity-Induced Effects on Bone Osteoblasts. *International Journal of Molecular Sciences*, *21*(10), Article 10. https://doi.org/10.3390/ijms21103638

Moreno-Villanueva, M., Feiveson, A. H., Krieger, S., Kay Brinda, A., Von Scheven, G., Bürkle, A., Crucian, B., & Wu, H. (2018). Synergistic Effects of Weightlessness, Isoproterenol, and Radiation on DNA Damage Response and Cytokine Production in Immune Cells. *International Journal of Molecular Sciences*, *19*(11), Article 11. https://doi.org/10.3390/ijms19113689

Moreno-Villanueva, M., Wong, M., Lu, T., Zhang, Y., & Wu, H. (2017). Interplay of space radiation and microgravity in DNA damage and DNA damage response. *Npj Microgravity*, *3*(1), 14. https://doi.org/10.1038/s41526-017-0019-7

Mosqueira, D., Pagliari, S., Uto, K., Ebara, M., Romanazzo, S., Escobedo-Lucea, C., Nakanishi, J., Taniguchi, A., Franzese, O., Di Nardo, P., Goumans, M. J., Traversa, E., Pinto-do-Ó, P., Aoyagi, T., & Forte, G. (2014). Hippo Pathway Effectors Control Cardiac Progenitor Cell Fate by Acting as Dynamic Sensors of Substrate Mechanics and Nanostructure. *ACS Nano*, *8*(3), 2033–2047. https://doi.org/10.1021/nn4058984

Murphy, S. V., & Atala, A. (2014). 3D bioprinting of tissues and organs. *Nature Biotechnology*, *32*(8), 773–785. https://doi.org/10.1038/nbt.2958

Neelam, S., Lee, A., Lane, M. A., Udave, C., Levine, H. G., & Zhang, Y. (2021). Module to Support Real-Time Microscopic Imaging of Living Organisms on Ground-Based Microgravity Analogs. *Applied Sciences*. https://doi.org/10.3390/app11073122

Neelam, S., Richardson, B., Barker, R., Udave, C., Gilroy, S., Cameron, M. J., Levine, H. G., & Zhang, Y. (2020). Changes in Nuclear Shape and Gene Expression in Response to Simulated Microgravity Are LINC Complex-Dependent. *International Journal of Molecular Sciences*. https://doi.org/10.3390/ijms21186762

Nguyen, H. P., Tran, P. H., Kim, K.-S., & Yang, S. (2021). The Effects of Real and Simulated Microgravity on Cellular Mitochondrial Function. *NPJ Microgravity*. https://doi.org/10.1038/s41526-021-00171-7

Ochola, D. O., Sharif, R., Bedford, J. S., Keefe, T. J., Kato, T. A., Fallgren, C. M., Demant, P., Costes, S. V., & Weil, M. M. (2018). Persistence of Gamma-H2ax Foci in Bronchial Cells Correlates With Susceptibility to Radiation Associated Lung Cancer in Mice. *Radiation Research*. https://doi.org/10.1667/rr14979.1

Ott, H. C., Matthiesen, T. S., Goh, S.-K., Black, L. D., Kren, S. M., Netoff, T. I., & Taylor, D. A. (2008). Perfusion-decellularized matrix: Using nature's platform to engineer a bioartificial heart. *Nature Medicine*, *14*(2), 213–221. https://doi.org/10.1038/nm1684

Pala, R., Cruciani, S., Manca, A., Garroni, G., EL Faqir, M. A., Lentini, V., Capobianco, G., Pantaleo, A., & Maioli, M. (2023). Mesenchymal Stem Cell Behavior Under Microgravity: From Stress Response to a Premature Senescence. *International Journal of Molecular Sciences*. https://doi.org/10.3390/ijms24097753

Panciera, T., Azzolin, L., Cordenonsi, M., & Piccolo, S. (2017). Mechanobiology of YAP and TAZ in physiology and disease. *Nature Reviews Molecular Cell Biology*, *18*(12), Article 12. https://doi.org/10.1038/nrm.2017.87

Pang, D., Chasovskikh, S., Rodgers, J., & Dritschilo, A. (2016). Short DNA Fragments Are a Hallmark of Heavy Charged-Particle Irradiation and May Underlie Their Greater Therapeutic Efficacy. *Frontiers in Oncology*. https://doi.org/10.3389/fonc.2016.00130

Pang, D., Nico, J. S., Karam, L. R., Timofeeva, O., Blakely, W. F., Dritschilo, A., & Dizdaroglu, M. (2014). Significant Disparity in Base and Sugar Damage in DNA Resulting From Neutron and Electron Irradiation. *Journal of Radiation Research*. https://doi.org/10.1093/jrr/rru059

Parazynski, S. E., Hargens, A. R., Tucker, B., Aratow, M., Styf, J., & Crenshaw, A. (1991). Transcapillary fluid shifts in tissues of the head and neck during and after simulated microgravity. *Journal of Applied Physiology*, *71*(6), 2469–2475. https://doi.org/10.1152/jappl.1991.71.6.2469

Parker, K. K., & Ingber, D. E. (2007). Extracellular matrix, mechanotransduction and structural hierarchies in heart tissue engineering. *Philosophical Transactions of the Royal Society B: Biological Sciences*, *362*(1484), 1267–1279. https://doi.org/10.1098/rstb.2007.2114

Piccolo, S., Dupont, S., & Cordenonsi, M. (2014). The Biology of YAP/TAZ: Hippo Signaling and Beyond. *Physiological Reviews*, *94*(4), 1287–1312. https://doi.org/10.1152/physrev.00005.2014

Pinto, A. R., Ilinykh, A., Ivey, M. J., Kuwabara, J. T., D'Antoni, M. L., Debuque, R., Chandran, A., Wang, L., Arora, K., Rosenthal, N. A., & Tallquist, M. D. (2016). Revisiting Cardiac Cellular Composition. *Circulation Research*, *118*(3), 400–409. https://doi.org/10.1161/CIRCRESAHA.115.307778

Pocaterra, A., Romani, P., & Dupont, S. (2020). YAP/TAZ functions and their regulation at a glance. *Journal of Cell Science*, *133*(2), jcs230425. https://doi.org/10.1242/jcs.230425

Polak, J. M. (2006). Stem Cells and Tissue Engineering: Past, Present, and Future. *Annals of the New York Academy of Sciences*, *1068*(1), 352–366. https://doi.org/10.1196/annals.1346.001

Puukila, S., Lemon, J. A., Lees, S. J., Tai, T. C., Boreham, D. R., & Khaper, N. (2017). Impact of Ionizing Radiation on the Cardiovascular System: A Review. *Radiation Research*, *188*(4.2), 539–546. https://doi.org/10.1667/RR14864.1

Radisic, M., Park, H., Martens, T. P., Salazar-Lazaro, J. E., Geng, W., Wang, Y., Langer, R., Freed, L. E., & Vunjak-Novakovic, G. (2008). Pre-treatment of synthetic elastomeric scaffolds by cardiac fibroblasts improves engineered heart tissue. *Journal of Biomedical Materials Research Part A*, *86A*(3), 713–724. https://doi.org/10.1002/jbm.a.31578

Radstake, W. E., Gautam, K., Miranda, S., Rompay, C. V., Vermeesen, R., Tabury, K., Verslegers, M., Dowson, A., Gorissen, J., W. Loon, J. J., L. Savage, N. D., Baatout, S., & Baselet, B. (2023). Gravitational Effects on Fibroblasts' Function in Relation to Wound Healing. *NPJ Microgravity*. https://doi.org/10.1038/s41526-023-00286-z

Ranieri, D., Proietti, S., Dinicola, S., Masiello, M. G., Rosato, B., Ricci, G., Cucina, A., Catizone, A., Bizzarri, M., & Torrisi, M. R. (2017). Simulated Microgravity Triggers Epithelial Mesenchymal Transition in Human Keratinocytes. *Scientific Reports*. https://doi.org/10.1038/s41598-017-00602-0

Rashedi, I., Talele, N., Wang, X.-H., Hinz, B., Radisic, M., & Keating, A. (2017). Collagen scaffold enhances the regenerative properties of mesenchymal stromal cells. *PLOS ONE*, *12*(10), e0187348. https://doi.org/10.1371/journal.pone.0187348

Raub, C. B., Suresh, V., Krasieva, T., Lyubovitsky, J., Mih, J. D., Putnam, A. J., Tromberg, B. J., & George, S. C. (2007). Noninvasive Assessment of Collagen Gel Microstructure and Mechanics Using Multiphoton Microscopy. *Biophysical Journal*, *92*(6), 2212–2222. https://doi.org/10.1529/biophysj.106.097998

Ren, L., Liu, W., Wang, Y., Wang, J.-C., Tu, Q., Xu, J., Liu, R., Shen, S.-F., & Wang, J. (2013). Investigation of Hypoxia-Induced Myocardial Injury Dynamics in a Tissue Interface Mimicking Microfluidic Device. *Analytical Chemistry*, *85*(1), 235–244. https://doi.org/10.1021/ac3025812

Ribas, J., Sadeghi, H., Manbachi, A., Leijten, J., Brinegar, K., Zhang, Y. S., Ferreira, L., & Khademhosseini, A. (2016). Cardiovascular Organ-on-a-Chip Platforms for Drug Discovery and Development. *Applied In Vitro Toxicology*, *2*(2), 82–96. https://doi.org/10.1089/aivt.2016.0002

Robertson, C., Tran, D. D., & George, S. C. (2013). Concise Review: Maturation Phases of Human Pluripotent Stem Cell-Derived Cardiomyocytes. *Stem Cells*, *31*(5), 829–837. https://doi.org/10.1002/stem.1331

Rudimov, E. G., Knjazev, E. N., Khaustova, N. A., Grigorieva, O. V., & Buravkova, L. B. (2017). Transcriptomic changes in human umbilical cord blood endothelial cells under simulated microgravity. *Doklady Biochemistry and Biophysics*, *472*(1), 1–4. https://doi.org/10.1134/S160767291701001X

Sacchetto, C., Vitiello, L., de Windt, L. J., Rampazzo, A., & Calore, M. (2020). Modeling Cardiovascular Diseases with hiPSC-Derived Cardiomyocytes in 2D and 3D Cultures. *International Journal of Molecular Sciences*, *21*(9), 3404. https://doi.org/10.3390/ijms21093404

Sadeghi, A. H., Shin, S. R., Deddens, J. C., Fratta, G., Mandla, S., Yazdi, I. K., Prakash, G., Antona, S., Demarchi, D., Buijsrogge, M. P., Sluijter, J. P. G., Hjortnaes, J., & Khademhosseini, A. (2017). Engineered 3D Cardiac Fibrotic Tissue to Study Fibrotic Remodeling. *Advanced Healthcare Materials*. https://doi.org/10.1002/adhm.201601434

Safar, M. E., Levy, B. I., & Struijker-Boudier, H. (2003). Current Perspectives on Arterial Stiffness and Pulse Pressure in Hypertension and Cardiovascular Diseases. *Circulation*, *107*(22), 2864–2869. https://doi.org/10.1161/01.CIR.0000069826.36125.B4

Sarker, M. D., Naghieh, S., Sharma, N. K., & Chen, X. (2018). 3D biofabrication of vascular networks for tissue regeneration: A report on recent advances. *Journal of Pharmaceutical Analysis*, *8*(5), 277–296. https://doi.org/10.1016/j.jpha.2018.08.005

Savoji, H., Mohammadi, M. H., Rafatian, N., Toroghi, M. K., Wang, E. Y., Zhao, Y., Korolj, A., Ahadian, S., & Radisic, M. (2019). Cardiovascular disease models: A game changing paradigm in drug discovery and screening. *Biomaterials*, *198*, 3–26. https://doi.org/10.1016/j.biomaterials.2018.09.036

Sawin, C. (2022). Extended Duration Orbiter Medical Project. *Aerospace Medicine and Human Performance*. https://doi.org/10.3357/amhp.6068.2022

Schröder, A., Neher, K., Krenmayr, B., Paddenberg, E., Spanier, G., Proff, P., & Kirschneck, C. (2023). Impact of PIEZO1-channel on Inflammation and Osteoclastogenesis Mediated via Periodontal Ligament Fibroblasts During Mechanical Loading. *European Journal of Oral Sciences*, *131*(1). https://doi.org/10.1111/eos.12913

Scott, K. E., Fraley, S. I., & Rangamani, P. (2021). A Spatial Model of YAP/TAZ Signaling Reveals How Stiffness, Dimensionality, and Shape Contribute to Emergent Outcomes. *Proceedings of the National Academy of Sciences*. https://doi.org/10.1073/pnas.2021571118

Seawright, J. W., Samman, Y., Sridharan, V., Mao, X. W., Cao, M., Singh, P., Melnyk, S., Koturbash, I., Nelson, G. A., Hauer-Jensen, M., & Boerma, M. (2017). Effects of low-dose rate γ-irradiation combined with simulated microgravity on markers of oxidative stress, DNA methylation potential, and remodeling in the mouse heart. *PLOS ONE*, *12*(7), e0180594. https://doi.org/10.1371/journal.pone.0180594

Sedelnikova, O. A., Nakamura, A., Kovalchuk, O., Koturbash, I., Mitchell, S. A., Marino, S. A., Brenner, D. J., & Bonner, W. M. (2007). DNA Double-Strand Breaks Form in Bystander Cells after Microbeam Irradiation of Three-dimensional Human Tissue Models. *Cancer Research*, *67*(9), 4295–4302. https://doi.org/10.1158/0008-5472.CAN-06-4442

Sero, J. E., & Bakal, C. (2017). Multiparametric Analysis of Cell Shape Demonstrates that β-PIX Directly Couples YAP Activation to Extracellular Matrix Adhesion. *Cell Systems*, *4*(1), 84-96.e6. https://doi.org/10.1016/j.cels.2016.11.015

Sheth, M. (2024). Three-Dimensional Matrix Stiffness Modulates Mechanosensitive and Phenotypic Alterations in Oral Squamous Cell Carcinoma Spheroids. *Apl Bioengineering*. https://doi.org/10.1063/5.0210134

Shi, J., Yao, H., Wang, B., Yang, J., Liu, D., Shang, X., Chong, H., Fei, W., & Wang, D.-A. (2024). Construction of a Decellularized Multicomponent Extracellular Matrix Interpenetrating Network Scaffold by Gelatin Microporous Hydrogel 3D Cell Culture System. *Macromolecular Rapid Communications*, *45*(5), 2300508. https://doi.org/10.1002/marc.202300508

Shi, L., Tian, H., Wang, P., Li, L., Zhang, Z., Zhang, J., & Zhao, Y. (2021). Spaceflight and simulated microgravity suppresses macrophage development via altered RAS/ERK/NFκB and metabolic pathways. *Cellular & Molecular Immunology*, *18*(6), Article 6. https://doi.org/10.1038/s41423-019-0346-6

Shreberk-Shaked, M., & Oren, M. (2019). New insights into YAP/TAZ nucleo-cytoplasmic shuttling: New cancer therapeutic opportunities? *Molecular Oncology*, *13*(6), 1335–1341. https://doi.org/10.1002/1878-0261.12498

Singh, K. P., Kumari, R., & DuMond, J. W. (2010). Simulated microgravity-induced epigenetic changes in human lymphocytes. *Journal of Cellular Biochemistry*, *111*(1), 123–129. https://doi.org/10.1002/jcb.22674

Smith, S. M., Heer, M. A., Shackelford, L. C., Sibonga, J. D., Ploutz-Snyder, L., & Zwart, S. R. (2012). Benefits for bone from resistance exercise and nutrition in long-duration spaceflight: Evidence from biochemistry and densitometry. *Journal of Bone and Mineral Research*, *27*(9), 1896–1906. https://doi.org/10.1002/jbmr.1647

Sokolovskaya, A., Korneeva, E., Zaichenko, D. M., Virus, E. D., Колесов, Д. В., Московцев, A. A., & Kubatiev, A. A. (2020). Changes in the Surface Expression of Intercellular Adhesion Molecule 3, the Induction of Apoptosis, and the Inhibition of Cell-Cycle Progression of Human Multidrug-Resistant Jurkat/A4 Cells Exposed to a Random Positioning Machine. *International Journal of Molecular Sciences*. https://doi.org/10.3390/ijms21030855

Soucy, K. G., Lim, H. K., Kim, J. H., Oh, Y., Attarzadeh, D. O., Sevinc, B., Kuo, M. M., Shoukas, A. A., Vazquez, M. E., & Berkowitz, D. E. (2011). HZE $^{56}$ Fe-Ion Irradiation Induces Endothelial

Dysfunction in Rat Aorta: Role of Xanthine Oxidase. *Radiation Research*, *176*(4), 474–485. https://doi.org/10.1667/RR2598.1

Sridharan, D., Asaithamby, A., Bailey, S. M., Costes, S. V., Doetsch, P. W., Dynan, W. S., Kronenberg, A., Rithidech, K. N., Saha, J., Snijders, A. M., Werner, E., Wiese, C., Cucinotta, F. A., & Pluth, J. M. (2015). Understanding Cancer Development Processes After HZE-Particle Exposure: Roles of ROS, DNA Damage Repair and Inflammation. *Radiation Research*. https://doi.org/10.1667/rr13804.1

Stewart, L., & Turner, N. A. (2021). Channelling the Force to Reprogram the Matrix: Mechanosensitive Ion Channels in Cardiac Fibroblasts. *Cells*, *10*(5), 990. https://doi.org/10.3390/cells10050990

Stiber, J. A., Seth, M., & Rosenberg, P. B. (2009). Mechanosensitive Channels in Striated Muscle and the Cardiovascular System: Not Quite a Stretch Anymore. *Journal of Cardiovascular Pharmacology*, *54*(2), 116–122. https://doi.org/10.1097/fjc.0b013e3181aa233f

Stiekema, M., M. Zandvoort, M. A., S. Ramaekers, F. C., & V. Broers, J. L. (2020). Structural and Mechanical Aberrations of the Nuclear Lamina in Disease. *Cells*. https://doi.org/10.3390/cells9081884

Stirling, D. R., Swain-Bowden, M. J., Lucas, A. M., Carpenter, A. E., Cimini, B. A., & Goodman, A. (2021). CellProfiler 4: Improvements in speed, utility and usability. *BMC Bioinformatics*, *22*(1), 433. https://doi.org/10.1186/s12859-021-04344-9

Sun, Z., Martinez-Lemus, L. A., Hill, M. A., & Meininger, G. A. (2008). Extracellular Matrix-Specific Focal Adhesions in Vascular Smooth Muscle Produce Mechanically Active Adhesion Sites. *Ajp Cell Physiology*, *295*(1), C268–C278. https://doi.org/10.1152/ajpcell.00516.2007

Svejgaard, B., Wehland, M., Ma, X., Kopp, S., Sahana, J., Warnke, E., Aleshcheva, G., Hemmersbach, R., Hauslage, J., Grosse, J., Bauer, J., Corydon, T. J., Islam, T., Infanger, M., & Grimm, D. (2015). Common Effects on Cancer Cells Exerted by a Random Positioning Machine and a 2D Clinostat. *Plos One*. https://doi.org/10.1371/journal.pone.0135157

Sa, E., Parfenov, V. A., Каралкин, П. А., Khesuani, Y. D., & Domnin, P. A. (2023). Experimentally Created Magnetic Force in Microbiological Space and on-Earth Studies: Perspectives and Restrictions. *Cells*. https://doi.org/10.3390/cells12020338

Takahashi, K., Kakimoto, Y., Toda, K., & Naruse, K. (2013). Mechanobiology in cardiac physiology and diseases. *Journal of Cellular and Molecular Medicine*, *17*(2), 225–232. https://doi.org/10.1111/jcmm.12027

Tan, S., Pei, W., Huang, H., Zhou, G., & Hu, W. (2020). Additive effects of simulated microgravity and ionizing radiation in cell death, induction of ROS and expression of RAC2 in human bronchial epithelial cells. *Npj Microgravity*, *6*(1), Article 1. https://doi.org/10.1038/s41526-020-00123-7

Thiel, C. S., Tauber, S., Lauber, B., Polzer, J., Seebacher, C., Uhl, R., Neelam, S., Zhang, Y., Levine, H. G., & Ullrich, O. (2019). Rapid Morphological and Cytoskeletal Response to Microgravity in Human Primary Macrophages. *International Journal of Molecular Sciences*. https://doi.org/10.3390/ijms20102402

Touchstone, H., Bryd, R., Loisate, S., Thompson, M. S., Kim, S., Puranam, K. L., Senthilnathan, A., Pu, X., Beard, R. S., Rubin, J., Alwood, J. S., Oxford, J. T., & Uzer, G. (2019). Recovery of Stem Cell Proliferation by Low Intensity Vibration Under Simulated Microgravity Requires LINC Complex. *NPJ Microgravity*. https://doi.org/10.1038/s41526-019-0072-5

Ugenskiene, R., Prise, K., Folkard, M., Lekki, J., Stachura, Z., Zazula, M., & Stachura, J. (2009). Dose response and kinetics of foci disappearance following exposure to high- and low-LET ionizing radiation. *International Journal of Radiation Biology*, *85*(10), 872–882. https://doi.org/10.1080/09553000903072462

Um Min Allah, N., Berahim, Z., Ahmad, A., & Kannan, T. P. (2017). Biological Interaction Between Human Gingival Fibroblasts and Vascular Endothelial Cells for Angiogenesis: A Co-culture Perspective. *Tissue Engineering and Regenerative Medicine*, *14*(5), 495–505. https://doi.org/10.1007/s13770-017-0065-y

van Amerongen, M. J., & Engel, F. B. (2008). Features of cardiomyocyte proliferation and its potential for cardiac regeneration. *Journal of Cellular and Molecular Medicine*, *12*(6a), 2233–2244. https://doi.org/10.1111/j.1582-4934.2008.00439.x

Venkateswarlu, R., Tamizh, S. G., Bhavani, M., Kumar, A., Alok, A., Karthik, K., Kalra, N., Vijayalakshmi, J., Paul, S. F. D., Chaudhury, N. K., & Venkatachalam, P. (2015). Mean frequency and relative fluorescence intensity measurement of γ-H2AX foci dose response in PBL exposed to γ-irradiation: An inter- and intra-laboratory comparison and its relevance

for radiation triage. *Cytometry Part A*, *87*(12), 1138–1146. https://doi.org/10.1002/cyto.a.22729

Vernice, N. A., Meydan, C., Afshinnekoo, E., & Mason, C. E. (2020). Long-Term Spaceflight and the Cardiovascular System. *Precision Clinical Medicine*. https://doi.org/10.1093/pcmedi/pbaa022

von Gise, A., Lin, Z., Schlegelmilch, K., Honor, L. B., Pan, G. M., Buck, J. N., Ma, Q., Ishiwata, T., Zhou, B., Camargo, F. D., & Pu, W. T. (2012). YAP1, the nuclear target of Hippo signaling, stimulates heart growth through cardiomyocyte proliferation but not hypertrophy. *Proceedings of the National Academy of Sciences of the United States of America*, *109*(7), 2394–2399. https://doi.org/10.1073/pnas.1116136109

Vorselen, D., Roos, W. H., MacKintosh, F. C., Wuite, G. J. L., & van Loon, J. J. W. A. (2014). The role of the cytoskeleton in sensing changes in gravity by nonspecialized cells. *The FASEB Journal*, *28*(2), 536–547. https://doi.org/10.1096/fj.13-236356

Vuorenpää, H., Ikonen, L., Kujala, K., Huttala, O., Sarkanen, J.-R., Ylikomi, T., Aalto-Setälä, K., & Heinonen, T. (2014). Novel *in vitro* cardiovascular constructs composed of vascular-like networks and cardiomyocytes. *In Vitro Cellular & Developmental Biology - Animal*, *50*(4), 275–286. https://doi.org/10.1007/s11626-013-9703-4

Wang, G., McCain, M. L., Yang, L., He, A., Pasqualini, F. S., Agarwal, A., Yuan, H., Jiang, D., Zhang, D., Zangi, L., Geva, J., Roberts, A. E., Ma, Q., Ding, J., Chen, J., Wang, D.-Z., Li, K., Wang, J., Wanders, R. J. A., … Pu, W. T. (2014). Modeling the mitochondrial cardiomyopathy of Barth syndrome with induced pluripotent stem cell and heart-on-chip technologies. *Nature Medicine*, *20*(6), 616–623. https://doi.org/10.1038/nm.3545

Wang, Y., Shi, J., & Tong, X. (2021). Cross-Talk Between Mechanosensitive Ion Channels and Calcium Regulatory Proteins in Cardiovascular Health and Disease. *International Journal of Molecular Sciences*, *22*(16), 8782. https://doi.org/10.3390/ijms22168782

Wang, Z., Lee, S. J., Cheng, H.-J., Yoo, J. J., & Atala, A. (2018). 3D bioprinted functional and contractile cardiac tissue constructs. *Acta Biomaterialia*, *70*, 48–56. https://doi.org/10.1016/j.actbio.2018.02.007

Watenpaugh, D. E. (2016). Analogs of microgravity: Head-down tilt and water immersion. *Journal of Applied Physiology (Bethesda, Md.: 1985)*, *120*(8), 904–914. https://doi.org/10.1152/japplphysiol.00986.2015

Wise, P. M., Neviani, P., Riwaldt, S., Corydon, T. J., Wehland, M., Braun, M., Krüger, M., Infanger, M., & Grimm, D. (2021). Changes in Exosome Release in Thyroid Cancer Cells after Prolonged Exposure to Real Microgravity in Space. *International Journal of Molecular Sciences*, *22*(4), Article 4. https://doi.org/10.3390/ijms22042132

Wnorowski, A., Sharma, A., Chen, H., Wu, H., Shao, N.-Y., Sayed, N., Liu, C., Countryman, S., Stodieck, L. S., Rubins, K. H., Wu, S. M., Lee, P. H. U., & Wu, J. C. (2019). Effects of Spaceflight on Human Induced Pluripotent Stem Cell-Derived Cardiomyocyte Structure and Function. *Stem Cell Reports*, *13*(6), 960–969. https://doi.org/10.1016/j.stemcr.2019.10.006

Wuest, S. L., Richard, S., Kopp, S., Grimm, D., & Egli, M. (2015). Simulated Microgravity: Critical Review on the Use of Random Positioning Machines for Mammalian Cell Culture. *BioMed Research International*, *2015*, 971474. https://doi.org/10.1155/2015/971474

Xie, R., Zheng, W., Guan, L., Ai, Y., & Liang, Q. (2020). Engineering of Hydrogel Materials with Perfusable Microchannels for Building Vascularized Tissues. *Small*, *16*(15), 1902838. https://doi.org/10.1002/smll.201902838

Xin, M., Kim, Y., Sutherland, L. B., Murakami, M., Qi, X., McAnally, J., Porrello, E. R., Mahmoud, A. I., Tan, W., Shelton, J. M., Richardson, J. A., Sadek, H. A., Bassel-Duby, R., & Olson, E. N. (2013). Hippo pathway effector Yap promotes cardiac regeneration. *Proceedings of the National Academy of Sciences*, *110*(34), 13839–13844. https://doi.org/10.1073/pnas.1313192110

Xin, M., Kim, Y., Sutherland, L. B., Qi, X., McAnally, J., Schwartz, R. J., Richardson, J. A., Bassel-Duby, R., & Olson, E. N. (2011). Regulation of Insulin-Like Growth Factor Signaling by Yap Governs Cardiomyocyte Proliferation and Embryonic Heart Size. *Science Signaling*, *4*(196). https://doi.org/10.1126/scisignal.2002278

Yamanouchi, S., Rhone, J., Mao, J.-H., Fujiwara, K., Saganti, P. B., Takahashi, A., & Hada, M. (2020). Simultaneous Exposure of Cultured Human Lymphoblastic Cells to Simulated Microgravity and Radiation Increases Chromosome Aberrations. *Life*, *10*(9), 187. https://doi.org/10.3390/life10090187

Yan, Y., Zhang, K., Zhou, G., & Hu, W. (2020). MicroRNAs Responding to Space Radiation. *International Journal of Molecular Sciences*. https://doi.org/10.3390/ijms21186603

Yang, Y., Leone, L. M., & Kaufman, L. J. (2009). Elastic Moduli of Collagen Gels Can Be Predicted from Two-Dimensional Confocal Microscopy. *Biophysical Journal*, *97*(7), 2051–2060. https://doi.org/10.1016/j.bpj.2009.07.035

Ye, G. J. C., Aratyn-Schaus, Y., Nesmith, A. P., Pasqualini, F. S., Alford, P. W., & Parker, K. K. (2014). The Contractile Strength of Vascular Smooth Muscle Myocytes Is Shape Dependent. *Integrative Biology*. https://doi.org/10.1039/c3ib40230d

Yu, X., Wang, H., Wang, P., Chen, B. P. C., & Wang, Y. (2010). The Ku-dependent Non-homologous End-joining Pathway Contributes to Low-dose Radiation-stimulated Cell Survival. *Journal of Cellular Physiology*. https://doi.org/10.1002/jcp.22342

Zevolis, E., Philippou, A., Moustogiannis, A., Chatzigeorgiou, A., & Koutsilieris, M. (2022). The Effects of Mechanical Loading Variations on the Hypertrophic, Anti-Apoptotic, and Anti-Inflammatory Responses of Differentiated Cardiomyocyte-like H9C2 Cells. *Cells*, *11*(3), Article 3. https://doi.org/10.3390/cells11030473

Zhang, C., Li, L., Chen, J., & Wang, J. (2015). Behavior of stem cells under outer-space microgravity and ground-based microgravity simulation: Microgravity and stem cells. *Cell Biology International*, *39*(6), 647–656. https://doi.org/10.1002/cbin.10452

Zhang, F., Qu, K.-Y., Zhou, B., Luo, Y., Zhu, Z., Pan, D.-J., Cui, C., Zhu, Y., Chen, M.-L., & Huang, N.-P. (2021). Design and fabrication of an integrated heart-on-a-chip platform for construction of cardiac tissue from human iPSC-derived cardiomyocytes and in situ evaluation of physiological function. *Biosensors and Bioelectronics*, *179*, 113080. https://doi.org/10.1016/j.bios.2021.113080

Zhang, H., Chen, J., Wang, H., Lu, X., Li, K., Yang, C., Wu, F., Xu, Z., Nie, H., Ding, B., Guo, Z., Li, Y., Wang, J., Li, Y., & Dai, Z. (2020). Serum Metabolomics Associating With Circulating MicroRNA Profiles Reveal the Role of miR-383-5p in Rat Hippocampus Under Simulated Microgravity. *Frontiers in Physiology*, *11*. https://www.frontiersin.org/journals/physiology/articles/10.3389/fphys.2020.00939

Zhang, W., Liu, Y., & Zhang, H. (2021). Extracellular matrix: An important regulator of cell functions and skeletal muscle development. *Cell & Bioscience*, *11*(1), 65. https://doi.org/10.1186/s13578-021-00579-4

Zhang, X., Ye, C., Sun, F., Wei, W., Hu, B., & Wang, J. (2016). Both Complexity and Location of DNA Damage Contribute to Cellular Senescence Induced by Ionizing Radiation. *Plos One*. https://doi.org/10.1371/journal.pone.0155725

Zhang, Y., Richards, J. T., Hellein, J. L., Johnson, C. M., Woodall, J., Sorenson, T., Neelam, S., Ruby, A. M. J., & Levine, H. G. (2022). NASA's Ground-Based Microgravity Simulation FacilityMicrogravity simulation facility. In E. B. Blancaflor (Ed.), *Plant Gravitropism: Methods and Protocols* (pp. 281–299). Springer US. https://doi.org/10.1007/978-1-0716-1677-2_18

Zhang, Y. S., Arneri, A., Bersini, S., Shin, S.-R., Zhu, K., Goli-Malekabadi, Z., Aleman, J., Colosi, C., Busignani, F., Dell'Erba, V., Bishop, C., Shupe, T., Demarchi, D., Moretti, M., Rasponi, M., Dokmeci, M. R., Atala, A., & Khademhosseini, A. (2016). Bioprinting 3D microfibrous scaffolds for engineering endothelialized myocardium and heart-on-a-chip. *Biomaterials*, *110*, 45–59. https://doi.org/10.1016/j.biomaterials.2016.09.003

Zhang, Y., Zegers, M. M. P., Nagelkerke, A., Rowan, A. E., Span, P. N., & Kouwer, P. H. J. (2021). Tunable Hybrid Matrices Drive Epithelial Morphogenesis and YAP Translocation. *Advanced Science*, *8*(2), 2003380. https://doi.org/10.1002/advs.202003380

Zhao, B., Li, L., Tumaneng, K., Wang, C.-Y., & Guan, K.-L. (2010). A coordinated phosphorylation by Lats and CK1 regulates YAP stability through SCFβ-TRCP. *Genes & Development*, *24*(1), 72–85. https://doi.org/10.1101/gad.1843810

Zhao, T., Tang, X., Umeshappa, C. S., Ma, H., Gao, H., Deng, Y., Freywald, A., & Xiang, J. (2016). Simulated Microgravity Promotes Cell Apoptosis Through Suppressing Uev1A/TICAM/TRAF/NF-κB-Regulated Anti-Apoptosis and p53/PCNA- and ATM/ATR-Chk1/2-Controlled DNA-Damage Response Pathways. *Journal of Cellular Biochemistry*, *117*(9), 2138–2148. https://doi.org/10.1002/jcb.25520

Zieman, S. J., Melenovsky, V., & Kass, D. A. (2005). Mechanisms, Pathophysiology, and Therapy of Arterial Stiffness. *Arteriosclerosis, Thrombosis, and Vascular Biology*, *25*(5), 932–943. https://doi.org/10.1161/01.ATV.0000160548.78317.29

# APPENDIX

# APPENDIX A. EQUIPMENT AND MATERIALS DETAILS AND SOURCE

Equipment utilised throughout the experiments are provided in Table 1. Chemicals, reagents and consumables utilised throughout the experiments are provided in Table 2.

*Appendix A - Table 1*

| **Equipment** | **Manufacturer** |
|---|---|
| Random Positioning Machine (RPM) | UTS |
| X-RAD 320 | Precision X-Ray Inc. |
| Class II Biosafety Cabinets | ThermoFisher |
| Cell Culture Incubator | ThermoFisher |
| LEICA Confocal Microscope | Leica Microsystem |
| EVOS M5000 microscope | ThermoFisher |
| Olmpusy D73 | Olympus |
| Plate Reader | ThermoFisher |
| BIO X | Cellink |
| QuantStudio 6 Flex Real-Time PCR System | Applied Biosystems |
| QuantStudio 12K Flex Real-Time PCR System | Applied Biosystems |

*Appendix A - Table 2.*

| **Consumables** | **Cat#** | **Supplier** |
|---|---|---|
| 19mm circular silicone pads | N/A | AliExpress |
| 384 well PCR Plates | 4453929 | ThermoFisher |
| 96 well PCR Plates | 4346906 | ThermoFisher |
| AeraSeal™ film | A9224 | Sigma |
| Alginate | A1112 | Sigma |
| Anti-Cardiac Troponin I antibody | ab47003 | abcam |
| Anti-N Cadherin antibody - Intercellular Junction Marker | ab18203 | abcam |
| Anti-TRPV4 antibody | T9075 | Sigma |
| Anti-Vinculin antibody | V9264-25UL | Sigma |
| BSA | A9647-10G | Sigma |
| calcein-AM | L3224 | ThermoFisher |
| Cardiac Troponin I | ab47003 | abcam |
| Circular waterproof and breathable membrane | N/A | AliExpress |
| Connexin 43 Monoclonal Antibody (CX-1B1) | # 13-8300 | ThermoFisher |
| DAPI | D9542 | Sigma |
| DMEM/F-12, HEPES, no phenol red | 11039047 | ThermoFisher |
| Ethidium Homodimer | L3224 | ThermoFisher |
| Fetal Bovine Serum | 26140079 | ThermoFisher |
| Gelatin | G2500 | Sigma |
| Goat anti-Mouse IgG (H+L) Cross-Adsorbed Secondary Antibody, Alexa Fluor™ 568 | A11004 | ThermoFisher |

| | | |
|---|---|---|
| Goat anti-Mouse IgG (H+L) Cross-Adsorbed Secondary Antibody, Alexa Fluor™ 594 | A11005 | ThermoFisher |
| Goat anti-Mouse IgG (H+L) Cross-Adsorbed Secondary Antibody, Cyanine5 | A10524 | ThermoFisher |
| Goat anti-Rabbit IgG (H+L) Cross-Adsorbed Secondary Antibody, Alexa Fluor™ 594 | A11012 | ThermoFisher |
| Goat anti-Rabbit IgG (H+L) Cross-Adsorbed Secondary Antibody, Cyanine5 | A10523 | ThermoFisher |
| Goat anti-Rabbit IgG (Heavy Chain), Superclonal™ Recombinant Secondary Antibody, Alexa Fluor™ 488 | A27034 | ThermoFisher |
| Goat Anti-Rabbit IgG H&L (Alexa Fluor® 488) | ab150077 | abcam |
| HCF Media | 316-500 | Sigma |
| Hoechst 33342 Solution | 62249 | ThermoFisher |
| iScript™ cDNA Synthesis Kit, 100 x 20 µl rxns | 1708891 | Bio-Rad |
| LIVE/DEAD™ Viability/Cytotoxicity Kit | L3224 | ThermoFisher |
| M5 nylon screw gasket | N/A | AliExpress |
| MesoEndo Media | 212-500 | Sigma |
| PBS | 10010023 | ThermoFisher |
| PDMS | DO-SYL184-11 | Darwin Microfluidics |
| Penicillin Streptomycin | 10378016 | ThermoFisher |
| PFA | 16005 | Sigma |
| Phalloidin–Tetramethylrhodamine B isothiocyanate | P1951 | Sigma |
| PrestoBlue™ Cell Viability Reagent | A13261 | ThermoFisher |
| RatCol® Rat Tail Collagen for 3D Hydrogels | 5153 | Advanced Biomatrix |
| Recombinant Anti-active YAP1 antibody | ab205270 | abcam |
| Recombinant Anti-Vimentin antibody | ab92547 | abcam |
| RNeasy Mini Kit | 74104 | Qiagen |
| Silicone Rubber Snap-on Grommet Hole Plugs (14mm) | XY-1004 | AliExpress |
| Silicone Rubber Snap-on Grommet Hole Plugs (6mm) | XY-1020 | AliExpress |
| SlowFade™ Glass Soft-set Antifade Mountant, with DAPI | S36920-5X2ML | ThermoFisher |
| SYBR Green | A25742 | ThermoFisher |
| TritonX-100 | X100-500ML | Sigma |
| TWEEN 20 | P1379 | Sigma |
| VE-cadherin Polyclonal Antibody | 36-1900 | ThermoFisher |
| Vybrant™ Multicolor Cell-Labeling Kit (DiO, DiI, DiD Solutions, 1 mL each) | V22889 | ThermoFisher |
| YAP1 Polyclonal Antibody | #PA1-46189 | ThermoFisher |

## APPENDIX B. MACRO FOR CELL VIABILITY ASSESSMENT

This macro automates the process of counting live and dead cells from GFP and Texas Red channel images, calculating cell viability, and storing the results in a table.

```
// Close all open images and tables to start with a clean workspace
run("Close All");

// Create a new table named "Live/Dead Cell Viability Analysis" to store analysis results
Table.create("Live/Dead Cell Viability Analysis");

// Initialize counters for live and dead cells and a variable for indexing
liveCount = 0;
deadCount = 0;
j = 0;

// Prompt user to select a directory containing the image files for analysis
inputDir = getDirectory("Choose input directory");

// Determine output directory based on the input directory's parent directory
outputDir = File.getParent(inputDir);

// Read the list of files in the input directory
fileList = getFileList(inputDir);

// Extract the sample type from the directory name
sampleType = File.getNameWithoutExtension(inputDir);

// Iterate over each file in the directory
for (i = 0; i < fileList.length; i++) {
   // Check if the current file corresponds to the GFP (Green Fluorescent Protein) channel
   if (endsWith(fileList[i], "_GFP.tif")) {
      // Extract the sample name from the filename
      sampleName = replace(fileList[i], "_GFP.tif", "");

      // Open the GFP channel image
      open(inputDir + fileList[i]);

      // Apply preprocessing steps: despeckling, Gaussian blur, and background subtraction
      run("Despeckle");
      run("Gaussian Blur...", "sigma=1");
      run("Subtract Background...", "rolling=20");

      // Perform thresholding and watershed algorithm for segmenting live cells
      run("Robust Automatic Threshold Selection", "noise=25 lambda=3 min=50");
      run("Watershed");

      // Analyze particles to count live cells, display masks, and exclude edge particles
      run("Analyze Particles...", "size=10-Infinity circularity=0.0-1.00 show=Masks exclude clear");
      liveCount = nResults;

      // Calculate total cells, viability percentage and update the results table
      totalCells = liveCount + deadCount;
      viability = liveCount / totalCells;
      Table.set("Sample", j, sampleType);
      Table.set("Wells", j, sampleName);
      Table.set("Live Count", j, liveCount);
      Table.set("Dead Count", j, deadCount);
      Table.set("Total Cells", j, totalCells);
      Table.set("Viability", j, viability);

      // Close the current image
      close();

   } else if (endsWith(fileList[i], "_Texas Red.tif")) {
      // Open sample
      sampleName = replace(fileList[i], "_Texas Red.tif", "");
      open(inputDir + fileList[i]);

// Close all open images and tables to start with a clean workspace
run("Close All");
```

```
        // Preprocess image
        run("Despeckle");
        run("Gaussian Blur...", "sigma=1");
        run("Subtract Background...", "rolling=20");

        // Quantify dead cells in Texas Red channel
        run("Robust Automatic Threshold Selection", "noise=25 lambda=3 min=50");
        run("Watershed");

        // Analyze particles to count dead cells, display masks, and exclude edge particles
        run("Analyze Particles...", "size=10-Infinity circularity=0.0-1.00 show=Masks exclude clear");
        deadCount = nResults;

        // Calculate and display results for this sample
        totalCells = liveCount + deadCount;
        viability = liveCount / totalCells;
        Table.set("Sample", j, sampleType);
        Table.set("Wells", j, sampleName);
        Table.set("Live Count", j, liveCount);
        Table.set("Dead Count", j, deadCount);
        Table.set("Total Cells", j, totalCells);
        Table.set("Viability", j, viability);

        // Close the current image
        close();

        // Increment the sample index after processing both GFP and Texas Red images for a sample
        j++;
    }
}

// Update and display the results table
Table.update();


        // Preprocess image
```

## APPENDIX C. EFFICIENCY OF PRIMER SETS UTILISED IN THE STUDY

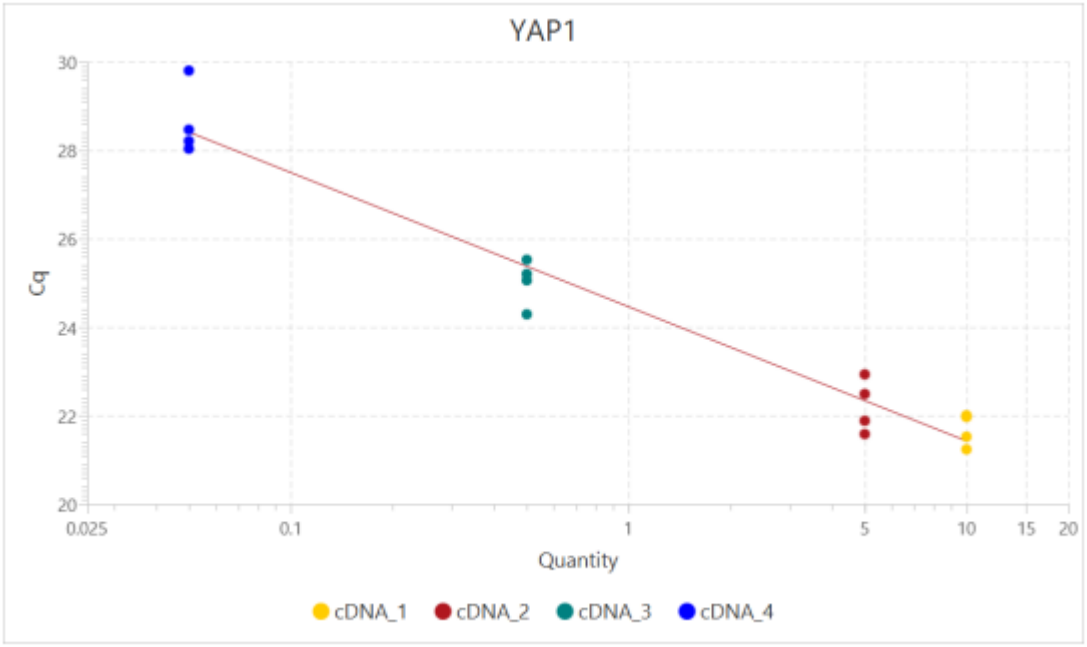


**Target:YAP1 Slope:-3.035 R²:0.958 Y-Inter:24.463 Eff:113.550 Error:0.170**

*Appendix Figure 1 Primer Efficiency of Primer YAP1*

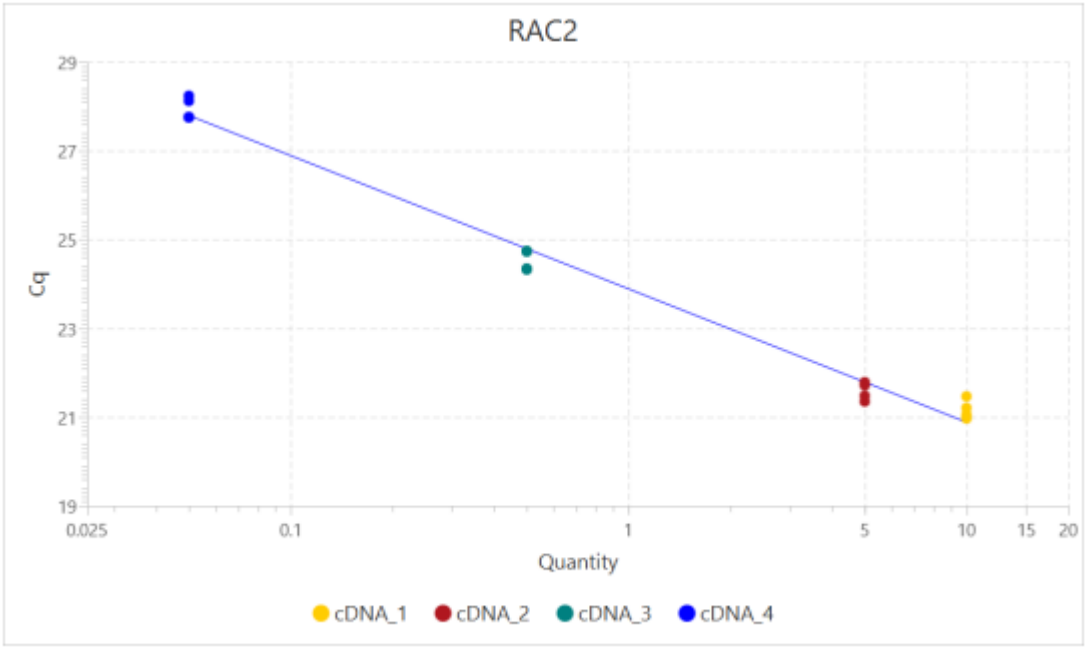


**Target:RAC2 Slope:-3.005 R²:0.987 Y-Inter:23.887 Eff:115.182 Error:0.091**

*Appendix Figure 2 Primer Efficiency of Primer RAC2*

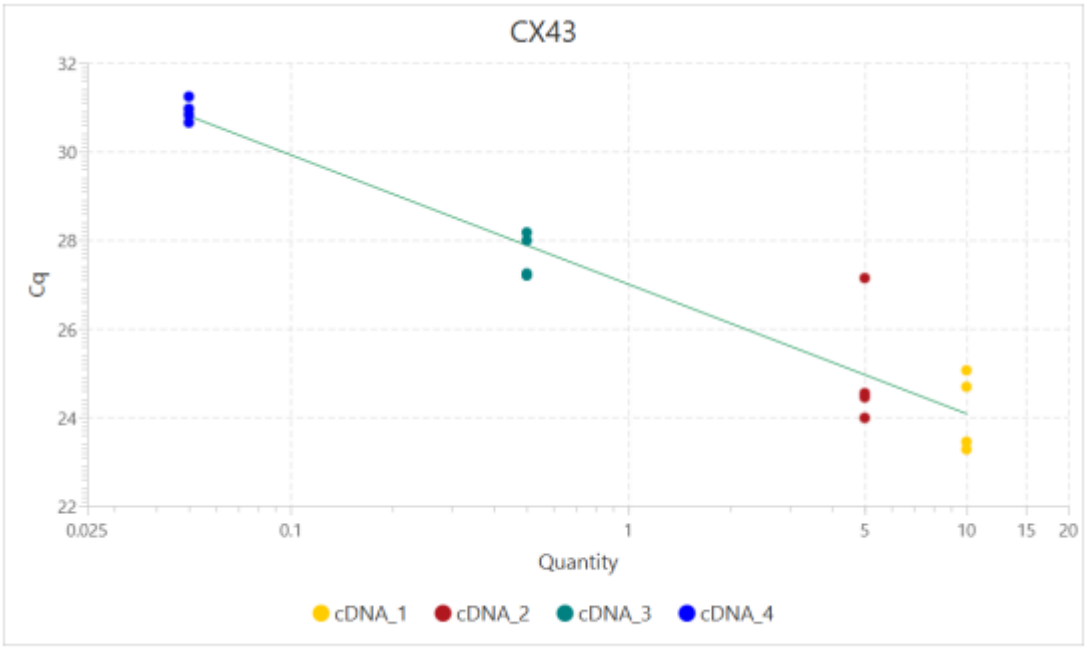


**Target:CX43 Slope:-2.921 R²:0.920 Y-Inter:27.003 Eff:119.952 Error:0.230**

*Appendix Figure 3 Primer Efficiency of Primer CX43*

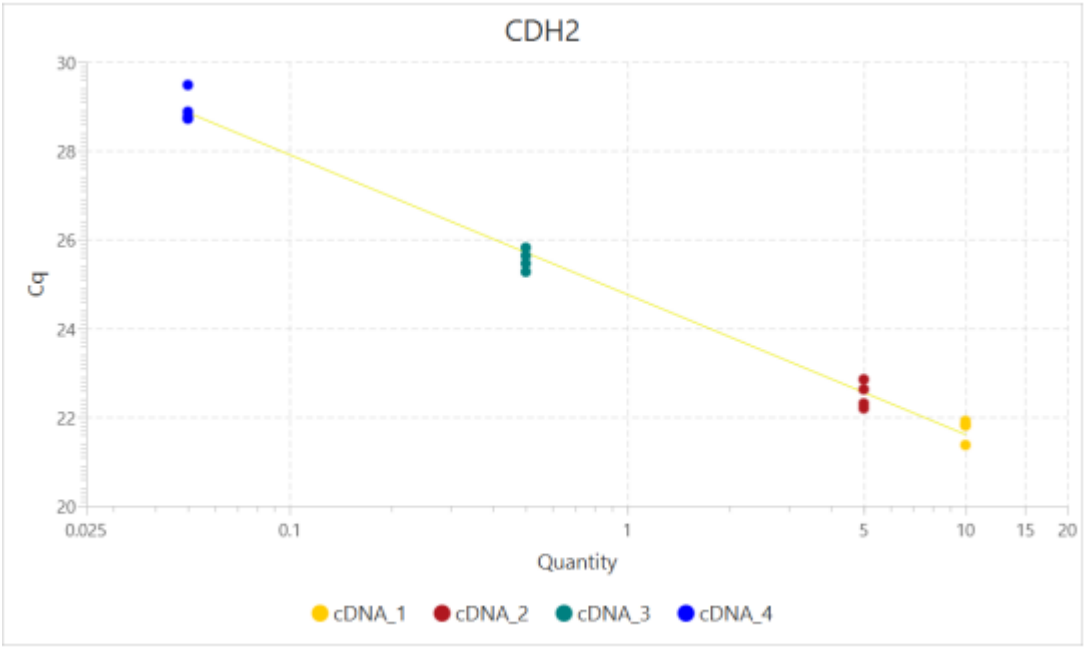


**Target:CDH2 Slope:-3.153 R²:0.991 Y-Inter:24.758 Eff:107.571 Error:0.081**

*Appendix Figure 4 Primer Efficiency of Primer CDH2*

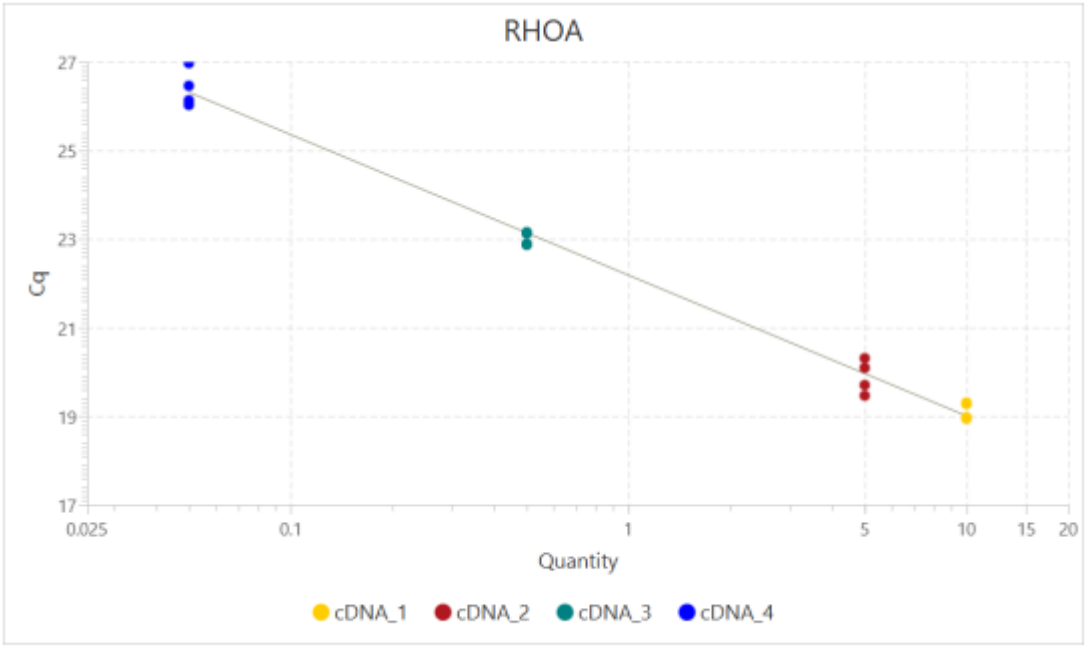


Target:RHOA Slope:-3.176 R²:0.990 Y-Inter:22.185 Eff:106.475 Error:0.085

*Appendix Figure 5 Primer Efficiency of Primer RHOA*

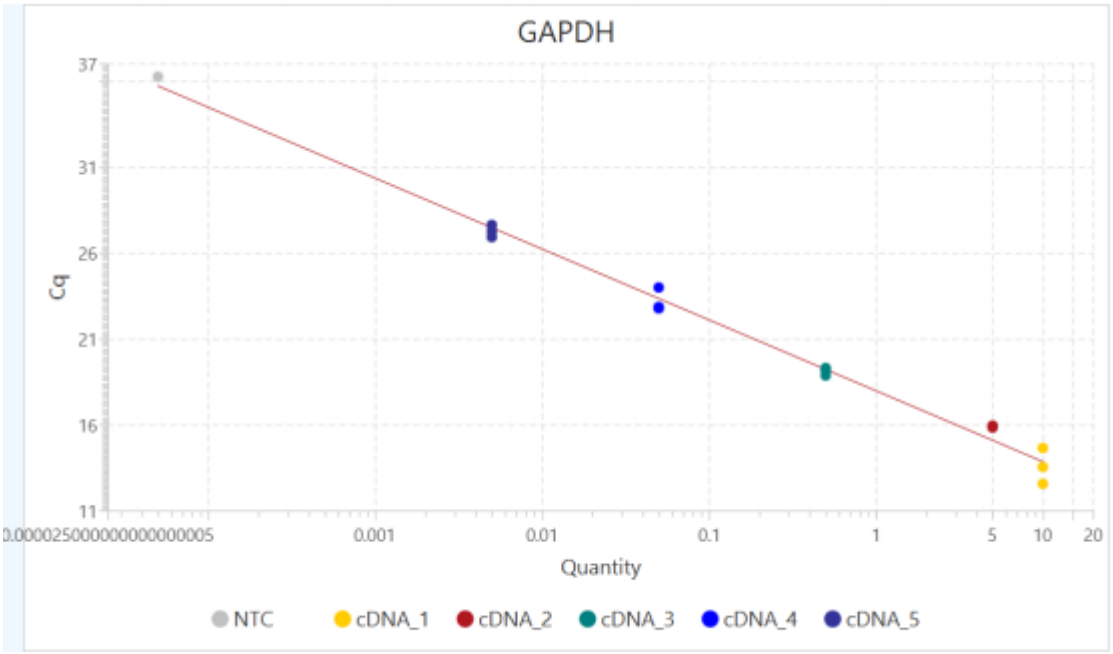


Target:GAPDH Slope:-4.121 R²:0.991 Y-Inter:17.969 Eff:74.850 Error:0.110

*Appendix Figure 6 Primer Efficiency of Primer GAPDH*

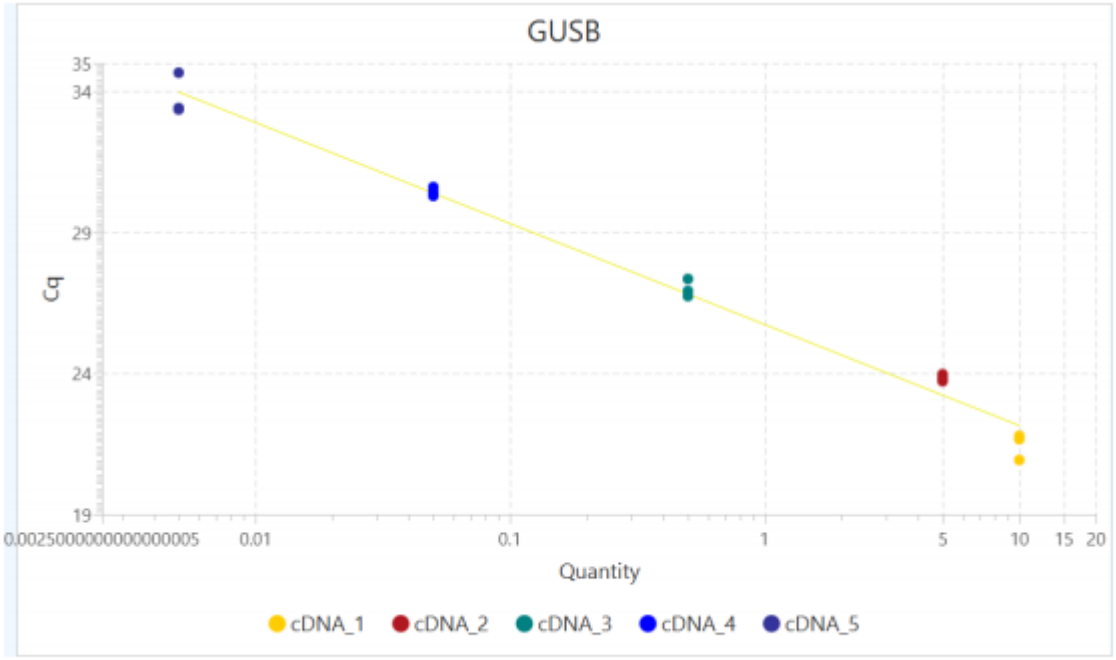


**Target:GUSB Slope:-3.583 R²:0.985 Y-Inter:25.728 Eff:90.155 Error:0.124**

*Appendix Figure 7 Primer Efficiency of Primer GUSB*

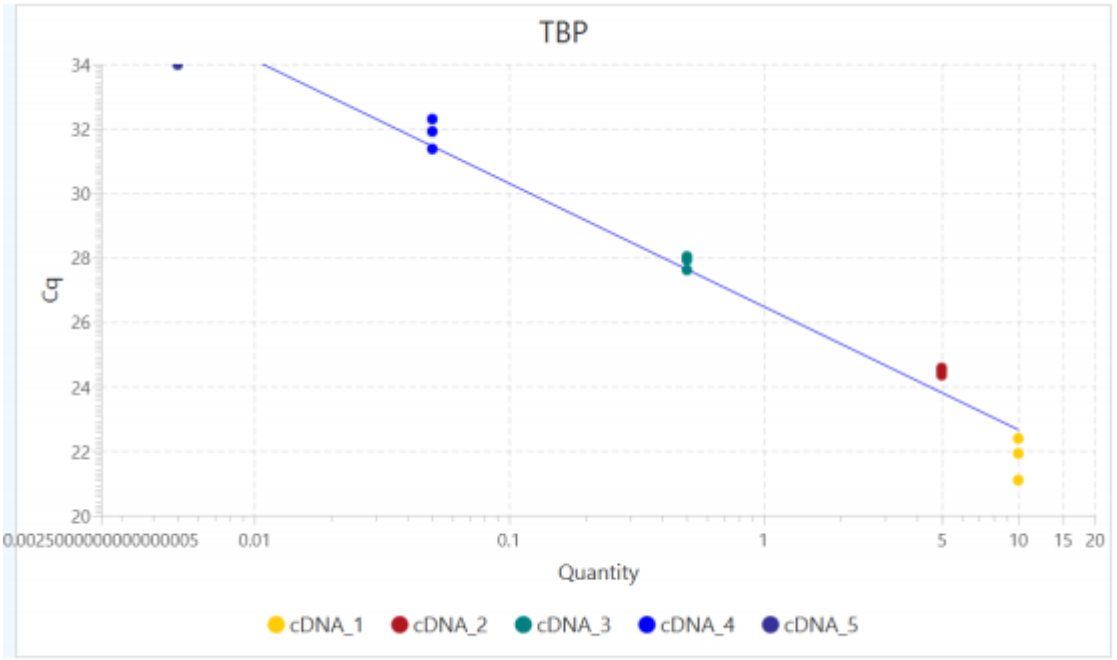


**Target:TBP Slope:-3.822 R²:0.968 Y-Inter:26.477 Eff:82.651 Error:0.211**

*Appendix Figure 8 Primer Efficiency of Primer TBP*

## APPENDIX D. CALCULATION AND INTERPRETATION OF ΔCT, ΔΔCT AND FOLD CHANGE

**Ct Values (Cycle Threshold):** The cycle number at which the fluorescence of a PCR product becomes detectable above the background level.
Interpretation: Lower Ct indicates higher initial amount of target nucleic acid; it's inversely proportional to the amount of target RNA/DNA.

**ΔCt (Delta Ct):** ΔCt = Ct of Housekeeping Gene (HKG) - Ct of Gene of Interest (GOI).
Purpose: Normalizes the expression of the GOI to a stable internal control (HKG), adjusting for sample-to-sample variability. The correct computation for the ΔCt value involves subtracting the Ct value of the gene of interest (GOI) from the Ct value of the housekeeping gene (HKG). This calculation is based on the premise that the expression of the housekeeping gene remains constant across all samples. By subtracting the Ct of the GOI from the Ct of the HKG, you normalize the expression of the GOI to the expression of the HKG.
Interpretation: Lower ΔCt indicates higher expression of the GOI relative to HKG.

**ΔΔCt (Delta Delta Ct):** ΔΔCt = ΔCt of experimental condition - ΔCt of control condition.
Purpose: Compares the relative expression of GOI in different experimental conditions to a control.
Interpretation: ΔΔCt values are already a form of log2 transformation because the PCR amplification process is exponential and doubles the amount of product with each cycle. Therefore, ΔΔCt directly represents the log2 fold change.

**Fold Change: 2^(ΔΔCt).**
Purpose: Converts the log2-transformed ΔΔCt values into a linear scale representing the actual fold increase or decrease in gene expression.
Interpretation: A fold change of 1 indicates no change, above 1 indicates upregulation, and below 1 indicates downregulation.

## APPENDIX E. DUNNET'S MULTIPLE COMPARISON TEST RESULTS FOR RADIATION DOSE RESPONSE

Two-way ANOVA revealed that both time post-IR and radiation dose significantly affected RFU, indicating changes in the proliferative capacity of AC-16 cardiomyocytes. A significant interaction effect was observed, showing that the impact of radiation on proliferation depends on the time elapsed since IR and vice versa. Dunnett's multiple comparison test was conducted at each time point to compare various radiation doses against the 0 Gy. These findings demonstrate that increasing radiation doses have a progressively negative effect on cardiomyocyte proliferation, with the impact becoming more pronounced as time post-IR increases.

*Appendix E - Table 1*

| | 24 hours | | 96 hours | | 120 hours | | 144 hours | | 160 hours | |
|---|---|---|---|---|---|---|---|---|---|---|
| | **Summary** | **P Value** | **Summary** | **P Value** | **Summary** | **P Value** | **Summary** | **P Value** | **Summary** | **P Value** |
| **0.5Gy vs. 0Gy** | ns | 0.7524 | *** | 0.0009 | **** | <0.0001 | ** | 0.0072 | ns | 0.5471 |
| **1Gy vs. 0Gy** | **** | <0.0001 | **** | <0.0001 | **** | <0.0001 | ** | 0.0023 | ns | 0.318 |
| **2Gy vs. 0Gy** | **** | <0.0001 | **** | <0.0001 | **** | <0.0001 | **** | <0.0001 | * | 0.0167 |
| **3Gy vs. 0Gy** | **** | <0.0001 | **** | <0.0001 | **** | <0.0001 | **** | <0.0001 | **** | <0.0001 |
| **Gy vs. 0Gy** | **** | <0.0001 | **** | <0.0001 | **** | <0.0001 | **** | <0.0001 | **** | <0.0001 |
| **5Gy vs. 0Gy** | **** | <0.0001 | **** | <0.0001 | **** | <0.0001 | **** | <0.0001 | **** | <0.0001 |
| **6Gy vs. 0Gy** | **** | <0.0001 | **** | <0.0001 | **** | <0.0001 | **** | <0.0001 | **** | <0.0001 |
| **8Gy vs. 0Gy** | ns | 0.9992 | **** | <0.0001 | **** | <0.0001 | **** | <0.0001 | **** | <0.0001 |
| **10Gy vs. 0Gy** | ns | 0.7835 | **** | <0.0001 | **** | <0.0001 | **** | <0.0001 | **** | <0.0001 |
| **12Gy vs. 0Gy** | **** | <0.0001 | **** | <0.0001 | **** | <0.0001 | **** | <0.0001 | **** | <0.0001 |

## APPENDIX F. REPRESENTATIVE IMAGE SEGMENTATION EXAMPLE

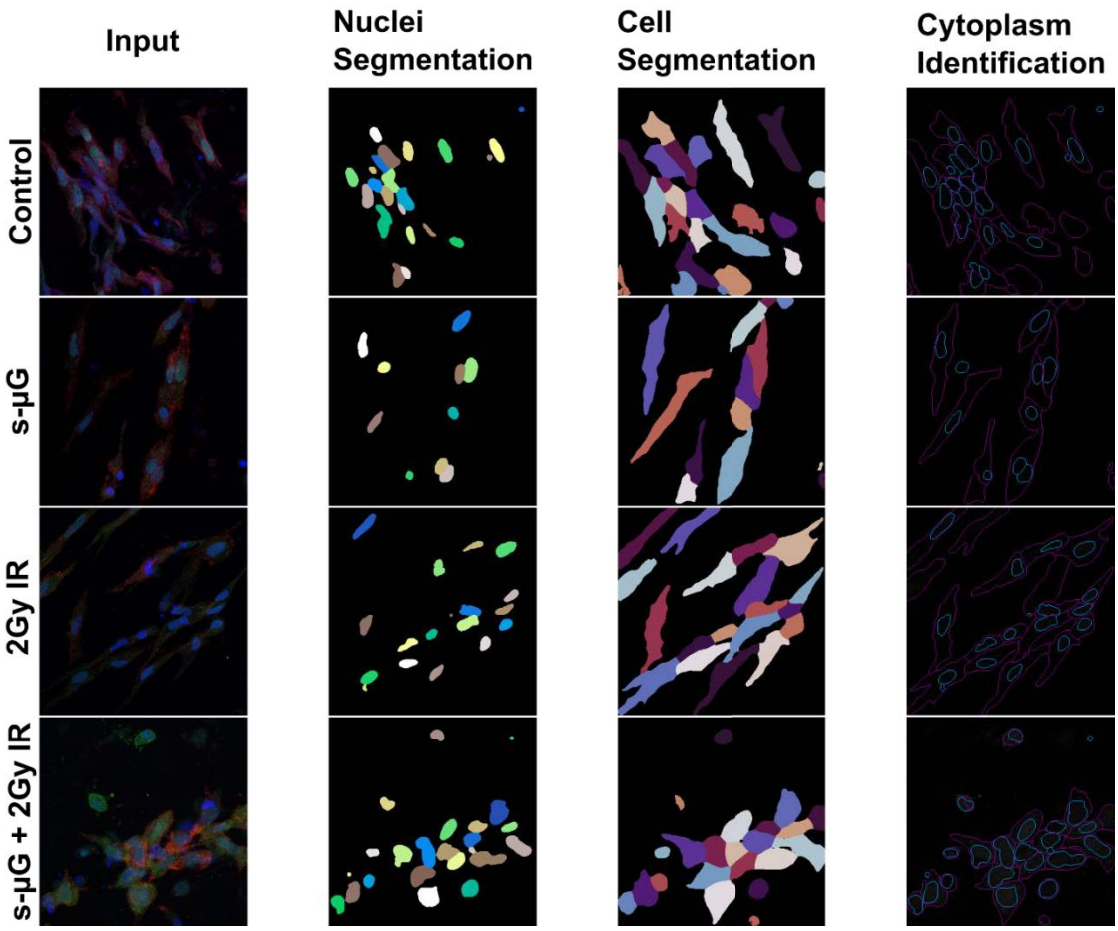


*Appendix Figure 9 Representative images showing fluorescently stained cells and corresponding segmentation masks used for analysis.*

The figure above illustrates the image segmentation process, aligned with the workflow presented in Figure 3.7. The left column displays the original stained images, showing nuclei, cytoplasm, and cellular structures. The middle columns depict the segmented masks generated through automated analysis, highlighting individual nuclei and cell bodies in distinct colours. The right column shows the overlaid outlines of segmented cells, identifying the cytoplasm and confirming the accuracy of the segmentation process. This sequence demonstrates the transition from raw data to segmented outputs, validating the steps outlined in the segmentation workflow for accurate quantification of cellular features.